2008

# A SYSTEMATIC STUDY OF THERMODYNAMIC AND TRANSPORT PROPERTIES OF LAYERED $Ca_{n+1}(Ru_{1-x}Cr_x)_nO_{3n+1}$

Vinobalan Durairaj
*University of Kentucky*, vinbalan@uky.edu

ABSTRACT OF DISSERTATION

Vinobalan Durairaj

The Graduate School
University of Kentucky
2008

# A SYSTEMATIC STUDY OF THERMODYNAMIC AND TRANSPORT PROPERTIES OF LAYERED $Ca_{n+1}(Ru_{1-x}Cr_x)_nO_{3n+1}$

---

ABSTRACT OF DISSERTATION

---

A dissertation submitted in partial fulfillment of the requirements for the degree of Doctor of Philosophy in the Department of Physics and Astronomy at the University of Kentucky

By
Vinobalan Durairaj

Lexington, Kentucky

Director: Dr. Gang Cao, Professor of Physics

Lexington, Kentucky

2008

# ABSTRACT OF DISSERTATION

## A SYSTEMATIC STUDY OF THERMODYNAMIC AND TRANSPORT PROPERTIES OF LAYERED $Ca_{n+1}(Ru_{1-x}Cr_x)_nO_{3n+1}$


Orbital degrees of freedom play vital role in prompting novel phenomena in ruthenium based Ruddlesden-Popper compounds through coupling of orbits to spin and lattice. Physical properties are then particularly susceptible to small perturbations by external magnetic fields and/or slight structural changes. Current study pertains to the impact when a more-extended 4d Ruthenium ion is replaced by a less-extended 3d Chromium ion.

Perovskite $CaRuO_3$ ($n=\infty$) is characterized by borderline magnetism and non-Fermi liquid behavior – common occurrences in quantum critical compounds. Remarkably, Cr substitution as low as $x=0.05$ abruptly drives $CaRu_{1-x}Cr_xO_3$ from a paramagnetic state to an itinerant ferromagnetic state ($M_S \sim 0.4\mu_B$/f.u.), where $T_C=123$K for $x=0.22$. The Cr-driven magnetism is highly anisotropic suggesting an important role of spin-orbit coupling. Unlike other chemical substitutions in the compound, Cr does not induce any Metal-Insulator transition that is expected to accompany the magnetic transition. The results indicate a coupling of Ru-4d and Cr-3d electrons that is unexpectedly favorable for itinerant ferromagnetism, which often exists delicately in the ruthenates.

Bilayered $Ca_3Ru_2O_7$ ($n=2$), an abode of huge anisotropy, exhibits a wide range of physical properties – Colossal Magnetoresistance occurring only when the spin polarized state is avoided, Antiferromagnetic-Metallic (AFM-M) state, Quantum Oscillations (periodic in 1/B and in B) that are highly angular dependent, to mention a few. Experimental results obtained so far provide a coherent picture illustrating that orbital order and its coupling to lattice and spin degrees of freedom drive the exotic electronic and magnetic properties in this Mott-like system. Transport and thermodynamic studies on $Ca_3(Ru_{1-x}Cr_x)_2O_7$ ($0 \leq x \leq 0.20$) reveal that AFM-M region is broadened with x that ultimately reaches 70K for $x=0.20$ (~8K for $x=0$). In this region, electron transport is enhanced and inhibited when B is applied along crystal's respective axes, confirming an intrinsic half-metallic behavior. Moreover, the difference in coercivities of Ru and Cr magnetic ions pave way for the first-ever observation of a strong spin-valve effect in bulk material, a quantum phenomenon so far realized only in multilayer thin films or

heterostructures. This discovery opens new avenues to understand the underlying physics of spin-valves and fully realize its potential in practical devices.

***Keywords:*** borderline magnetism and enhanced ferromagnetism, orbital ordering, CMR, half-metallic behavior, spin-valve effect

Vinobalan Durairaj

02 September, 2008

# A SYSTEMATIC STUDY OF THERMODYNAMIC AND TRANSPORT PROPERTIES OF LAYERED $Ca_{n+1}(Ru_{1-x}Cr_x)_nO_{3n+1}$

By

Vinobalan Durairaj

Dr. Gang Cao
*Director of Dissertation*

Dr. Joseph W Brill
*Director of Graduate Studies*

02 September, 2008
*Date*

RULES FOR THE USE OF DISSERTATIONS

Unpublished dissertations submitted for the Doctor's degree and deposited in the University of Kentucky Library are as a rule open for inspection, but are to be used only with due regard to the rights of the authors. Bibliographical references may be noted, but quotations or summaries of parts may be published only with the permission of the author, and with the usual scholarly acknowledgments.

Extensive copying or publication of the dissertation in whole or in part also requires the consent of the Dean of the Graduate School of the University of Kentucky. A library that borrows this dissertation for use by its patrons is expected to secure the signature of each user.

Name Date

_____

_____

_____

_____

_____

_____

_____

_____

_____

_____

_____

_____

_____

_____

_____

_____

_____

_____

DISSERTATION

Vinobalan Durairaj

The Graduate School

University of Kentucky

2008

# A SYSTEMATIC STUDY OF THERMODYNAMIC AND TRANSPORT PROPERTIES OF LAYERED $Ca_{n+1}(Ru_{1-x}Cr_x)_nO_{3n+1}$

---

DISSERTATION

---

A dissertation submitted in partial fulfillment of the requirements for the degree of Doctor of Philosophy in the Department of Physics and Astronomy at the University of Kentucky

By
Vinobalan Durairaj

Lexington, Kentucky

Director: Dr. Gang Cao, Professor of Physics

Lexington, Kentucky

2008

DEDICATION

To my dad, Mr. A.K. Durairaj, for being my best friend ever and for instilling in me the confidence through his immense support, guidance and encouragement

To the living memory of my mom, Mrs. A.K.D. Selvarangammal, who did not know anything in this world than to spend her entire life showering unconditional love and warm affection on her kids

To my duteous fiancée Ms. V.S. Shakila Devi for her guileless and indulgent love…

ACKNOWLEDGEMENTS

During the slow and often interrupted evolution of this dissertation I have accumulated many debts, only a proportion of which I have space to acknowledge here. However, I am grateful to all, who have helped extend my involvement in material science and who, through their own research, comments and questions, have encouraged, supported and enlightened me.

My first thanks and appreciation should go to Dr. Gang Cao for persevering with me as my advisor throughout the time it took me to complete this research and write the dissertation. I am fortune enough to have got an advisor like him as it is easy for anyone to draw from him an inspiration to do an intense and aggressive research. I have infinite number of reasons for thanking him, a finite pickings include, his perceptive advice, his prompt assistance when in need, his constructive criticism and his emotional support that he offered during my short stint as his student. The extensive research amenities I enjoyed in our 'Novel Materials Lab' were invaluable, be it the unlimited liquid Helium supply to do an uninterrupted set of low temperature experiments or the state-of-the-art crystal growth capability to develop novel materials. Add to them, the opportunities I was presented to use the facilities in the labs that are of ORNL's and NHMFL's standards, I should admit that I had an incredible research life at the University of Kentucky. I should also thank him for all the verbal and financial encouragements that he bestowed me with to attend conferences like APS March meetings and the Indo-US conference, which paved a fluid path for me to have useful interactions with eminent researchers in addition to showcasing and discussing the experimental results. I should store special thanks to him for hosting the '1$^{st}$ Workshop on Novel Electronic Materials' in 2004, which had enhanced my collaborative research by a sizeable aggregate.

I am grateful to Dr. Joseph Warren Brill, the Director of Graduate Studies, for his immense professional support. His role as a Ph.D. Advisory Committee member is irreplaceable as he guided me with his expertise in specific heat measurements on novel materials when I was working in his lab as a Research Assistant for a semester. As a graduate physics course instructor, his teaching could only set off my understanding in statistical mechanics to the next level.

I am indebted to my Ph.D. Advisory Committee member, Dr. Kwok-Wai Ng for his invaluable suggestions and recommendations in my literature search, particularly during the times when I had not decided on my research area. I should also thank him for his endowed collaborative research in the characterization of one of the two compounds that I have emphasized in this thesis. I owe a great deal to Dr. Sean Parkin, a member of the Ph.D. Advisory Committee, for all his help in resolving the crystal structures of our compounds, which forms the essential base for our material research. I cannot miss acknowledging here, the training he provided me in XRD by teaching the basics along with the elegant technique itself. I would like to extend my thanks to Dr. Lance DeLong for serving as an active member in my Ph.D. Advisory Committee. Also I should thank him for the discussions that I had with him, both in-class and informal, which inculcated the fundamentals of Condensed Matter Theory.

I wish to acknowledge the help I got from the technical staff in the machine shop and electronics shop who lent their helping hands whenever I was in need of them, be it devising a new probe or improvising the existing ones. I would like to express my thanks particularly to Mr. James Morris for his help in building vacuum pump fixtures and Mr. Gene Baber for his assistance with vacuum testing, prompt cryogenic fluid refill – to name a few. I should thank Mr. Larry Rice for training me in EDS to resolve the chemical composition in our compounds, which is vital for chemical substitution studies. Similarly, I would like to thank all the personnel, who made our experiments possible in the NHMFL (Tallahassee, FL) and ORNL (Oak Ridge, TN). My sincere thanks should go to (Late) Dr. Jack Crow, Founder and then Director of NHMFL, for approving our several proposals for the high magnetic field experiments that were crucial for my research studies.

It gives me an immense pleasure to acknowledge the debt I owe to our collaborators from who I have learnt much in the way of working with them. The technical discussions I had with Dr. Wen Hai Song and Dr. Yu Ping Sun – the visiting professors from Institute of Solid State Physics (Hefei, P R China), along with their help in setting up various experimental stations in our lab, are worth being recognized here. Though I did not do a big deal of LabView programming, the credit for whatever little I learnt should go to Dr. Song. I wish to thank Dr. Robert Guertin from Tufts University,

for the assistance in material characterization through his expertise in high pressure studies. Thanks should also be saved for Prof. Jae-Hoon Park and his research group from Pohang University of Science and Technology (Pohang, South Korea), who extended their help by performing spectroscopy studies on our compounds. Though I did not include a significant part of the results from all of these collaborative works due to various constraints, the professional interactions I had with these intellectuals helped enhance my quest for digging deep. I owe a lot to Dr. Ganapathy Baskaran from Institute of Mathematical Sciences (Chennai, India), as his friendship meant a great deal to me. The professional exposure he gave me, by being an undesignated mentor in my research student life, was priceless indeed.

I would like to express my thanks to Dr. Mike Cavegnero, for all his help as a chair of the Physics department. My research would not have been possible at the first place without the exclusive support from the academic committee that played a role in my admission to the Graduate School. In particular, I owe a great deal to the then Director of Graduate Studies, Dr. Thomas Troland also for his effective nomination letter in support of my Dissertation Year Fellowship application. I should like to acknowledge all the professors in the department, who enlightened me through different advanced graduate level courses. My special thanks are due to Dr. Ganapathy Murthy and Dr. Yuri Sushko, who taught me the basics of solid state physics extensively. In this context, my thanks also go to every individual that helped to organize the seminars in the department and offered me a chance both to disseminate and learn in equal proportions.

No research is ever a product of one person's efforts alone and certainly this one was no exception. This work would never have become reality without the help and suggestions of many supportive friends and colleagues. In that point of view, my biggest thanks should go to the friends from my lab that include Dr. Xiunu Lin, Ms. Shalinee Chikara, Mr. Oleksandr Kornetta, Mr. Alec Sim, Mr. Tongfei Qi, Ms. Esmat Elhami and Ms. Angela Douglass for their cooperation, who helped me in one way or the other in data collection and analysis portion of my research. I am particularly grateful to the discussions I had with Ms. Vijayalakshmi Varadarajan, which helped me put forward the developed ideas. I thank her specifically for the thoughtful and creative comments and more generally for exploring with me the boundaries of professional friendship. Apart

from the technical help I got from my lab colleagues, I would like to acknowledge the help I perceived from Mr. Rupak Dutta and Dr. Mridupawan Deka during the initial part of my graduate student life in understanding the basics of Electromagnetism and Quantum Mechanics.

I would like to appreciate Ms. Jean Carver and her sub-ordinates in the chemistry-physics library for offering their timely help with unlimited books for my literature search. The pleasure of being a research student in the department of physics was greatly enhanced by the gracious assistance of the administrative staff in the department office. I appreciate them for they have extended their helping hand all the time when I was in need of one. Particularly nothing could eclipse the patience of Mrs. Eva Ellis in dealing with the helium order complications that happens more often than not. The administrative help I got from Laurie, Joanna, Sharon, Emily, Rick, Carol and Sarah is not in any context less important.

I owe a great deal to Mr. Geoffrey William West and my other colleagues in West Physics Consulting for helping me fulfill my job responsibilities without compensating my thesis writing part. They provided material and spiritual support at critical and opportune times; my sincere thanks to them too. I wish to thank Ms. Sarojini Priyadarshini Rajachidambaram for taking special interest in serving me with critical comments on a draft of this work that helped shaping the thesis to whatever final form it has attained now.

Not least, perhaps, I should thank my family, for their patience and forbearance, whilst I have spent thousands of hours away from home working on my research. I strongly believe that the blessings, sacrifices, support, motivation and encouragement that my parents, brothers and sisters extended to me laid the foundation for the heights I reached.

I should not forget to acknowledge the funding agencies, which helped us turn the initial proposals into final results. I wish to thank the Graduate School, University of Kentucky for having supported me with Dissertation Year Fellowship and scholarships viz. Kentucky Graduate Scholarship, Commonwealth Research Awards etc. during the course of my graduate student life. The international and domestic travel support I

received for attending physics conferences also should not go unnoticed. Finally I would like to thank National Science Foundation for making all our projects possible.

To all the above individuals and to several colleagues whose names I cannot continue listing and who have assisted me in one way or another, especially in challenging me with alternative views, I feel very much indebted. While I believe that all of those mentioned have contributed to an improved final product, none other than me is, of course, responsible for the remaining weaknesses in this work.

Table of Contents

Acknowledgements ..... iii
List of Tables ..... xi
List of Figures ..... xii
Chapter One Introduction – A quick glance at the layered ruthenates
1.1 Introduction 1
1.2 Strongly correlated electron systems 2
1.3 Ruddlesden-Popper series 5
1.4 Chromium substitution 8
1.5 Outline of this dissertation 9
Chapter Two Theoretical Background
2.1 Introduction 11
2.2 Orbital contribution to magnetism 12
2.3 Contribution of charge carriers to magnetism 13
2.4 Magnetic interactions 15
2.5 Effects of extended d-electron orbitals 19
2.5.1 Crystal electric field 20
2.5.2 Hund's rule interaction 23
2.5.3 Spin-Orbit coupling 25
2.5.4 p-d electron hybridization 27
2.5.5 Electron-Phonon interaction 28
2.6 Metal-Insulator transition 32
2.7 Metals in strong applied fields 33
2.8 Magnetoresistance 37
Chapter Three Experimental Techniques
3.1 Introduction 41
3.2 Material synthesis 41
3.2.1 The importance of single crystals 42
3.2.2 Floating-Zone technique 43
3.2.3 Flux technique 51

3.3 Structure determination 54
3.4 Magnetic property measurement 59
3.5 Transport property measurement 62
3.6 Specific heat measurement 65
Chapter Four Thermodynamics and transport properties of $Ca_{n+1}(Ru_{1-x}Cr_x)_nO_{3n+1}$
4.1 Introduction 67
4.2 Evolution of physical properties 67
4.3 Perovskite ruthenates (n=∞) 71
4.3.1 Itinerant ferromagnet $SrRuO_3$ 73
4.3.2 Effect of chemical perturbation in $SrRuO_3$ 78
4.3.3 Enhanced ferromagnetism in $SrRu_{1-x}Cr_xO_3$ 79
4.3.4 Paramagnetic "bad" metal $CaRuO_3$ 82
4.3.5 $CaRuO_3$'s response to chemical substitution 87
4.3.6 Induced ferromagnetism in $CaRu_{1-x}Cr_xO_3$ 88
4.4 Mott-like bi-layered Calcium ruthenate (n=2) 103
4.4.1 A few intriguing problems in $Ca_3Ru_2O_7$ 103
4.4.2 Crystal structure 104
4.4.3 Magnetic ground state and thermodynamics 106
4.4.4 Antiferromagnetic metallic state 110
4.4.5 Nearly half-metallic characteristic 113
4.4.6 Tunneling Magnetoresistance 115
4.4.7 Colossal Magnetoresistance by avoiding a FM state 117
4.4.8 The orbital physics 122
4.4.9 Shubnikov-de Haas oscillations 128
4.4.10 Oscillatory magnetoresistance periodic in B 135
4.4.11 Non-linear conduction 138
4.4.12 Sensitivity of $Ca_3Ru_2O_7$ to chemical doping 139
4.4.13 Impact of Cr substitution on $Ca_3Ru_2O_7$ 141
Chapter Five Conclusions and Recommendations
5.1 Conclusions 169
5.1.1 Perovskite ruthenates 169

5.1.2 Bi-layered calcium ruthenate 172
5.2 Recommendations 175
References ..... 180
Vita ..... 188

List of Tables:

Table 3.1 Growth parameters for some of the successful systems tried in our lab. ..... 49

Table 4.1 Curie temperature ($T_C$) and the modified Curie-Weiss fit parameters ($\theta_{CW}$, $\chi_0$ and $\mu_{eff}$) tabulated for different x. ……..... 93

Table 4.2 $B_{C1}$ and $B_{C2}$ in $Ca_3Ru_2O_7$ for various temperatures when Bǁa axis. …..… 125

Table 4.3 Lattice parameters and unit cell volume tabulated for different x in $Ca_3(Ru_{1-x}Cr_x)_2O_7$. ……. 141

Table 4.4 Ordering temperatures ($T_{MI}$ and $T_N$), Curie-Weiss fit parameters ($\theta_{CW}$, $\chi_0$ and $\mu_{eff}$) and saturation moment ($M_S$) along a axis for $Ca_3(Ru_{1-x}Cr_x)_2O_7$ ($0 \leq x \leq 0.20$). ..... 145

Table 4.5 Electron and phonon contributions to the specific heat of $Ca_3(Ru_{1-x}Cr_x)_2O_7$ at B=0. …… 148

Table 4.6 $\Delta T_N/\Delta B$ for x=0.17 when B||a axis and B||b axis. …….. 155

List of Figures:

Figure 1.1 Density of states vs. band energy for electrons that are (a) independent (b) nearly independent (weakly correlated) (c) strongly correlated and (d) localized[7] (Courtesy of G Kotliar and D Vollhart, Physics Today 57 53 (2004)). ……. 3

Figure 1.2 A revised periodic table[9] of the d and f series of chemical elements based on the magnetic and transport properties. …..……. 4

Figure 1.3 Ruddlesden-Popper series of compounds, $A_{n+1}B_nO_{3n+1}$, for n=1, 2, 3 and ∞ with n increasing from left to right. ……... 6

Figure 1.4 A schematic representation of spin configuration for $Ru^{4+}$ ion (a) in an isolated ion, where the energy levels are degenerate and (b) in an octahedral field environment, where the degeneracy between $e_g$ and $t_{2g}$ levels is lifted due to CEF……... 6

Figure 1.5 A Simplified phase diagram of the RP Series of $(Ca,Sr)_{n+1}Ru_nO_{3n+1}$. ……. 7

Figure 1.6 Spin configuration in (a) $Cr^{3+}$ (S=3/2) and (b) $Cr^{4+}$ (S=1) ions in an octahedral field environment. …….. 9

Figure 2.1 $1/\chi$ vs. T plot for a paramagnet (PM), ferromagnet (FM) and antiferromagnet (AFM) following Curie–Weiss law. …… 14

Figure 2.2 A schematic representation of super-exchange interactions in TMOs. ….. 17

Figure 2.3 A schematic illustration of Stoner criterion for the stability of (a) paramagnetic and (b) ferromagnetic phases. ……..... 18

Figure 2.4 A diagrammatic representation of the origin of crystal field splitting in octahedral complexes. …….. 21

Figure 2.5 Crystal field splitting diagram for a crystal in a spherical and an octahedral field. ……...……. 22

Figure 2.6 Spin configurations in $Ru^{4+}$ ion describing the situations of a (a) low spin state and (b) high spin state. ……...…….. 24

Figure 2.7 Illustration of Jahn-Teller distortions and the eventual degeneracy removal in a tri-fold degenerate $t_{2g}$ and bi-fold degenerate $e_g$ orbitals. …….……... 30

Figure 2.8 Quantized Landau tubes in the presence of a magnetic field. ……..... 36

Figure 2.9 Scattering of electrons possessing representative spins in (a) a ferromagnet and (b) an antiferromagnet. ……..……... 38

Figure 3.1 A diagrammatic representation of Floating Zone Furnace technique that uses a double elliptic mirror. ..... 43
Figure 3.2 A molten zone (a) in normal state, (b) when power is excessive and (c) when power is insufficient. ..... 44
Figure 3.3 (a) An illustration of temperature profile in the double mirror furnace. (b) A sample rod at high temperatures. Red spots represent the melted area. (c) Illustrated temperature (in $^{o}$C) around the horizontal plane (in angle $^{o}$) in the furnace. ..... 46
Figure 3.4 Temperature cycle used for sintering the powdered material and the feed rod for the crystal growth. ..... 47
Figure 3.5 (a) The Au plated double elliptic mirror of the FZ furnace in action during a crystal growth. (b), (c), (d) & (e) Different stages in a $MnTiO_3$ crystal growth in the order of increasing time. The bright spots indicate the melting zone, where the temperature could be as high as 2000$^{o}$C. ..... 48
Figure 3.6 (*Top panel*) $MnTiO_3$ crystal (a) actual size and (b) magnified 60 times (actual size ~ 1 x 1 x 1 mm$^3$). (*Bottom panel*) Bluish $Nd_2WO_6$ crystals magnified (c) 10 and (d) 60 times (actual size ~ 2 x 1.5 x 1 mm$^3$). ..... 50
Figure 3.7 Temperature cycle used for growing single crystals of $Ca_3Ru_2O_7$ by the flux method. ..... 52
Figure 3.8 Flux grown $Ca_3Ru_2O_7$ crystals that are magnified (a) 10, (b) 60 and (c) 200 times (actual size of a single crystal ~ 0.5 x 0.4 x 0.4 mm$^3$). ..... 53
Figure 3.9 A diagrammatic explanation of Bragg's law. ..... 55
Figure 3.10 Working principle of an x-ray powder diffractometer. ..... 56
Figure 3.11 Intensity vs. 2θ graph for the powdered single crystals of $Ca_3Ru_2O_7$ at room temperature. ..... 57
Figure 3.12 A schematic representation of the working of an SEM[61]. ..... 58
Figure 3.13 An EDS spectrum of $CaRu_{0.82}Cr_{0.18}O_3$ showing Ca, Ru, Cr and O peaks. ..... 59
Figure 3.14 A schematic representation of the working principle of a SQUID magnetometer[63]. ..... 60
Figure 3.15 (a) Voltage measurement vs. position (b) A polycrystalline sample measurement using a SQUID magnetometer[65]. ..... 62

Figure 3.16 Circuit diagrams representing (a) Two probe and (b) Four probe techniques of resistivity measurements. ……. 63
Figure 3.17 A representative balanced bridge showing a "null" on the indicator. ….. 64
Figure 4.1 (a) Magnetization, M, and (b) Electrical resistivity in the basal plane, $\rho_{ab}$, as a function of temperature for $Sr_{n+1}Ru_nO_{3n+1}$[11]. ……... 69
Figure 4.2 Temperature dependence of (a) Magnetic Susceptibility ($\chi$) and (b) basal plane electrical resistivity ($\rho_{ab}$) for $Ca_{n+1}Ru_nO_{3n+1}$[82, 83, 84]. ……..……... 70
Figure 4.3 Crystal structure of (a) $SrRuO_3$ and (b) $CaRuO_3$[85]. Note that the structure of $SrRuO_3$ is more ideal and less distorted than that of $CaRuO_3$. …… 71
Figure 4.4 Magnetic susceptibility, $\chi$, of both $SrRuO_3$ and $CaRuO_3$ as a function of temperature, T, for $1.7 \leq T \leq 350$ K. Note that the susceptibility for $CaRuO_3$ is multiplied by 100 for convenience. ……... 72
Figure 4.5 (a) Temperature dependence of Magnetization, M (T), of $SrRuO_3$ at B=0.01 T, showing the Curie Temperature, $T_C$ (b) $1/\Delta\chi$ vs. T that shows a positive Curie-Weiss temperature, $\theta_{CW}$ confirming the ferromagnetic interactions between $Ru^{4+}$ spins. …. 75
Figure 4.6 (a) Basal plane resistivity, $\rho_{ab}$, as a function of T at B=0 T for $1.7 \leq T \leq 350$ K. (b) Fermi liquid behavior of $\rho_{ab}$ at B=0 T for $1.7 \leq T \leq 20$ K. ……...……. 77
Figure 4.7 Magnetic and electronic phase diagram as a function of Mn content in $SrRu_{1-x}Mn_xO_3$. …… 79
Figure 4.8 Temperature dependence of (a) magnetization, M, at B=0.01 T and (b) basal plane resistivity, $\rho_{ab}$, at B=0 T for $SrRu_{1-x}Cr_xO_3$ ($0 \leq x \leq 0.20$) in the temperature range $1.8 \leq T \leq 300$ K. ……... 81
Figure 4.9 Magnetic isotherms, M (B), at T=2 K for $SrRu_{1-x}Cr_xO_3$ ($0 \leq x \leq 0.20$), when magnetic field is applied along the basal plane in the range $0 \leq B \leq 7$ T. ……... 82
Figure 4.10 (a) Magnetic susceptibility as a function of temperature at B=0.05 T for $1.7 \leq T \leq 350$ K. (b) $1/\Delta\chi$ as a function of temperature at B=0.05 T for $1.7 \leq T \leq 350$ K. $\chi$ (T) follows the modified Curie-Weiss law with $\theta_{CW}$=-175 K. ……... 84
Figure 4.11 (a) Resistivity, $\rho$, as a function of temperature at B=0 T for $1.7 \leq T \leq 350$ K. (b) Non-Fermi liquid behavior of $\rho$ at B=0 T (*left scale*) and B=7 T (*right scale*) for $1.7 \leq T \leq 20$ K. …….. 86

Figure 4.12 (a) Lattice parameters for a-, b- (*left scale*) and c-axis (*right scale*) and (b) the volume of the unit, V, as a function of Cr concentration, x, for $CaRu_{1-x}Cr_xO_3$. The x dependence of lattice parameters suggests no presence of $Cr^{3+}$ and/or $Ru^{5+}$ ions in the compounds. …….. 89

Figure 4.13 (a) Temperature dependence of a-axis magnetization, $M_a$, for a few representative concentrations in $CaRu_{1-x}Cr_xO_3$ (b) Temperature dependence of the c-axis magnetization, $M_c$, for a few representative x. …… 91

Figure 4.14 $1/\Delta\chi$ vs. T curves for a few representative x viz. 0, 0.05, 0.18 and 0.36. Note that the x intercept ($\theta_{CW}$) is negative only for x=0 and are positive for all x > 0. Solid lines are guide to the eyes. ……... 92

Figure 4.15 (a) The Curie temperature, $T_C$, (*left scale*) and the Curie-Weiss temperature, $\theta_{CW}$, (*right scale*) as a function of x. (b) The x dependence of effective moment, $\mu_{eff}$, (*left scale*) and temperature-independent susceptibility, $\chi_0$, (*right scale*) estimated from the Curie-Weiss fit in the temperature range $150 \leq T \leq 350$ K. …… 94

Figure 4.16 Isothermal magnetization, M (B), at T=2 K for $CaRu_{1-x}Cr_xO_3$ along a axis. …….. 96

Figure 4.17 (a) Isothermal magnetization, M (B), along a axis for x=0.15 for various temperatures (b) Temperature dependence of $B_{C1}$ and $B_{C2}$ (*left scale*) and of saturation moment, $M_S$ (*right scale*). The shaded region in green displays the meta-stable region. …….. 97

Figure 4.18 (a) Isothermal magnetization, M, for a axis and c axis at T=2 K for x=0.15. (b) The saturation moment, $M_S$, for a- and c- axis directions at T=2 K. ……... 99

Figure 4.19 (a) Basal plane resistivity, $\rho_{ab}$, on a logarithmic scale vs. temperature for x=0, 0.05, 0.08, 0.15, 0.18 and 0.36. (b) $\rho_{ab}$, (*left scale*) and magnetization, M, (*right scale*) as a function of temperature for x=0.36. …… 101

Figure 4.20 A simplified x-T phase diagram of $CaRu_{1-x}Cr_xO_3$ for $0 \leq x \leq 0.36$. ….. 102

Figure 4.21 (a) Crystal structure of $Ca_3Ru_2O_7$, projected along the c axis (*top figure*) and the ab plane (*bottom figure*). (b) The TEM image depicts the double layered nature of the compound and (c) the electron diffraction image reveals the anisotropic nature within the basal plane of $Ca_3Ru_2O_7$[113]. ……... 105

Figure 4.22 Temperature dependence of Magnetization, M (T), for magnetic fields applied parallel to the three principal crystal axes with B=0.5 T. ……..…….. 106
Figure 4.23 Magnetic isotherms, M (B), for magnetic field applied along different crystallographic axes at T=2 K. ……. 107
Figure 4.24 Spin configuration in $Ca_3Ru_2O_7$ for (a) $B < B_C$ and (b) $B > B_C$. …… 108
Figure 4.25 Temperature dependence of resistivity for $Ca_3Ru_2O_7$ at B=0 T for $1.7 \leq T \leq 350$ K. ……. 110
Figure 4.26 Temperature dependence of (a) inter-plane ($\rho_c(T)$) and intra-plane ($\rho_a(T)$) resistivities in the left scale and lattice parameter c in the right scale. (b) Zoomed portion of the $\rho_c(T)$ curve for $45 \text{ K} \leq T \leq 60$ K to show the region of antiferromagnetic metallic state ($48 \text{ K} \leq T \leq 56$ K)[115]. ……. 112
Figure 4.27 $R_H$ vs. T in $Ca_3Ru_2O_7$ for $1.7 \leq T \leq 300$ K when B||c axis=7 T. ……..... 113
Figure 4.28 Temperature dependence of the *c*-axis resistivity, $\rho_c$, at a few representative B up to 28 T applied along (a) a axis and (b) b axis for $1.7 \leq T \leq 80$ K[128]. …….. 114
Figure 4.29 Field dependence of the inter- layer resistivity, $\rho_c(B)$, (*left scale*) and that of the magnetization, M (B), (*right scale*) at T=5 K showing the coupling of spin polarization with the electron transport[115]. …… 116
Figure 4.30 Electron conduction processes in Ru-O/Ca-O/Ru-O layer junction when the magnetic layers are (a) antiferromagnetic ($B \leq 6$ T) and (b) ferromagnetic ($B > 6$ T). ……... 116
Figure 4.31 Magnetic field dependence of Magnetization, M (B), (left scale) and that of the inter-plane resistivity ($\rho_c(B)$) (right scale) at T=0.4 K for all the crystallographic axes. The drop in resistivity for B||b axis is much more than that for B||a axis, suggesting the dominance of orbitals on the electronic conductivity. Note that the resistivity measurements were performed in an applied field up to B=45 T. …….…… 118
Figure 4.32 Magnetic field dependence of the intra-plane resistivity ($\rho_a(B)$) at T=0.4 K for $0 \leq B \leq 33$ T along the three crystallographic axes. ……. 119
Figure 4.33 Magnetic field dependence of the inter-plane ($\rho_c$) and intra-plane ($\rho_a$) resistivities at T=0.4 K for $0 \leq B \leq 33$ T applied along b axis. …….. 121

Figure 4.34 A schematic representation of spin configuration in $Ru^{4+}$ ion (a) in an isolated ion (b) in an octahedral field (c) in $Ca_3Ru_2O_7$ after Jahn-Teller distortions. (d) The range of energy distribution in the d orbitals after the degeneracy is being lifted by Jahn-Teller distortion. ……..……... 122

Figure 4.35 Isothermal magnetization, M (B), for field applied parallel to (a) a axis and (b) b axis for temperature range $40 \leq T \leq 52$ K. Magnetic field dependence of inter-plane resistivity ($\rho_c(B)$) when field applied along (c) a axis and (d) b axis in the same temperature range. …….. 124

Figure 4.36 (a) Temperature dependence of M (*triangles*) and $\Delta\rho/\rho(0)$ (*solid circles, right scale*) at 7 T for B||a and b axes. (b), (c) Phase diagrams plotted as B vs T summarizing various phases for B||a and b axes, respectively. .....…..... 126

Figure 4.37 $\rho_c$ as a function of B for field applied along different angles in the ac plane at T=0.6 K. ……. 129

Figure 4.38 (a) $\rho_c$ for B rotating in the ac-plane with $\theta$=0 and 90° corresponding to B||a and B||c, respectively; (b) Enlarged $\rho_c$ for clarity. Note that $\rho_c$ is in logarithmic scale in (a) and B changes from 11 to 45 T in both (a) and (b). ……. 131

Figure 4.39 The amplitude of the quantum oscillations as a function of inverse field, $B^{-1}$ for various $\theta$ and for (a) T=0.4 and (b) 1.5 K. ……...… 133

Figure 4.40 Estimation of frequency of oscillations using FFT for a particular temperature and angle (1.5 K and $26^o$ away from a axis). ……. 134

Figure 4.41 The angular dependence of the frequency (solid circles for $B > B_C$, and empty circle for $B < B_C$) for T=0.4 K and 1.5 K and the metamagnetic transition $B_C$ (solid squares) (*right scale*). ……. 135

Figure 4.42 (a) The amplitude of the quantum oscillations as a function of B for B||[110] and T=0.5 K and (b) for various temperatures up to 15 K. (c) The amplitude of the quantum oscillations as a function of inverse field $B^{-1}$ for B||[110] and T=0.5 K and (d) for various temperatures up to 15 K. ……. 136

Figure 4.43 The amplitude of the quantum oscillations for various temperatures up to 15 K. ……... 138

Figure 4.44 Temperature dependence of a axis resistivity, $\rho_a(T)$, for as grown ($Ca_3Ru_2O_7$) and oxygenated ($Ca_3Ru_2O_{7+\delta}$) samples. ……. 140

Figure 4.45 Magnetization, M, as a function of temperature, T, for (a) a axis, $M_a$, and (b) b axis, $M_b$, at B = 0.5 T for all x. ……... 143
Figure 4.46 The magnetic isotherms for (a) a ($M_a$) and (b) b ($M_b$) axes at T=2 K for all x. ……... 144
Figure 4.47 (a) Temperature dependence of specific heat, C, expressed as C/T vs. T at B=0 T for x=0, 0.17 and 0.20. (b) Zoomed portion of C/T vs. T for x=0.17 and 0.20 to show the broadened AFM-M state. ……...…. 147
Figure 4.48 The x dependence of $T_N$ and $T_{MI}$ for $Ca_3(Ru_{1-x}Cr_x)_2O_7$ ($0 \leq x \leq 0.20$). .. 149
Figure 4.49 I-V characteristics at B=0 T for (a) x=0.05, (b) x=0.17 and (c) x=0.20 for different temperatures. ……... 150
Figure 4.50 x dependence of (a) critical current ($I_C$) and (b) threshold voltage ($V_T$) for different temperatures viz. T= 20, 30, 40 and 60 K at B=0. …….. 151
Figure 4.51 The temperature dependence of magnetization M for x = 0.17 for both a axis ($M_a$) and b axis ($M_b$) at B = 0.5 T (*left scale*). *Right scale*: C/T for x = 0.17 as a function of T. …… 153
Figure 4.52 The temperature dependence of magnetization M for x = 0.17 (a) for a-axis ($M_a$) and (b) b-axis ($M_b$) for various magnetic inductions B up to 7 T. …… 154
Figure 4.53 C/T vs. T for x=0.17 (a) when B=0 and 9 T along ab plane and c axis (b) when B=0, 3, 3.5, 4 and 9 T along ab plane. .....…….. 156
Figure 4.54 C/T vs. $T^2$ for x=0.17 when B=0 and 9 T along ab plane and c axis in the temperature range $1.8 \leq T \leq 9$ K. ……... 158
Figure 4.55 Temperature dependence of (a) $\rho_c$ for B||a-axis, ||b-axis and ||c-axis for B = 0 and 7 T. (b) $\rho_{ab}$ for both B||a-axis and B||b-axis at B = 0 and 12 T for x=0.17. …… 159
Figure 4.56 Temperature dependence of the c-axis resistivity, $\rho_c$, for x = 0.17 for (a) B||a-axis and (b) B||b-axis for various magnetic inductions up to 7 T. ……. 161
Figure 4.57 Electronic contribution to the specific heat, $\gamma$, vs. B when B||ab (*left scale*) and metal-insulator transition temperature, $T_{MI}$, vs. B when B||b (*right scale*) for x=0.17. *Note*: $T_{MI}$ for B=9 T is obtained from specific heat measurements done with B||ab. ……... 162

Figure 4.58 Field dependence of M for (a) $M_a$ and (b) $M_b$ and field dependence of the magnetoresistivity ratio defined as $[\rho_c(B)-\rho_c(0)]/\rho_c(0)$ for (c) B||a-axis and (d) B||b-axis for $2 \leq T \leq 85$ K. …… 163

Figure 4.59 The field dependence of $[\rho_c(B)-\rho_c(0)]/\rho_c(0)$ and M (*right scale*) for B||b-axis at (a) T = 40 K, (b) 43 K and (c) 47 K. …….. 165

Figure 4.60 Spin configuration in $Ca_3(Ru_{1-x}Cr_x)_2O_7$, x=0.17 for (a) $B < B_{C2}$, (b) $B_{C2} < B < B_{C1}$ and (c) $B > B_{C1}$. Note that the double-line arrow indicates spin in the Cr-O layer. ……... 167

Figure 4.61 T-B diagram that represents different spin configurations in $Ca_3(Ru_{0.83}Cr_{0.17})_2O_7$. ……... 168

Figure 5.1 Isothermal magnetic field dependence of magnetization, M, (*left scale*) and magnetoresistance, MR, (*right scale*) when (a) B||I and (b) B⊥I at T=1.7 K for $CaRu_{0.82}Cr_{0.18}O_3$ in the applied field range $-7 \leq B \leq 7$ T. …….. 177

# Chapter One

## A quick glance at the layered ruthenates

### 1.1 Introduction:

Focus in studying complex materials, transition metal oxides[1] (TMOs) in particular, is stimulated by their wealth of inherent novel properties, the complexities in the underlying physics and their promising technological applications. It should not be surprising that TMOs have been in the forefront of materials research, in the last few decades. For instance, studies on High Temperature Superconductors (HTSC)[2] spearheaded materials research during the late 80's and the years that followed; colossal magnetoresistance (CMR) in manganites[3,4] unveiled fascinating physics that had been challenging our fundamental understanding of materials. The orbital occupation and its fluctuations strongly influence the magnetic and other properties of these systems. On the other hand, the 4d-electron based ruthenates possessing more extended 4d orbitals than the 3d-counterparts are only more complex as one has to include the more pronounced orbital degrees of freedom in the energy scale. Indeed, these TMOs comprise beguiling properties and present us profound intellectual challenges that will last well into next decade.

Privileged to have a broad range of interesting and intriguing physical properties, the TMOs can be tailored for a wide variety of applications including low-loss power delivery, quantum computing using Cooper pairs, ultra high-density magnetic data storage and more recently spintronic[5] applications. Giant magnetoresistance (GMR)[6], a spintronic effect that utilize a weak magnetic field to align the spins of electrons, is the technology used in modern computer hard drives for dense data storage that could be read quickly. Computers with spintronic memory will be able to store more data in a smaller area, access that data faster and consume less power than the traditional semiconductor RAM chips. Some of the materials of our interest exhibit the CMR[3] effect, where the magnetic resistance changes several orders of magnitude larger than in GMR. These magnetic materials have broad applications in magnetic sensor technology (GMR read-write head, magneto-optic storage) and in device structures (MRAM, spin-injection transistors) that are being developed for microelectronics and communication technology.

Indeed, the colossal magnetoresistive materials have potential to serve as new generation magnetic storage devices.

The descriptions on the materials' potential applications are beyond the scope of this thesis. However, a material's contribution to technological advancements should only motivate and drive us more in the direction of investigating the exciting physics behind its fascinating physical behavior.

**1.2 Strongly correlated electron systems:**

Coupling of the mobile electrons with the atomic or molecular network in a material determines whether they would behave as free electrons or nearly free electrons or strongly correlated ones. Physical systems that we understand well correspond to ensembles of free particles. This simple approach is valid because the Coulomb energy of electrons is much smaller than their kinetic energy in most cases. But in materials comprised of transition metals, the electrons experience strong Coulombic repulsion because of their spatial confinement in the d orbitals. As a result of the prevailing competition between the correlation and the kinetic energies, the local density of states (DOS) depends on the ratio of the correlation strength and the bandwidth. The variations of DOS with the ratio of interaction energy (U) and the kinetic energy of electrons (W) are shown in **Fig. 1.1**[7].

When electrons are completely independent (U=0), the DOS takes up a shape of a half ellipse with Fermi energy ($E_F$) being located in the middle of the band as shown in **Fig. 1.1 (a)**, which represents the characteristics of a pure metal. On the other hand, when U is larger than W, the condition depicts the picture of a localized electron system and the DOS peaks at the ionization energy and the electron affinity of the atom (**Fig. 1.1 (d)**). But the evolution of DOS between these well-established limits could not be explained using either the density functional theory (DFT)[8] or the atomic theory. It demands a much more advanced dynamical mean field theory (DMFT)[7] approach that treats both the quasiparticle features and the Hubbard bands on the same footing, since a three peak feature appears in the intermediate correlation region. In the nearly independent electrons picture (U<W), however, the electrons are described as quasiparticles (weakly correlated) and the Fermi liquid model accounts for the distinguished peak at $E_F$ (see **Fig. 1.1 (b)**). But in the strongly correlated regime (U~W)

(**Fig 1.1 (c)**), the central quasiparticle peak at $E_F$ is complimented by two broadened peaks close to the ionization energy and electron affinity of the atom. The additional peaks originated from local atomic excitations (Hubbard bands) are broadened as a result of electrons hopping away from the atom.

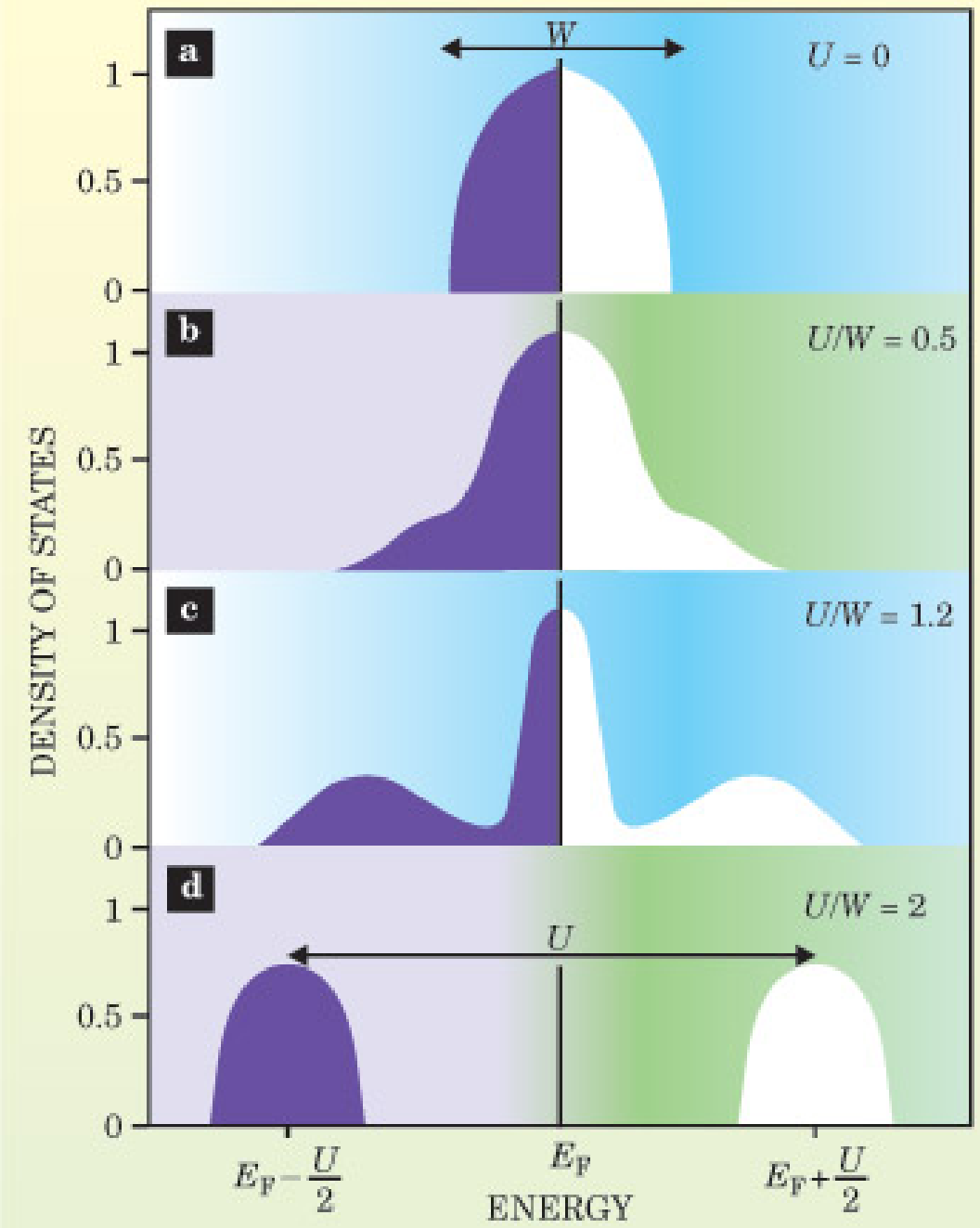


**Fig. 1.1** Density of states vs. band energy for electrons that are **(a)** independent **(b)** nearly independent (weakly correlated) **(c)** strongly correlated and **(d)** localized[7] (Courtesy of G Kotliar and D Vollhart, Physics Today **57** 53 (2004)).

The d and f series in the modern periodic table of chemical elements was rearranged by James Smith et. al.,[9] based on the magnetic and transport properties as shown in **Fig. 1.2**. The elements highlighted by the diagonal whitish stripe form a rough dividing line between the localized (magnetism) and itinerant (superconductivity) long range collective behavior. Therefore, the d and f electrons in those elements that lie in the enhanced region, Ru and Cr for instance, are poised between localization and itinerancy. They form the strongly correlated regime displayed and discussed in **Fig. 1.1** and have unpredictable ground states describing them.

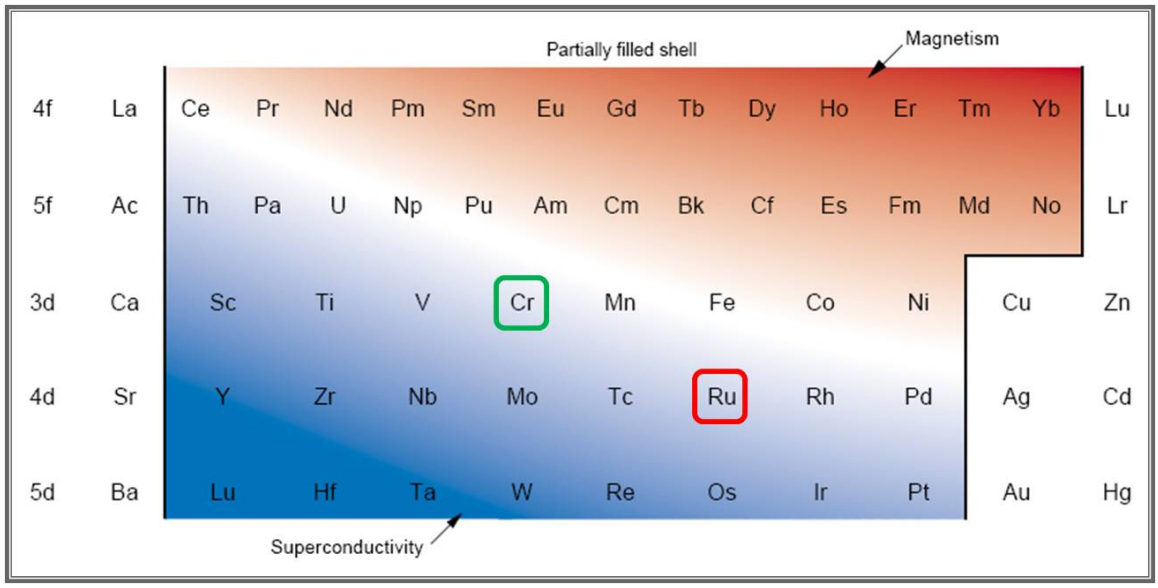


**Fig. 1.2** A revised periodic table[9] of the d and f series of chemical elements based on the magnetic and transport properties.

Obviously many-particle systems in which the strong local repulsion between electrons plays a crucial role are in the center of present physical interest. The subtle coupling and competition between electron, lattice, orbital and spin degrees of freedom are the essence of those Strongly Correlated Electron Systems (SCES)[10]. The electronic correlations can cause striking many-body effects like electronic localization, magnetism and charge ordering which cannot be described in the generally very successful independent particle picture. These interactions lead to the emergence of exciting novel ground states and phase transitions where a new picture for quasiparticles needs to be defined. Examples of such systems are cuprates[2], manganites[3,4], ruthenates[11] and other transition-metal oxides. The interplay of the d orbital electrons' internal degrees of

freedom – spin, charge and orbital moment, makes these systems extremely sensitive to small external perturbations such as temperature, pressure or doping. The drastic effects can range from huge changes in resistivity inducing a metal insulator transition to influencing exceptionally high transition temperatures. A few such compounds are discussed in this thesis.

**1.3 Ruddlesden-Popper series:**

Ruddlesden-Popper (RP) series[12] are layered compounds with general formula $A_{n+1}B_nO_{3n+1}$, where A (=Ca, Sr, La etc.), B (=Ru, Cu, Mn, Cr etc.) represent cations and O represents oxygen (an anion). Here n denotes the number of transition metal layers (BO) in a unit cell. The compounds are structured in such a way that the metallic BO layers are separated by the insulating AO layers along the c axis as shown in **Fig. 1.3**. Hence a progression in 'n' from 1 to infinity corresponds to a change in the dimensionality of the compounds as shown in the figure. A tetravalent transition metal, Ru for example, in the structure is surrounded by six O ions and an octahedron is formed with B as the central ion. The $BO_6$ octahedra are corner sharing and hence the B–B interaction is mediated through oxygen. The interactions of magnetic B ions through non-magnetic O ligands dictate the physical properties of the compound.

Even though a fleet of materials of our interest extends throughout the spectrum of transition metal oxide series that includes Ru, Rh, and Ir, the main focus of the thesis remains on the calcium and strontium ruthenium oxides, $(Ca, Sr)_{n+1}Ru_nO_{3n+1}$. The central characteristic of these 4d-shell based transition metal oxides is the more extended nature of d-orbitals of the Ru-ion compared to those of the 3d-shell ions. This leads to comparable and thus competing energies, as discussed in chapter 2, mainly due to the more pronounced orbital degree of freedom. The energies due to crystalline field effect[13], Hund's rule interactions[14], spin-orbit coupling[15], p-d electron hybridization[16] and electron-lattice coupling[17] are comparable making the system highly susceptible to external perturbations. For instance, the Crystalline Electric Field (CEF) in a $Ru^{4+}$ ($4d^4$) ion is so large that the Hund's rules partially break down, yielding a low spin state with S=1 ($_3T^1g$) rather than an expected high spin state with S=2 for free ions (see **Fig. 1.4**). The significance of crystal field splitting and the role of these competing energies will be realized soon once the physical properties of these compounds are discussed.

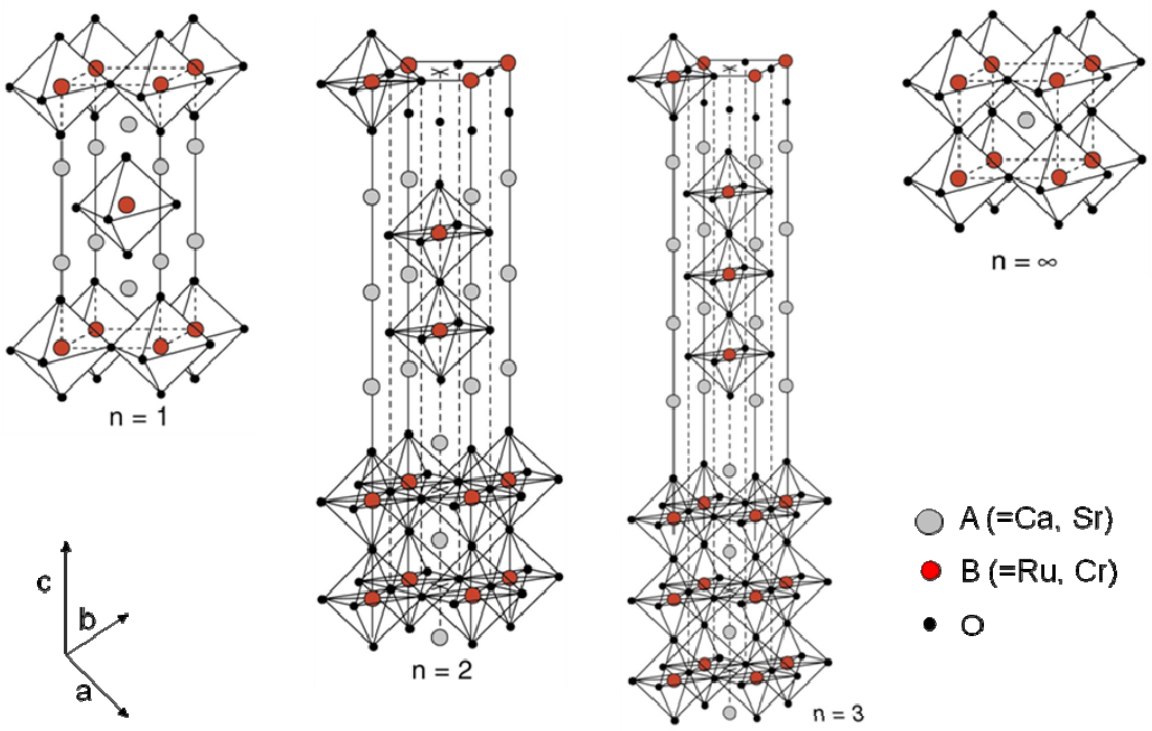


**Fig. 1.3** Ruddlesden-Popper series of compounds, $A_{n+1}B_nO_{3n+1}$, for n=1, 2, 3 and ∞ with n increasing from left to right.

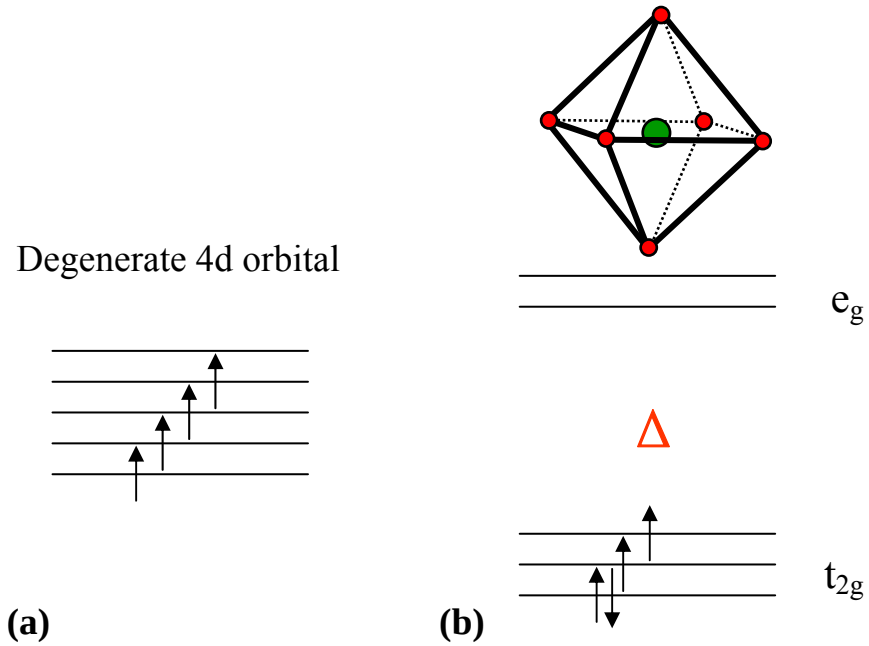


**Fig. 1.4** A schematic representation of spin configuration for $Ru^{4+}$ ion **(a)** in an isolated ion, where the energy levels are degenerate and **(b)** in an octahedral field environment, where the degeneracy between $e_g$ and $t_{2g}$ levels is lifted due to CEF.

RP series form the class of SCES, showing a broad spectrum of physical properties and hence serving as a useful tool in exploring the unconquered territories in physics. Particularly, many extraordinary properties are intimately linked to the complexity of these nature-designed layered structures. The rich phase diagram of the Ca and Sr ruthenates[18] as reproduced in **Fig. 1.5** reveals the fact that the ground states of these compounds are critically linked to the structural distortions. The simplified phase diagram clearly indicates that moving from one end to the other in the $(Ca_{1-x}Sr_x)_{n+1}Ru_nO_{3n+1}$ series, one witnesses a trend from antiferromagnetic insulating ground state (Ca ruthenates) to ferromagnetic metallic ones (Sr ruthenates). The bands in Ca ruthentes are very narrow that tend to localize the electrons. When n is increased i.e. when the compounds become more three dimensional, they tend to give an itinerant flavor to the electrons and hence they show better metallic behaviors. On the other hand, the Sr compounds have bands wider enough to exhibit ferromagnetism and itinerancy.

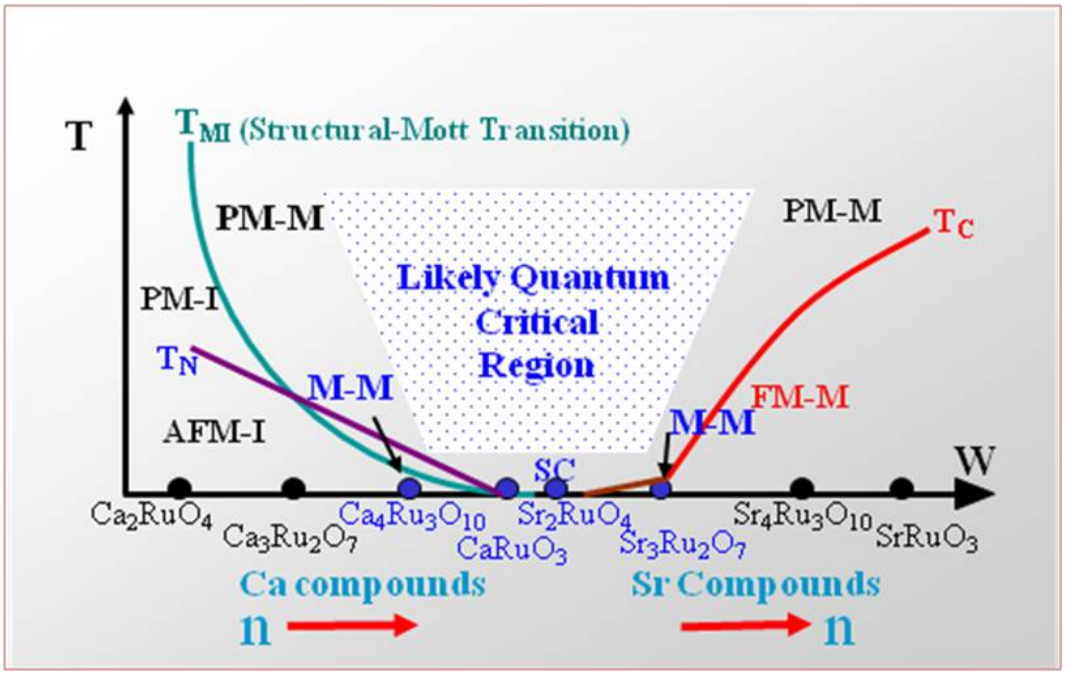


**Fig. 1.5** A Simplified phase diagram of the RP Series of $(Ca,Sr)_{n+1}Ru_nO_{3n+1}$

Another striking behavior of these compounds is the strong structural dimensionality dependence of the physical properties. The observed physical properties of any member depend sensitively on its structural dimension and a change in dimension through an increase/decrease in RuO octahedral layers is promptly reflected in its ground state. To add to the unlimited credentials of the series, the calcium and strontium

compounds behave uniquely differently when done so. As the number of Ru-O layers is increased from 1 through ∞, the magnetic interactions are suppressed in the Ca compounds unlike the Sr compounds, where the ferromagnetic coupling between spins is enhanced as 'n' is increased. Along with all the salient characteristics, the system's sensitivity to the external perturbations is also exposed in this thesis.

**1.4 Chromium substitution:**

Once the ground states of the Ca and Sr ruthenates are probed through the thermodynamic and transport measurements, the compounds' sensitivity to chemical perturbations are exploited. For my study, I considered a 3d transition metal, Chromium (Cr), as the main dopant for Ru. The primary idea is to study the coupling between 4d and 3d electrons by substituting some of the Ru ions in $(Ca, Sr)_{n+1}Ru_nO_{3n+1}$ by Cr ions and to study the impact of this coupling on the compounds' physical behavior.

Cr ions substitute either as trivalent ($Cr^{3+}$, $3d^3$) or tetravalent ($Cr^{4+}$, $3d^2$) species. In an octahedral crystal symmetry, for $Cr^{3+}$, each of the three $t_{2g}$ orbitals is half-filled, yielding S = 3/2, while for $Cr^{4+}$, only two of the three $t_{2g}$ orbitals are singly occupied with the third orbital empty, yielding S = 1. The ionic radius of $Cr^{3+}$ (0.615 Å) is nearly identical to that of the $Ru^{4+}$ ion (0.620 Å) and should be favored with regard to local strain effects. However, the occurrence of $Cr^{4+}$ (0.550 Å) would be more consistent with local electrostatic neutrality.

$Cr^{4+}$ ion based compounds have two 3d-electrons (as shown in **Fig. 1.6**) in rather contracted $t_{2g}$ orbitals, which could provide both fairly narrow band and strong exchange interactions. This is certainly true for Chromium (IV) oxide ($CrO_2$), a well known half-metal. $CrO_2$ is an itinerant ferromagnet with $T_C$=450 K, where the exchange splitting between spin-up and spin-down electrons is comparable to the $t_{2g}$ bandwidth and makes 100% spin polarization possible, at least for $T<<T_C$. The substitution of $Ru^{4+}$ by $Cr^{4+}$ replaces the 4d-electron with a more localized 3d-electron and the hybridization between the Cr 3d and Ru 4d electrons would narrow the bandwidth (W). The narrowing may be significant enough to enhance the DOS ($W\sim1/N(E_F)$), which motivates the occurrence of ferromagnetism according to the Stoner model. It is also possible for ferromagnetism to readily occur if the Fermi surface ($E_F$) lies close to a sharp peak of $N(E_F)$. Based on the Stoner criterion for the ferromagnetic instability $U_c=1/N(E_F)$, where $U_c$ is the critical

value of the exchange interaction between parallel-spin electrons. This could facilitate a U even smaller than W to satisfy the Stoner criterion.

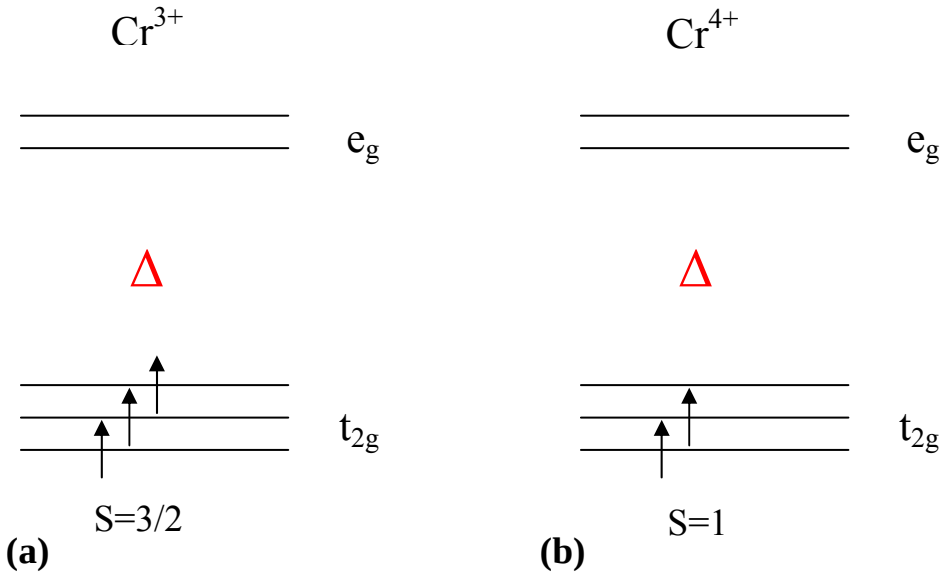


**Fig. 1.6** Spin configuration in **(a)** $Cr^{3+}$ (S=3/2) and **(b)** $Cr^{4+}$ (S=1) ions in an octahedral field environment.

Hence for ruthenium compounds that lie on the borderline magnetism, Cr might induce ferromagnetism as evidenced in $CaRuO_3$. For compounds that show weak ferromagnetic coupling along any of the directions as found in $Ca_3Ru_2O_7$, the difference in the coercivities of Cr and Ru lead to intriguing physical properties.

**1.5 Outline of this dissertation:**

In this thesis, I will discuss the physical properties of ruthenium based layered compounds that fall into this category of materials. As a result of strong correlations between the conduction electrons, these layered systems display both conventional and unconventional magnetic and transport properties. In a motive to exploit the sensitivity of these compounds to external perturbations, I used the chemical doping tool for my study. The central theme of the dissertation revolves around the discussion of the impact of Cr substitution on Ru.

This thesis has been divided into five chapters. An introduction to SCES and RP series is given in this chapter (**Chapter one**). The introduction gave an overview of the layered ruthenates, the physical properties of which will be described later in the

following chapters. That was followed by the motivation of Cr substitution in the compounds, which is the primary objective of this thesis.

In **Chapter two**, I have included a theoretical discussion that covers the basics of magnetism, metal-insulator transition and orbital ordering. This would be helpful later on when we discuss the complexities in the compounds' physical behavior.

**Chapter three** concisely describes the experimental techniques that are being used by our group for our material synthesis and characterization. The chapter explains the need for single crystals in materials research and elaborates two elegant techniques to grow single crystals and explains few established techniques for material characterization viz. DC magnetic susceptibility measurement, four point probe resistivity measurement, and thermal calorimetry specific heat measurements.

Once well equipped with the theory and experimental details, the observed results of our experiments are discussed. **Chapter four**, under the topic 'Thermodynamics and transport properties of $Ca_{n+1}(Ru_{1-x}Cr_x)_nO_{3n+1}$', covers the results and discussion part of the thesis. This chapter describes the conventional and unconventional physical phenomena in layered ruthenates, particularly the perovskite and the double layered ones in detail.

The inferences from the experimental observations are given in **Chapter five** that lead to some important conclusions drawn from the results. The chapter also presents some recommendations for the follow-up research, which, hopefully, might lend a helping hand to open a door to novel physics.

# Chapter Two

# Theoretical Background

## 2.1 Introduction:

The phenomenon of magnetism is an extremely complex one since magnetic effects are due to a number of causes. In a crystalline solid we may separate, to some extent, the effects due to current carriers and those due to ions at the lattice points of the crystal. For the latter, magnetic effects arise from two main causes: (1) uncompensated electron spins giving the ions a magnetic moment, which leads normally to paramagnetism. But when there is a strong coupling between the spins of neighboring ions we have cooperative phenomena giving ferromagnetism or antiferromagnetism; (2) the diamagnetic effect of the ions. A particularly interesting thermodynamic property of solids is the contribution of the conducting electrons to the magnetic susceptibility of the material. The contribution to the magnetic moment of the crystal when placed in a magnetic field from the free carriers also arises from paramagnetism due to their spin and diamagnetism due to their motion. In the absence of interactions, all magnetism due to electrons are described by Dirac equation, which governs the relativistic quantum dynamics of an electron in a static field viz. electric field, $\vec{E} = -\vec{\nabla}\Phi$ and magnetic field, $\vec{B} = \vec{\nabla} \times \vec{A}$. Now, the Hamiltonian[18] for such a system could be written as,

$$H = H_0 + H_S + H_{SO} + V(r) \qquad (2\text{-}1)$$

neglecting the non-magnetic relativistic terms. Here, without going into details, $H_0$ is the Hamiltonian of a free spinless particle in a magnetic field, $H_S$ is the spin Hamiltonian, $H_{SO}$ describes the spin-orbit interaction and V(r) is the electrostatic potential. The Hamiltonian for a spinless particle, in turn, depends upon two terms:

$$H_0 = \frac{p^2}{2m} + H_D \qquad (2\text{-}2)$$

where $H_D$ is a diamagnetic orbital contribution. Whereas a much detailed derivation for these various contributions to the Hamiltonian is described in standard text books, the important results are discussed in this chapter.

## 2.2 Orbital contribution to magnetism:

Since the orbital motion of an electron in a magnetic field is quantized, the electron energy eigenvalues and hence the total energy depend on the magnetic field. The diamagnetic orbital contribution, $H_D$ in equation 2-2 is expressed as

$$H_D = \frac{e^2B^2}{8m}(x^2 + y^2) \tag{2-3}$$

And the magnetization in the ground state |0> is

$$M = -\frac{\partial}{\partial B}(< 0|H_D|0 >) \tag{2-4}$$

Since the energy increases quadratically with B, the magnetization in the ground state is negative and in the opposite direction to B. This quantum mechanical contribution to the susceptibility[19] is remarkable that the contribution we expect on the basis of classical theory is identically zero. The modified Hamiltonian[20] for the system that satisfies the Schroedinger wave equation yields the energies of the electron states in the magnetic field as

$$E_{n,k_z,k_y} = \hbar\omega_c\left(n + \frac{1}{2}\right) + \frac{\hbar^2k_z^2}{2m} \tag{2-5}$$

when the magnetic field, B, is applied perpendicular to the plane of the motion of the electron. Here $\omega_c$=eB/m is the cyclotron frequency, $k_z$ is the component of momentum in the z direction and m is the mass of the electron. If we use this energy to evaluate the susceptibility of the system, we get[21]

$$\chi_D = -\frac{e^2k_F}{12\pi^2mc^2} \tag{2-6}$$

where $k_F$ is the magnitude of the Fermi wave vector and is derived from the electron density of states. The susceptibility is independent of temperature as this is an average effect and does not require the spacing of the levels be greater than kT. The parameter 'n' is equation 2-5 is an integer indicating the Landau levels that ranges from 0 to N and the factor $\hbar\omega_c$ is the periodic spacing between those levels. Now as the applied field B is raised, the separation $\hbar\omega_c$ increases, and the quantum states are collected together. As a result of this bunching, the density of states should change periodically since the Landau levels are spaced equally. A detailed theoretical description of this periodic behavior will be presented later in the chapter.

**2.3 Contribution of charge carriers to magnetism:**

According to the Langevin model[22] for materials with non interacting localized electrons, the magnetic moments are randomly oriented as a result of thermal agitation. In the presence of a magnetic field however, the moments tend to line up preferentially in the field direction and produce a net magnetization. Since the moments line up in the direction of the field and enhance the external field, the susceptibility $\chi$ is greater than zero for a paramagnet. As the temperature increases, then the thermal agitation will increase and it will become harder to align the atomic magnetic moments and hence the susceptibility will decrease. The magnetic susceptibility through various steps of calculations[23] would be deduced as

$$\chi = \frac{N\mu_v\mu_m^2}{3kT} \tag{2-7}$$

where N is the Avogadro number, $\mu_v$ is the permeability of vacuum, $\mu_m$ is the magnetic moment, k is the Boltzmann constant and T is the absolute temperature. This statement that the magnetic susceptibility of a paramagnetic arrangement of dipoles should vary as 1/T is known as Curie law. The material constant defined as $C=N\mu_v\mu_m^2/3k$ is the Curie constant. In fact the Curie law is a special case of the more general Curie-Weiss law

$$\chi = \frac{C}{T-\theta_{CW}} \tag{2-8}$$

which incorporates a temperature constant ($\theta_{CW}$). This law derives from Weiss theory[24], proposed for ferromagnetic materials, that incorporates the interaction between magnetic moments.

In equation (2-8) $\theta_{CW}$ could either be positive, negative or zero. Clearly when $\theta_{CW} = 0$ then the Curie-Weiss law equates to the Curie law (**Fig. 2.1**). When $\theta_{CW}$ is non-zero then there is an interaction between neighboring magnetic moments and the material is only paramagnetic above a certain transition temperature. If $\theta_{CW} > 0$, then the material is ferromagnetic below the transition temperature and the value of $\theta_{CW}$ corresponds to the transition temperature (Curie temperature, $T_C$). If $\theta_{CW} < 0$, then the ground state is antiferromagnetic below the transition temperature (Néel temperature, $T_N$) with $\theta_{CW}$ corresponding to $T_N$. Curie's law only works for samples in which only a relatively small fraction of the atoms are aligned, on the average, with the magnetic field. When the aligned fraction becomes larger, Curie's law no longer holds because it predicts that the

magnetization just goes up forever with increasing applied magnetic field. It is also not valid for many metals as the electrons contributing to the magnetic moment are not localized. However, the law does apply to some metals, e.g. the rare-earths, where the 4f electrons, that create the magnetic moment, are closely bound.

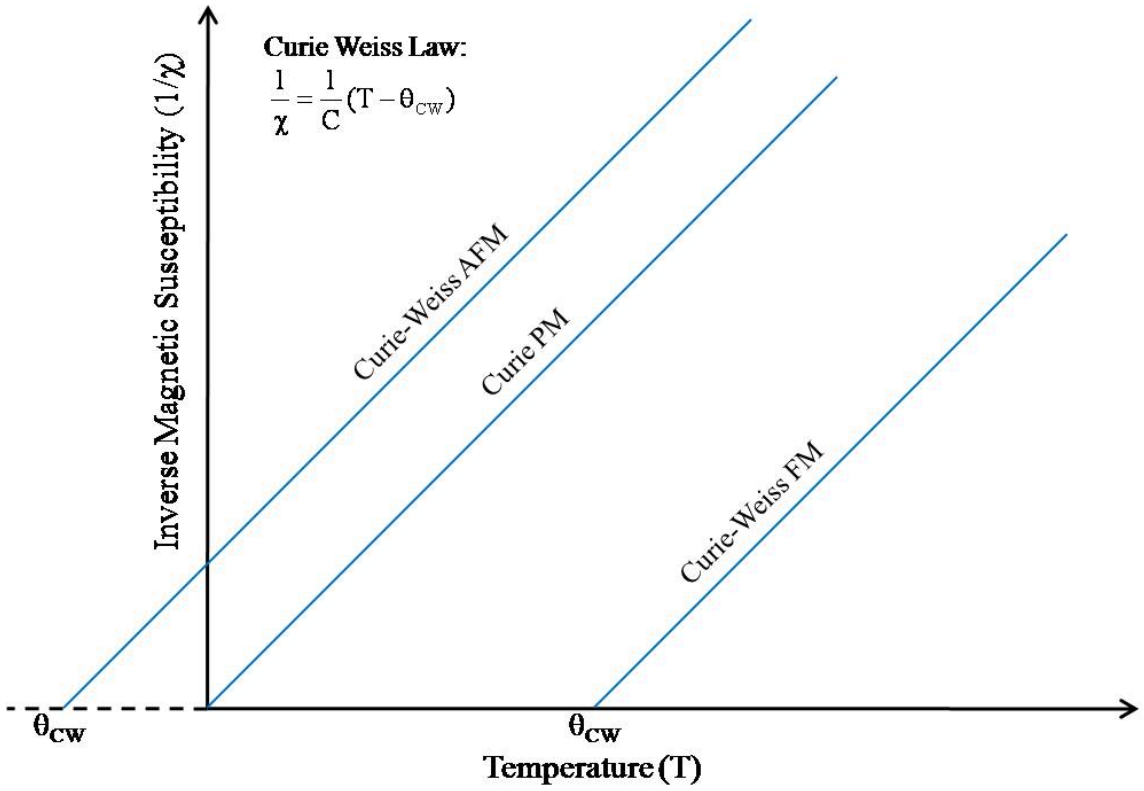


**Fig. 2.1** 1/χ vs. T plot for a paramagnet (PM), ferromagnet (FM) and antiferromagnet (AFM) following Curie–Weiss law.

For materials where the electrons are free and interact to form a conduction band, the Pauli model[25] for paramagnetism is valid. When no magnetic fields are present each band state is double degenerate, one having spin-up and the other spin-down. Under an applied field, an imbalance between electrons with opposite spin is set up leading to a low magnetization in the same direction as the applied field. However, the Fermi energy of the system is a constant and hence the electrons are transferred from spin down to spin up band. By knowing the density of states of a given spin per unit energy at the Fermi energy, we could evaluate the susceptibility as

$$\chi_P = \frac{e^2 k_F}{4\pi^2 mc^2} \qquad (2\text{-}9)$$

The susceptibility is independent of temperature, although the electronic band structure may be affected, which will then have an effect on the susceptibility. This positive magnetic susceptibility is hence a direct measure of the density of states at the Fermi level. Note that the magnitude of Pauli susceptibility is exactly three times that of the Landau term (2-6).

To make a proper computation of the susceptibility even in weak fields, it is necessary to know the energy of the stationary states, or alternatively the partition function, to the second order in the field B. In certain materials, the orbital angular momentum of the ground state has zero expectation as a consequence of invariance under time reversal. It might be thought that magnetism then be purely due to spin in the ground state. In fact certain excited states have orbital angular momentum and these contribute to the ground state magnetism in second order perturbation theory. Therefore a magnetic Hamiltonian acting on spin states in the ground state to the second order should be considered. Such an effective Hamiltonian[18] is described as

$$H_{eff} = \frac{g_s|e|}{2m} S.B - \sum_n \frac{|<n|g_L|e|^{L.B}/_{2m} + \lambda L.S|0>|^2}{E_n - E_0} \qquad (2\text{-}10)$$

where the sum is taken over all excited states n of the system and λ is the spin orbit interaction coefficient. The eigenvalues for this effective Hamiltonian is evaluated by expanding the square of the matrix in equation 2-10. Now the magnetic susceptibility elucidated from this evaluation carries two distinct terms: the temperature dependent Langevin susceptibility as given in equation 2-7 and the Van Vleck susceptibility[18,26], which is temperature independent. The anisotropic Van Vleck contribution can be significant when the ground state is singlet, where the curie susceptibility is zero. It is particularly important in molecular structures which form preferentially in S=0 states i.e. antiferromagnetism, because of superexchange. Also at high temperatures where the curie term is small, the Van Vleck term proves to be dominant.

**2.4 Magnetic interactions:**

The strong coupling of the localized electron spins in the neighboring ions contributes to the collective ferromagnetic or antiferromagnetic behavior in a system. For a lattice of localized moments interacting through Heisenberg exchange, the spin Hamiltonian mentioned in equation 2-1 intuitively takes the form

$$H_S = -\sum_{ij} J_{ij} \vec{S_i}.\vec{S_j} - \beta \vec{H}.\sum_i \vec{S_i} \quad (2\text{-}11)$$

where $J_{ij}$ ($=E_{singlet} - E_{triplet}$) is the exchange integral for the interaction between spins $\vec{S_i}$ and $\vec{S_j}$ and β is the Bohr magneton. The ground state of the system is determined between singlet (antiferromagnet) and triplet (ferromagnet) states by the sign of the exchange constant and is governed by Hund's rule. For instance, if the exchange integrals are positive, the Hamiltonian favors the alignment of spins since a parallel alignment of spins is an eigenstate of the Heisenberg exchange for a two-electron state. According to the Weiss model[24] for ferromagnetism, an internal field is produced due to exchange interaction between the neighboring spins and the corresponding internal field constant is defined as $\lambda \propto J_{ij}$. Without going into the details of the calculations, the internal field helps align the spins parallel below certain temperature and the magnetic ordering temperature, $T_C$, could then be expressed in terms of the internal field constant as

$$T_C = \frac{n\lambda\mu_{eff}^2}{3K_B} \quad (2\text{-}12)$$

where the effective moment, $\mu_{eff} = g_J\sqrt{J(J+1)}\mu_B$. Hence, from equation 2-12 it is clear that no long range ordering is possible if λ=0.

If the exchange interactions were negative and coupled only by neighboring spins an antiferromagnetic nature of spin alignment is favored. However, such a state is not an eigen state of Heisenberg exchange and operation on such a state with the exchange operator would lead to states with neighboring spins flipped with respect to the postulated state. The true antiferromagnetic ground state is quite complicated then and is approximated by Heisenberg exchange. However, in oxides of the transition metals, where antiferromagnetism is a common occurrence, the origin of the exchange interaction between moments on the transition metal ions is described by superexchange[14] (SE): a transition metal ions' interaction through intermediary oxides. The spin on one transition-metal ion ($B^{n+}$) polarizes neighboring oxygen ($O^{2-}$) which in turn interacts with the other neighboring transition-metal ion as shown in **Fig. 2.2**. The actual calculation of this effect is somewhat subtle, but it explains, in principle, the observed phenomena. The antiferromagnets are in general visualized as two sublattices of spontaneous ferromagnetism and from the point of view of a single spin ferromagnetism and antiferromagnetism seem similar. The expression for the ordering temperature, $T_N$, is

hence derived using an analogous treatment as that for a ferromagnet with a |λ| instead of λ, as the antiferromagnets have a negative λ.

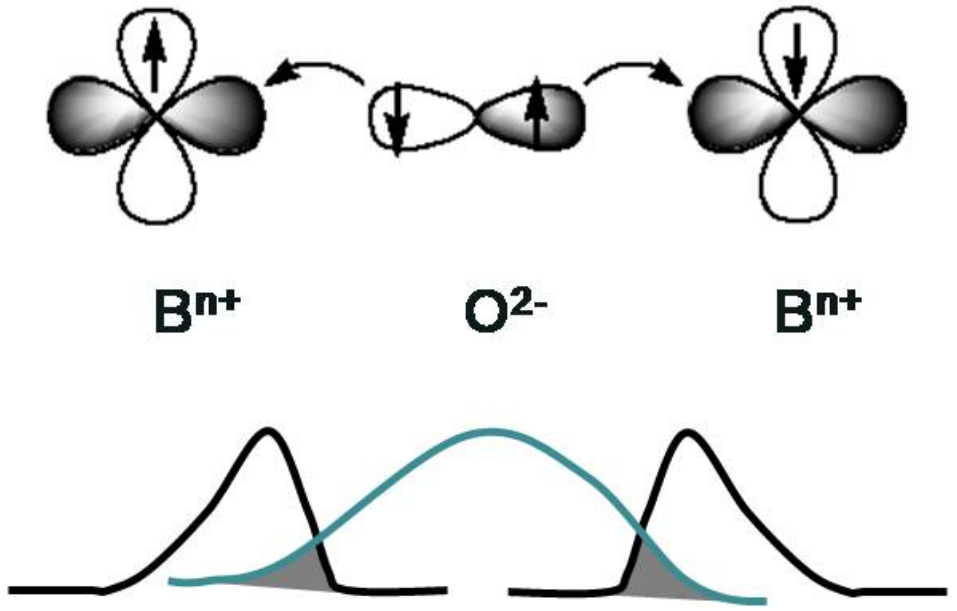


**Fig.2.2** A schematic representation of super-exchange interactions in TMOs.

The localized spin model has its own limitations and requires serious reconsideration from the first principles to explain, for instance, ferromagnetism in transition elements. In transition metals, the complication lies in the itinerant nature of d-electrons that are not strictly localized on particular ions but lie in states that overlap from atom to atom to form a narrow band. This band, in turn, hybridizes with the ordinary s-band where electrons conduct very freely. In a normal metal, we would assume equal population of electrons with spin-up and spin-down and the exchange potential would be the same for electrons of either spins. The energy bands would then be identical to each other and each will have a self-consistent solution. On the other hand if we were to populate the spin up states to a greater extent than the spin down states we would find a larger exchange potential for the electrons of spin up. Since this potential is attractive, these bands would be lowered in energy in comparison to the spin down bands. The calculations done in this spin set up ordinarily would not lead to Fermi levels of same energy for the two spins. There could be some choice of net non-zero spin that leads to a self consistent solution as is the case in a transition metal that has an irregular density of states. In such a non-zero total spin, the difference in energy has the contributions from

the kinetic energy of the shift in spin-up and spin-down bands and the interaction energy between the electrons. Hence the total energy change is given by

$$\Delta E = N(E_F)\delta E^2(1 - \frac{K_{11}}{N_a}N(E_F)) \quad (2\text{-}13)$$

where δE is the shift between the spin-up and spin-down bands, $K_{11}$ denotes the single site Coulomb integral and $N_a$ is the number of atoms. The paramagnetic state is unstable when this change of total energy is negative and hence leads to the Stoner criterium for ferromagnetic instability

$$IN(E_F) > 1 \quad (2\text{-}14)$$

where I is the Stoner parameter, which describes the effective exchange interactions between electrons. When systems meet this criterion electron correlation i.e. the interaction energy dominates the kinetic energy and hence leads to magnetic ordering in metals as illustrated in **Fig. 2.3 (b)**. Band ferromagnetism had been discussed in a more phenomenological way by Stoner[27]. The itinerant magnetism is caused by the exchange interaction between valence electrons. This interaction originates from the Pauli Exclusion Principle and favors spin polarization. On the other hand, hybridization, which causes band formation, favors a paramagnetic ground state. Therefore it is the competition between the exchange interaction and hybridization which will decide whether a particular system will exhibit itinerant magnetism or not.

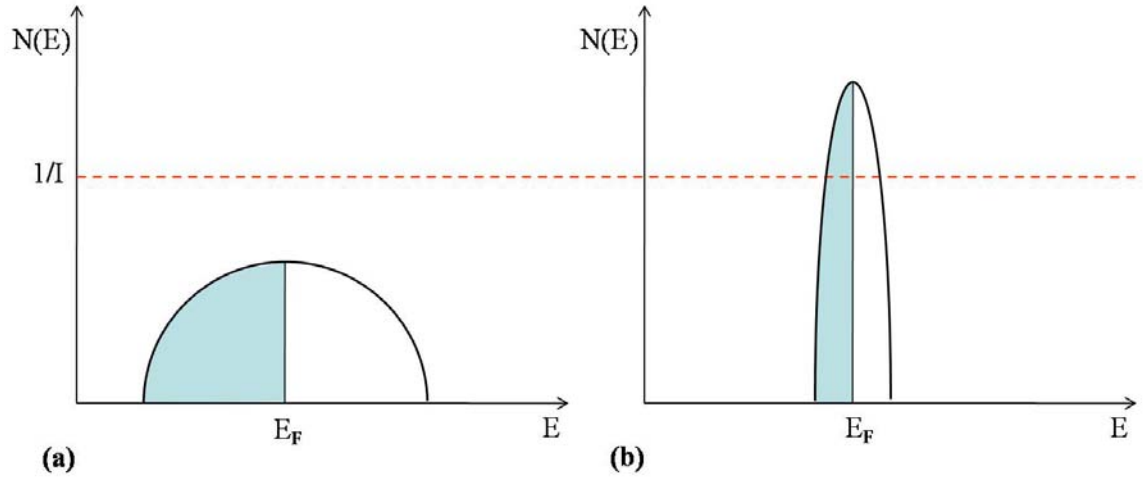


**Fig. 2.3** A schematic illustration of Stoner criterion for the stability of **(a)** paramagnetic and **(b)** ferromagnetic phases.

To understand antiferromagnetism in pure metals similar itinerant electron picture could be considered. To visualize the situation quantitatively, any conduction electron

with a prevalent spin, either up or down, when travelling through an established antiferromagnetic spin configuration of localized electrons will experience the exchange interaction. This effective field experienced by the electron would have the periodicity of the magnetic superlattice and hence give rise to an energy discontinuity at a subzone boundary inside the usual Brillouin zone. This feature in the band structure would be reflected as a superlattice of electron density for the up or down spin electrons. The condition for magnetic ordering is given by Overhauser[28] in terms of q-dependent magnetic response function $\chi_0(q)$ as

$$I\mu^{-2}\chi_0(q) > 1 \qquad (2\text{-}15)$$

where $\mu = g\beta s$ is the magnetic moment due to the spin of the electron. The condition for ferromagnetism (equation 2-14) is a special case where q=0.

There are subtle differences between magnetic behavior of itinerant and localized states. When localized moments couple, they create a macroscopic total magnetic moment. As the temperature increases, the ordering weakens and above the ordering temperature, $T_C$, the total magnetic moments are completely disordered, but they retain their original magnitude. On the contrary, the itinerant moments disappears completely as the temperature rises above $T_C$. Because itinerant magnetization is influenced by the exchange interaction, the moment is strongly volume dependent. Unlike itinerant moment, localized moments show a very weak dependence on volume, perfect examples being the rare earth systems.

**2.5 Effects of extended d-electron orbitals:**

The theoretical aspects discussed in the above sections leave out many important effects. For instance, the hybridization between the compact d electrons and the more diffused sp electrons is ignored. Likewise, the correlation effects are not explicitly included, although these effects are known to be important. Correlations are particularly significant when involving the systems like Ru based compounds, whose central feature is the extended 4d-electron orbitals. As a result of the extended orbitals, the inter-atomic interactions are so huge that they might be comparable to the intra-atomic interactions. The spatial extension of the orbitals will also lead to a scenario where there is a strong coupling between charge, spin, orbit and lattice. Moreover, the central Ru ion along with the surrounding O ions in these compounds forms an octahedral as described in chapter 1.

The deformations and relative orientations of these corner-shared octahedra crucially determine the crystalline-field splitting, the band structure, and hence the magnetic and transport properties, which will be explained in the chapters 4 and 5. The large crystal structural distortions in the compounds i.e. rotations, tilting or flattening of $RuO_6$ narrows the d-band and hence a small kinetic energy, W. On the other hand the coulomb interaction, U is smaller when compared to that of the 3d systems. Thus there is a subtle balance between W and U (W/U ~ 1) that dictates the system to be in an unstable ground state that is sensitive to any external perturbations. Depending upon which interaction factor dominates, the ground state will be determined. Let us look at these competing and comparable set of energies one at a time in the following paragraphs.

**2.5.1 Crystal electric field:**

For magnetic ions in certain crystals one cannot usually ignore the interactions between an atom and its immediate surroundings and for many materials they are large and significant. The size and nature of these crystal electric field (CEF) effects[29] depend crucially on the symmetry of the local environment. The local environments are often not spherically symmetric so that different orbitals will behave in different ways. As a result of the crystal fields, a split in the otherwise-degenerate d orbitals occurs. The crystal field splitting depends upon a string of factors viz. the nature of the metal ion and its oxidation state, the nature and arrangement of ligands around it[29]. A common case to consider is the octahedral environment because in many transition metal compounds, such as the one in my study, a transition metal ion sits at the center of an octahedron with an anion such as oxygen on each corner. The CEF in this case arises mainly from the electrostatic repulsion from the negatively charged electrons in the oxygen orbitals. In the compounds of our interest i.e. $Ca_{n+1}Ru_nO_{3n+1}$, which are fine examples of octahedral complexes, each $Ru^{4+}$ ion is surrounded by six $O^{2-}$ ions arranged toward the corners of an octahedron, as shown in the **Fig. 1.3**.

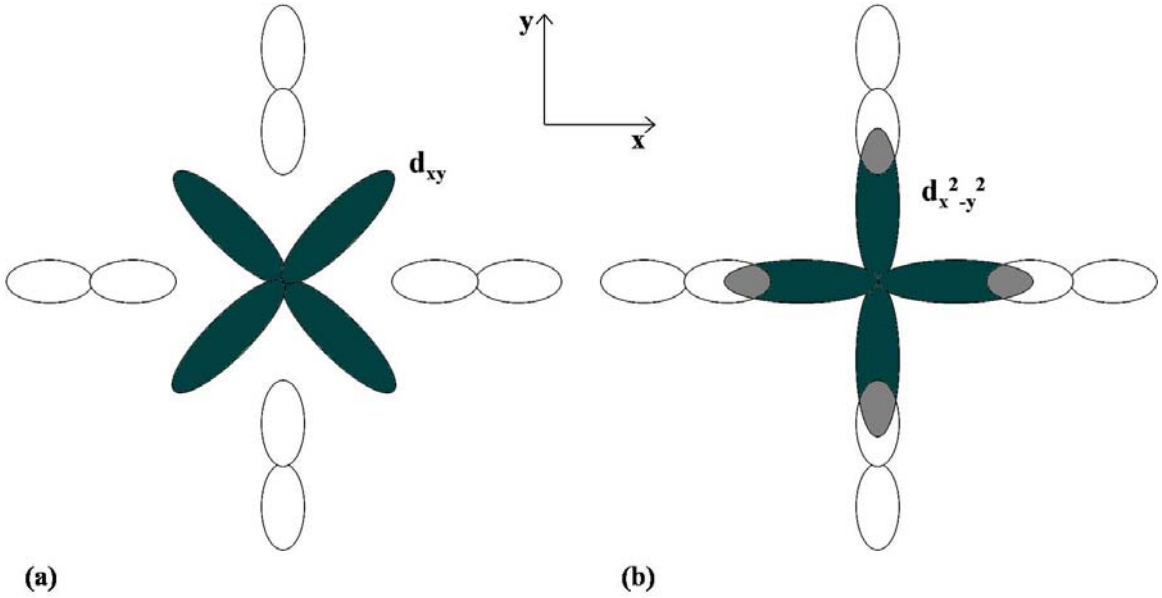


**Fig. 2.4** A diagrammatic representation of the origin of crystal field splitting in octahedral complexes.

**Fig 2.4** explains the origin of crystal field splitting in octahedral complexes such as ruthenates. For non-distorted crystal structures, the O p orbitals always lie along the three principal axes whereas the Ru d orbitals orient in the corresponding planes too ($d_{xy}$ for example, as shown in the figure). This preference in the spatial arrangement of electrons in the ions leaves way to a difference in interactions between the d-p orbitals and hence an energy difference. In this crystal symmetry, the d-orbitals split into two sets with the energy difference, $\Delta_o$, where the $d_{xy}$, $d_{xz}$ and $d_{yz}$ orbitals will be lower in energy than the $d_z^2$ and $d_{x^2-y^2}$. The former set of orbitals (forming $t_{2g}$) will have lower energy because the orbitals are farther away from the ligand orbitals than the latter set of orbitals (forming $e_g$) and therefore experience less repulsion[14] (**Fig. 2.4**). Tetrahedral complexes are the second most common type, where four ligands form a tetrahedron around the metal ion. In a tetrahedral crystal field splitting, the d-orbitals again split into two groups, with an energy difference of $\Delta_t$ where the lower energy orbitals will be $d_z^2$ and $d_{x^2-y^2}$, and the higher energy orbitals will be $d_{xy}$, $d_{xz}$ and $d_{yz}$ - the opposite way round to the octahedral case. Furthermore, since the ligand electrons in tetrahedral symmetry are not oriented directly towards the d-orbitals, the energy splitting will be lower than in the octahedral case ($\Delta_0 = {}^9/_4\ \Delta_t$).

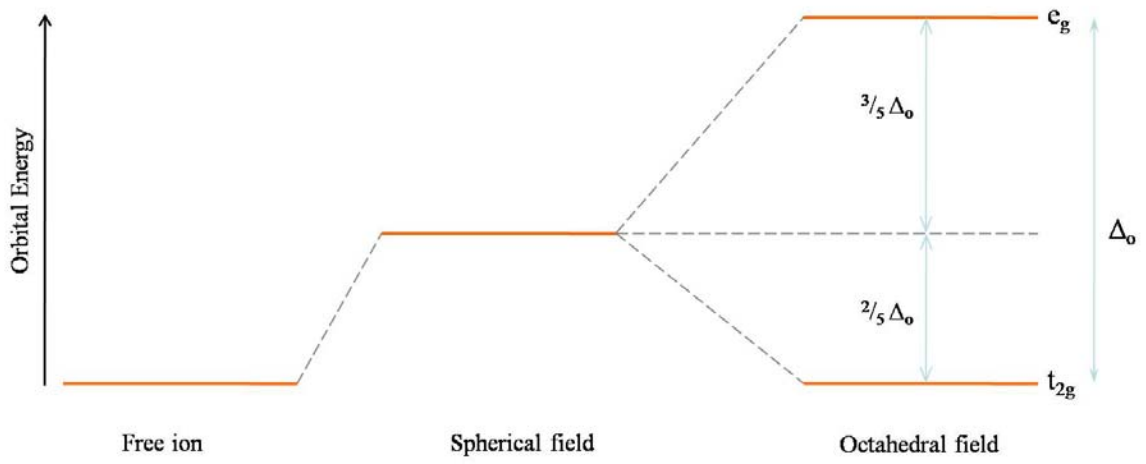


**Fig. 2.5** Crystal field splitting diagram for a crystal in a spherical and an octahedral field.

Crystal Field Stabilization Energy (CFSE)[29], which denotes the stability that results from placing a transition metal ion in the crystal field generated by a set of ligands, is shown in **Fig. 2.5**. It arises due to the fact that when the d orbitals are split in a ligand field, as described above, some of them become lower in energy than before with respect to a spherical field known as the barycenter in which all five d orbitals are degenerate[29]. For example, in an octahedral case, the $t_{2g}$ set becomes lower in energy than the orbitals in the barycenter. As a result of this, if there are any electrons occupying these orbitals, the metal ion is more stable in the ligand field relative to the barycenter by an amount of the CFSE. Conversely, since the $e_g$ orbitals are higher in energy than in the barycenter, putting electrons in these reduces the amount of CFSE. If the splitting of the d orbitals in an octahedral field is $\Delta_o$, the three $t_{2g}$ orbitals are stabilized relative to the barycenter by $^2/_5\ \Delta_o$, and the $e_g$ orbitals are destabilized by $^3/_5\ \Delta_o$. As examples, let us consider the $Ru^{4+}$ ions, which have $d^4$ configuration. Since the ion has 4 electrons in the d orbital, the two spin configurations viz., low and high are possible. In the low spin state, the ion has all the four electrons in the $t_{2g}$ orbitals, so the total CFSE is $4 \times {}^2/_5\ \Delta_o = {}^8/_5\ \Delta_o$. In the hypothetical high-spin state, where there are 3 $t_{2g}$ and 1 $e_g$ electrons, the CFSE is $(3 \times {}^2/_5\ \Delta_o) - (1 \times {}^3/_5\ \Delta_o) = {}^3/_5\ \Delta_o$. Here, the higher the value of CFSE, the more stable the complex would be. Crystal Field stabilization is applicable to transition-metal complexes of all geometries. Indeed, the reason that many $d^8$ complexes are square-planar is the very large amount of crystal field stabilization that this geometry produces with this number of

electrons. The preference of electron occupation and hence the complex stability in ruthenates are discussed in the later part of the chapter.

### 2.5.2 Hund's rule interactions:

Once we know the relative energies of the d orbitals in a transition-metal complex, we have to worry about how these orbitals are being filled. Simple, empirical rules tell us how atomic shells are filled. These are the three Hund's rules. The first and the second rule determine the spin and orbital moments of an atomic shell. The third rule specifies the way in which spin and orbital moments are coupled to each other. Degenerate orbitals, in general, are filled according to Hund's rules[30].

- One electron is added to each of the degenerate orbitals in a subshell before a second electron is added to any orbital in the subshell.
- Electrons are added to a subshell with the same value of the spin quantum number until each orbital in the subshell has at least one electron.

Octahedral transition-metal ions with $d^1$, $d^2$ or $d^3$ configurations can therefore be easily described by the rule. When we try to add a fourth electron to the orbital, which is the case with $Ru^{4+}$ ion ($4d^4$), we are faced with a problem. This electron could be used to pair one of the electrons in the lower energy ($t_{2g}$) set of orbitals, to make it a low spin state configuration (**Fig. 2.6 (a)**), or it could be placed in one of the higher energy ($e_g$) set of orbitals, to exhibit a high spin state (**Fig. 2.6 (b)**). The same problem occurs with octahedral $d^5$, $d^6$ and $d^7$ complexes. But for octahedral $d^8$, $d^9$ and $d^{10}$ complexes, there is only one way to write satisfactory configurations as was the case for $d^1$, $d^2$ and $d^3$ complexes. As a result, we have to worry about high-spin versus low-spin octahedral complexes only when there are four, five, six or seven electrons in the d orbitals. The choice between high-spin and low-spin configurations for octahedral $d^4$, $d^5$, $d^6$ or $d^7$ complexes is made plausible through the CSFE calculations[29] explained in the previous section. In a nutshell, it is done by comparing the energy it takes to pair electrons with the energy it takes to excite an electron to the higher energy ($e_g$) orbitals. If it takes less energy to pair the electrons, the complex exhibits low-spin whereas if it takes less energy to excite the electron, the complex has high-spin. The amount of energy required to pair electrons in the $t_{2g}$ orbitals of an octahedral complex is more or less constant. The amount of energy needed to excite an electron into the higher energy ($e_g$) orbitals, however,

depends on the value of $\Delta_0$ for the complex. As a result, we expect to find low-spin complexes among metal ions and ligands that lie toward the high-field end of the spectrochemical series. High-spin complexes are expected among metal ions and ligands that lie toward the low-field end of these series.

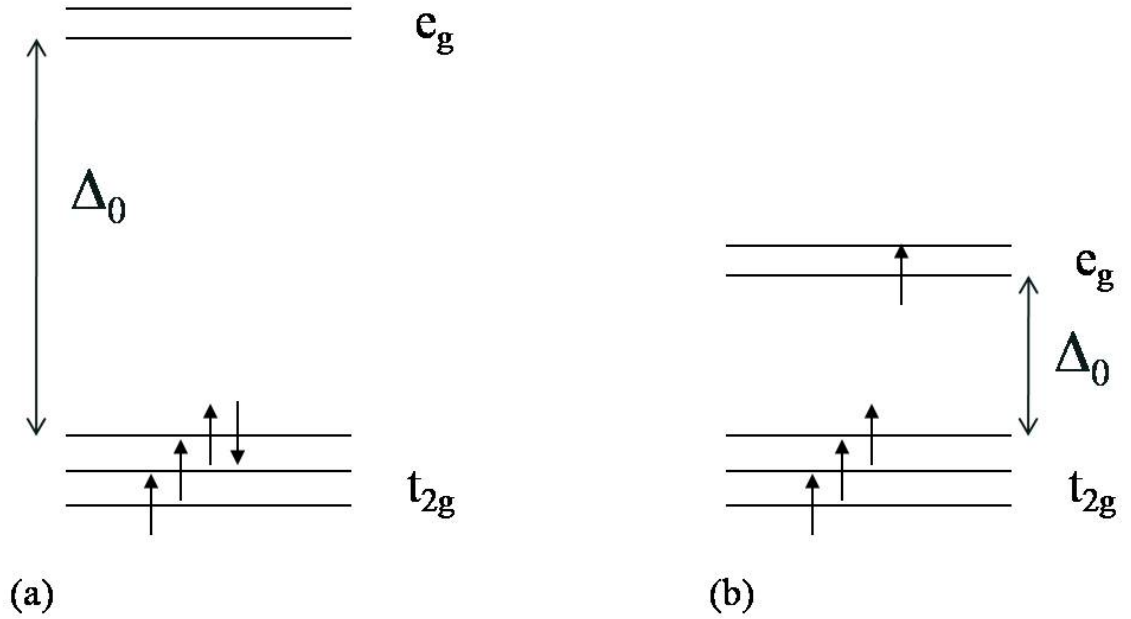


**Fig. 2.6** Spin configurations in $Ru^{4+}$ ion describing the situations of a **(a)** low spin state and **(b)** high spin state.

In the ruthenates, with $Ru^{4+}$ ($4d^4$) ions, the Hund's rule energy maximizing the total spin at each Ru site is not large enough to overcome the $e_g$-$t_{2g}$ crystalline field splitting, so that the $e_g$ levels are not populated. Hence, one $t_{2g}$ orbital is doubly occupied, while the other two host a single electron each as in **Fig. 2.6 (a)**. Since the compounds in which all of the electrons are paired show a diamagnetic behavior, they are repelled by both poles of a magnet. On the other hand, the compounds that contain one or more unpaired electrons are paramagnetic and they are attracted to the poles of a magnet. The force of attraction between paramagnetic complexes and a magnetic field is proportional to the number of unpaired electrons in the complex. We can therefore determine whether a complex is high-spin or low-spin by measuring the strength of the interaction between the complex and a magnetic field.

### 2.5.3 Spin-Orbit coupling:

The Spin-Orbit (SO) coupling mechanism might be essential in the insulating compounds of late 3d-ions and also in 4d-ruthenates. The basis of the SO coupling lies in the fact that the effective current from the motion of an electron in a circular orbit generates an effective magnetic field. The interaction of this magnetic field with the spin magnetic moment is given by:

$$H_{SO} = -\vec{\mu}.\vec{B} \tag{2-16}$$

where $\vec{\mu}$ is the magnetic moment of the electron and $\vec{B}$ is the effective magnetic field it experiences. Semiclassical electrodynamics and non-relativistic quantum mechanics could be used to obtain an expression for B in terms of the total orbital angular momentum, L, of the electrons.

$$\vec{B} = \frac{1}{mec^2}\frac{1}{r}\frac{\partial U(r)}{\partial r}\vec{L} \tag{2-17}$$

where $U = Ve$ is the potential energy of the electron in the central field and L is obtained by the coupling of individual orbital angular momenta $l_i$. It is worth mentioning that the magnetic field is parallel to the orbital angular momentum of the electron. The magnetic moment of the electron is

$$\vec{\mu} = \frac{-g_S \mu_B \vec{S}}{\hbar} \tag{2-18}$$

where $\vec{S}$ is the magnitude of the total spin angular momentum obtained by the interactions of individual spins, $s_i$, within themselves, $\mu_B$ is the Bohr Magneton and $g_S \sim 2$ is the electron spin g-factor. Here the magnetic moment is antiparallel to the spin angular momentum. Substituting the derived expressions and considering the Thomas precession effect[31], the interaction energy, $H_{SO}$, is

$$H_{SO} = \frac{\mu_B}{\hbar mec^2}\frac{1}{r}\frac{\partial U(r)}{\partial r}(\vec{L}.\vec{S}) \tag{2-19}$$

The energy shift could now be evaluated exactly and hence a basis that diagonalizes both the unperturbed Hamiltonian and the first order perturbation, $H_{SO}$ by defining a total angular momentum $\vec{J}=\vec{L}+\vec{S}$, the Russel-Saunders or LS coupling[32]. Taking the dot product of this with itself and rearranging the terms, we get

$$\vec{L}.\vec{S} = \frac{1}{2}(\vec{J}^2 - \vec{L}^2 - \vec{S}^2) \tag{2-20}$$

Now the energies could be evaluated from

$$< \vec{L}.\vec{S} >= \frac{\hbar^2}{2}(j(j+1) - l(l+1) - s(s+1)) \quad (2\text{-}21)$$

where j, l and s are the total angular momentum, orbital angular momentum and spin quantum numbers respectively. The approximation of L and S coupling to give J is good only for weak magnetic fields. However, in larger magnetic fields, these two momenta decouple, giving rise to a different splitting pattern in the energy levels giving rise to the Paschen-Back effect[30] and the size of LS coupling term becomes small. In heavier atoms, SO interactions are frequently as large as spin-spin interactions or orbit-orbit interactions. In that situation, each orbital angular momentum ($l_i$) tends to combine with each individual spin angular momentum ($s_i$) to give individual total angular momenta ($j_i$). These $j_i$s then add up to form the total angular momentum J (jj coupling) given as

$$J = \sum_i j_i = \sum_i (l_i + s_i) \quad (2\text{-}22)$$

In solids, the spin-orbit coupling effect leads to a spin-splitting of electrons moving in the solid even in the absence of any magnetic field suggesting the vital role of the symmetries of the crystal lattice. The effective magnetic moment could be estimated for a magnetic system as given by

$$\mu_{eff} = \mu_B g_J \sqrt{J(J+1)} \quad (2\text{-}23)$$

where $g_J$ is the Land´e g factor, given by

$$g_J = \frac{3}{2} + \frac{(S(S+1) - L(L+1))}{2J(J+1)} \quad (2\text{-}24)$$

But the experimental results for magnetic moments are often closer to the values if L=0. Hence the value of $g_J$, as evaluated from equation 2-24 would be 2 always and J=S. The modified effective magnetic moment could be then written as

$$\mu_{eff}(L=0) = 2\mu_B \sqrt{S(S+1)} \quad (2\text{-}25)$$

The explanation for this discrepancy lies in knowing the impact of crystal field effect on the system's magnetism. And in a number of cases the crystal field splitting is more important than the spin-orbit coupling. As mentioned in the previous section, when the crystal field effects are large enough, Hund's third rule will not be able to define the total angular momentum J in terms of L and S. Instead, J=S simply as the orbital contribution is quenched (L=0). This orbital quenching effect just means that the orbital moments are strongly coupled to the crystal lattice and are therefore unable to change direction when a

magnetic field is applied. Hence the crystal symmetry influences the behavior of the spins through this strong coupling.

### 2.5.4 p-d electron hybridization:

Valence-bond theory[33] considers the overlap of the atomic orbitals of the participation atoms to form a chemical bond. However, the atomic orbitals for bonding may not be "pure" atomic orbitals directly from the solution of the Schrodinger Equation. Often, the bonding atomic orbitals have a character of several possible types of orbitals and hence are called hybridized orbitals. Though hybridization theory succeeded in explaining the mechanism behind the s-p hybridization, it has failed in a few aspects, notably in explaining the energy considerations when d-orbitals are involved in chemical bonding. In general, the d-orbitals are large and comparatively distant from the nucleus. Radial distances of orbitals from the nucleus seem to reveal that d-orbitals are far too high in energy to 'mix' with s- and p- orbitals. Thus, at first sight, it seems improbable for any sp-d hybridization to occur. However, in transition elements the inner d states are not all filled, but lie close to s or p valence states which themselves form an ordinary covalent bond. The narrow d band with a density of states capable of holding upto 10 electrons per atom, lies within the s-p band and hybridizes it where they cross[21]. Such a molecular wavefunction construction is perceived by a quantum mechanical approach by combining the atomic wavefunctions to give new hybrid wavefunctions. Now a d-band is represented by the matrix of an Linear Combination of Atomic Orbitals (LCAO)[21] such as

$$\psi_k = \sum_{ij} e^{i\boldsymbol{k}.\boldsymbol{R}} \beta_j \phi_a^{(j)}(\boldsymbol{r} - \boldsymbol{R}) \qquad (2\text{-}26)$$

where $\phi_a^{(j)}(\boldsymbol{r} - \boldsymbol{R})$ is one of the set of different atomic orbitals at **R**. Once a model Hamiltonian is set with suitable pseudo-potential components, the atomic orbitals themselves are destroyed by the overlap of potentials. The hybridization matrix is then defined by linking the matrix of LCAOs and the pseudo-potentials.

The electrons in d orbitals do not generally occur in the outermost shell of an atom and therefore do not normally take part in ‘pure’ covalent binding. The incompletely filled d orbitals of the penultimate shell in transition series differ little in energy from the s and p orbitals of the outermost shell[34]. If one or more of the d electrons is promoted to the outermost shell, hybridization of the (n-1)d, ns and np electrons may

occur. Such a hybrid is termed a $d^x s^y p^z$ hybrid, where the superscripts indicate the number of electrons of each type involved and the sequence of orbitals in the symbol implies that the energy of the d orbital is lower than that of s. Alternatively s and p orbitals may be promoted to vacant d orbitals in the same shell. In this case hybridization would involve the ns, np and nd electrons and would give rise to $s^x p^y d^z$ hybrids. Configurations of particularly common occurrence in crystals are the $d^2sp^3$ and $sp^3d^2$ hybrids giving rise to bonds directed to the corners of a regular octahedron. In ruthenates, $Ru4d_{xy,\ yz,\ xz}$ – O2p hybridization is favorable as reported in the superconductor $Sr_2RuO_4$[35], because of the proximity of 4d orbitals to the 2p orbitals. LSDA band structure calculations done on the compound shows that the $e_g$ – pσ bonding states lie at the bottom of the valence band with their corresponding antibonding states lying above the $E_F$. However, the notable feature in the study is the three hybridized 4d $t_{2g}$ derived bands around the $E_F$ corresponding to the $d_{xy}$, $d_{yz}$ and $d_{xz}$ orbitals.

Once achieved, the hybridization phenomenon is very important in a solid's magnetic and electron transport properties point of view. A decrease in the distance between the atoms enhances the hybridization energies as such. Hence we expect the hybridization energies to increase as the mechanical pressure on a solid increase. In the compounds of our interest, a similar effect of pressure is provided by the distortion and deformation in the B-$O_6$ octahedral caused by the ionic size mismatches of the constituent ions. An increase in the p-d hybridization will lead to a stronger SE between the transition metal ions and hence to a higher $T_N$ of the compound. Due to the wavefunction overlapping, the electrons are expected to be localized in the bond region. The strength of p-d hybridization is connected with the activation energy of the ionic conduction. It is shown that the ionic conductivity of the silver halide, AgX[36], where X is any halide, is high because of the combination of the deformability of d shell and the weakness of p-d hybridization.

**2.5.5 Electron-Phonon interaction:**

The crystal field effect in an octahedral crystal geometry is effectively stronger than the Hund's rule interactions and hence lifts the degeneracy between the $e_g$ and $t_{2g}$ sublevels of the d orbital. But the sublevels are still degenerate within themselves i.e. $e_g$ is doubly degenerate ($d_{x^2-y^2} = d_{z^2}$) and $t_{2g}$ is threefold degenerate$\left(d_{xy} = d_{yz} = d_{xz}\right)$.

This degeneracy could further be removed by the coupling of lattice distortion to the $e_g$ or $t_{2g}$ electrons that might lead to an orbitally ordered state. In the case of $Ru^{4+}$ ion based compound, which has the above mentioned orbital configuration when the crystal is undistorted, a splitting will occur when the crystal is distorted. According to the Jahn-Teller (JT) theorem[37], any molecule or complex ion in an electronically degenerate state will be unstable relative to a configuration of lower symmetry in which the degeneracy is absent. A rough illustration of the orbital degeneracy removal through a JT distortion is shown in **Fig. 2.7**.

In compounds like ruthenates the B-$O_6$ octahedra, where B is a metal ion, are severely deformed because of the cationic size mismatches. The deformations of octahedra can be visualized either as an elongation or a compression along the z axis as shown in the figure. When the octahedral is compressed along the z axis, the central $Ru^{4+}$ and $O^{2-}$ ions have moved closer along z axis increasing the interaction between their electrons along this direction. This is hence a situation where the $d_{xy}$ orbitals lie lower in the energy scale when compared to the $d_{xz}$ and $d_{yz}$ orbitals. Using similar argument one can explain the energy level split in the $e_g$ orbitals too where $d_{x^2-y^2}$ has lower energy than $d_{z^2}$. Exact opposite of this happens when the octahedral is distorted by an elongation along the z axis. In this case the $d_{xy}$ level of the $t_{2g}$ and $d_{x^2-y^2}$ level of the $e_g$ orbitals are higher in the energy scale than the z counterparts.

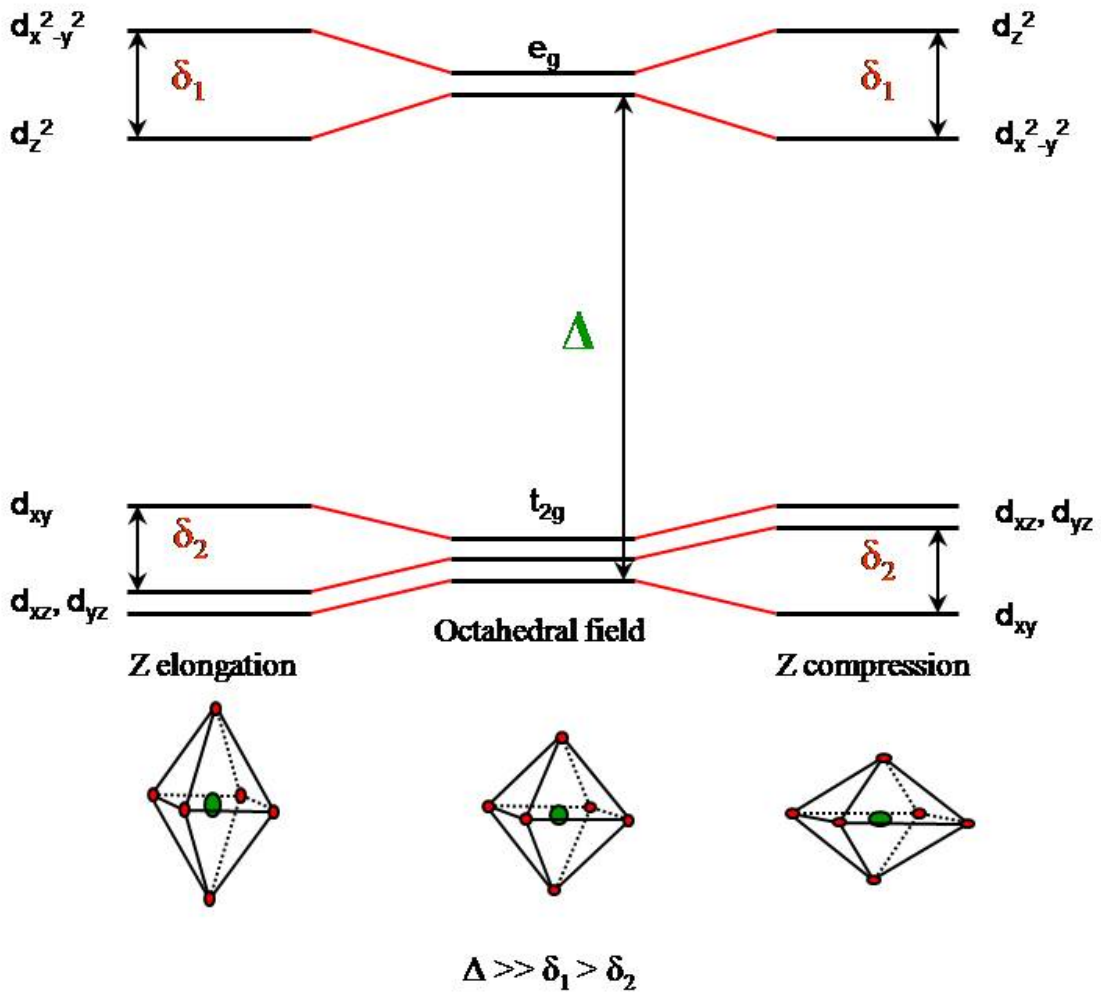


**Fig. 2.7** Illustration of Jahn-Teller distortions and the eventual degeneracy removal in a tri-fold degenerate $t_{2g}$ and bi-fold degenerate $e_g$ orbitals.

Now the electrons filling these levels have preferences among these otherwise-degenerate orbitals. For instance, the fourth 4d electron, in $Ru^{4+}$ ion, will be restricted to occupy one or two of the $t_{2g}$ orbitals depending on the type of distortion the Ru-$O_6$ octahedral undergoes: $d_{xy}$ for compressed z and $d_{xz}/d_{yz}$ for elongated z. Note that the energy split in $e_g$ is higher than that in $t_{2g}$ levels. The effect of $t_{2g}$ electrons is much weaker, showing that $e_g$ electrons are normally much more important from the point of view of bonding with neighbors. Since the electrons have their preferences now in the otherwise degenerate orbitals, the nature of the neighboring orbitals determines the strength of the electron hopping. The origin of orbital ordering is explained perturbatively in the electron hopping by considering a hopping matrix only connecting the same

orbitals with a non-zero hopping parameter t. The hopping process thus introduces certain level of ordering in the arrangement of orbitals, if it were to favor electronic conduction. Therefore, in our compounds, orbital-ordering is coupled with JT distortion. As a result of an ordered nature of orbitals, the electron-transfer interaction tends to be anisotropic. This means that it favors or disfavors the double-exchange interaction or super-exchange interaction in an orbital direction-dependent manner and hence gives a complex spin-orbital coupled state for the compound.

JT effect essentially depends on the magnitude of the electron phonon coupling constant ( $\lambda_{el-ph} \propto \sqrt{E_{JT}}$) . For metals with broad bands and almost completely delocalized electron states, the electron phonon coupling constant is small and hence the JT effect is weak. This convinces one to believe that the narrower the conduction band the stronger is the electron lattice coupling, leading to a stronger JT effect. Now this argument will lead to a situation where we would assume the strongest JT effect to exist for the narrowest possible band. But a more subtle effect of the electron-phonon interaction is the apparent increase in electron mass that occurs because the electron drags the heavy ion cores with it. Hence, if the band is too narrow it is less likely for JT effect to be prominent as the carrier mobility is then limited.

According to Goodenough[38], the basic physical mechanisms that quench the orbital degrees of freedom in a solid are (1) the electron-lattice JT distortions (2) relativistic SO coupling and (3) electron-electron SE interactions. Usually in a particular material of interest, it is not easy to single out any mechanism in terms of dominance. As a rule, one would expect strong JT interactions for the orbitals of $e_g$-symmetry as they were directed towards the ligands. On the other hand the ions with $t_{2g}$ degeneracy viz. Ti, V, Ru etc. are regarded as "weak JT" ions and the other interactions will be equally or more important in compounds based on these ions[39]. The crystal field effects have a strong impact on the effectiveness of a compound's SO interactions as discussed in section 2.5.3. The SE mechanism becomes increasingly effective near the Mott metal-insulator transitions (This subject will be covered in detail in the next section) because the intensity of virtual charge fluctuations, which are ultimately responsible for the exchange interactions, is large in small charge-gap systems. An increased virtual kinetic energy of electrons near the Mott transition – in other words, the proximity to metallic

state – can make the electronic exchange more efficient in lifting the degeneracy than the electron-lattice coupling[40].

**2.6 Metal-Insulator transition:**

Now that we learnt the origin and the range of interactions between the different degrees of freedom, we are ready to look at one or more of the impacts of their presence on a material's ground state; a direct consequence being a metal to insulator transition (MIT). The insulating phase associated with MITs can be described as either a band insulator (such as silicon) or a Mott insulator[41] (such as nickel oxide). A band insulator has an even number of electrons per unit cell that can be described adequately by an independent electron theory, where all of the bands are either filled or empty at 0 K. Although band theory is capable of explaining all the observed properties of metals and is the basis of most of the semiconductor properties, the biggest failure of it, however, lies in its prediction of metallicity always when the number of electrons in the unit cell is odd. But we have real-world examples that are insulators with odd number of electrons in their unit cell. For instance, a material having an onsite Coulomb interaction (U – intra-atomic) comparable to the bandwidth (W – inter-atomic) can become a Mott insulator irrespective of the electron count. And the transition from strongly correlated ($U > W$) to weakly correlated ($U < W$) electrons as a result of a change of bandwidth W is thus termed a Mott transition[42].

Over the past two decades, the Mott-insulating phase transition has received a great deal of attention as a prototypical example of a quantum phase transition in a strongly-correlated system for which quantum fluctuations drive the phase transition at zero temperature. Metal-insulator transitions of this type are, for example, found in transition metal oxides with partially filled bands near the Fermi level, which were predicted to be metals by band theory. According to the band theory, when a large number of atoms are brought closer, bands will be formed to make the solid a conductor as a result of an intensified wavefunction overlap. But with the strong interaction between the electrons being a definite possibility in the TMOs, a set of localized states may be a better trial wavefunction for the system than the set of delocalized band states. The most famous example is $V_2O_3$ doped with Cr[43]. A proper understanding of this phenomenon is made difficult by the fact that one is here dealing with an intermediate coupling p.roblem

whose investigation requires non-perturbative techniques. As is well-known, LDA does not treat the effects of strong local Coulomb correlations adequately. To overcome this drawback, recently there have been some very interesting new developments in this field due to the application of the dynamical mean-field theory (DMFT) for the infinite-dimensional Hubbard model[44]. The Hubbard Hamiltonian basically appends a correlation term to the Tight Binding (TB) approximation and hence has the form,

$$H = -t \sum_{<i,j>,\sigma} c_{i,\sigma}^{\dagger} c_{j,\sigma} + U \sum_{i=1}^{N} n_{i\uparrow} n_{i\downarrow} \qquad (2\text{-}27)$$

where 't' is the hopping integral as defined in the TB model. This Hamiltonian sets up a competition between the hopping integral and the onsite repulsion and the model can therefore explain the transition from conductor to insulator in certain TMOs. The advantage of LDA+DMFT method of calculation is that it combines the strength of the LDA in describing weakly correlated electrons in the s- and p-orbitals, with the DMFT treatment of the dynamics due to local Coulomb interactions.

Normally, the MIT for a band insulator is accompanied by a structural phase transition that changes or breaks the symmetry. In contrast, an inherent Mott transition should be purely electronic in origin and not assisted by a structural transition. In practice, almost all of the highly correlated materials with a large enough ratio of U/W to be Mott insulators exhibit close coupling between charge, spin, and lattice, so that the Mott transition is nearly always accompanied by a structure transition. This situation complicates the understanding of the basic mechanism of a Mott MIT as a transition driven by the electron-electron (e-e) correlations as observed in the layered perovskite $Ca_{1.9}Sr_{0.1}RuO_4$[45].

The inter- and intra-atomic interactions could be altered by changes in inter-atomic distances, brought about through temperature or pressure variations or by introducing an alloying element. Since the competition between U and W determines the ground state of a system, a transition from the Mott insulating phase to the metallic phase can be induced by temperature, pressure, magnetic field, or doping.

**2.7 Metals in strong applied fields:**

The Fermi surface (FS) of metals is a constant energy surface in reciprocal space corresponding to the FE. Since the Fermi energy is inversely proportional to the effective mass, m*, and directly proportional to the concentration of electrons, n, the larger the

electron concentration the bigger is the FS as in good electrical conductors. The momentum of the conduction electrons in this constant energy surface is sensitive to the applied electric and magnetic fields, strongly so under extreme field conditions as depicted in Lorentz force equation,

$$\hbar \frac{d\vec{k}}{dt} = -e(\vec{E} + \frac{1}{c}\vec{v}\mathrm{x}\vec{H}) \qquad (2\text{-}28)$$

where $\vec{k}$ is the momentum of the mobile electrons. This response of electrons to high fields, when the applied field is strong enough to dictate a cyclotron frequency greater than the collision rate, is in the form of periodic oscillations. The Quantum Oscillations (QO) will hence be an indirect way to measure Fermi surface but still more intrinsic than many other measurement probes. Observation and analysis of these oscillations is widely agreed to be the best way of obtaining detailed, microscopic knowledge of the electronic structure and the low energy excitations that define the metallic state. But observation of QO is not straight forward as it requires having ideal conditions to realize the response of electrons.

In the absence of applied magnetic field, the time and electric field dependent electron momentum could be obtained by solving equation (2-28) with B=0. Now $\hbar k(t) = -eEt$ and the electrons decelerate and reverse its direction at the Brilloiun zone boundary in a DC electric field. Hence a DC bias produces an AC current (i.e.) Bloch oscillations. But the electrons have a large collision time that hinders this effect significantly. For electrons to complete a cycle, it should follow the relation, $\frac{eET}{\hbar} = \frac{2\pi}{a}$ that gives a definition for the period of an oscillation as $T = \frac{h}{eEa}$. This condition hence enables one to estimate the range of T for a field as high as $10^4$ V/cm and for a=1Å as $10^{-10}$ s. But the electron collision time is $10^{-14}$ s in normal metals, which establishes a scenario where the electron can never reach the boundary and hence no oscillations discerned for fields upto as high as $10^4$ V/cm. There are few manipulations that could be suggested in order to push the electrons to revolve in an orbit and to produce the oscillations. Increasing the field much more than $10^4$ V/cm is obviously a choice, whereas increasing the lattice constant 'a' will bear fruitful results too. Using high quality single crystals definitely will enhance the possibility of an electron completing a cycle as the collision time will be reduced for the electrons in this case. Though these are

theoretically possible manipulations, we have to accept that experimentally they still remain open challenges.

Now let us look at the second effect in Lorentz equation. The magnetic field contribution to the Lorentz force equation (equation 2-28) suggests that the change in the vector $\vec{k}$ is normal to the direction of $\vec{H}$, normal to $\vec{v}$, which itself is normal to the energy surface. This means that $\vec{k}$ must be confined to the orbit, which is defined by the intersection of the FS with a plane normal to $\vec{H}$. Thus $\vec{H}$ simply drives the representative electron along this orbit (round the FS) without any change of energy[21]. This orbit in k space could either trace out a closed curve or in the periodically extended zone scheme, the trajectory is an open orbit. In the open orbit case, the representative electron passes from one zone to the adjacent one and never returns to its starting point. Since the velocity of an electron is perpendicular to the constant-energy surface, the average velocity of an electron in perpendicular to both H and the average direction of the orbit in k space. Thus for H in the z direction there exists an open orbit directed along $k_x$, the electron in this orbit will carry a current in the y direction. These open orbits are not responsible for oscillation as the magnetic field does not bring the representative point back to where it started. In the closed orbit case, the average velocity vanishes and the closed orbits hence will give rise to the oscillations. Open orbits are present because of many factors like scattering that spoils the periodic nature of the electron orbits, strong B etc.

Landau quantization theory suggests that the electrons in a metal exist only as a series of orbitally quantized states in the presence of a magnetic field. In a 3-dimensional model these levels will take the form of cylindrical tubes as shown in **Fig. 2.8**. For a magnetic field applied along z axis, the Landau level energy is given by equation 2-5, where the energy E is continuous in the bulk limit. Now, states with $E>E_F$ are empty and $E<E_F$ are occupied from $k_z$=-$k_{z\ max}$ to +$k_{z\ max}$, where $k_{z\,max} = (\frac{2m}{\hbar^2})^{\frac{1}{2}}(E_F - \hbar\omega_C\left(n + 12)12\right.$. The total number of electrons could be deduced as

$$N = (\frac{V\hbar\omega_c}{2\pi^2})(\frac{2m}{\hbar})^{\frac{3}{2}}\sum_{n=0}^{n_{max}}(E_F - \hbar\omega_c\left(n+\frac{1}{2}\right))^{\frac{1}{2}} \qquad (2\text{-}29)$$

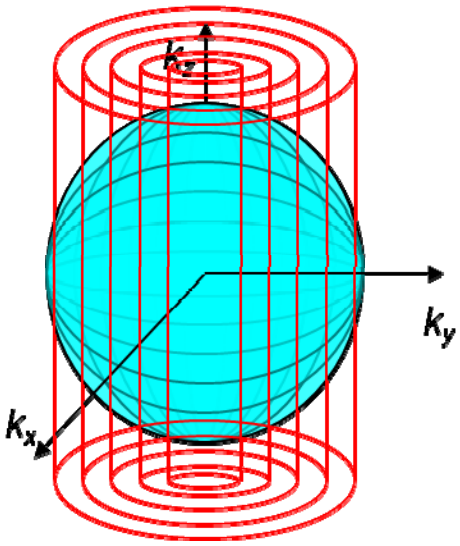


**Fig. 2.8** Quantized Landau tubes in the presence of a magnetic field.

In the Landau cylinder, the energy is constant in the base but not necessarily along the length ($k_z$). So for different $k_z$ we have different energy. Furthermore, from equation 2-5, we can deduce that $k_{\perp}^2 = \frac{2m}{\hbar}\omega_c\left(n+\frac{1}{2}\right)$ and the area in k orbit is given by $S = \pi k_{\perp}^2$. Therefore,

$$S_n = \frac{2\pi m}{\hbar}\omega_c(n+\tfrac{1}{2}) \tag{2-30}$$

Now the change in area between two adjacent levels is hence, $\Delta S = \frac{\pi m \omega_c}{\hbar}$ where $\omega_c = \frac{eB}{m}$. The radius of the cylinders is proportional to $B^{1/2}$ and so they expand as B increases. Thus, when

$$\frac{1}{B} = \frac{2\pi e}{\hbar S}\left(n+\frac{1}{2}\right) \tag{2-31}$$

the $n^{th}$ cylinder just touches the FS and will pass beyond it if B is increased ever so lightly. This just means that the cylinders of constant n are pushed out of FS one by one as B is increased. Whenever, a landau tube crosses the Fermi level we get a peak and so on to give periodic oscillations. Another way of looking at this classic behavior is that initially $E_F$ is at n and then there is a decrease in 1/B as B increases and by then the $E_F$ will go below n (an equivalent situation of Landau level n being pushed up). So the lowest n-1 level is at $E_F$ with $\Delta\frac{1}{B} = \frac{2\pi e}{\hbar S}$. In the foregoing discussions, S is considered to be constant for these Landau cylinders. But in reality we might have a variable S where

we get oscillations with linear combination of two or more frequencies. In such a case the Landau levels are no more just cylinders, as evidenced in $Ca_3Ru_2O_7$.

There are basically two appropriate experimental conditions for the observation of oscillatory effects, similar to the conditions required for observing Bloch oscillations. First, the thermal spread of the distribution function must be small compared to the spacing between orbitally quantized levels so that the effect of quantization is not washed out. Thus we require that $\hbar\omega_c \gg k_B T$ and when $\hbar\omega_c \gg k_B T$, since N needs to be constant, when $\hbar\omega_c$ increases $E_F$ decreases. The second effect is that $\hbar\omega_c$ in the square root part of equation (2-29) increases making $E_F$ to increase. These are the two competing effects as a result of an applied B. Now, when $E_F$ is oscillating in B we see oscillations in properties related to $E_F$. Common examples include oscillatory behaviors observed in the susceptibility (deHaas Van Alphen (dHVA) Effect), the conductivity (Shubnikov deHaas (SdH) Effect), the magnetostriction etc.

The second favorable condition to realize an oscillation is that the sample must be extremely pure and the temperature should be sufficiently low so that the relaxation time for the charge carriers is long. The uncertainty broadening of the levels will prevent the appearance of well defined oscillations otherwise. To meet these two conditions we must work with materials in which the electron density is high enough, when B has attained the necessary magnitude. If this vital requirement on the FE is not fulfilled all electrons will have condensed into the lowest orbital state before any oscillations can be observed.

**2.8 Magnetoresistance:**

The physics of the phenomenon where the resistance of certain materials changes dramatically as a magnetic field is applied, magnetoresistance (MR), has generated enormous interest in the recent years. In the simplest terms, an MR is defined as

$$MR = \frac{\rho(B)-\rho(0)}{\rho(0)} \qquad (2\text{-}32)$$

where ρ(B) and ρ(0) are the resistances at applied and zero magnetic fields respectively. It is typical that Δρ (=ρ(B) – ρ(0)) is proportional to $B^2$ for small fields but it tends to saturate at high fields. But the situation could be modified as in the case of the transverse MR, where the magnetic field is perpendicular to the direction of the current. In the direction of the open orbit, transverse MR increases as $B^2$ without saturation. This striking phenomenon is of importance in the study of the FS. An inspection of the MR of

single crystals as a function of orientation relative to the magnetic and electric fields provides evidence of the topology of the surface. For instance, if the directions of non-saturation are observed then the FS must be connected from zone to zone in the repeated zone scheme. It cannot consist of closed regions of electrons and holes unless these are of exactly equal volume.

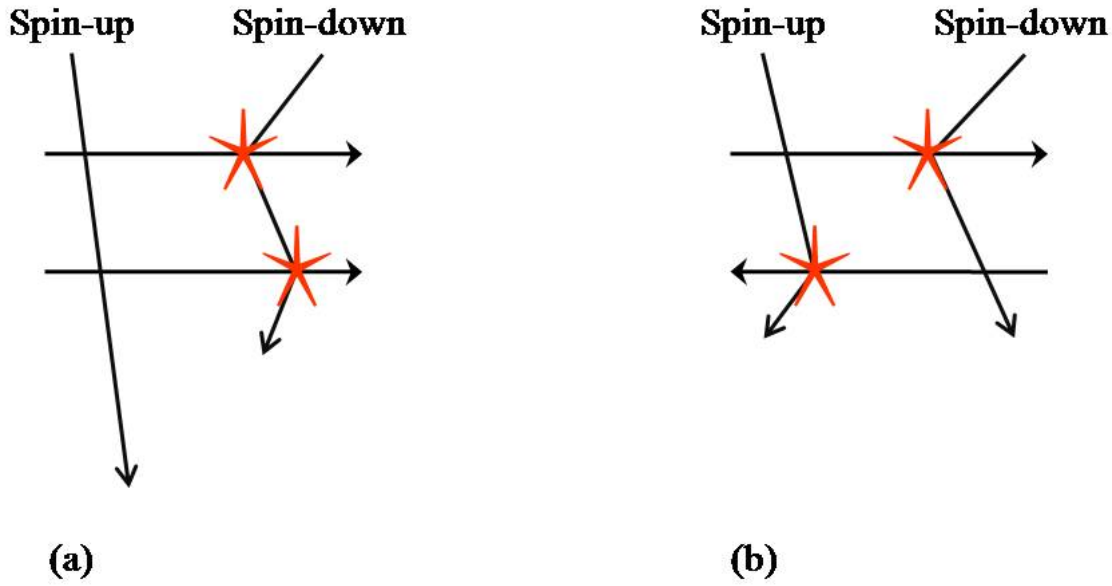


**Fig. 2.9** Scattering of electrons possessing representative spins in **(a)** a ferromagnet and **(b)** an antiferromagnet.

The effect is most usually seen in magnetic multilayered structures, where two magnetic layers are closely separated by a thin spacer layer a few nm thick. It is analogous to a polarization experiment, where an aligned set of polarizers allows light to pass through, but the crossed ones do not. The first magnetic layer allows electrons in only one spin state to pass through easily. Now, if the second magnetic layer is aligned then that spin channel can easily pass through the structure, and the resistance is low. If the second magnetic layer is misaligned then neither of the spins can get through the structure easily and the electrical resistance is high. This is illustrated in **Fig. 2.9** that explains the electron conduction processes in a ferromagnet (**Fig. 2.9 (a)**) and an antiferromagnet (**Fig. 2.9 (b)**). Obviously, the electrical resistance is much lower when the spins are coupled ferromagnetically than that when they are antiferromagnetically coupled together.

In a more technical sense, the band structure in a ferromagnet is exchange split such that the DOS is not the same for spin-up and spin-down electrons at the Fermi level. Fermi's golden rule states that scattering rates are proportional to the DOS at the state being scattered into, the Fermi level in this case. The scattering rates are thus different for electrons of different spin, which explains the vast difference in the resistances. These ideas were used as early as 1936 by Sir Neville Mott[42] to explain the sudden decrease in resistivity of ferromagnetic metals as they are cooled through the Curie point. Thus MR effectively measures the difference in angle between the two magnetizations in the magnetic layers, where small angles (parallel alignment) give a low resistance and large angles (antiparallel alignment) give a higher resistance. The strength of the MR depends on the mean free path of the electrons which carry the current. It is possible for electrons of appropriate spin to pass through many aligned magnetic layers and have a very long mean free path. This means that the distance between scatters is increased the most when the layers become magnetically parallel and hence contributing to a small resistance.

There is an interesting scenario when two materials with different switching fields are engineered to form junctions. Then as we apply the reverse field one layer will switch before the other and we have a 'pseudo spin valve'. There are also structures called spin-valves. These are structures where one layer moves in a field, whilst the other does not, and is used as a reference magnetic moment. This will give a bipolar output with a very high sensitivity in an optimized device. Though there are a number of different schemes in which it is possible to do this, a general reliable method is the exchange-biasing. It is possible to exchange couple one of a pair of magnetic layers to another back layer of antiferromagnetic material. These types of structures are very sensitive to magnetic fields and were not observed in any bulk material before we reported in our Cr doped $Ca_3Ru_2O_7$ single crystals.

While the quantum mechanical phenomenon of MR is in general associated with the spin scattering process of conduction electrons, the origins of various kinds of it are vastly different. The Giant MR (GMR) observed in magnetic metallic multilayer structures can be qualitatively explained using the two-current model, corresponding to up-spin and down-spin electrons. Tunneling MR (TMR), often seen in magnetic tunnel junctions separated by an insulating spacer layer, is a consequence of spin-polarization.

On the other hand, Colossal MR (CMR), seen only in the mixed valence manganites and layered ruthentes so far, originates from a metal-insulator transition in the vicinity of the transition temperature driven primarily by double exchange due to the hopping of $e_g$ electrons of $Mn^{3+}$ ions in manganites and the JT effect in ruthenates. As the name indicates, the CMR compounds exhibit resistance drops of upto a few orders of magnitude, whereas the other two types of magnetoresistance yield a difference in resistance by only few percent at the maximum. The CMR compounds exhibit various types of ordering including charge, spin and orbital ordering. In the multilayered ruthenates orbital ordering plays a vital role in dictating the physical properties of a compound as explained in chapter 4.

# Chapter Three

# Experimental Techniques

## 3.1 Introduction:

Our motivation in materials research is two-fold: (1) To develop and synthesize high quality novel and exotic electronic materials and (2) To carry out an intense investigation on the physical phenomena that those materials behold.

There is a famous saying about performing research in materials physics that states, "If you want to do good physics, you have to have either novel techniques or novel materials". In our lab, we have decided to go for novel materials. The way we pursue physics is to design, grow or discover samples of new or exotic materials in single-crystal form and then do relatively simple measurements on them. In the recent years, we have been focusing our attention to growing single crystals of transition metal oxides (TMOs), which are strongly correlated electron systems. The second manifestation of our research lays in the experimental studies of the synthesized crystals, giving emphasis to the structure, thermodynamics and transport properties of the systems. The compounds of my interest have in themselves a wide range of complex phenomena that are extremely rich in physics. This alarms us to do a careful investigation on the samples under consideration.

In this chapter, I will hence focus on the experimental techniques that we apply in our lab – to grow single crystals and to study the physical properties of the grown single crystals.

## 3.2 Material synthesis:

The driving force for crystallization comes from the lowering of the potential energy of the atoms or molecules when they form bonds to each other. The growth of a real crystal is governed on one hand by molecular kinetic processes at interfaces and on the other by heat and mass transfer at such faces[46]. Hence, given 'all' thermochemical and thermophysical information on a specific material, one should be able to devise or select the optimum crystal growth method (preparation of starting material, growth and after-treatment of crystal) for it. The ideal system[47] for any crystal growth, based on the above facts, should consist of a pure element or congruently melting compound with

- Low vapor pressure

- Low melting point
- High thermal conductivity
- Low heat of solidification, having no solid state phase transitions between its melting point and room temperature

However, if we ask ourselves a question whether growing a single crystal is easy, the answer would not be a simple 'yes' most of the times. First, only in few cases will one be fortunate as to deduce "all" the relevant information. Secondly, one has to realize that non-scientific parameters will influence and most times determine the selection of a method. Taking these various factors into consideration, we found two elegant techniques to be extremely useful in growing our crystals of TMOs that are explained in section 3.2.2 and 3.2.3.

**3.2.1 The importance of single crystals:**

Fundamental understanding of advanced electronic materials requires the critical capability to synthesis single crystals of new materials. But the art of growing good quality single crystals is one of the most underrated activities in science. As fittingly mentioned by Tony Feder[48], the condensed matter physics community in the country could not help but lag in the discovery of new materials and their applications, if this perilous condition persists. This indispensable fact induces our motivation in materials research to have an important role for material synthesis as mentioned in the introduction part of this chapter.

We strongly believe that single crystals are instrumental in carrying out an extensive research in materials physics. Access to single crystals is vital for our research for two, if not more, reasons. The primary reason that we rely on single crystals for our measurements is that it is much easier to study the anisotropic or directionally dependent properties of a material. This factor is particularly relevant for the exotic compound $Ca_3Ru_2O_7$ that exhibits strongly anisotropic physical properties. Looking at a polycrystalline sample of such a material would hide these anisotropies, because of the variable orientation of the crystallites that the sample is composed of. The second reason access to single crystals is important is that they do not exhibit artificial effects due to strain or impurities. Crystals, in general, can belong to one of several crystal systems, each of which is characterized by certain symmetries. A polycrystalline sample of a

compound that belongs to one of the non-cubic crystal systems can have significant built-in strain. In a nutshell, for looking at the intrinsic properties of a crystalline material, one should do measurements on a single crystal. Since we understand the importance of high quality single crystals in materials research, we synthesis our own crystals for the studies.

The expertise of our novel materials lab is to synthesize large, quality single crystals. The state-of-the-art bulk crystal growth facility in our novel materials lab permits growth of single crystals of a wide range of materials from the melt at temperatures even greater than 2000$^{o}$C.

### 3.2.2 Floating-Zone technique:

One of the two techniques we use to grow single crystals is the Floating-Zone (FZ) method. Currently our lab is operating an image furnace from NEC®[49]. Our image furnace is a focus heating one, well equipped with a double rotary elliptic surface mirror.

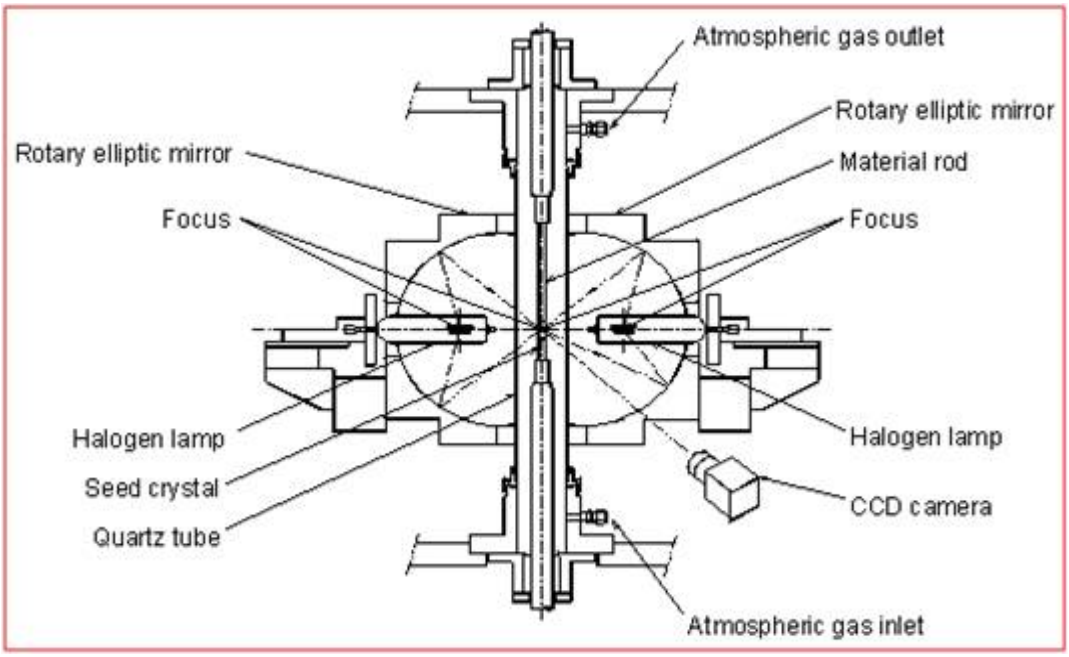


**Fig. 3.1** A diagrammatic representation of Floating Zone Furnace technique that uses a double elliptic mirror.

**Fig. 3.1** explains the principle of operation of a double elliptic type image furnace. As a heat source, two halogen lamps of 1.5 KW power are installed in the mirrors' outer focus. Au plating is applied to the inside surface of the mirror to increase the reflectance. Refer to the instruction manual[49] from NEC for further technical details on the furnace.

In order to grow single crystals with optical floating zone furnace the following conditions are necessary[50].

1. Achieving high temperature with high efficiency,
2. Deep temperature distribution along the vertical direction and
3. Homogeneous temperature distribution around the horizontal plane.

Using a double elliptic mirror enables us to achieve a high temperature at the inner focus. For instance, the image furnace having two halogen lamps with the above mentioned power is capable of reaching 2050$^{o}$C at the molten zone. The infra red rays emitted from the lamps are converged into the inner focus of both mirrors to melt the material and the seed crystal (Preparation of polycrystalline material rod and seed are discussed in the following paragraphs). The melt is held by surface tension between the polycrystalline material (feed) rod (upper shaft) and the seed crystal (lower shaft). For a proper growth this molten zone should be monitored closely and carefully for any deflections from the vertical axis like the ones shown in **Fig. 3.2**. The deflections might happen as a result of excessive power as in **Fig. 3.2 (b)** or because of insufficient power as in **Fig. 3.2 (c)**. In either case, the power has to be gradually tuned to the optimal level so that the melt is smooth. A steady growth is possible only if the molten zone appears like the one in **Fig. 3.2 (a)**.

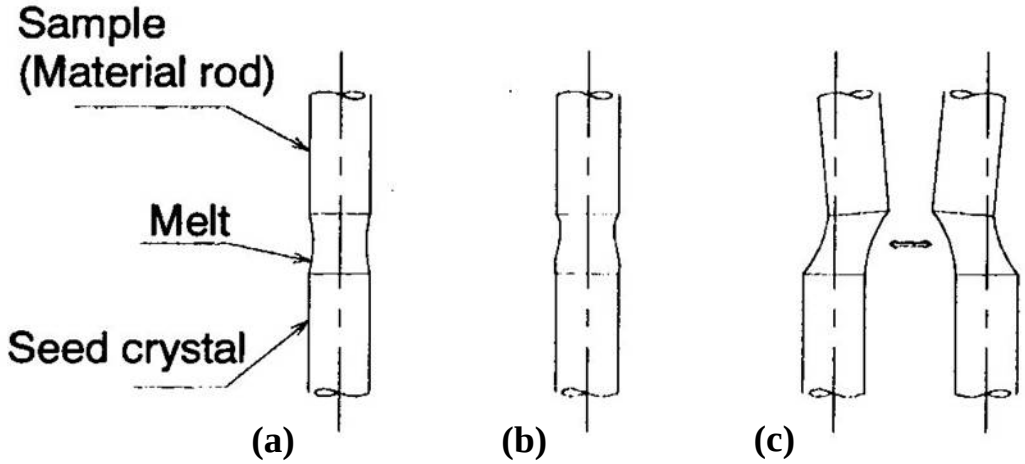


**Fig. 3.2** A molten zone **(a)** in normal state, **(b)** when power is excessive and **(c)** when power is insufficient.

The temperature profile in a traditional double elliptic mirror furnace is shown in **Fig. 3.3 (a)**. The temperature distribution around the horizontal plane in the furnace is not

homogeneous (see **Fig. 3.3 (c)**) and this is disadvantageous for the growth of high quality single crystals. As a result of the temperature inhomogeneity, only the sides of the feed rod that are close to the lamps are melted as displayed in **Fig. 3.3 (b)**. Maintaining a homogeneous temperature distribution is critical for the growth and rotation along the vertical axis diminishes the temperature inhomogeneity in the horizontal plane. So the feed rod and the seed crystal are directed to spin in opposite directions, with the same speed, to guarantee a homogenous melt. If the rods are not rotated, the inhomogeneity will have strong and unexpected influences on the growth of high quality single crystals. Moreover, the solid liquid interface is convex under normal circumstances and its shape depends on the rotation rates of the charge rod and the growing crystal. The convexity of the interface is decreased with increasing rotation rate[51]. The convex shape of the solid liquid interface is an important factor in decreasing the number of grains as the crystal growth proceeds. So a nominal rotation rate should be maintained for a good growth. The shape of the growing interface also depends on other growth parameters such as the travelling rate, the diameter of the growing crystal, the thermal gradient, etc[51]. These crystal parameters cannot be chosen arbitrarily as we will see in the following sections.

Once the molten zone is thus stabilized, the crystal growth is initiated by a slow downward translation of the upper and lower shafts simultaneously. This effectively corresponds to the melt traveling along the feed rod. As floating melt zone comes down and a temperature gradient is maintained, crystals start growing. The optimum/maximum growth speed depends on the material and varies between a few tenth of a millimeter and several centimeters per hour. The diameter of the crystal is controlled by the ratio of the translation velocity for the feed rod and the lower shaft. Feed rod, melt and crystal are protected within a sealed quartz tube, which allows us to grow crystals in different gas atmospheres. The external gas supply could be maintained at a required pressure too using the gas inlet and outlet shown in the **Fig. 3.1**. Care should be taken in applying an optimal pressure as any excess pressure developed might cause serious accidents during the growth. However, the set up is capable of handling a maximum pressure of 0.97 MPa. The entire growth process could be video captured by a CCD camera attached to the mirror. The infrared window between the camera and the melting zone helps us to view

the growth clearly above certain temperatures. Hence the whole process is monitored and the growth factors are controlled using a computer.

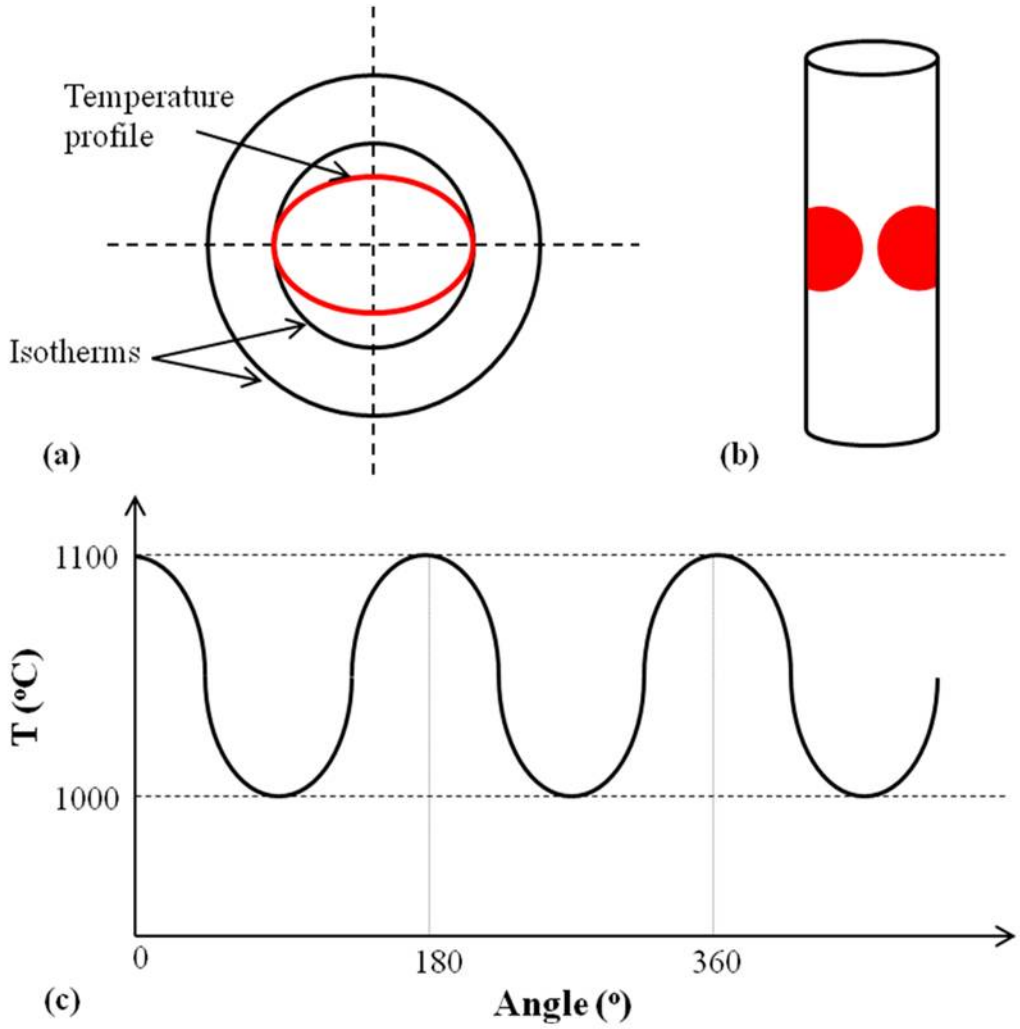


**Fig. 3.3 (a)** Illustration of temperature profile in the double mirror furnace. **(b)** The sample rod at high temperatures. Red spots represent the melted area. **(c)** Illustrated temperature (in $^{o}$C) around the horizontal plane (in angle $^{o}$) in the furnace.

In the growth of single crystals by FZ method, the molten zone is sustained by the feed rod through surface tension and therefore the qualities of the feed rod are very important and have strong influence on the stability and successful formation of the molten zone. Thus a great deal of effort has to be spent on creating a straight and uniform diameter rod. To prepare the feed and seed rods, the material to be grown is mixed in proper proportion as in the prescription. The stoichiometric ratio of the required chemicals is then ground to a fine powder using a mortar before being fired in high

temperatures in any furnace. The sintering is performed in air or other required environment viz. Nitrogen, Oxygen, Argon etc. usually up to 1000°C for 15 hours. The temperature cycle, ABCD, used for firing the powder is displayed in **Fig. 3.4**. The sintered powder is then molded into the form of a rod (of diameter around 6 mm) using commercially available balloons and pressed under high pressures (~ 30 MPa). A hand-operated hydraulic pump ($P_{max}$ ~ 100 MPa) is used to press the powdered material into the feed and seed rods. The obtained rod is removed from the balloon and fired again using the temperature cycle in **Fig. 3.4** but let to stay at the highest temperature (1000°C in this case) for 20 hours before cooling down to the room temperature. Now this regular polycrystalline rod is ready for the crystal growth.

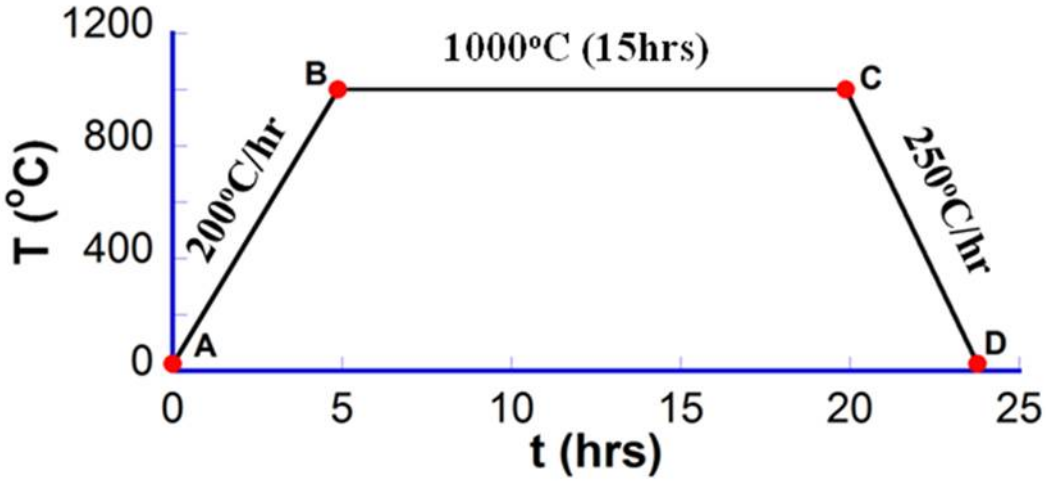


**Fig 3.4** Temperature cycle used for sintering the powdered material and the feed rod for the crystal growth.

For compounds with components that do not have a homogenous melting, it becomes increasingly difficult to grow them using this technique. Compounds based on chromium and ruthenium oxides that we tried so far faced difficulties due to this problem. I tried many times without success, to grow the Cr substituted strontium and calcium ruthenates for my study. For every trial, the thermophysical and thermochemical variable parameters including, but not limited to, temperature cycle, chemical concentration, rod pressure, shaft feed i.e. speed of the motion of the rod, gas environment and/or external pressure were altered or modified to optimize the conditions for a successful growth, which did not help. The degree of inhomogeneity in material melting was so high that some amount of material start to evaporate while the others were still solid. Just a trace of

Cr included in the material was sufficient to form bubbles that affected the melt connection process and hence the overall growth significantly. The trend was similar when I tried to grow $Nd_3Ru_{1-x}Cr_xO_7$ too. As a result of inhomogeneous melting, the material was in a rough colloidal state right through the growth process making it impossible to form any single crystal in the end.

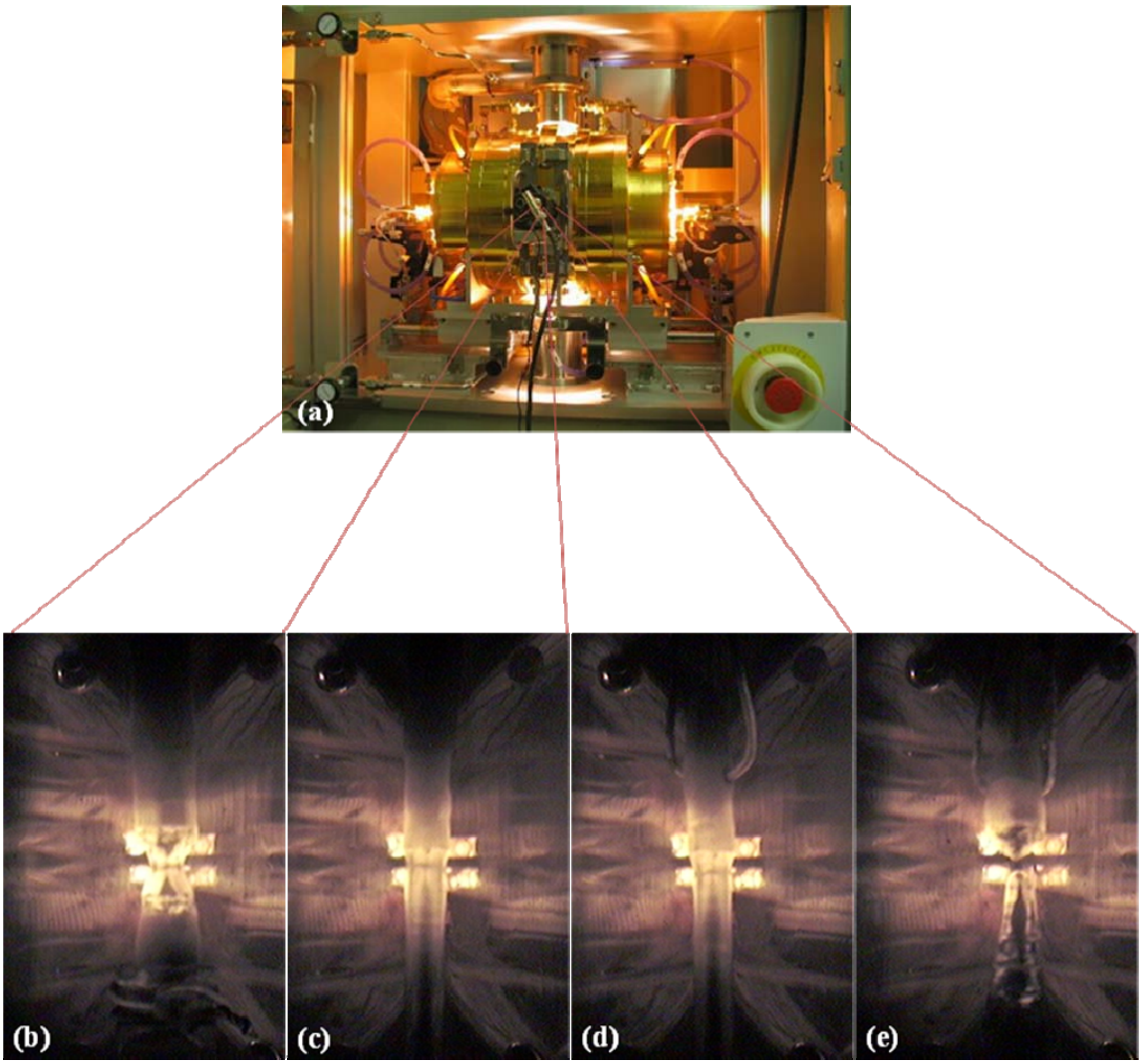


**Fig. 3.5 (a)** The Au plated double elliptic mirror of the FZ furnace in action during a crystal growth. **(b)**, **(c)**, **(d)** & **(e)** Different stages in a $MnTiO_3$ crystal growth in the order of increasing time. The bright spots indicate the melting zone, where the temperature could be as high as 2000$^{o}$C.

Although most of the crystals for my study were grown using flux technique that I will discuss in the next subsection, I have used this technique to successfully grow

transition metal oxide compounds including $MnTiO_3$, $Nd_3RuO_{7+\delta}$, $Nd_2WO_6$ and iron doped strontium and calcium ruthenate compounds. **Fig. 3.5** exhibits the Floating zone furnace during the growth process and the different stages in a $MnTiO_3$ crystal growth as monitored in the console.

**Table 3.1** *Growth parameters for some of the successful systems tried in our lab.*

| S. No. | Compounds | | Melting Voltage (V) | Travelling rate (mm/hr) | | Environment | |
|---|---|---|---|---|---|---|---|
| | Final product | Starting ratio | | Shaft feed | Gap adjust--ment | Type | Pressure (MPa) |
| 1 | $BaTiO_3$ | Ba:Ti (1:1) | 54.40 | 5 | 0.30 | 100% $O_2$ | 0.25 |
| 2 | $Ca_2Fe_2O_5$ | Ca:Fe (3:2) | 43.10 | 20 | 0.20 | 100% $O_2$ | 0.30 |
| 3 | $Ca_3Ru_2O_7$* | Ca:Ru (3:2) | 73.00 | 35 | 0.15 | 30% $O_2$ – 70% $N_2$ | 0.20 |
| 4 | $Ca_2(Ru_{1-x}Ti_x)O_4$; x=0.05 | Ca:Ru:Ti (2:0.95:0.05) | 64.00 | 11 | 0.15 | 100% $O_2$ | 0.30 |
| 5 | $MnTiO_3$ | Mn:Ti (1:1) | 39.7 | 15 | 0.15 | 100% $O_2$ | 0.30 |
| 7 | $Nd_3RuO_{7+\delta}$ | Nd:Ru (2:1.2) | 60.50 | 20 | 0.20 | 30% $O_2$ – 70% $N_2$ | 0.25 |
| 8 | $Nd_2WO_6$ | Nd:W (2:1) | 55.30 | 5 | 0.15 | 10% $O_2$ – 90% $N_2$ | 0.15 |
| 9 | $Sr(Ru_{1-x}Fe_x)O_3$ x=0.10 | Sr:Ru:Fe (1:0.90:0.10) | 56.40 | 10 | 0.18 | 30% $O_2$ – 70% $N_2$ | 0.25 |

***Note:*** The rotation rates are not included in the table as they were fixed at 25 rpm for all the growths. However, for $Ca_3Ru_2O_7$ the rate was 18 rpm.

**Table 3.1** lists the growth parameters for some of the crystals grown using this technique. All the parameters are equally important in a crystal growth point of view. But for an individual compound, there might be, and are, preferences to consider. Though all the mixtures are almost treated similarly in terms of the temperature cycles, there were

few exceptions in terms of the applied pressure to form the polycrystalline rod. $Nd_3RuO_{7+\delta}$ rod for instance, has to be pressed at 40 MPa whereas for other systems it is sufficient to be done at 30 MPa. For growing $Ca_3Ru_2O_7$ single crystals, the material mixture was cooked at 400°C for 10 hours to remove any moisture from the powder before being sintered at 900°C for 15 hours (twice). The thermally treated material then was pressed into a rod and then the prepared rod was treated at 1000°C for 20 hours to be used for the growth with the parameters mentioned in **Table 3.1**. A detailed description of the optimized growth conditions for $Ca_3Ru_2O_7$ is discussed in the reference[52]. Some of the grown crystals are displayed in **Fig. 3.6** that encloses black $MnTiO_3$ (**Fig. 3.6 (a) & (b)**) and bluish $Nd_2WO_6$ (**Fig. 3.6 (c) & (d)**) single crystals grown using FZ technique.

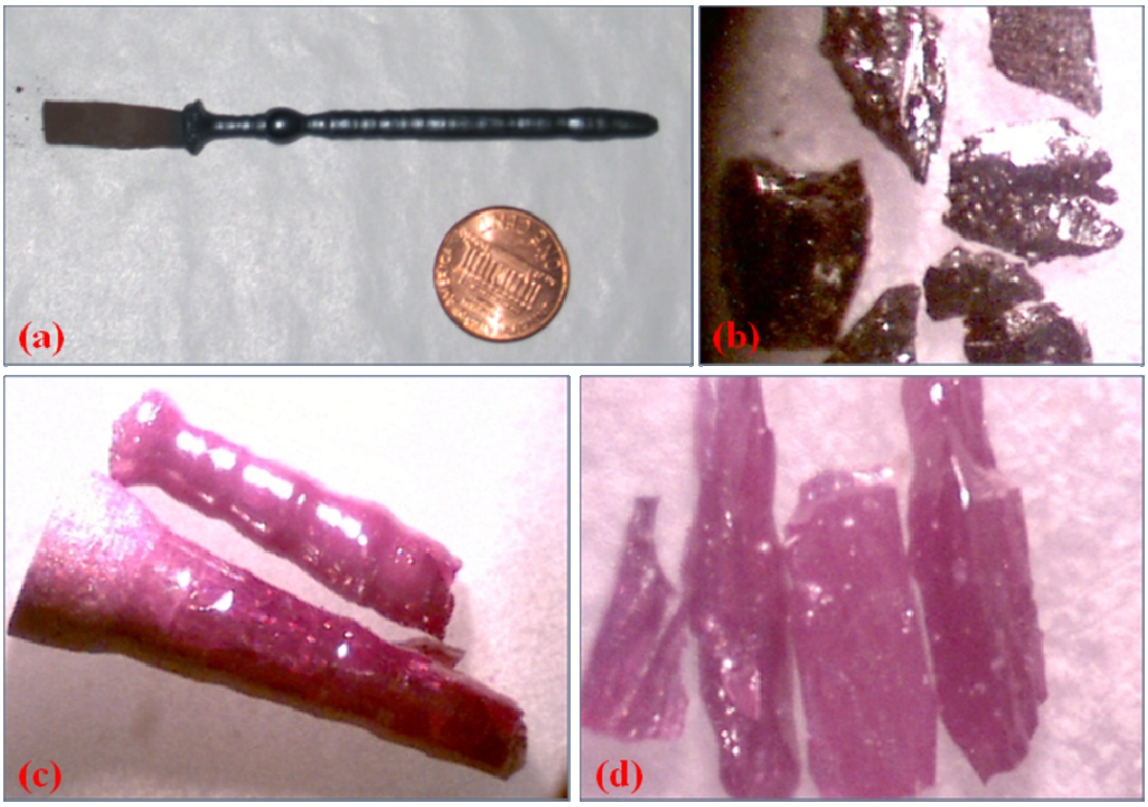


**Fig. 3.6** (*Top panel*) $MnTiO_3$ crystal **(a)** actual size and **(b)** magnified 60 times (actual size ~ 1 x 1 x 1 $mm^3$). (*Bottom panel*) Bluish $Nd_2WO_6$ crystals magnified **(c)** 10 and **(d)** 60 times (actual size ~ 2 x 1.5 x 1 $mm^3$).

***Advantages of using FZ technique:***

The major advantage in using this technique is that crystals can be grown without getting into contact with other materials, such as crucibles, hence eliminating a major

source for contaminations. Also crystals could be grown in different environments viz., gas like $O_2$, $N_2$ or a mixture of both and a positive pressure, to manipulate the oxygen or other chemical content in the final product and so on. The nature of the technique allows one to manually control the parameters viz. speed of the growth, melting temperature etc. and hence to improvise the growth process. Another advantage is the size of the crystals this technique is capable of producing. With our latest model floating zone furnace, crystals with high melting point (2050°C) as well as a large length (150 mm) can be grown. **Fig. 3.6** that displays $MnTiO_3$ and $Nd_2WO_6$ crystals gives an idea of the size of typical single crystals grown using the FZ furnace. Long growth is particularly important in the case of incongruent melting systems, where large deviations between the nominal composition and that of the grown crystal are observed in the beginning of the growth experiment. Also it becomes a requirement for us to grow larger crystals to perform neutron scattering experiments, an elegant tool to probe the magnetic ground state of a material, which needs single crystals with dimensions of the order of a millimeter.

### 3.2.3 Flux technique:

The second technique that we use to grow our single crystals is the flux technique, which is relatively simple when the growing conditions are specified. However, to devise the optimal conditions for a particular growth requires a lot of efforts and trials. Since the growth could not be monitored and controlled as in the FZ technique, one has to be 100% certain about the various growth factors for a particular compound beforehand to have a successful yield. The technique is useful particularly for Cr doping studies as Cr and Ru have inhomogeneous melting to maintain a melting zone, which makes it nearly impossible to grow these single crystals using FZ technique. The crystals are grown out of a solvent that reduces the melting point of the starting materials – the flux. The definition of a good flux denotes that it should not react with the materials to give other byproducts[53]. In my case, Calcium Chloride ($CaCl_2$) is used as a flux, when growing $Ca_3Ru_2O_7$.

To describe the process in a nutshell, the starting materials are mixed in non-stoichiometric proportion and treated in heat with the appropriate temperature cycles as shown in **Fig. 3.4** with severe modifications in the cooling cycle. When allowed to cool sequentially after reaching the highest required temperature, the crystals are formed in the

provided platinum crucibles. $Ca_3Ru_2O_7$ single crystals were grown in Pt crucibles using this technique[54] from off-stoichiometric quantities of $RuO_2$, $CaCO_3$, and $CaCl_2$. The mixture was heated to 1480°C in partially capped Pt crucibles and fired continuously for 25 hours in a box furnace. The material is then subjected to a slow cooling process where the mixture is allowed to cool at 2–3°C/hr to reach 1350°C as shown in **Fig. 3.7**. This slow cooling is followed by a rapid cooling to room temperature at a rate of around 100°C/hr.

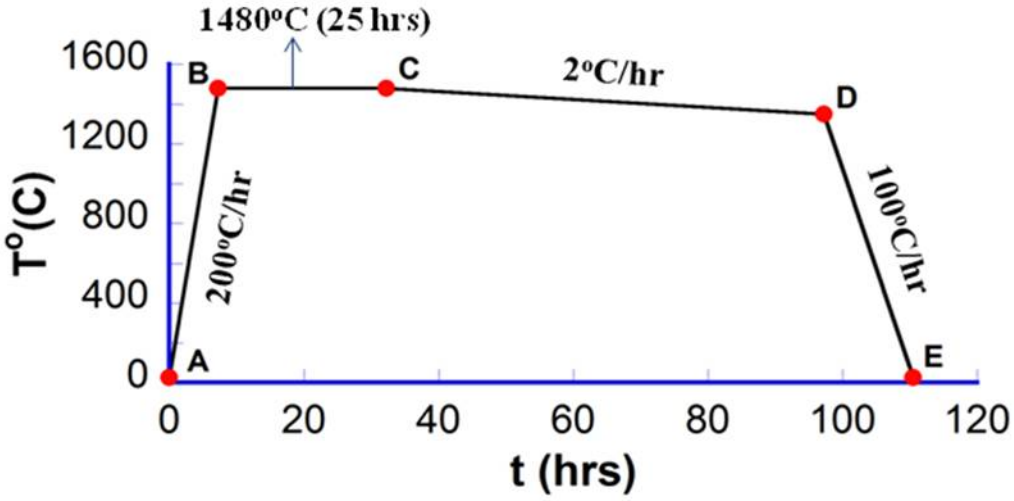


**Fig. 3.7** Temperature cycle used for growing single crystals of $Ca_3Ru_2O_7$ by the flux method.

The resulting shape of $Ca_3Ru_2O_7$ tend to be plate-like with an average size of the single crystals being around 1 x 1 x 0.4 $mm^3$ as shown in **Fig. 3.8** with the *c* axis along the shortest dimension. The starting ratio of Ca:Ru and the thermal treatments are critical to the growth and have a large influence not only on the form of crystals but also on the ratio of Ca:Ru in the final product. The balance in the starting ratio in particular is vital as the nucleation of its sister compounds $CaRuO_3$ and $Ca_2RuO_4$ is also energetically favorable.

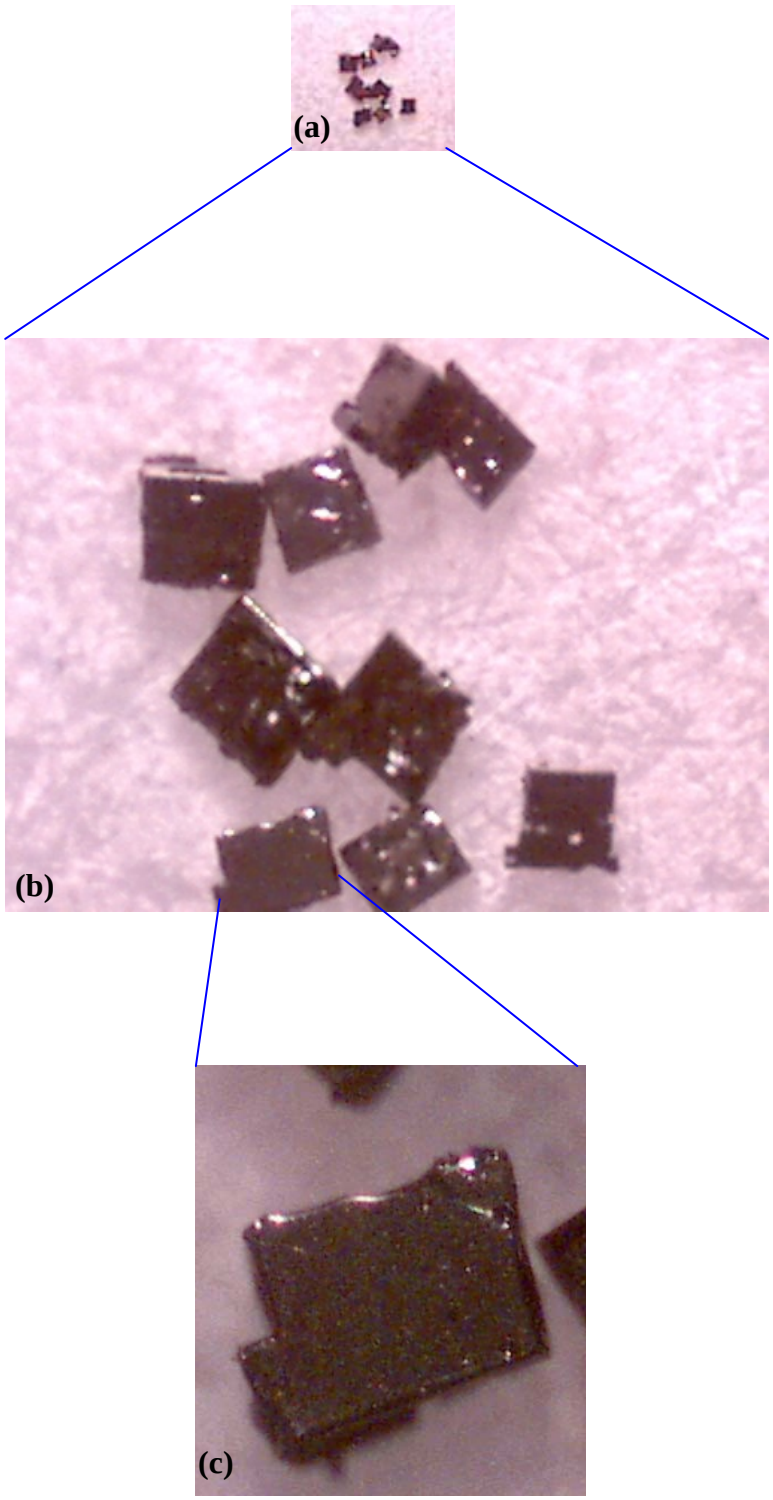


**Fig. 3.8** Flux grown $Ca_3Ru_2O_7$ crystals that are magnified **(a)** 10, **(b)** 60 and **(c)** 200 times (actual size of a single crystal ~ 0.5 x 0.4 x 0.4 $mm^3$).

***Advantages of using Flux technique:***

Flux technique, as one of the widely used technique to grow single crystals, has the following merits.

1. A variety of crystals can be grown simultaneously using this procedure
2. The crystals can be grown relatively quickly when compared to the other techniques
3. It doesn't require elaborate apparatus to grow a crystal in this method

It is the preferred approach for any program that is interested in single crystals of new materials simply because of its ability to make so many materials rapidly and simultaneously. It allows one to explore so much phase space simultaneously that the probability of growing entirely new crystals is quite high.

**3.3 Structure determination:**

Once materials are grown, the next step is to determine the structure of the crystals before we could study their physical properties. As our main motivation is to research on novel materials, the structure determination forms an integral part of it. The grown single crystals are duly characterized by X-ray Diffraction (XRD)[55] and Scanning Electron Microscopy (SEM)[56] techniques.

XRD is a high-tech, non-destructive technique for analyzing a wide range of materials including fluids, metals, minerals, polymers, catalysts, plastics, pharmaceuticals, thin-film coatings, ceramics and semiconductors. To determine the structure of a crystal, the grown crystal is mounted on a goniometer and bombarded with X-rays, producing a diffraction pattern of regularly spaced spots known as reflections. The crystal is gradually rotated and a diffraction pattern is collected for each distinct orientation of the crystal. These two-dimensional images are converted into a three-dimensional model of the density of electrons within the crystal using the mathematical method of Fourier transforms and chemical data on the sample. The positions of the atomic nuclei are deduced from this electron density and chemical data, producing a model of the atoms within the crystal. The working principle of the XRD technique is based on the Bragg's law[57] defined by,

$$2dsin\theta = n\lambda \qquad (3\text{-}1)$$

where d is the inter-plane spacing in the atomic lattice, θ is the angle between the incident beam and the scattering planes, n is an integer and λ is the wavelength of the incident X-rays as shown in **Fig. 3.9**.

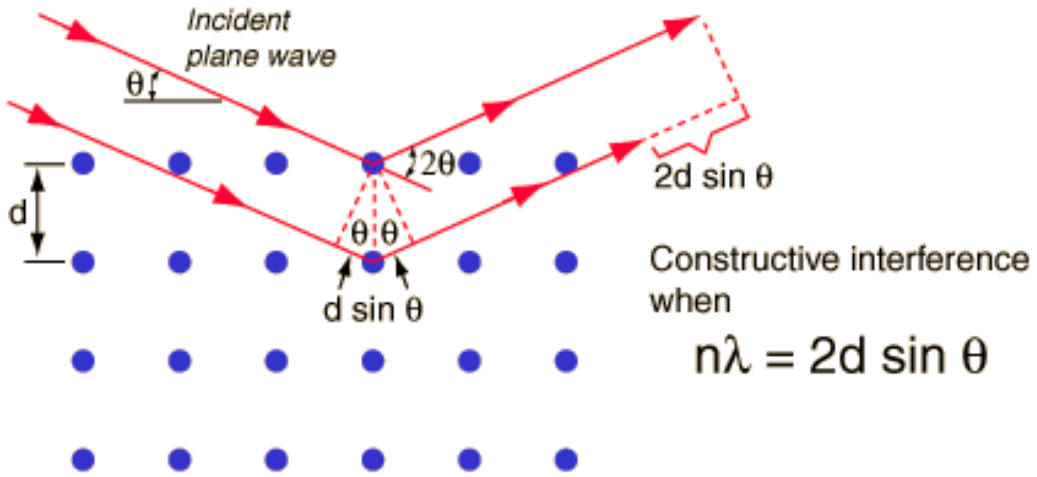


**Fig. 3.9** A diagrammatic explanation of Bragg's law.

In XRD, we normally distinguish between single crystal and polycrystalline or powder applications. The single crystal diffractometer and associated computer package is used mainly to elucidate the molecular structure of novel compounds. The Scintag powder X-ray diffractometer housed in our lab is mainly used for "finger print identification" of various solid materials. In powder or polycrystalline diffraction it is important to have a sample with a smooth plane surface. We normally grind the sample down to particles of about 0.002 mm to 0.005 mm cross section. The ideal sample is homogeneous and the crystallites are randomly distributed. The sample is pressed into a sample holder so that we have a smooth flat surface. Ideally we now have a random distribution of all possible h, k, l planes. Only crystallites having reflecting planes (h, k, l) parallel to the specimen surface will contribute to the reflected intensities. If we have a truly random sample, each possible reflection from a given set of h, k, l planes will have an equal number of crystallites contributing to it. We only have to rock the sample through the glancing angle θ in order to produce all possible reflections. The distance from the X-ray focal spot to the sample is the same as from the sample to the detector. If we drive the sample holder and the detector in a 1:2 relationship, the diffracted beam will stay focused on the circle of constant radius. The detector moves on this circle[58]. For the θ: 2-θ goniometer, such as the one in our lab, the X-ray tube is stationary, the sample

moves by the angle θ and the detector simultaneously moves by the angle 2-θ as shown in **Fig. 3.10**.

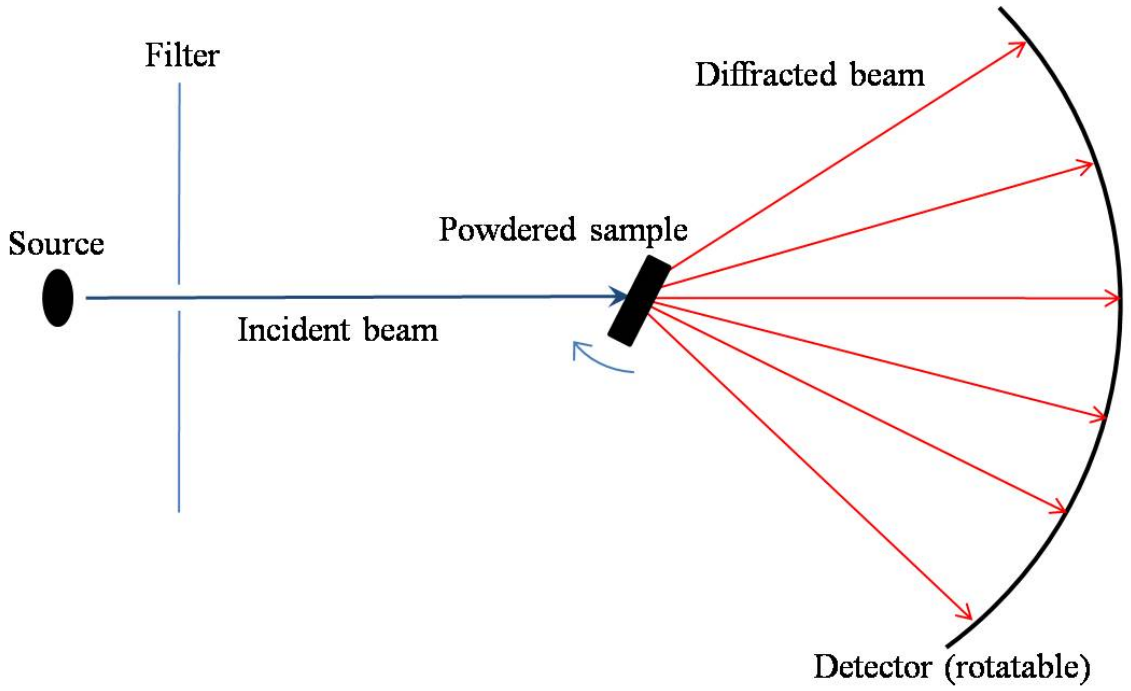


**Fig. 3.10** Working principle of an x-ray powder diffractometer.

In powder diffraction we normally utilize the line focus or line source of the tube. The line source emits radiation in all directions, but in order to enhance the focusing it is necessary to limit the divergence in the direction along the line focus. This is realized by passing the incident beam through a slit, which contains a set of closely spaced thin metal plates. Moreover, in order to maintain a constant focusing distance it is necessary to keep the sample at an angle θ and the detector at an angle of 2-θ with respect to the incident beam.

A typical diffraction spectrum consists of a plot of reflected intensities versus the detector angle 2-θ as displayed in **Fig. 3.11**. The 2-θ values for the peak depend on the wavelength of the anode material of the X-ray tube. It is therefore customary to reduce a peak position to the inter-planar spacing d that corresponds to the h, k, l planes that caused the reflection. The values of the d-spacing depend only on the shape of the unit cell. We get the d-spacing as a function of 2-θ from Bragg's law as given in 3-1. Each reflection is fully defined when we know the d-spacing, the intensity (area under the peak)

and the indices h, k, l. If we know the d-spacing and the corresponding indices h, k, l we can calculate the dimension of the unit cell.

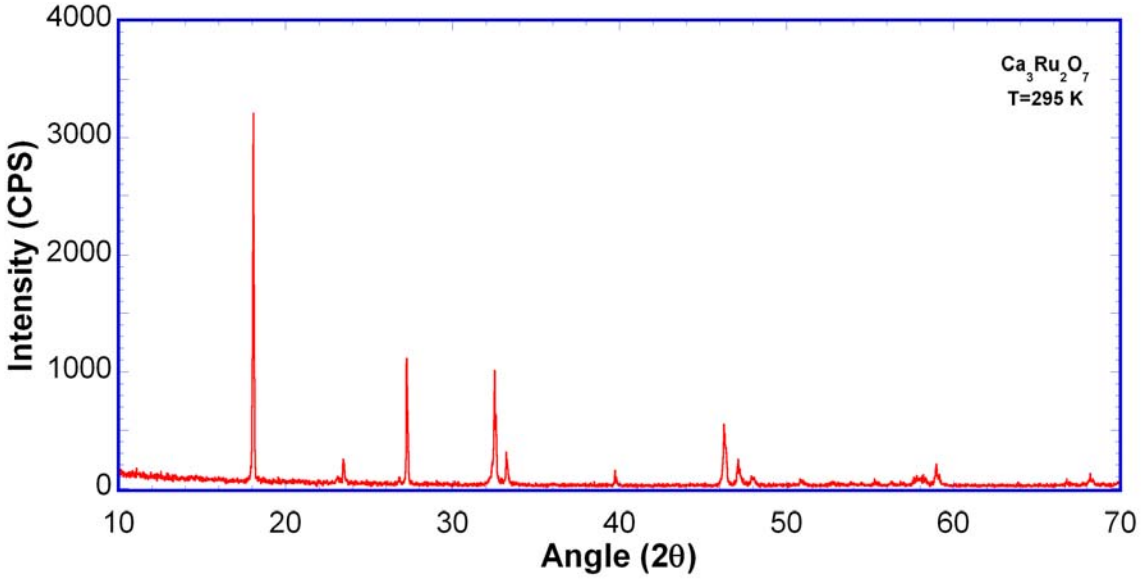


**Fig. 3.11** Intensity vs. 2θ graph for the powdered single crystals of $Ca_3Ru_2O_7$ at room temperature.

For resolving the structure of novel materials we use the single crystal XRD technique. The X-Ray laboratory at the department of chemistry in our university has a Nonius kappaCCD machine with a sealed-tube molybdenum X-ray source and a new specially configured machine based on the Bruker-Nonius X8 Proteum. A detailed description pertaining to the single crystal diffraction technique can be learned from the department's webpage[59]. The XRD spectrum in general posses the following features in chemical crystallography

- The overall symmetry of the diffraction pattern is given by symmetry of the lattice.
- Intensities of spots are determined by the basis of atoms at each lattice point.
- Sharpness and shape of spots are determined by the perfection of a crystal and liquids, glasses, and other disordered materials hence produce broad fuzzy rings instead of sharp spots.
- Any defect and/or disorder in crystals also result in diffuse scattering.

A Scanning Electron Microscope in the user facility[60] also is useful in determining the atomic composition of a crystal. It is particularly useful to know the

exact concentrations of individual elements in the chemically substituted compounds. Surface study optical microscopes use lenses to bend light and thus magnify an object. The SEM instead uses a beam of electrons controlled by electromagnets to bombard its target. When the beam strikes the object, electrons are emitted and are read by a detector which converts them to a signal. Using the same principle that creates television images, the signal is converted to an image for viewing[56]. Because the SEM provides very high magnification, it is especially useful for failure analysis and materials characterization. We use this facility for the latter application where the technique helps us in determining the phase and atomic composition of the chemically substituted compounds.

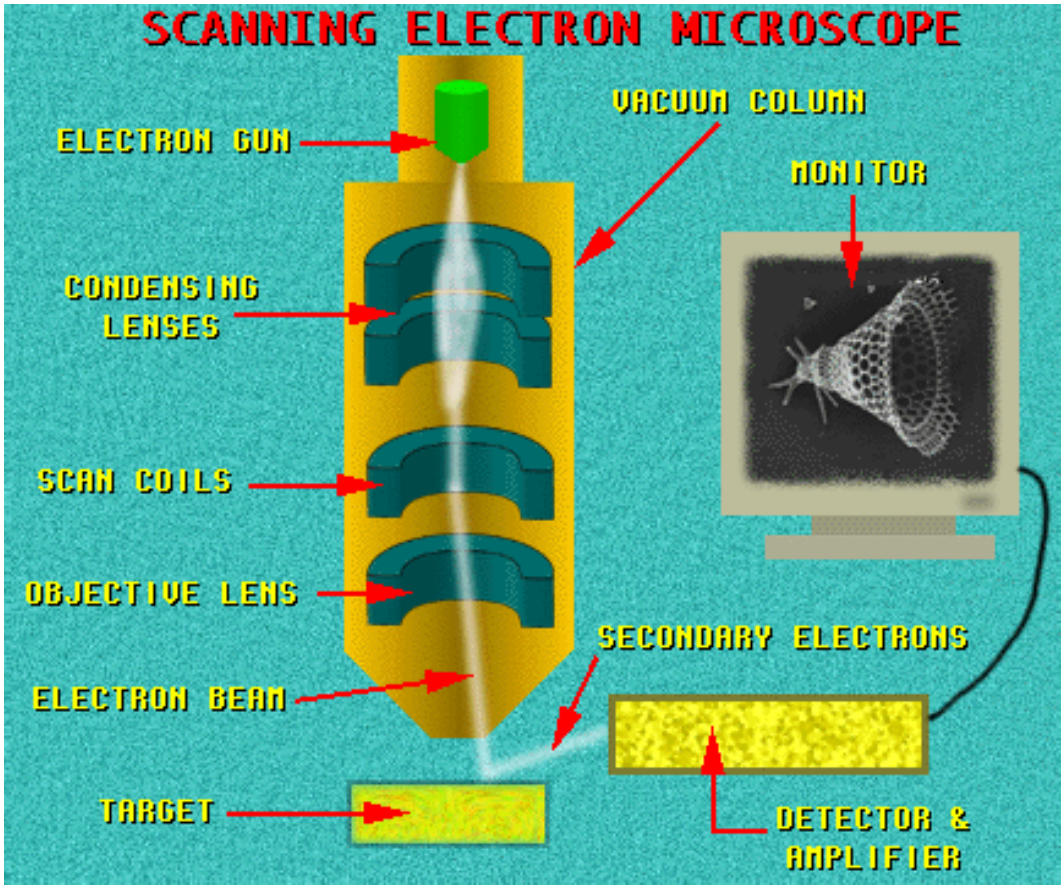


**Fig. 3.12** A schematic representation of the working of an SEM[61].

The schematic representation of an SEM is reproduced in **Fig. 3.12** (Courtesy: Museum of Science, Boston). An electron gun [at the top] emits a beam of high energy electrons. This beam travels downward through a series of magnetic lenses designed to focus the electrons to a very fine spot. Near the bottom, a set of scanning coils moves the focused beam back and forth across the specimen, row by row. As the electron beam hits

each spot on the sample, secondary electrons are knocked loose from its surface. The vacated positions are filled by higher energy electrons i.e. the electrons from the outer orbit, which emit x-rays in the process. The generated X-rays are characteristics of a particular element and by analyzing the emitted x-rays by energy dispersive X-ray analysis (EDS)[62], the elemental composition of the sample can be determined. The energy-dispersive analysis separates and detects X-rays of specific energy and displays in the form of histograms. **Fig. 3.13** shows an EDS spectrum of $CaRu_{0.82}Cr_{0.18}O_3$ that is achieved by constructing an index of X-rays collected from a particular spot on the specimen surface. The spectrum is viewed as X-ray intensity vs. X-ray energy and shows different peaks corresponding to and labeled as Ca, Ru, Cr and O.

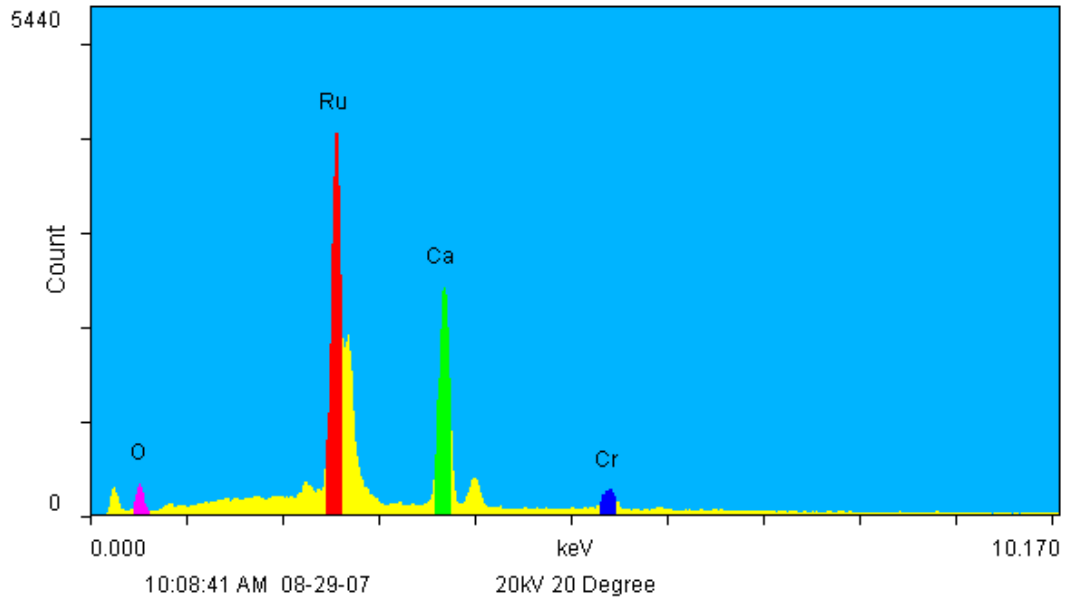


**Fig. 3.13** An EDS spectrum of $CaRu_{0.82}Cr_{0.18}O_3$ showing Ca, Ru, Cr and O peaks.

### 3.4 Magnetic property measurement:

We use DC magnetic susceptibility measurement technique to study the magnetic property of our systems. A Superconducting Quantum Interference Device (SQUID) is the most sensitive available device for measuring magnetic fields. Based on this sensitive device the so called 'SQUID magnetometers' have been developed. SQUID magnetometers are used to characterize materials when the highest detection sensitivity over a broad temperature range and using applied magnetic fields up to several Tesla is

needed. The system is designed to measure the magnetic moment of a sample, from which the magnetization and magnetic susceptibility can be obtained. The commercially available SQUID magnetometer from Quantum Design, MPMS® XL, in our lab has the capability of measuring samples in the temperature range $1.7 < T < 400$ K and in the field range $-7 < B < 7$ T.

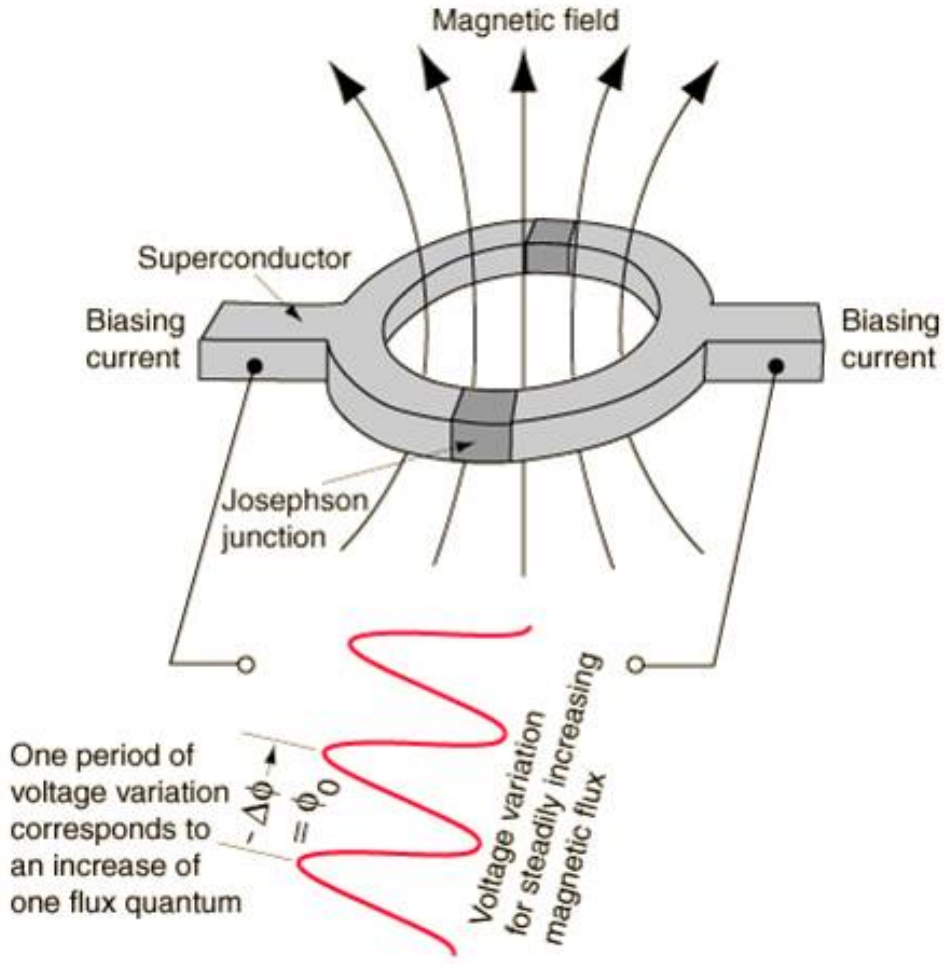


**Fig. 3.14** A schematic representation of the working principle of a SQUID magnetometer[63].

SQUID magnetometers are classified within the flux methods of measuring magnetization of a sample. A SQUID uses the properties of electron-pair wave coherence and Josephson junctions to detect very small magnetic fields. It consists of two superconductors separated by thin insulating layers to form two parallel Josephson junctions. The critical current across the junctions is much less than that of the whole ring. This produces a very low current density making the momentum of the electron-

pairs small. The wavelength of the electron-pairs is thus very long leading to little difference in phase between any parts of the ring. Now if a magnetic field is applied perpendicular to the plane of the ring, a phase difference is produced in the electron-pair wave along the opposite paths across the junctions. A small current is also induced to flow around the ring, producing a phase difference across the junctions. Normally the induced current would be of sufficient magnitude to cancel the flux in the hole of the ring but the critical current of the junctions prevents this. The circulating current has a periodic dependence on the magnitude of the applied magnetic field with a period of variation of $\Phi_0$, a very small amount of magnetic flux given in terms of quantized units as

$$\Phi_0 = \frac{2\pi\hbar}{(2e)} \sim 2.0678 \text{ x } 10^{-15}\ T.m^2 \qquad (3\text{-}2)$$

If a constant biasing current is maintained in the SQUID device, the measured voltage oscillates with the changes in phase at the two junctions, which depends upon the change in the magnetic flux. Counting the oscillations allows one to evaluate the flux change which has occurred. **Fig. 3.14** illustrates schematically its principle; the measurement of the flux change through a pick-up coil system with a SQUID. This signal is proportional to the magnetic moment of a sample which is magnetized by the magnetic field produced by a superconducting magnet[64].

The main components of a SQUID magnetometer are: (a) a superconducting magnet, which is a solenoid made of superconducting wire that must be kept at liquid helium temperature in a liquid-helium dewar. The uniform magnetic field is produced along the axial cylindrical bore of the coil. (b) Superconducting detection coil which is coupled inductively to the sample. The coil is a single piece of superconducting wire configured as a second-order gradiometer (see **Fig. 3.15**). This pick-up coil system is placed in the uniform magnetic field region of the solenoidal superconducting magnet[64]. (c) A SQUID, connected to the detection coil, which is usually a thin film that functions as an extremely sensitive current-to-voltage-converter. High sensitivity is possible because this device responds to a fraction of the flux quantum. As shown in **Fig. 3.15**, a measurement is done in this equipment by moving the sample through the second-order gradiometer. Hence, the magnetic moment of the sample induces an electric current in the pick-up coil system. A change in the magnetic flux in these coils changes the persistent current in the detection circuit. So, the change in the current in the detection coils

produce variation in the SQUID output voltage proportional to the magnetic moment of sample[64]. (d) Superconducting magnetic shield is used to shield the SQUID sensor from the fluctuations of the ambient magnetic field of the place where the magnetometer is located and from the large magnetic field produced by the superconducting magnet. A detailed description each of the components could be viewed from reference[65].

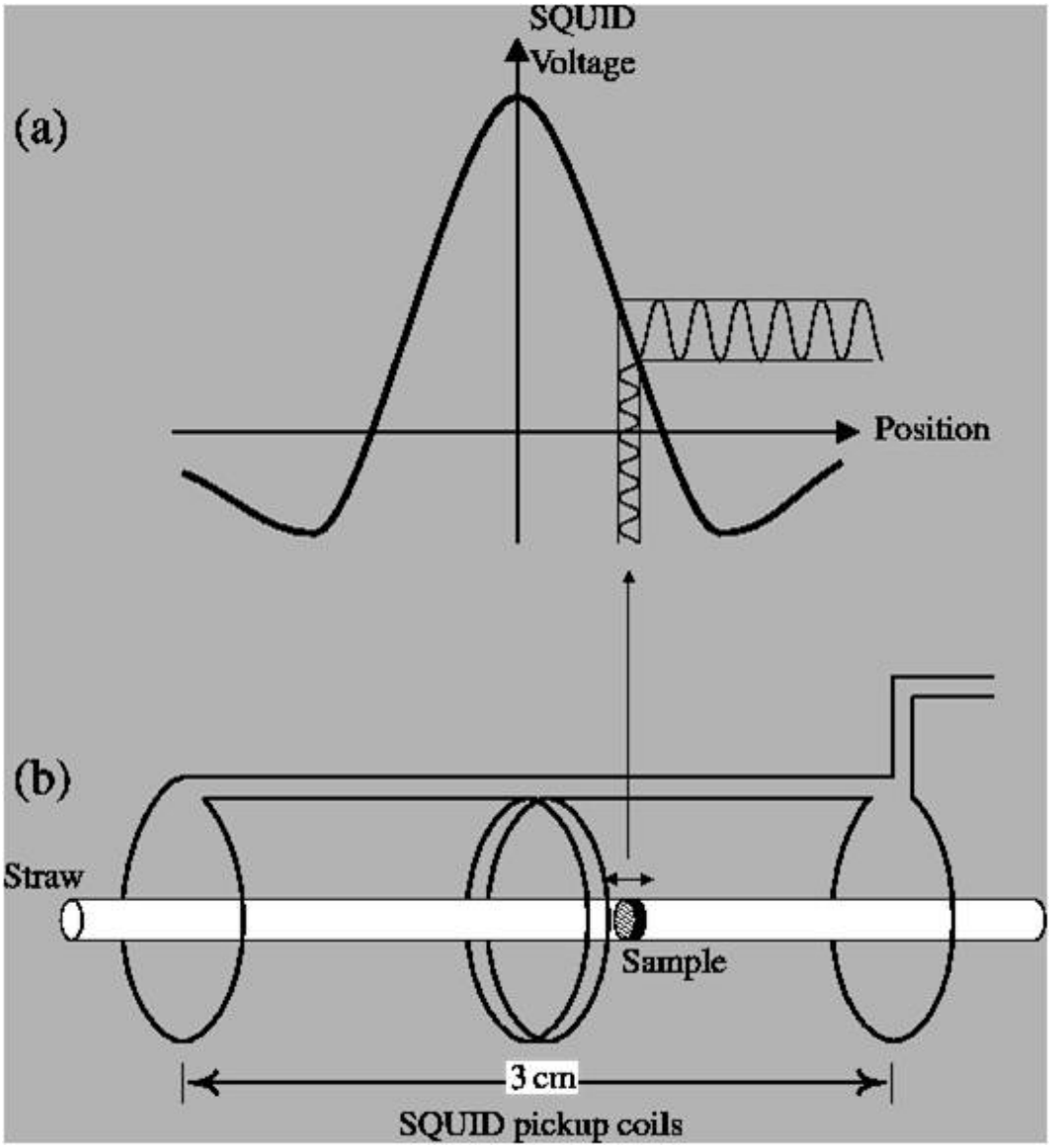


**Fig. 3.15 (a)** Voltage measurement vs. position **(b)** A polycrystalline sample measurement using a SQUID magnetometer[65].

### 3.5 Transport property measurement:

Electron transport properties of the grown crystals are determined by performing simple resistance measurements.

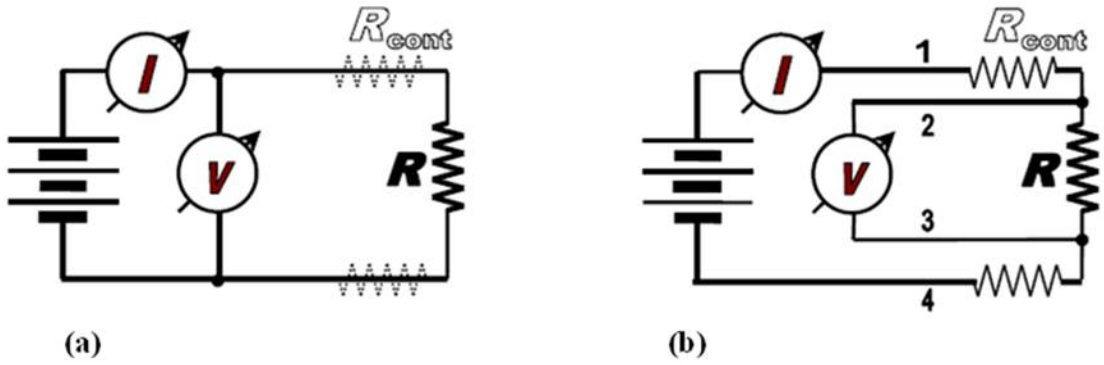


**Fig. 3.16** Circuit diagrams representing **(a)** Two probe and **(b)** Four probe techniques of resistivity measurements.

In a two-probe measurement such as the one shown in **Fig. 3.16 (a)**, the contact resistances ($R_{cont}$) add to the unknown resistance of connecting wires (R) and contribute to the measured voltage (V). Hence,

$$V = I(R + 2R_{cont}) \sim IR \text{ for } R_{cont} \ll R \qquad (3\text{-}3)$$

Typically the resistance of the point of contact is far smaller than the resistance of the sample, and can thus be ignored. However, when one is measuring a very small sample resistance, especially under variable temperature conditions, the contact resistance can dominate and completely obscure changes in the resistance of the sample itself. This is the situation that exists for superconductors. The measurement then becomes erroneous and unreliable. To overcome this error in resistivity measurement a four probe technique is used where separate contacts are used for current and voltage leads as shown in **Fig. 3.16 (b)** to eliminate the effects of contact resistance. In this diagram, four wires have been attached to the test sample denoted by a resistance R. A constant current is made to flow the length of the sample through probes labeled 1 and 4 in the figure that are usually called "current probes". If the sample has any resistance to the flow of electrical current, then there will be a drop of potential (or voltage) as the current flows along the sample, for example between the two wires (or probes) labeled 2 and 3 in the figure ("voltage probes"). The resistance of the sample between probes 2 and 3 is the ratio of the voltage registering on a voltmeter connected to the leads to the value of the output current of the power supply. Since the high impedance of the voltmeter minimizes the current flow through the portion of the circuit comprising the voltmeter, there is no potential drop across the contact resistance associated with probes 2 and 3. Hence only the resistance

associated with the sample between probes 2 and 3 is measured. In our lab we use a Keithley SourceMeter (Model 2400)[66] as power supply and a Nanovoltmeter (Model 2182)[67] to measure the resistivity of samples.

For high precision results, we also use a LR 700 ac bridge that employs a four lead AC technique to measure the sensor. Two leads are used to apply a fixed amplitude ac current to the sensor resistor. Two additional leads send the resultant sensor voltage back to the bridge to be balanced against an equal and opposite ac voltage. Knowing the equal and opposite value of the AC voltage gives the value of the sensor resistance.

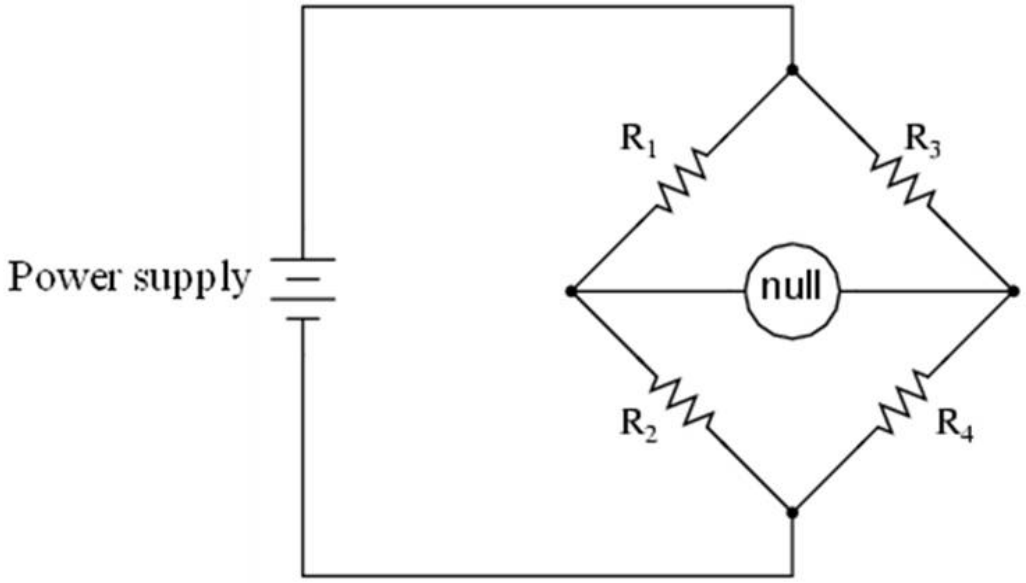


**Fig. 3.17** A representative balanced bridge showing a "null" on the indicator.

The bridge circuit works as a pair of two-component voltage dividers connected across the same source voltage, with a null-detector meter movement connected between them as shown in **Fig. 3.17** to indicate a condition of "balance" at zero volts. Any one of the four resistors in the above bridge can be the resistor of unknown value, and its value can be determined by a ratio of the other three, which are "calibrated," or whose resistances are known to a precise degree. When the bridge is in a balanced condition (zero voltage as indicated by the null detector), the ratio works out to be

$$\frac{R_1}{R_2} = \frac{R_3}{R_4} \tag{3-4}$$

One of the advantages of using a bridge circuit to measure resistance is that the voltage of the power source is irrelevant. Practically speaking, the higher the supply voltage, the

easier it is to detect a condition of imbalance between the four resistors with the null detector, and thus the more sensitive it will be. A greater supply voltage leads to the possibility of increased measurement precision. However, there will be no fundamental error introduced as a result of a lesser or greater power supply voltage unlike other types of resistance measurement schemes. Also the AC technique allows for voltage resolution down to the sub-nanovolt region.

While measuring the resistivity of samples, a broad temperature range could be covered in our lab, say $1.7 < T < 900$ K, involving different cryostats. The Displex closed cycle cryostat (Advanced Research Systems DE202) is mainly used for high temperature measurements (9-900 K) whereas the added transport function to our MPMS® XL takes care of the low temperature (1.7-400 K) and infield (±7 T) measurements. The electrical contacts in the crystals were made using 0.001' gold wires attached through less resistive silver epoxies (EPOXY E3084 + EPOXY T6081). And the samples were fixed to the sample holder in the probe using thermally conducting and electrically insulating glue (AREMCO Ceramabond 865) for high temperature measurements.

**3.6 Specific heat capacity measurement:**

The heat capacity of our crystals at constant pressure is measured by the heat capacity function added to the Quantum Design PPMS®. Using this function, the measurement could be performed in the temperature range $1.8 < T < 400$ K and in an applied field of ±9 T. The heat capacity function uses the thermal relaxation technique[68] that controls the heat added to and removed from a sample while monitoring the resulting change in temperature. A known amount of heat is applied at constant power for a fixed time and then this heating period is followed by a cooling period of the same duration.

The heat capacity puck utilizes the standard PPMS 12-pin format for electrical connections, and it provides a small microcalorimeter platform for mounting the sample[69]. Samples are mounted to this platform by a standard cryogenic grease or adhesive such as Apiezon N or H Grease. The sample platform is suspended by eight thin wires that serve as the electrical leads for an embedded heater and a thermometer connected to the bottom of the platform. These small wires not only form a well-defined thermal connection between the sample platform and the puck but also provide a structural support for the platform. An additional thermometer embedded in the puck

provides a highly accurate determination of the puck temperature, and a thermal shield aids in maintaining stable sample temperature and uniformity.

A single heat capacity measurement consists of several distinct stages. First, the sample platform and puck temperatures are stabilized at some initial temperature. Power is then applied to the sample platform heater for a predetermined length of time, causing the sample platform temperature to rise. When the power is terminated, the temperature of the sample platform relaxes towards the puck temperature. The sample platform temperature is monitored throughout both heating and cooling, providing the raw data of the heat capacity calculation. Two separate algorithms fully automate the analysis of the raw data. The most general analysis method invokes the two-tau model[70] which assumes that the sample is not in good thermal contact with the sample platform. The values of the heat capacity and other physical parameters are determined by optimizing the agreement between the measured data and the two-tau model. In the two-tau model, the first time-constant ($\tau_1$) represents the relaxation time between the sample platform and the puck, and the second time constant ($\tau_2$) represents the relaxation time between the sample platform and the sample itself. A second analysis is also performed using a simpler model that assumes perfect thermal coupling between the sample and the sample platform. The heat capacity software determines which model best fits the measured data and automatically saves the values of the sample heat capacity, addenda heat capacity, thermal coupling between the sample and the platform, thermal time-constants, and other information to the data file.

These are few of the experimental techniques available to-date in our lab. The exciting results from the experiments done using these techniques will be discussed in detail in Chapter 4.

## Chapter Four

## Thermodynamics and transport properties of $Ca_{n+1}(Ru_{1-x}Cr_x)_nO_{3n+1}$

### 4.1 Introduction:

The extended nature of the 4d orbitals in ruthenates gives way to competing energies in CEF, Hund's rule interaction, p-d hybridization, SO interaction and Electron-Phonon coupling. These competing interactions enhance strong correlation between electrons and hence a remarkable range of complex physical behaviors in the compounds is inevitable. The observed physical properties of the series are very sensitive to structure dimensionality as we will see in the next section. The diversity of the observed electronic and magnetic properties in these compounds is amazing, as the compounds are all based on the $Ru^{4+}$ ion in octahedral environments with corner sharing topologies as discussed in chapter 1. In numerous strongly correlated electron systems, such as the RP series, different degrees of freedom, such as the spin, orbitals and lattice deformations are inextricably coupled. These degrees of freedom are coupled usually by Coulomb interactions and the specifics of the crystal structure. The coupling could also be due to alloying. Such systems are often characterized by competing ground states that are susceptible to external perturbations viz. magnetic field, pressure or chemical doping. Tuning the external parameters in these compounds may lead to a quantum critical point and stabilize different ground states with exotic properties as illustrated in the cuprate superconductors[71].

In this chapter, I will give an overview of the physical properties of the layered ruthenates in the initial paragraphs before discussing in detail the properties of selected members of the series viz. robust itinerant ferromagnetic $SrRuO_3$, paramagnetic "bad" metal $CaRuO_3$ and Mott-like bi-layered $Ca_3Ru_2O_7$, towards the later part of the chapter. For all these compounds, I will discuss the intrinsic physical properties before disclosing their sensitivity to chemical substitution, through some of our doping studies – giving more emphasis to Cr substitution.

### 4.2 Evolution of physical properties:

The layered ruthenates, i.e., the RP series $(Sr, Ca)_{n+1}Ru_nO_{3n+1}$ (n=number of Ru-O layers/ unit cell), are a class of correlated electron materials showing a rich variety of properties. The physical properties of the ruthenates are critically linked to n and to the

cation (Ca or Sr), which lead to different ground states and inter- and intra- layer magnetic couplings. The Ru ions are surrounded by O ions forming octahedral such that two Ru ions interact only through O as explained in chapter 1. The deformations and relative orientations of these corner-shared octahedra crucially determine the crystalline-field splitting, the band structure, and hence the magnetic and transport properties in these compounds.

As a result, $Sr_{n+1}Ru_nO_{3n+1}$ compounds are metallic and tend to be ferromagnetic with the single layered $Sr_2RuO_4$ (n=1)[72-75] being an exception, which is a p wave superconductor ($T_C$=1.8 K). The double layered $Sr_3Ru_2O_7$ (n=2)[76,77] is a paramagnet showing an enhancement in magnetic susceptibility at T=20 K (**Fig. 4.1(a)**). The triple layered compound $Sr_4Ru_3O_{10}$ (n=3)[78] shows a ferromagnetic behavior with $T_C$=105 K when magnetic field is applied parallel to the c axis. On the other hand, for magnetic field applied perpendicular to the c axis it shows a metamagnetic transition at $B_C$=3 T (not shown here), suggesting a borderline magnetism[79] existing in the compound. The perovskite $SrRuO_3$ (n=∞)[80, 81] is a robust itinerant ferromagnet with $T_C$=165 K. All these compounds in the series show metallic behavior for a broad range of temperatures, 1.7 < T < 800 K as shown in **Fig. 4.1(b)**. For temperatures above $T_C$, they all show a linear dependence on temperature as a consequence of the scattering off short-range spin fluctuations at the proximity to $T_C$, which is expected according to Fisher-Langer theory. In general, all the Sr related compounds tend to be metallic ferromagnets and the strength of the ferromagnetic coupling increases as we increase the number of Ru-O octahedral layers as seen in **Fig. 4.1(a)**.

But the Calcium based compounds behave in a completely different manner under the same physical conditions. The n=1 compound, $Ca_2RuO_4$[82] is a Mott insulator ($T_{MI}$=357 K) with antiferromagnetic ordering at $T_N$=110 K (see **Figs. 4.2 (a)** and **(b)**). The bi-layered $Ca_3Ru_2O_7$ (n=2)[83] shows a metal insulator transition at T=48 K and an antiferromagnetic ordering at $T_N$=56 K. On the other hand, the perovskite $CaRuO_3$ (n=∞)[84] compound is a paramagnetic metal up to the lowest possible temperatures suggesting the critical temperature, $T_C$~0 K, if any present. In general, the calcium related compounds are all antiferromagnetic and are on the verge of metal insulator transitions unlike their sister compounds with Sr cations. Also in contrast to the increasing

ferromagnetic coupling strength in Sr related compounds, the antiferromagentic coupling gets weaker as we progress through the number of Ru-O octahedral layers in the Ca compounds as shown in **Fig. 4.2(a)**.

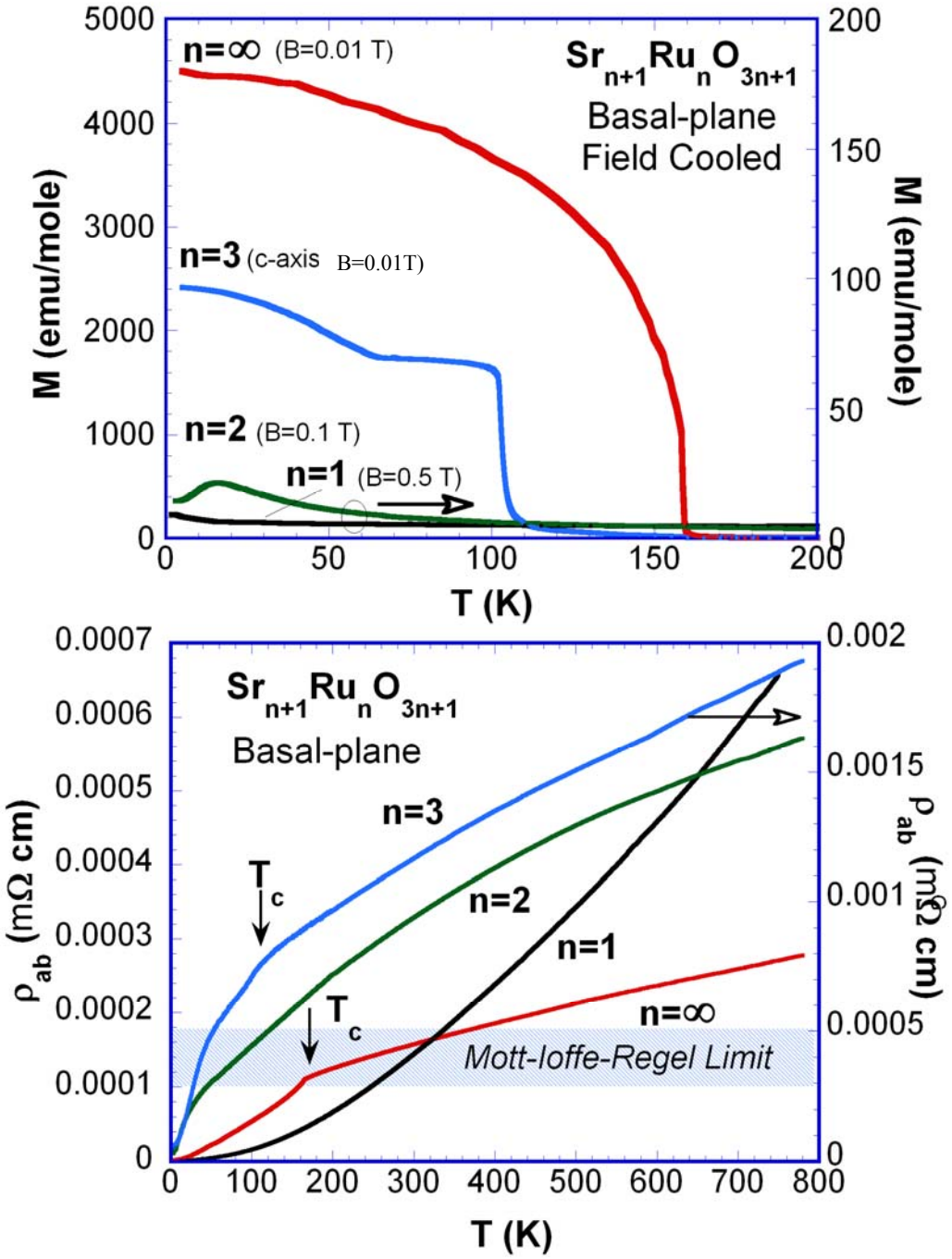


**Fig. 4.1 (a)** Magnetization, M, and **(b)** Electrical resistivity in the basal plane, $\rho_{ab}$, as a function of temperature for $Sr_{n+1}Ru_nO_{3n+1}$[11].

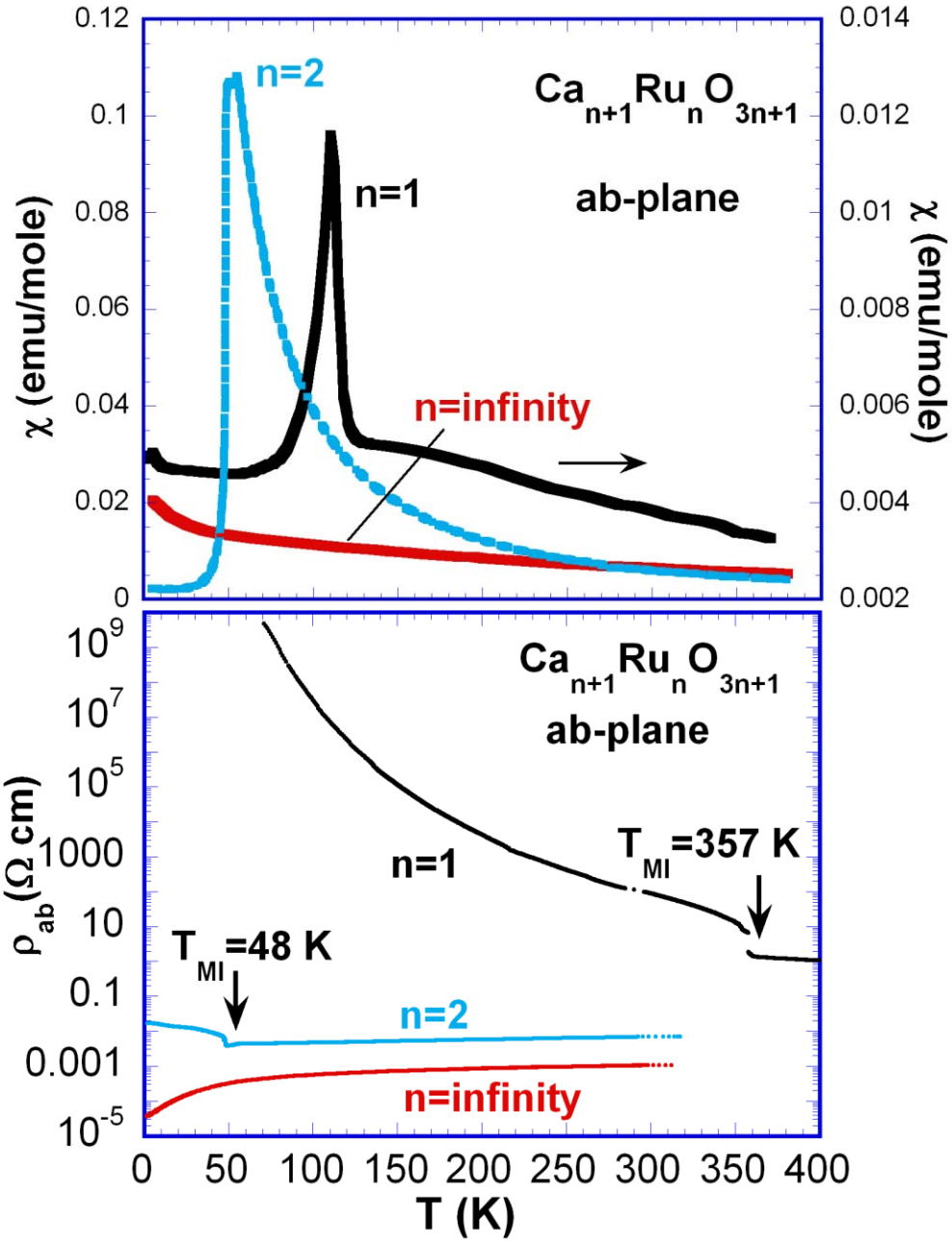


**Fig. 4.2** Temperature dependence of **(a)** Magnetic Susceptibility (χ) and **(b)** basal plane electrical resistivity ($\rho_{ab}$) for $Ca_{n+1}Ru_nO_{3n+1}$[82, 83, 84].

The difference in the ground state of the iso-electronic compounds (Sr, Ca)$_{n+1}Ru_nO_{3n+1}$ is attributed to the coupling of physical properties to the structural distortion in the Ca related compounds as a result of the difference in the ionic sizes. $Ca^{2+}$ ion is smaller ($r_{Ca}^{2+}$ ~ 1 Å) when compared to that of the $Sr^{2+}$ ion ($r_{Sr}^{2+}$ ~ 1.18 Å). The

smaller ionic size of $Ca^{2+}$ forces a tilting and rotation of the Ru-O octahedral by an angle that helps in narrowing the band width that is not favorable for a ferromagnetic ground state whereas the less distorted Ru-O octahedral in Sr compounds favors a ferromagnetic ground state. Hence, controlling the orientation of the octahedra by changing the chemical composition therefore opens a unique opportunity to systematically tune physical properties in these materials. No such behavior has been observed in other transition-metal RP systems, which makes these compounds special. It is also worth mentioning that as a result of the more distorted structure, the calcium ruthenates are very sensitive to oxygenation (Sensitivity of $Ca_3Ru_2O_7$ to oxygen will be discussed in section 4.4.12), whereas the Strontium counterparts, the less distorted structures of the two, are less sensitive to oxygen treatment.

**4.3 Perovskite ruthenates (n=∞):**

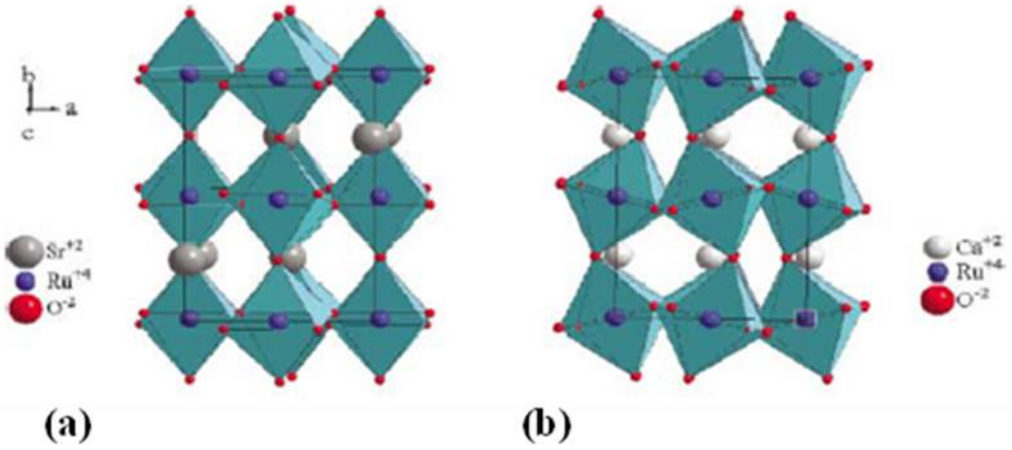


**Fig. 4.3** Crystal structure of **(a)** $SrRuO_3$ and **(b)** $CaRuO_3$[85]. Note that the structure of $SrRuO_3$ is more ideal and less distorted than that of $CaRuO_3$.

The most extensively studied ruthenates to-date in the RP series are the perovskite compounds viz. $CaRuO_3$ and $SrRuO_3$. The three dimensional $SrRuO_3$ and $CaRuO_3$ are members of the $(Ca, Sr)_{n+1}Ru_nO_{3n+1}$ series with n=∞, the number of Ru-O layers. Both the compounds crystallize in $GdFeO_3$ type orthorhombic perovskite structure with different structural distortions. A schematic representation of the crystal structure of $SrRuO_3$ and $CaRuO_3$ is displayed in **Fig. 4.3**. The crystal structure of $SrRuO_3$ (**Fig. 4.3 (a)**) is less distorted and is close to an ideal perovskite structure. On the other hand, in the $CaRuO_3$ structure (**Fig. 4.3 (b)**), the $RuO_6$ octahedra are severely distorted because of the smaller

ionic size of the $Ca^{2+}$ ion in the structure. This dissimilarity in the structure is reflected promptly in the observed physical properties and will be discussed in the following paragraphs.

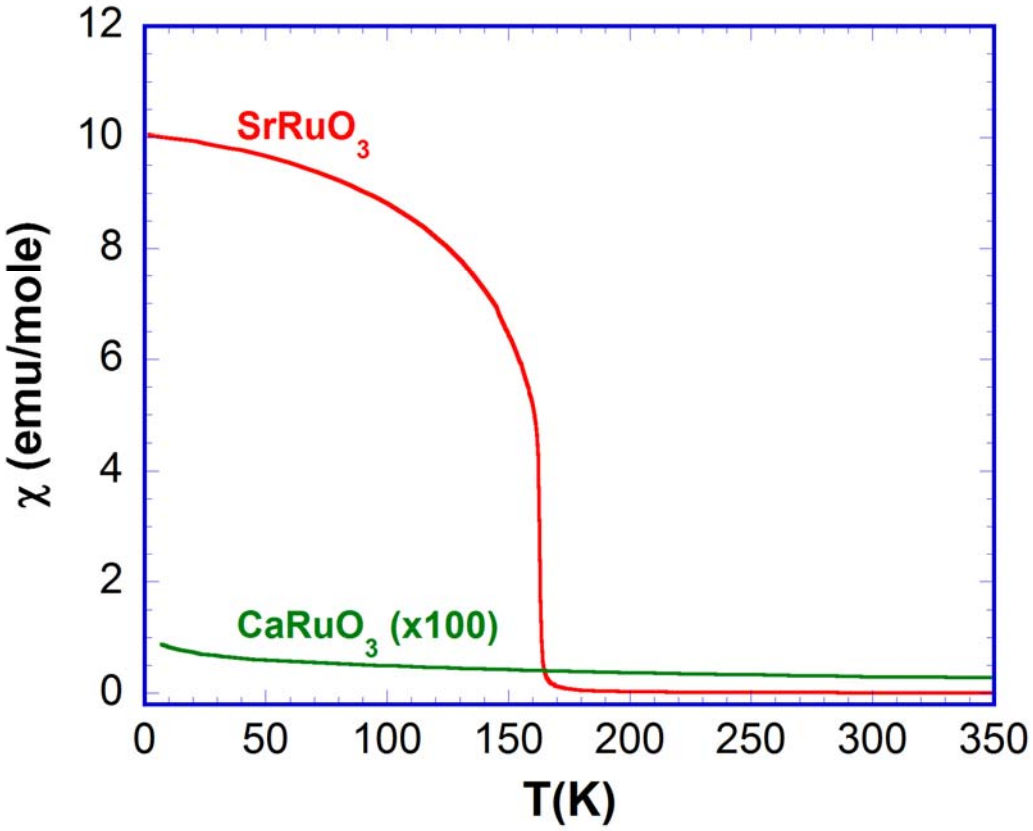


**Fig. 4.4** Magnetic susceptibility, $\chi$, of both $SrRuO_3$ and $CaRuO_3$ as a function of temperature, T, for $1.7 \leq T \leq 350$ K. Note that the susceptibility for $CaRuO_3$ is multiplied by 100 for convenience.

Electronic band structure calculations indicate that the perovskite ruthenates are poised between nearly energetically equivalent antiferromagnetic and ferromagnetic ground states[86]. The experimental results on magnetic measurements are shown in **Fig. 4.4**, where the magnetic susceptibilities of the perovskite ruthenate compounds are exhibited. $SrRuO_3$ is characterized by a robust ferromagnetic transition[80, 81] at the Curie temperature, $T_C$=165 K. It is one of only a few known ferromagnetic systems among the 4d-related transition metal oxides[87]. On the other hand, $CaRuO_3$ exhibits a paramagnetic ground state up to the lowest possible temperatures. But the high temperature Curie-Weiss analysis suggests an otherwise antiferomagnetic ground state for the compound.

Hence irrespective of the fact that they both share the same crystal symmetry, their magnetic ground state displays extreme diversity: one of them shows a ferromagnetic instability whereas the other lies proximal to antiferromagnetic interactions between their spins.

The closed shell s-like character of Sr and Ca do not contribute to the density of states at the Fermi surface and therefore could not be the origin for the different magnetic ground states of these two compounds. Since the magnetic contribution could then come solely from the magnetically active $Ru^{4+}$ ion in ruthenates, one would expect a similar magnetic ground state for both the compounds as they differ only by a non-magnetic, iso-electronic ion. But their distinctness in the physical properties is as obvious as it is shown in **Fig. 4.4**. This difference in the ground state is then attributed to the basic dissimilarity in the crystal structure as a result of the disparate ionic sizes of $Sr^{2+}$ and $Ca^{2+}$ ions. The less distorted crystal structure in $SrRuO_3$ favors ferromagnetism whereas the Ru-O octahedral distortions in $CaRuO_3$ structure make it less favorable for possessing a long range order.

### 4.3.1 Itinerant ferromagnet $SrRuO_3$:

The perovskite $SrRuO_3$ is by far the most studied compound in the $Sr_{n+1}Ru_nO_{3n+1}$ series (see, for example, Refs. 11, 80, 81, 84, 86-91), so I will not spend much time and space explaining in detail all the physical phenomena observed in the system. However, I would not refrain myself from mentioning a few features of the compound that would help us later on to appreciate the effect of chemical substitution on them.

State-of-the-art band structure calculations carried out for $SrRuO_3$ in the ideal perovskite structure predicted an itinerant ferromagnetic ground state and yielded a spin moment of 1.17 $\mu_B$ per formula unit[86]. Experimental results witness that $SrRuO_3$ is indeed an itinerant ferromagnet with $T_C$=165 K (see **Fig. 4.5 (a)**) and a saturation moment of 1.10 $\mu_B$/Ru aligned within the basal plane[84]. The temperature dependence of magnetization exhibits a huge hysteresis (not shown in the figure) between field cooled (FC) and zero field cooled (ZFC) sequences that converge at $T_C$=165 K, which is a salient feature of a ferromagnet. The high temperature ($T > T_C$) paramagnetic phase follows a modified Curie-Weiss law,

$$\chi = \chi_0 + \frac{C}{(T - \theta_{CW})} \tag{4-1}$$

as shown in **Fig. 4.5 (b)**, where $\chi_0$ is the temperature independent susceptibility, C is the Curie constant and $\theta_{CW}$ is the Curie-Weiss temperature. The estimated positive value for $\theta_{CW}$ (=163 K) confirms the ferromagnetic interactions between the $Ru^{4+}$ spins that resulted in the spin polarization at $T_C$=165 K. The effective moment obtained from the Curie-Weiss fit ( $\mu_{eff} = 2.82\sqrt{C}$ ) is comparable to the theoretical value ( $\mu_{eff} = g\sqrt{S(S+1)}$ ) that is expected for an S=1 spin system. The estimated experimental value is 2.57 $\mu_B$ against 2.83 $\mu_B$, the calculated value. The third quantity from the fit, the temperature independent susceptibility ($\chi_0$), is a measure of DOS near the Fermi energy, $E_F$. The estimated $\chi_0$ (=1.45 x $10^{-4}$ emu/mole) hence suggests an enhanced DOS.

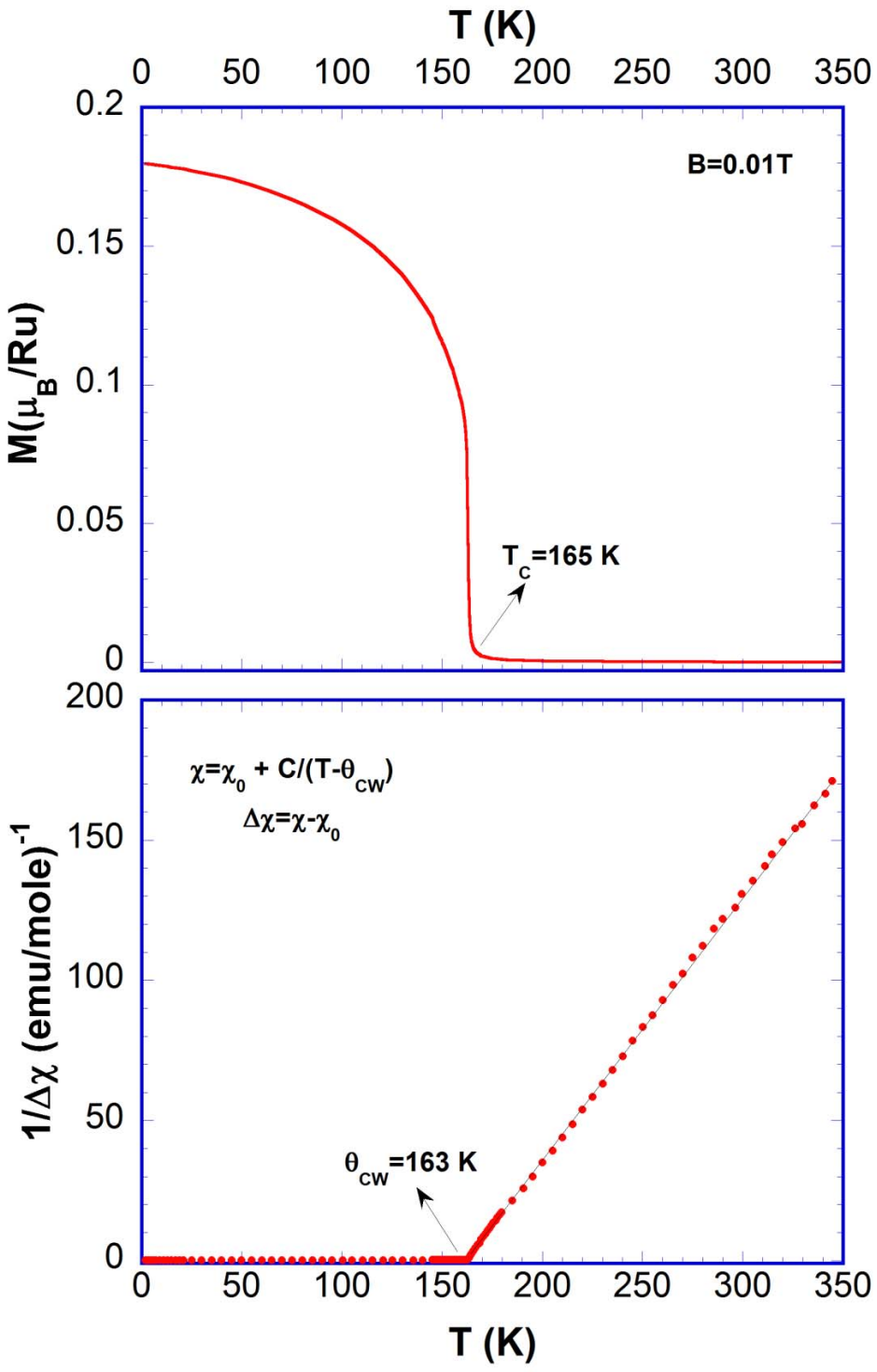


**Fig. 4.5 (a)** Temperature dependence of Magnetization, M(T), of $SrRuO_3$ at B=0.01 T, showing the Curie Temperature, $T_C$ **(b)** $1/\Delta\chi$ vs. T that shows a positive Curie-Weiss temperature, $\theta_{CW}$ confirming the ferromagnetic interactions between $Ru^{4+}$ spins.

The transport properties of $SrRuO_3$ shown in **Fig. 4.6** reflect the itinerant nature of electrons. The temperature dependence of the basal plane resistivity, $\rho_{ab}$, is shown in **Fig. 4.6 (a)**, which depicts a robust Fermi-liquid behavior[11, 84, 90] for $T < T_C = 165$ K as shown in **Fig. 4.6 (b)**. According to the s-d model, one would expect a $T^3$ resistivity response for transition metal compounds. But the $T^2$ temperature dependence observed in $SrRuO_3$ might suggest a very strong electron-electron interaction. The Fermi liquid fit,

$$\rho = \rho_0 + AT^2, \tag{4-2}$$

in the range $1.7 < T < 20$ K yields $\rho_0$=2.07 μΩ cm and A=9.7x$10^{-3}$ μΩ cm/$K^2$. The value of A persuades an enhanced value for the electron's effective mass[84] (A~$m^{*2}$) affirming the strong correlation between the itinerant electrons. The quantum oscillations reported at low temperatures confirms the well defined FS in the system. The transport behavior at high temperatures is anomalous as evidenced by a linear temperature dependence of the resistivity up to 900 K (not shown here). This linear increase in resistivity violates the Mott-Ioffe-Regel limit[11] and suggests an inapplicability of Boltzmann approach to transport, as a saturation in ρ(T) is expected when $K_F l \sim 1$, where $K_F$ is the Fermi wave vector and $l$ is the mean free path of the quasiparticle. The behavior is similar to that of other "bad" metals and might suggest that a local picture for transport is required for $SrRuO_3$ against the band description[91] for the same.

The appearance of a ferromagnetic metallic state at low T in $SrRuO_3$ could be associated with self-doping by the O 2p-electrons. In $SrRuO_3$, the large CEF breaks the first Hund's rule, and the four 4d electrons from $Ru^{4+}$ ion then partially fill the $t_{2g}$ states, giving rise to a local spin S=1 at each site (see **Fig. 1.7 (b)**). Even though the degeneracy between the $t_{2g}$ and $e_g$ levels are lifted by the CEF, the degeneracy among the $t_{2g}$ levels still exists. The $t^4_{2g}$ configuration hence implies a threefold orbital degeneracy since the fourth electron can go into any of the three $t_{2g}$ orbitals. This scenario would expect $SrRuO_3$ to be an S=1 antiferromagnetic Mott insulator. Band structure calculations[92], however, point to an important role of self-doping in this system. A small concentration of holes is introduced into the O-2p band via charge transfer processes, which puts a small concentration of additional electrons into the $t_{2g}$ orbitals. An enhanced density of states near $E_F$[86] leads to stoner instability, which in turn helps in inducing magnetism in $SrRuO_3$.

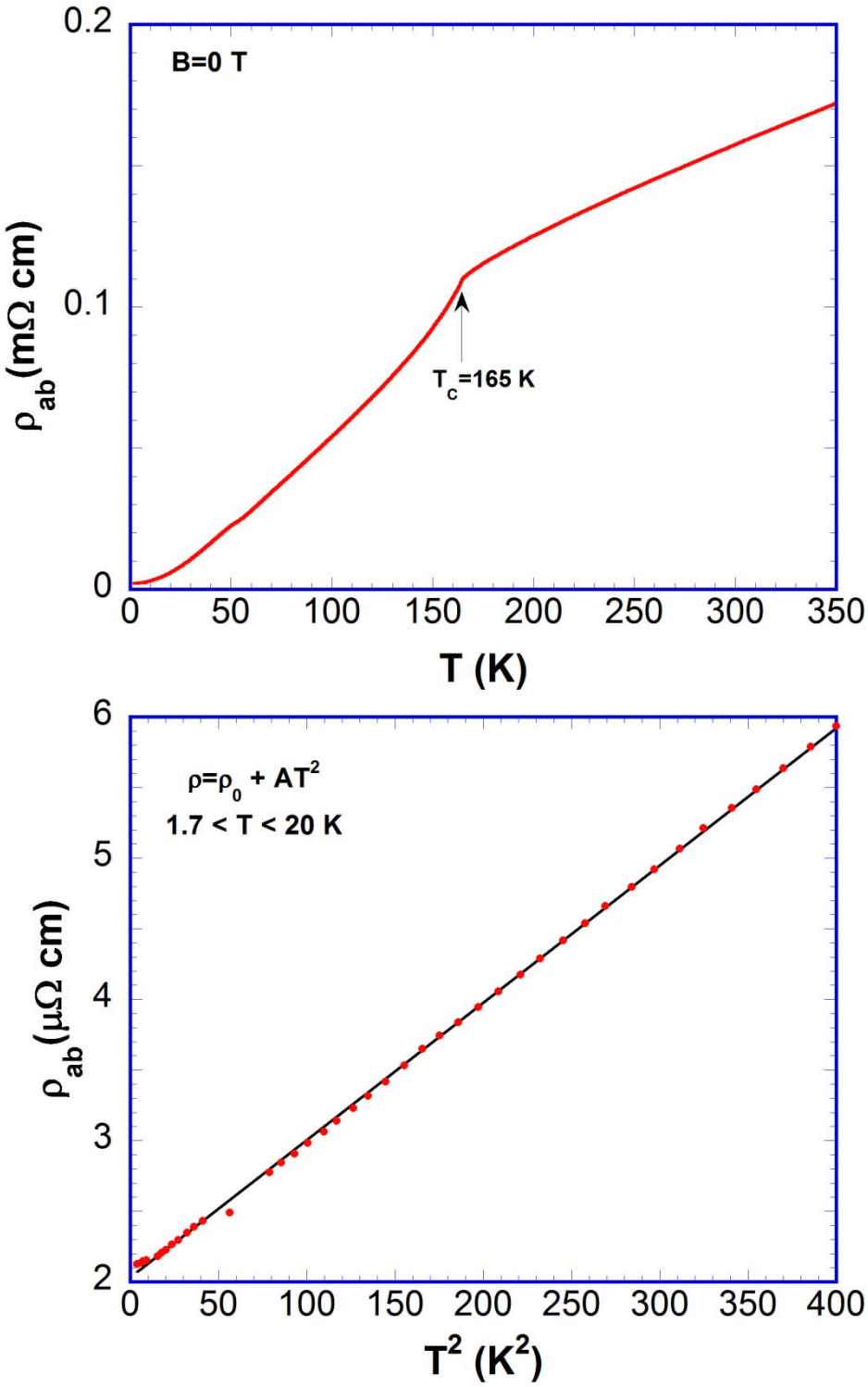


**Fig. 4.6 (a)** Basal plane resistivity, $\rho_{ab}$, as a function of T at B=0 T for $1.7 \leq T \leq 350$ K. **(b)** Fermi liquid behavior of $\rho_{ab}$ at B=0 T for $1.7 \leq T \leq 20$ K.

### 4.3.2 Effect of chemical perturbation in $SrRuO_3$:

$SrRuO_3$ exhibits a ferromagnetic metallic state as a result of the itinerant 4d $t_{2g}$ orbitals due to self-doping by the O 2p-electrons. The transport and magnetic properties strongly depend on the relative orientation of the corner-shared Ru-O octahedra. Any alteration done to the octahedra would trigger a change in the system's ground state. The Ca doping on the Sr site of $SrRuO_3$ does exactly that. The Ca ion inclusion in the structure triggered a metal insulator transition and killed the ferromagnetic ground state of the pure $SrRuO_3$. Studies[84] on single crystal $Sr_{1-x}Ca_xRuO_3$ indicates that the magnetic coupling is highly sensitive to perturbations in the Ru-O-Ru bond length and angle caused by substituting $Sr^{2+}$ with the iso-electronic smaller $Ca^{2+}$ ion. This gives rise to a rotation of the $RuO_6$ octahedron and thus a subtle change in the electron hopping between octahedra, yielding a state that is less favorable for ferromagnetism. Consequently, $T_C$ decreases monotonically with Ca concentration and vanishes for x=0.8[84]

A similar interplay between lattice and electronic properties that leads to an antiferromagnetic insulating ground state with $T_N$=26 K in the double perovskite $Sr_2YRuO_6$ was observed by G Cao et. al.[93]. The results from the studies suggest that $Sr_2YRuO_6$ has essentially the same crystal structure as $SrRuO_3$, but with every second Ru substituted by Y. Although the critical temperature ($T_N$) is reduced to 26 K, the estimates of the saturation magnetization are even higher than the parent compound (M~3 $\mu_B$). The antiferromagnetism in insulating $Sr_2YRuO_6$ is, however, due to super-exchange via two oxygen ions.

On the other hand, Mn doping on $SrRuO_3$[94] drives the system from a ferromagnetic state to an antiferromagnetic state abruptly at a critical Mn concentration ($x_C$~0.39). This magnetic transition is accompanied by a Mott insulator transition, where the electron conduction in the insulating state is governed by a variable range hopping mechanism. The critical concentration, $x_C$=0.39, hence sharply divides the two regimes, namely the ferromagnetic metal from the antiferromagnetic insulator as explained in the x-T phase diagram (see **Fig. 4.7**). These abrupt changes in the physical properties are believed to be driven by the localized Mn $t_{2g}$ electrons substituted for the itinerant Ru $t_{2g}$ electrons. Since the Mn $t_{2g}$ levels are all occupied with one electron, the only possibility of hopping would be to temporarily fill one of the $e_g$ levels. This process is, however,

energetically unfavorable. Hence, as a consequence of the large crystalline-field splitting in the $MnO_6$ octahedra, the Mn sites interrupt the dynamics of the 4d $t_{2g}$ electrons, and the metallic and ferromagnetic character of the Ru end compound gradually disappears with increasing x.

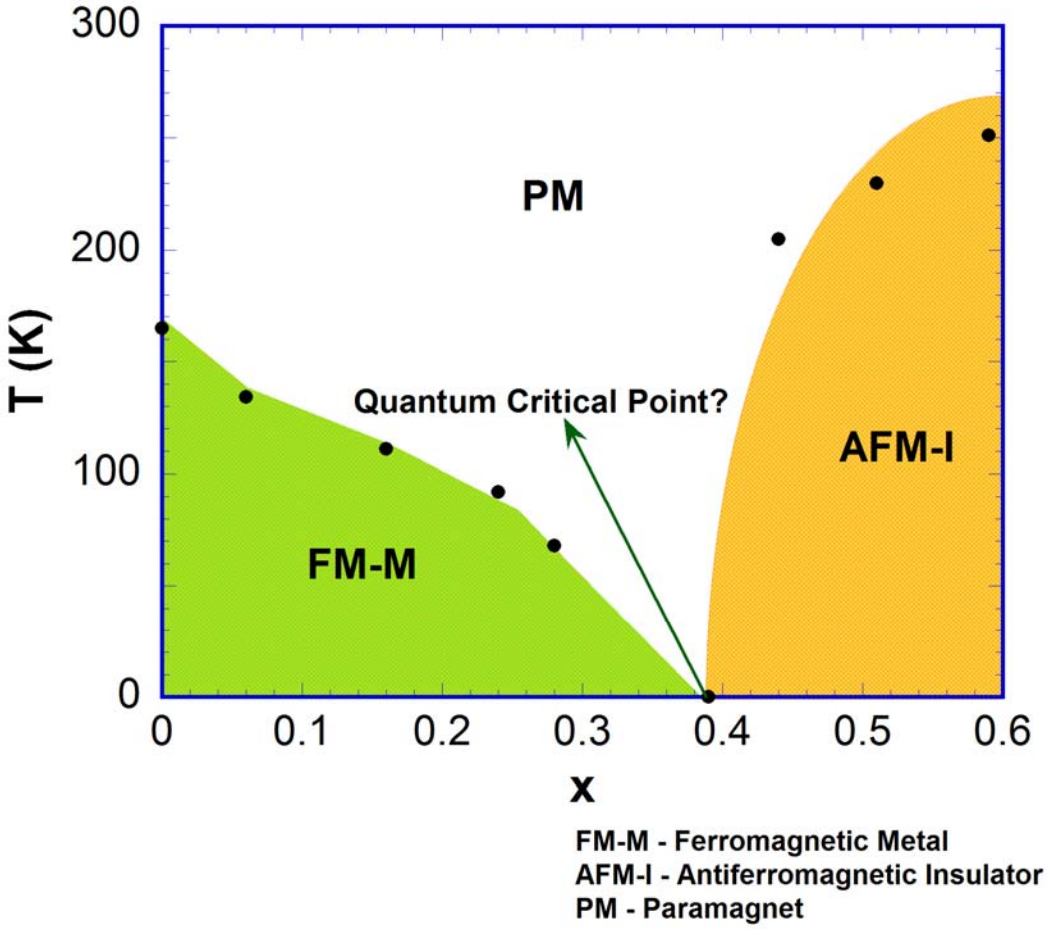


**Fig. 4.7** Magnetic and electronic phase diagram as a function of Mn content in $SrRu_{1-x}Mn_xO_3$.

### 4.3.3 Enhanced ferromagnetism in $SrRu_{1-x}Cr_xO_3$:

Even though different cation substitution in $SrRuO_3$ showed a range of physical behaviors, they had one thing in common: they resulted in the suppression of the ferromagnetic ground state of the parent compound. But recent studies on Cr doped $SrRuO_3$ polycrystalline samples reveal a completely opposite picture as an increase in the Curie temperature, $T_C$, to 188 K for x=0.11 is observed[95, 96]. Thermodynamic and transport properties measurements done on our single crystals of $SrRu_{1-x}Cr_xO_3$ affirm the enhanced ferromagnetic behavior as shown in **Fig. 4.8**. **Fig. 4.8 (a)** shows the field

cooled sequence of the temperature dependence of magnetization for x=0, 0.04 and 0.20 at B=0.01 T. It is evident that the Cr doping enhances the Curie temperature of the system from $T_C$=165 K for x=0 to $T_C$=192 K for x=0.20. This trend, i.e. an increasing Curie temperature with x, is not curtailed by any critical concentration. In fact, with a further increase in the Cr concentration, there is a prompt increase in $T_C$ to higher temperatures. It is new and striking that $T_C$ becomes as large as 290 K for x=0.30 though $T_C$ is largely broadened (not shown here). According to the Nuclear Magnetic Resonance (NMR) studies[96], the increase in $T_C$ is as a result of the presence of mixed valences for Ru ion and hence the double exchange interaction involving $Cr^{3+}$ ion. The magnetization, however, shows a trend by becoming weaker as x is increased as shown in **Fig. 4.8 (a)**.

**Fig. 4.8 (b)** displays the temperature dependence of the basal plane resistivity in the temperature range $1.7 < T < 350$ K for the representative Cr concentrations in zero applied magnetic field. Up to x=0.20, the system retains the metallic behavior but with a decrease in Residual Resistance Ratio (RRR=$\rho$(300 K)/$\rho$(2 K)) as x is increased. For x=0, RRR ~ 75 whereas for x=0.20 the ratio is estimated to be ~ 2, suggesting more elastic scattering (and hence an enhanced $\rho_0$) for higher Cr concentration. Like in the pure compound, the observed Fermi liquid behavior gives way to the Fisher-Langer behavior at $T_C$ as an indication of the domination of short range spin fluctuations near the critical temperature.

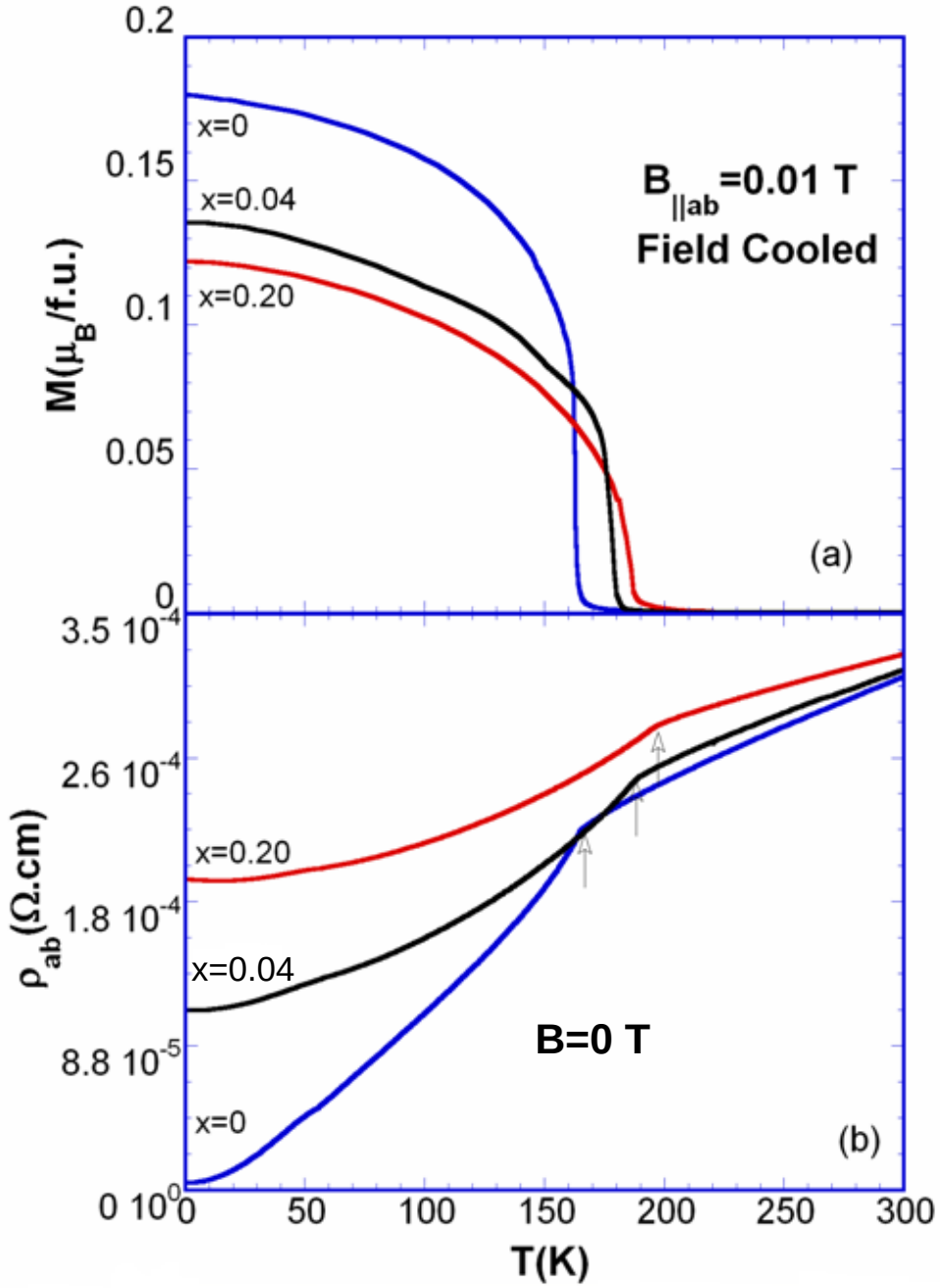


**Fig. 4.8** Temperature dependence of **(a)** magnetization, M, at B=0.01 T and **(b)** basal plane resistivity, $\rho_{ab}$, at B=0 T for $SrRu_{1-x}Cr_xO_3$ ($0 \leq x \leq 0.20$) in the temperature range $1.8 \leq T \leq 300$ K.

Displayed in **Fig. 4.9** is the isothermal magnetization for the $SrRu_{1-x}Cr_xO_3$ crystals at T=2 K with the magnetic field applied along the basal plane. The spins are readily polarized at low magnetic fields resembling the spins in the pure compound. The

field dependence of the magnetization for all x stays essentially unchanged but the saturation moment, $M_S$, decreases with increasing x. $M_S$ is reduced from 1.1 $\mu_B$/f.u. for x=0 to 0.40 $\mu_B$/f.u. for x=0.20 (see **Fig. 4.9**). For x=0.30, which recorded a Curie temperature of 290 K, the $M_S$ is observed to be 0.1 $\mu_B$/f.u. (not shown in the figure). The decrease in $M_S$ with increasing x is consistent with the low temperature magnetization shown in the **Fig. 4.8 (a)**.

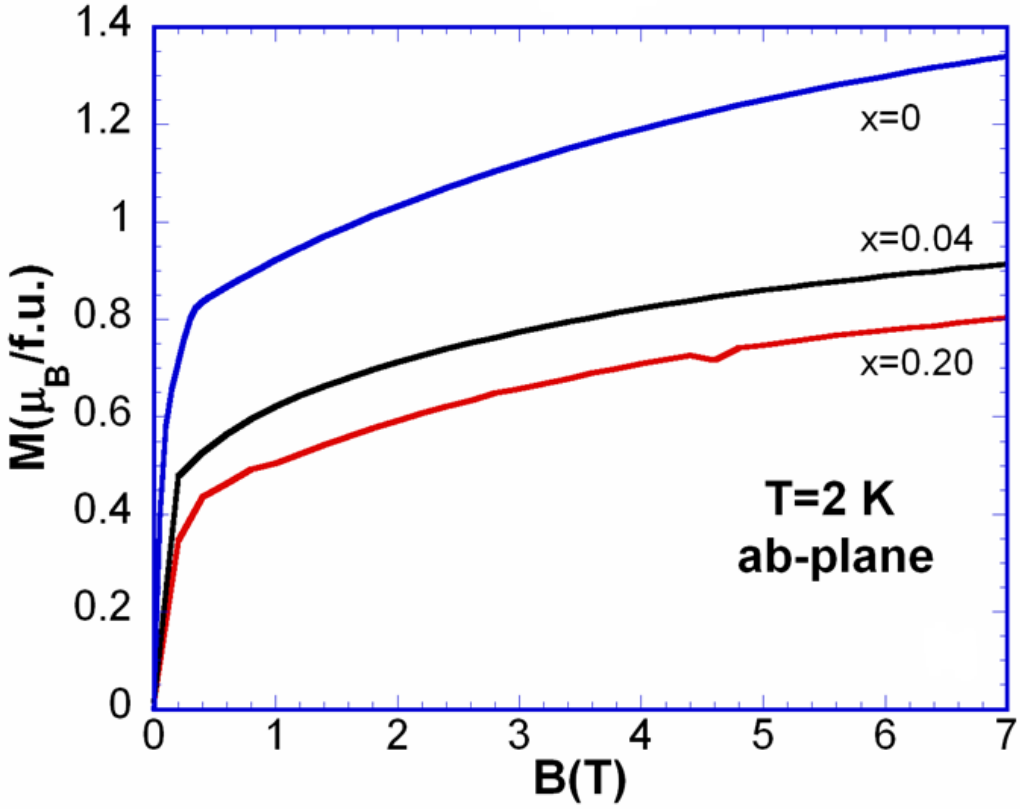


**Fig. 4.9** Magnetic isotherms, M (B), at T=2 K for $SrRu_{1-x}Cr_xO_3$ ($0 \leq x \leq 0.20$), when magnetic field is applied along the basal plane in the range $0 \leq B \leq 7$ T.

This enhanced ferromagnetic behavior induced by Cr substitution in $SrRuO_3$ provided a strong motivation for an intensive study of Cr doping on its counterparts, $Ca_{n+1}(Ru_{1-x}Cr_x)_nO_{3n+1}$.

### 4.3.4 Paramagnetic "bad" metal $CaRuO_3$:

As displayed in **Fig. 4.3 (b)**, the crystal structure of $CaRuO_3$ is more distorted as a result of the tilting and rotation of Ru-O octahedra. These structural distortions in $CaRuO_3$ are antagonistic to magnetism and the compound is on the verge of magnetic ordering and readily evolves into a magnetically ordered phase[84, 89, 95, 97]. This belief has

been justified by the experimental results such as the one shown in **Fig. 4.10**. The magnetization shows paramagnetic temperature dependence as displayed in **Fig. 4.10 (a)** for low magnetic fields (B=0.05 T). The system shows no long range order even up to a temperature as low as 30 mK[98].

A Curie-Weiss fit, as given in equation 4-1, to the high temperature (50 < T < 350 K) susceptibility reveals a negative $\theta_{CW}$ (see **Fig. 4.10 (b)**) suggesting an antiferromagnetic interaction between spins. The estimated $\theta_{CW}$ (=-175 K) is comparable to the reported value ($\theta_{CW}$ =-162 K) in reference[99]. However, substantial works[100-103] have been done on $CaRuO_3$ where it is considered to be a nearly ferromagnetic metal rather than a classical Curie-Weiss antiferromagnet. Hence $CaRuO_3$ is not a classical paramagnet but is verging on collective magnetism. The effective moment estimated from the fit (=2.1$\mu_B$) is smaller than but close to the proposed Hund's rule value for an S=1 system (=2.8 $\mu_B$). The temperature independent susceptibility, $\chi_0$, is estimated to be 2.86 x $10^{-4}$ emu/mole is close to the value (=4.9 x $10^{-4}$ emu/mole) reported earlier[89].

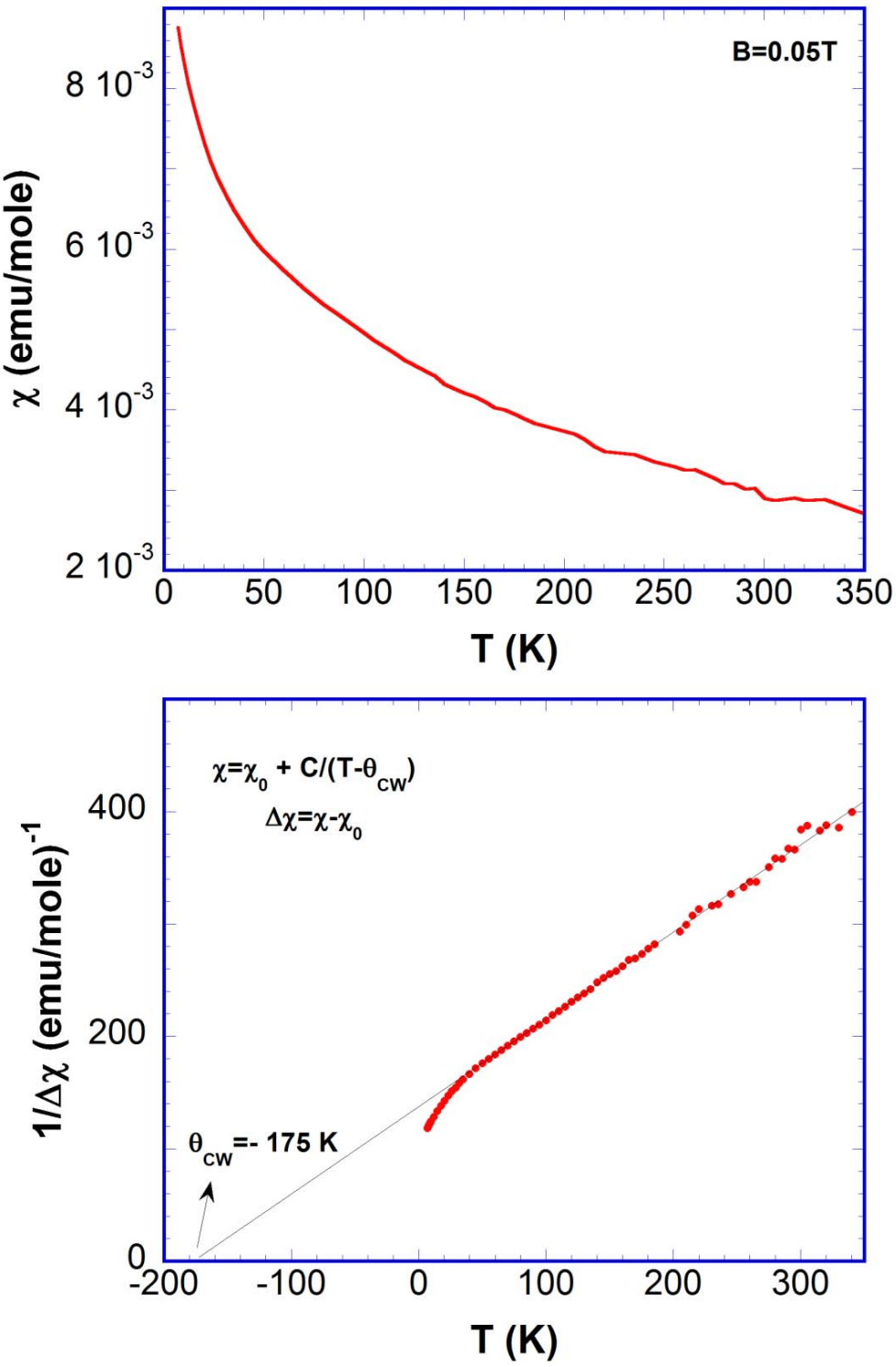


**Fig. 4.10 (a)** Magnetic susceptibility as a function of temperature at B=0.05 T for $1.7 \leq T \leq 350$ K. **(b)** $1/\Delta\chi$ as a function of temperature at B=0.05 T for $1.7 \leq T \leq 350$ K. $\chi$ (T) follows the modified Curie-Weiss law with $\theta_{CW}$=-175 K.

The electrons in the compound are itinerant, as evident from the metallic behavior shown for the full range of available temperatures. The temperature dependence of the basal plane resistivity, $\rho_{ab}$, for 1.7 < T < 350 K in zero magnetic field is shown in **Fig 4.11 (a)**. For T > 20 K, the resistivity follows a linear dependence in T suggesting a domination of short range spin fluctuations in the electron conduction mechanism at higher temperatures. However, at lower temperatures, for T < 20 K, $CaRuO_3$ does not follow a Fermi liquid behavior expected for metals (equation 4-2). On the contrary, it follows a $T^{3/2}$ behavior i.e.

$$\rho = \rho_0 + AT^{\frac{3}{2}} \qquad (4\text{-}3)$$

as shown in **Fig 4.11 (b)** (left scale). In the presence of a magnetic field as high as B=7 T, the overall temperature dependence of ρ remains the same. In particular, the unusual $T^{3/2}$ behavior at lower temperatures persist for fields up to B=7 T (see **Fig 4.11 (b)** (right scale)). This non Fermi liquid behavior in resistivity may be linked to the magnetic instability that arises at T=0 as observed in the nearly ferromagnetic $SrIrO_3$[104]. The system's Quantum Critical Point (QCP), if any present, could be tuned by control parameters such as chemical composition as explained in the next few paragraphs.

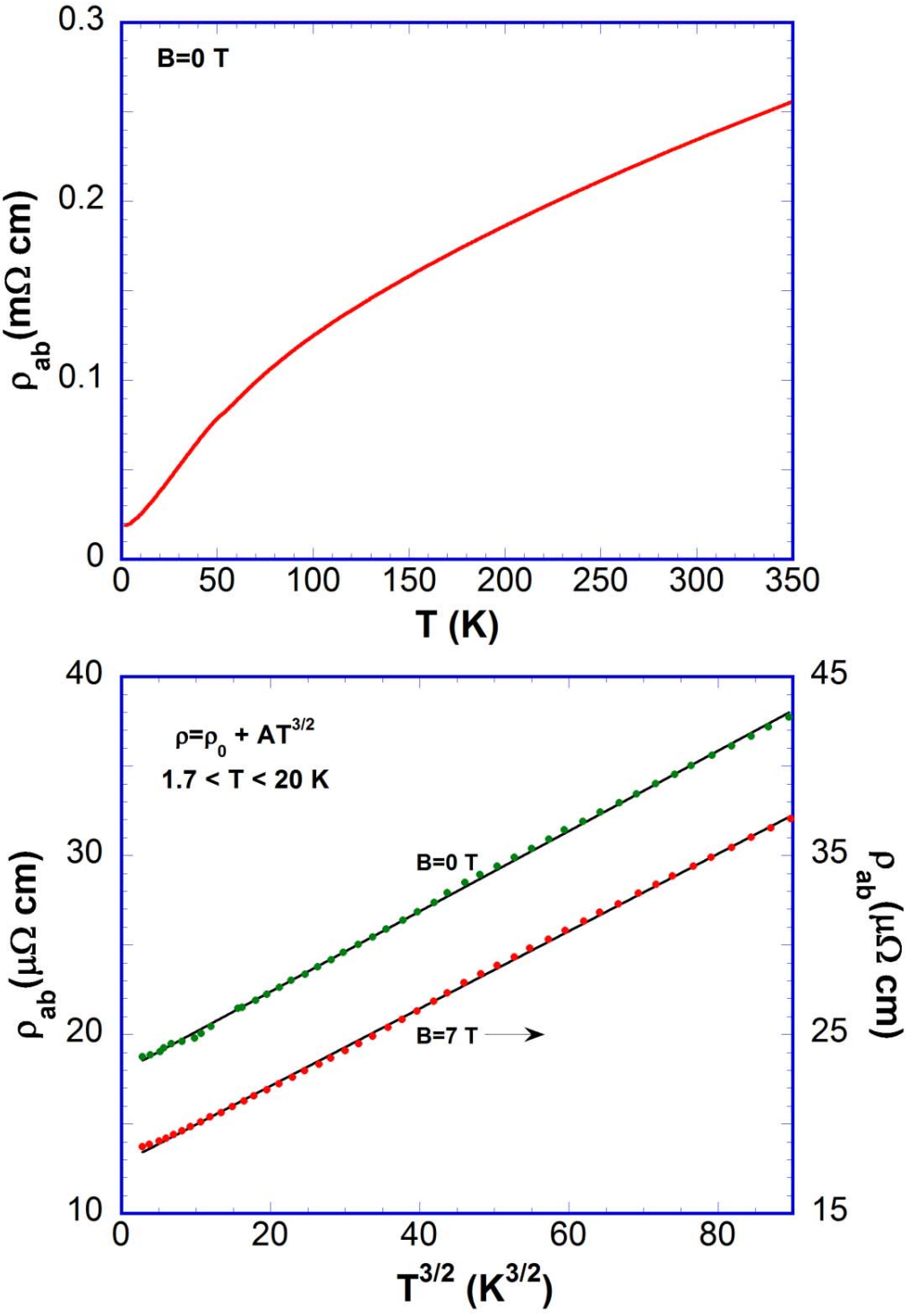


**Fig. 4.11 (a)** Resistivity, ρ, as a function of temperature at B=0 T for 1.7 ≤ T ≤ 350 K. **(b)** Non-Fermi liquid behavior of ρ at B=0 T (*left scale*) and B=7 T (*right scale*) for 1.7 ≤ T ≤ 20 K.

### 4.3.5 $CaRuO_3$'s response to chemical substitution:

As discussed in the previous section, $CaRuO_3$ is not paramagnetic but rather shows the characteristics of short-range magnetic interactions. It is also true that $CaRuO_3$, though a good conductor, is on the verge of localization due to the narrow nature of the 4d band. The nature of the magnetism and transport properties in this compound, and other ruthenates with narrow 4d-bands, strongly depend on the degree of band filling and bandwidth. The ground state's closeness to quantum fluctuations creates a fair amount of chance to tilt the scale in favor of one of the ground states by external perturbation. Hence chemical substitution on each Ca and/or Ru sites will constitute a powerful tool to study the physical properties of this system. Indeed, 5% of Sr or Na substitution for Ca induces anti-ferromagnetic or spin glass ordering at T=10 and 55 K respectively[84, 105].

Sn doping[89] on $CaRuO_3$ also show distinct changes in the magnetic properties. A well defined peak in $\chi(T)$ indicative of a magnetic ordering occurs for lower concentration of Sn i.e. for small x. The hysteresis effect is seen throughout the doping range where this magnetic ordering is observed. The magnetic ordering gets weaker as x increases before vanishing eventually for $x > 0.10$. This instability of the ordered phase coupled with the hysteresis in $\chi(T)$ implies a spin frustration or spin-glass behavior. This can be attributed to spin depletion from Ru sites introduced by nonmagnetic Sn, resulting in frustrated neighboring spins.

Polycrystalline Rh doping study on $CaRuO_3$[106] reveals a magnetic behavior reminiscent of a ferromagnet. However, the negative Curie–Weiss temperature extrapolated from fitting $\chi(T)$ to the Curie–Weiss law seems to suggest that at high temperatures the correlations are dominated by antiferromagnetic coupling. It may be inferred that magnetic spins in the doped samples are primarily antiferromagnetically coupled but somehow canted, resulting in a hidden ferromagnetic component characterized by the ferromagnetic-like behavior. This occurrence of the enhanced spin correlation is accompanied by an itinerant-to-localized electron transition. These observations are attributed to the band narrowing resulted by Rh substitution on the Ru site. Slight Rh doping, while retaining the crystal structure, effectively narrows the 4d-band. The band narrowing leads to an abrupt departure from the itinerant electron extreme and also to an enhanced local moment coupling.

Magnetic studies of polycrystalline $CaRu_{1-x}Ti_xO_3$ ($0<x<0.1$) reveal a ferromagnetic transition at $T_C$=34 K, regardless of the nonmagnetic Ti concentration[107]. Substitution of nonmagnetic $Ti^{4+}$ and $Sn^{4+}$ for $Ru^{4+}$ represents only lattice frustration and magnetic dilution of the Ru sublattice, whereas $Rh^{4+}$ (S=1/2) or $Rh^{3+}$(S=0) ions act as magnetic impurities (different S), or as charge frustration producers. He and Cava[99] have recently shown that, for M = Mn, Fe, and Ni, "inhomogeneous" ferromagnetic materials are formed. In these $CaRu_{1-x}M_xO_3$ systems, $T_C$ depends also only on the dopant ion, and not on its concentration. It is thus assumed, that small ferromagnetic clusters with an intrinsic $T_C$ (depending on M) are formed, and they increase in size and volume fraction with increasing dopant concentration.

### 4.3.6 Induced ferromagnetism in $CaRu_{1-x}Cr_xO_3$:

Sensitivity of the ground state of $CaRuO_3$ to different chemical substitutions was discussed in section 4.3.5. It appears to be a common occurrence that with only a slight impurity doping the paramagnetic $CaRuO_3$ inevitably evolves to a magnetically ordered state followed by a metal to insulator transition. But the Cr substitution on the perovskite calcium ruthenate reveals a different story altogether. In this section, I will discuss the effects of Cr substitution on the physical properties of $CaRuO_3$ i.e. the thermodynamics and transport properties of $CaRu_{1-x}Cr_xO_3$[108] in detail.

Similarity in the geometries of the calcium perovskite ruthenate and chromate makes the Cr substitution study viable. $CaCrO_3$ has the same crystal structure and symmetry as $CaRuO_3$ with a space group of pbnm and lattice parameters a=5.287 Å, b=5.316 Å and c=7.486 Å[109]. This structural compatibility provides an advantage for a thorough study of $CaRu_{1-x}Cr_xO_3$ by controlling electron correlation strength without significantly altering the on-site and inter-site Coulomb interaction. Shown in **Fig. 4.12 (a)** are the lattice parameters for a-, b- (left scale) and c-axis (right scale) as a function of Cr concentration, x, ranging from 0 to 0.36 for $CaRu_{1-x}Cr_xO_3$. For x=0 ($CaRuO_3$), the lattice parameters are in good agreement with those reported earlier[80, 84]. The orthorhombic symmetry is retained as a function of x. Within the error of the measurement, the lattice parameters generally decrease with x, consistent with the fact that the ionic radius of $Cr^{4+}$ (0.550 Å) is smaller than that of $Ru^{4+}$ (0.620 Å).

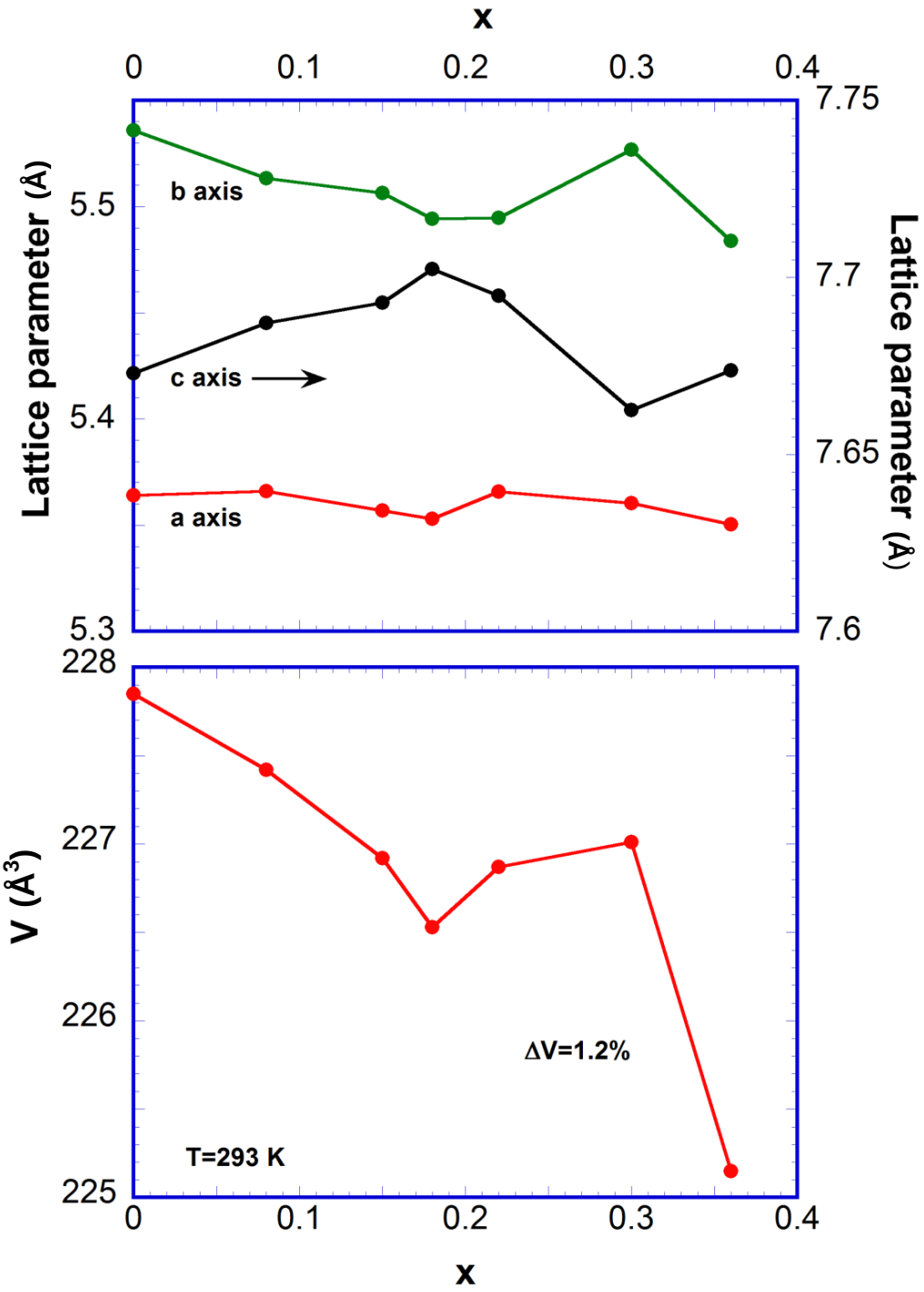


**Fig. 4.12 (a)** Lattice parameters for a-, b- (*left scale*) and c-axis (*right scale*) and **(b)** the volume of the unit, V, as a function of Cr concentration, x, for $CaRu_{1-x}Cr_xO_3$. The x dependence of lattice parameters suggests no presence of $Cr^{3+}$ and/or $Ru^{5+}$ ions in the compounds.

The changes in the lattice parameters result in a shrinkage of the unit-cell volume by about 1.2% (x=0.36) as shown in **Fig. 4.12 (b)**[108]. The results do not seem to suggest a presence of the $Cr^{3+}$ ion (0.615 Å) and/or $Ru^{5+}$ (0.565 Å), which would lead to x-dependence of the lattice parameters opposite to that shown in **Fig. 4.12**. Even though no drastic changes in the crystal structure are observed, the magnetic ground state of the system involves surprise changes. An abrupt transition from paramagnetism to itinerant ferromagnetism[108] is induced when Cr is substituted for Ru in $CaRuO_3$. Shown in **Fig. 4.13** is the temperature dependence of the magnetization, M, for representative compositions taken in a field cooled sequence for $1.7 < T < 200$ K. The major feature is the instantaneous presence of the ferromagnetic behavior upon Cr doping. There is a strong hysteresis effect between the field cooled and zero field cooled sequences (not shown). The Curie temperature $T_C$ increases from 67 K for x=0.05 to 115 K for x=0.15, peaks at 123 K for $0.18 < x < 0.22$ and decreases to 100 K for x=0.36 (see **Fig. 4.15**). ($T_C$ is determined as the maximum of the derivative dM/dT). The high temperature Curie-Weiss analysis discussed in the following paragraphs affirms the ferromagnetic coupling between the spins.

Another interesting feature of the Cr substitution is the induced anisotropy in the magnetic behavior. As shown in **Fig. 4.13 (b)**, the c-axis magnetization, $M_c$, is much weaker than $M_a$. Since the crystals are cubic, the difference in the value of M (around a factor of 5) could not be attributed to the difference in demagnetization factor, N, along the different crystallographic axes. N for all the three crystallographic axes in a cube is the same and hence this anisotropy in magnetization is unexpected in the perovskite compounds such as these. No observable anisotropy is reported in the pure $CaRuO_3$ and $SrRuO_3$ confirming that it is not common to have anisotropy in cubic crystals. Moreover, Cr substitution in the more idealistic perovskite $SrRuO_3$ does not induce any anisotropic properties. The anisotropy in Cr doped $CaRuO_3$ might hence suggest a role of spin-orbit coupling in the system's physical properties[108].

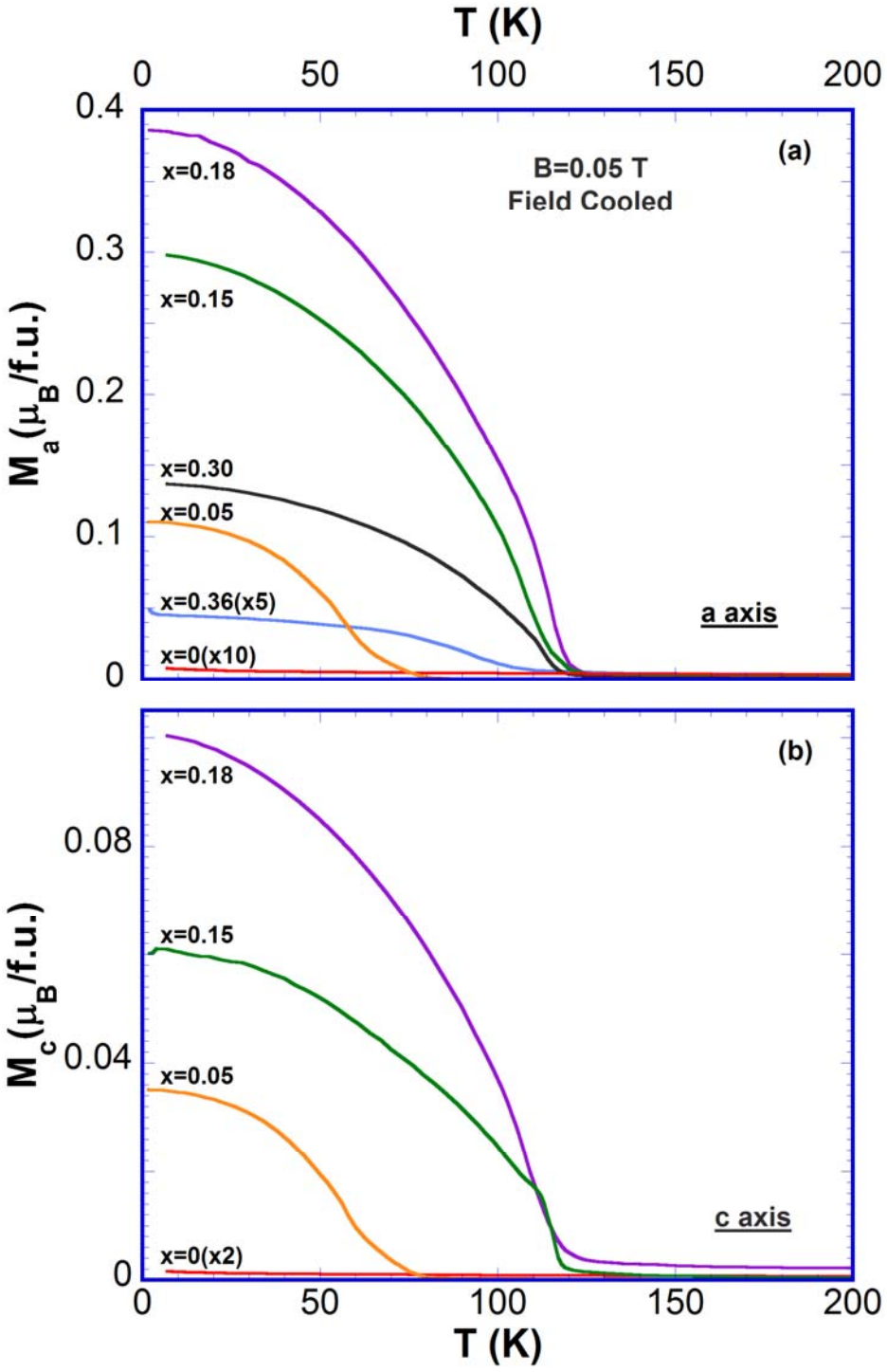


**Fig. 4.13 (a)** Temperature dependence of a-axis magnetization, $M_a$, for a few representative concentrations in $CaRu_{1-x}Cr_xO_3$ **(b)** Temperature dependence of the c-axis magnetization, $M_c$, for a few representative x.

The data for 150 < T < 350 K in **Fig. 4.13** were fitted to the modified Curie-Weiss law for 0 < x < 0.36. The susceptibilities in the paramagnetic phases are essentially isotropic giving the same fit parameters along each direction. Shown in **Fig. 4.14** are the $1/\Delta\chi$ vs. T curves for a few representative concentrations i.e. x=0, 0.05, 0.18 and 0.36 of Cr doping, where $\Delta\chi$ ($=\chi-\chi_0$) is estimated from the Curie-Weiss law of the form, $\chi = \chi_0 + \frac{C}{(T-\theta_{CW})}$, as in equation 4-1. The $\theta_{CW}$ is then determined from the x intercepts of these straight lines, whereas their slopes yield the Curie constant. Hence, from the figure it is clear that the Curie-Weiss temperature, $\theta_{CW}$, changes from a negative value for x=0 to positive values for x > 0. The estimated $\theta_{CW}$ for the crystals maintain their trend by increasing up to x=0.18 and decreasing for x > 0.18, which reflects the nature of the interaction between the spins.

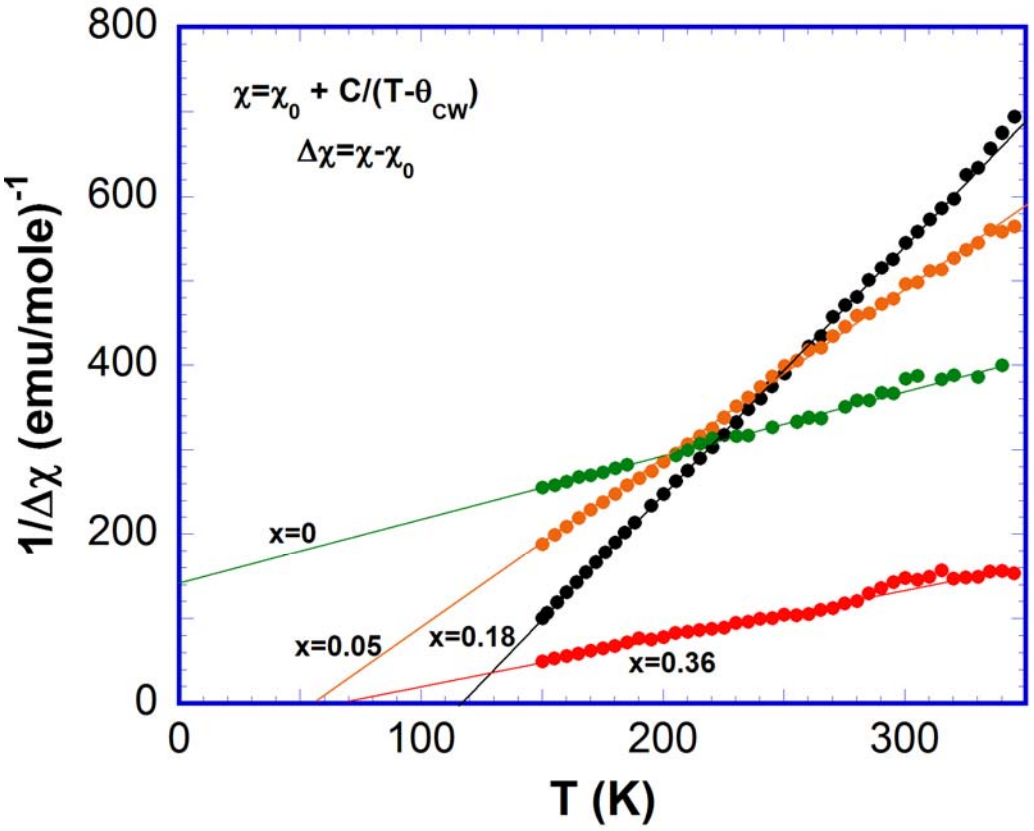


**Fig. 4.14** $1/\Delta\chi$ vs. T curves for a few representative x viz. 0, 0.05, 0.18 and 0.36. Note that the x intercept ($\theta_{CW}$) is negative only for x=0 and are positive for all x > 0. Solid lines are guide to the eyes.

The set of physical parameters obtained from the Curie-Weiss fit done on the data displayed in **Fig 4.13** are listed down in **Table 4.1**. Remarkably, the Curie-Weiss temperature, $\theta_{CW}$, shows x-dependence with the same general trend of that of $T_C$, changing from -175 K for x=0 through zero eventually to +120 K for x=0.18 (see **Fig. 4.15 (a)**). The change in sign is associated with the change in tendency from antiferromagnetic to ferromagnetic exchange coupling, consistent with the onset of ferromagnetism with increasing Cr content[108]. Also illustrated in the **Fig. 4.15** is the temperature-independent susceptibility $\chi_0$ (right scale in **Fig. 4.15 (b)**), which stays essentially unchanged for $x < 0.18$, but rises rapidly near x=0.18 and peaks at x=0.22 where $T_C$ reaches the maximum. $\chi_0$ is usually associated with a Pauli susceptibility and a measure of the density of states at the Fermi level, $N(E_F)$, i.e., $\chi_0 \sim N(E_F)$. The rapid increase of $\chi_0$ may then be attributed to an increase in the density of the states. Another quantity estimated from the Curie-Weiss fit is the effective moment, $\mu_{eff}$, which is displayed in **Fig. 4.15 (b)** (left scale). A monotonic decrease in $\mu_{eff}$ with an increase in x is observed for the entire doping range as shown in the figure.

**Table 4.1** *Curie temperature ($T_C$) and the modified Curie-Weiss fit parameters ($\theta_{CW}$, $\chi_0$ and $\mu_{eff}$) tabulated for different x.*

| S. No. | Cr concentration x | Curie temperature $T_C$ (K) | Curie-Weiss temperature $\theta_{CW}$ (K) | Temperature independent susceptibility $\chi_0$ (x$10^{-3}$ emu/mole) | Effective moment $\mu_{eff}$ ($\mu_B$/f.u.) |
|---|---|---|---|---|---|
| 1 | 0 | 0 | -175 | 0.2860 | 2.7600 |
| 2 | 0.05 | 67 | 68 | 1.3647 | 2.3160 |
| 3 | 0.08 | 76 | 73 | 4.3270 | 2.1300 |
| 4 | 0.15 | 115 | - | 1.4230 | 1.9730 |
| 5 | 0.18 | 123 | 117 | 1.3919 | 1.8630 |
| 6 | 0.22 | 121 | 119 | 63.083 | 1.7540 |
| 7 | 0.30 | 118 | 108 | 29.832 | 1.7200 |
| 8 | 0.36 | 94 | 64 | 17.234 | 1.6900 |

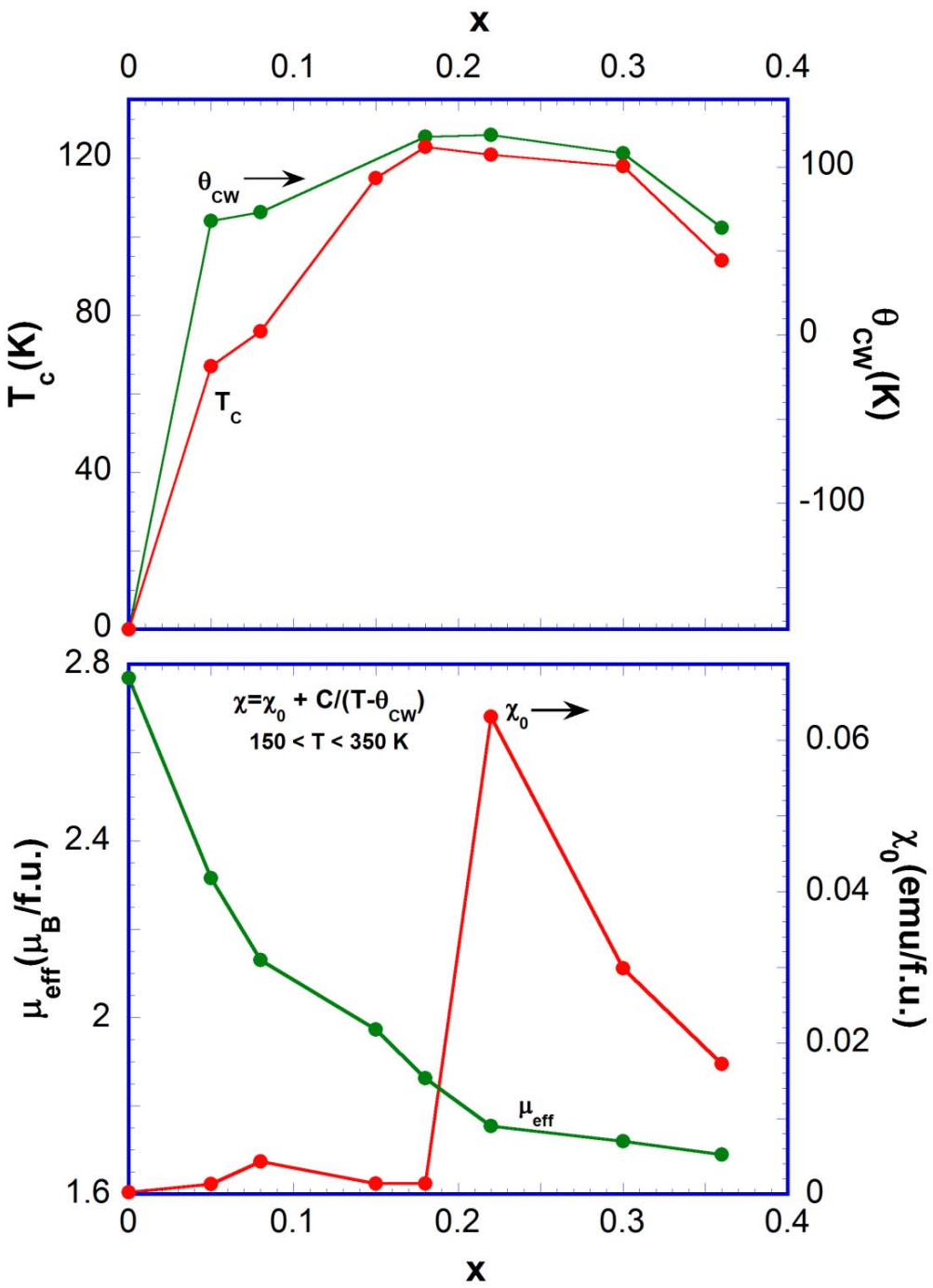


**Fig. 4.15 (a)** The Curie temperature, $T_C$, (left scale) and the Curie-Weiss temperature, $\theta_{CW}$, (right scale) as a function of x. **(b)** The x dependence of effective moment, $\mu_{eff}$, (left scale) and temperature-independent susceptibility, $\chi_0$, (right scale) estimated from the Curie-Weiss fit in the temperature range $150 \leq T \leq 350$ K.

The effective moment estimated from the Curie constant, C, decreases monotonically from 2.76 $\mu_B$/f.u. for x=0 to 1.7 $\mu_B$/f.u. for x=0.36 (see **Fig. 4.15**). These values are smaller but close to those for both $Ru^{4+}$ ($4d^4$, low spin state) and $Cr^{4+}$ ($3d^2$), which have S=1. On the other hand, the effective magnetic moments for $Ru^{5+}$ ($4d^3$) and $Cr^{3+}$ ($3d^3$) are considerably larger as is the total spin, S=3/2. Hence the Curie constant is consistent only with the anticipated tetravalent Ru and Cr ions for all compositions[108]. These results are in good agreement with the structural data shown in **Fig. 4.12**.

Even though both $Ru^{4+}$ and $Cr^{4+}$ ion based compounds have a total spin-one configuration, the substitution of $Ru^{4+}$ by $Cr^{4+}$ replaces four 4d electrons with two 3d electrons. The two 3d electrons of Cr are located in more contracted $t_{2g}$ orbitals and as a result a narrower band and stronger exchange interactions between the electrons are possible. The mismatch between the energy levels and the symmetries of the wave functions reduces the effective hybridization and narrows the effective bandwidth W. Since the bandwidth, W, and the density of states, $N(E_F)$, are inversely related, a significant local reduction in W may enhance $N(E_F)$. This enhancement in density of states favors ferromagnetism according to the Stoner model.

The induced ferromagnetism in the compounds is complemented by unexpected magnetization isotherms at low temperatures. **Fig. 4.16** shows isothermal magnetization, M(B), for the a-axis at T=2 K. For x=0, the magnetization is linear in applied field up to B=7 T along both directions, corresponding to the paramagnetic ground state. However, for x > 0, $M_a(B)$ does not follow a linear behavior throughout the range of applied field anymore[108]. The linear response in B survives up to a critical field, $B_C$, at which a metamagnetic-like transition occurs starting at x=0.05 (**Fig. 4.16**). The jump in magnetization reaches a saturation value around 0.3 $\mu_B$/f.u. at B=7 T. A strong hysteresis in M is also observed when the field is swept down to zero where the system never reaches the initial zero field cooled value. The transition then develops into a two-step transition as x is increased to 0.15. The temperature dependence of this two-step transition is shown in **Fig. 4.17**. When x=0.18, the jump in M is so abrupt that it resembles a magnetic switching effect. The field dependence might suggest that x=0.18 compound is a nearly single domain ferromagnet.

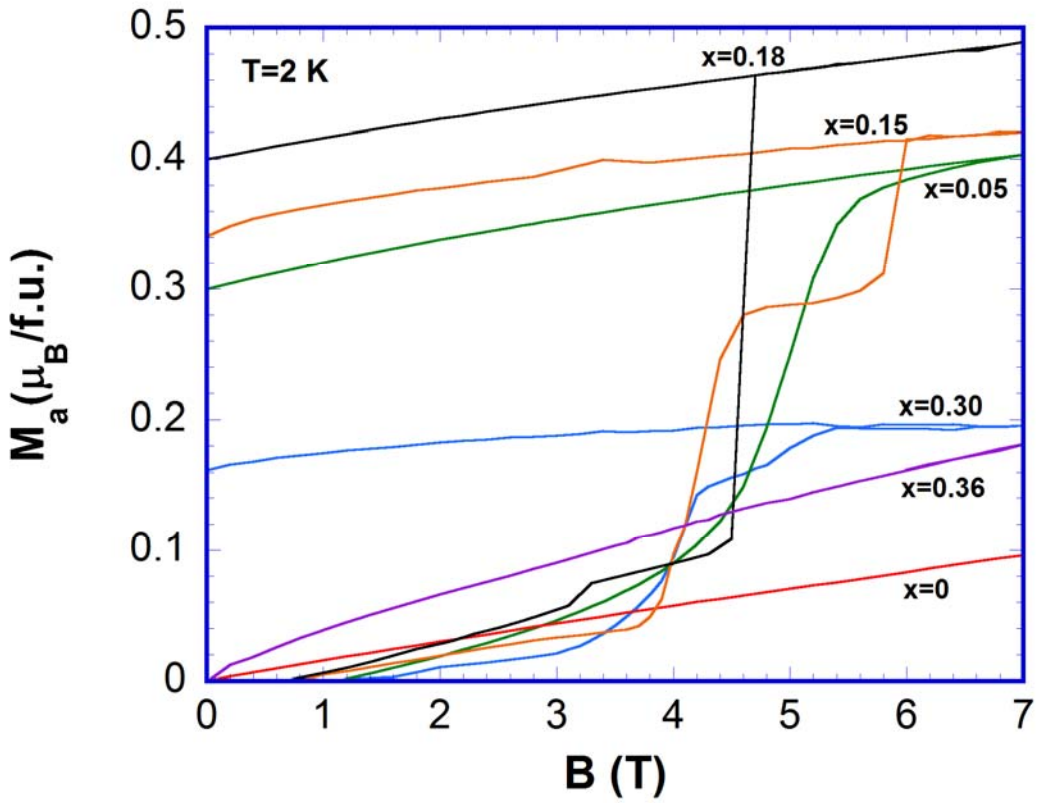


**Fig. 4.16** Isothermal magnetization, M (B), at T=2 K for $CaRu_{1-x}Cr_xO_3$ along a axis

For x=0.15, the transition shows a step like behavior at low temperatures with distinct critical fields ($B_{C1}$ and $B_{C2}$) creating a meta-stable state between these two fields. The behavior might be a reminiscent of the difference in the coercivity between $Ru^{4+}$ and $Cr^{4+}$ ions, which is more obvious in $Ca_3(Ru_{1-x}Cr_x)_2O_7$ as explained in the later part of this chapter. This two-step transition depends sensitively on temperature as shown in **Fig. 4.17 (a)**. As the temperature is increased from T=2 K, the meta-stable region ($B_{C1} < B < B_{C2}$) becomes smaller before it vanishes for T > 40 K (see **Fig. 4.17 (b)**). The two critical fields viz. $B_{C1}$ and $B_{C2}$ show strong temperature dependence. Both the critical fields follow an exponential law given as,

$$B_C = B_{C0}e^{(-aT)} \qquad (4\text{-}4)$$

However, the magnitude of $M_S$ shows only weak dependence on temperature. It decreases from 0.33 $\mu_B$/f.u. for T=2 K to 0.26 $\mu_B$/f.u. for T=50 K.

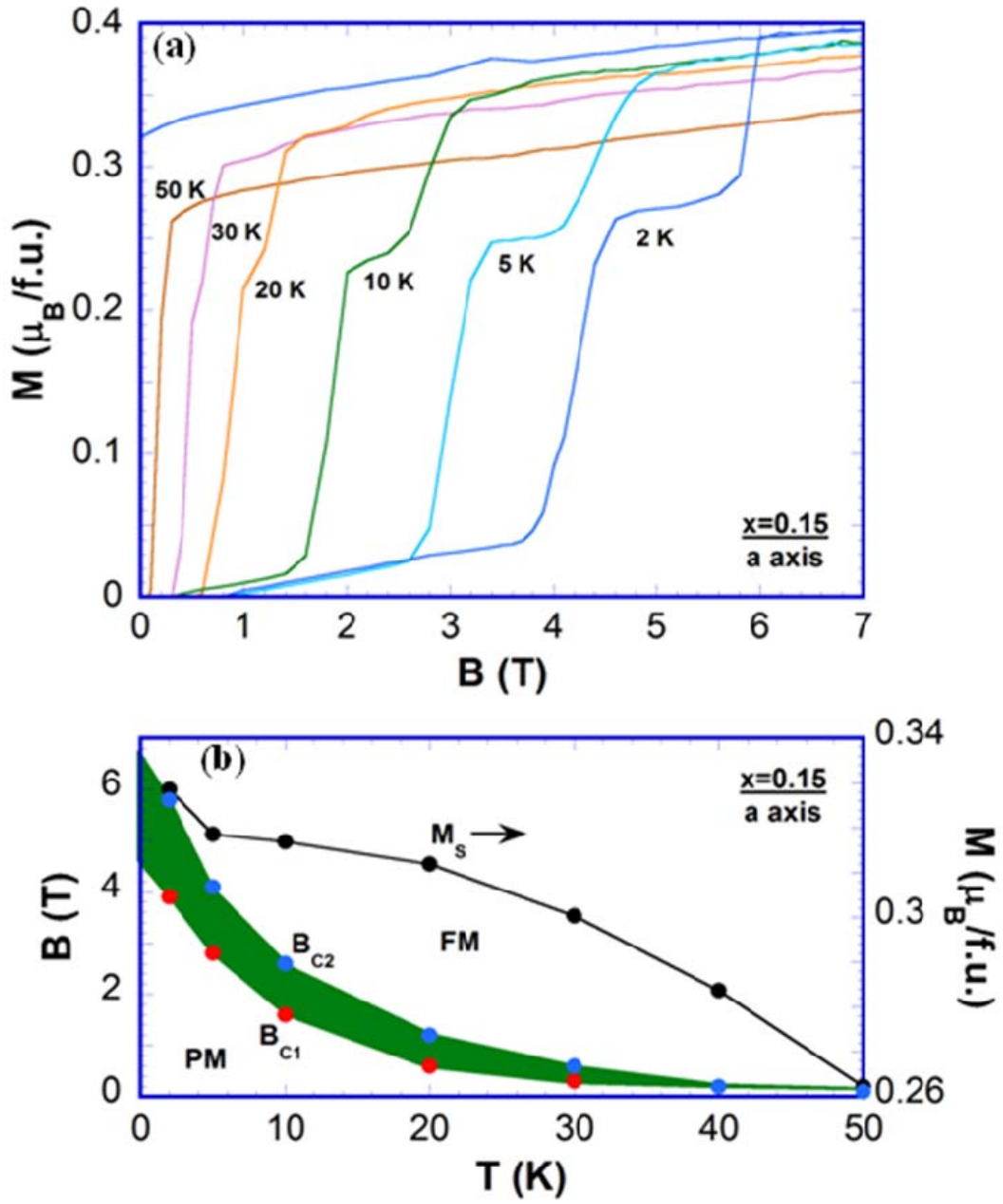


**Fig. 4.17 (a)** Isothermal magnetization, M (B), along a axis for x=0.15 for various temperatures **(b)** Temperature dependence of $B_{C1}$ and $B_{C2}$ (*left scale*) and of saturation moment, $M_S$ (*right scale*). The shaded region in green displays the meta-stable region.

Another unusual behavior in these compounds is their anisotropy in magnetic properties. From the discussions in section 4.3.3, it is clear that the magnetic responses are isotropic along different crystal directions for $SrRu_{1-x}Cr_xO_3$, as expected for these perovskite systems. But in the case of $CaRu_{1-x}Cr_xO_3$ compounds, despite the fact that the structure symmetry is not very different from that of the Sr counterparts, the properties

tend to be more anisotropic. As seen in the temperature dependence of the magnetization, the field dependence along a axis and c axis are different too. **Fig 4.18 (a)** shows the isothermal magnetization along a axis and c axis for x=0.15 at T=2 K. The saturation moment along a axis is around 3.5 $\mu_B$/f.u. whereas $M_S$ along c axis is less than half of that (0.14 $\mu_B$/f.u.)[108]. Also, the distinct two-step behavior, a unique characteristic of this concentration at low temperatures, is not well defined when magnetic field is applied along the c axis for all temperatures.

The anisotropy in magnetization is not restricted to x=0.15 alone and is realized for all the Cr concentration up to x=0.36. The ordered moment, $M_S$, for both a axis and c axis of the crystals of $CaRu_{1-x}Cr_xO_3$ at T=2 K is displayed in **Fig. 4.18 (b)**. $M_S$ for a-axis increases initially with x from 0 for x=0 to 0.4 $\mu_B$/f.u. for x=0.18 and then decreases for x > 0.18. In contrast, $M_S$ for the c-axis is much smaller. However, $M_S$ along c axis also shows a peak at x=0.18 similar to a axis ordered moments (see **Fig. 4.18 (b)**). The anisotropy in the magnetic properties along different crystal directions suggests an important role of the spin-orbit coupling.

The variations of both $\chi_0$ and $M_S$ with Cr concentration show a peak simultaneously in the vicinity of x=0.18. As $\chi_0$ is proportional to the density of states, this implies an intimate correlation between the density of states and the ordered moment. It is this concentration at which $T_C$ and $\theta_{CW}$ shows a maximum too. This concentration is much less than expected from nearest neighbor site percolation of bonds ($x_c \sim 0.307$), but larger than for nearest and next-to-nearest neighbor site percolation of bonds ($x_c \sim 0.137$). This could be an indication that bonds are not just "on or off," but that there is a distribution of bond strengths[108].

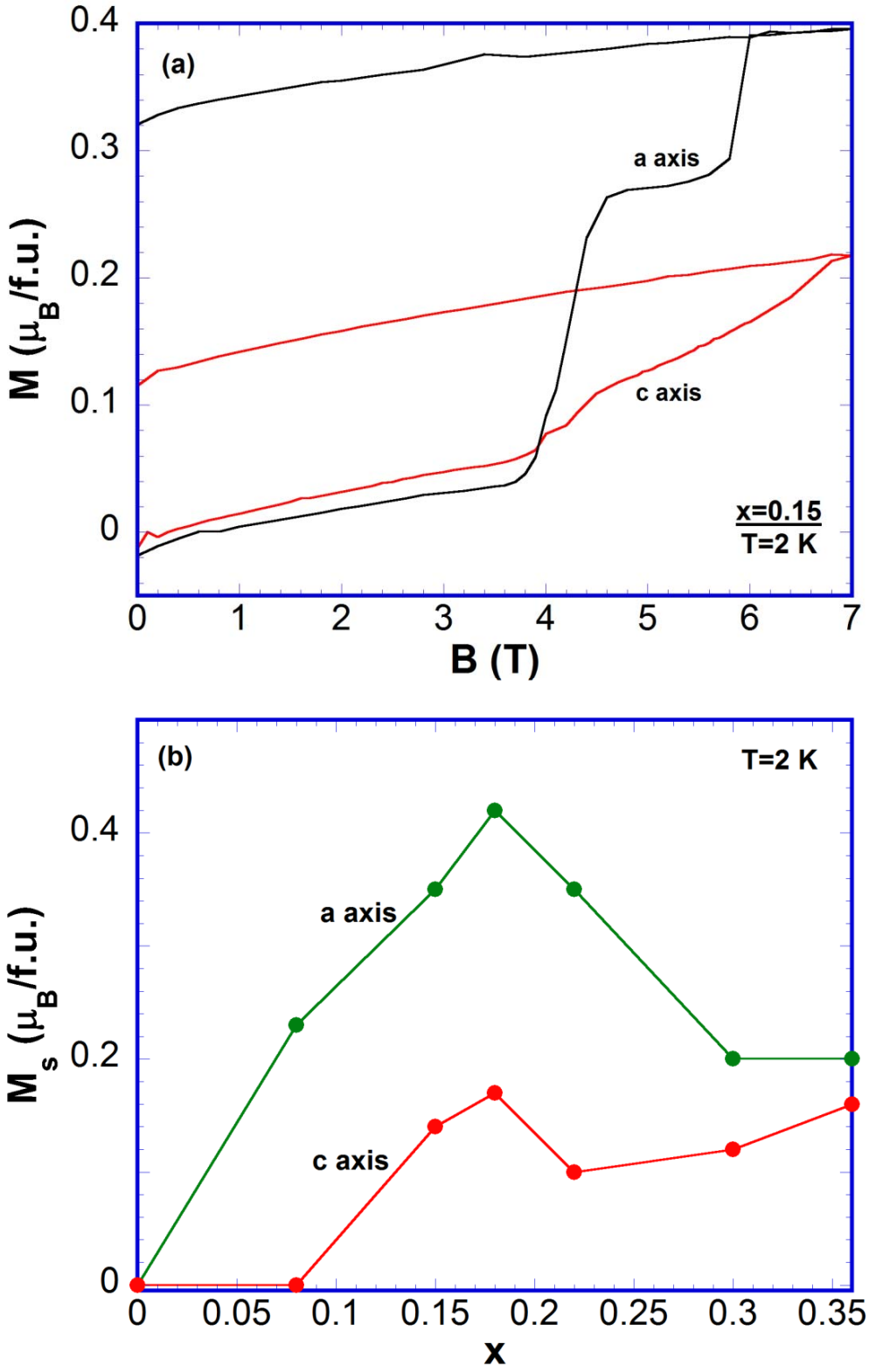


**Fig. 4.18 (a)** Isothermal magnetization, M, for a axis and c axis at T=2 K for x=0.15. **(b)** The saturation moment, $M_S$, for a- and c- axis directions at T=2 K.

Similar to $SrRu_{1-x}Cr_xO_3$, in spite of showing exaggerated changes in magnetic properties, the Cr substitution in $CaRuO_3$ does not result in any severe change in transport properties. The temperature dependence of the basal plane resistivity, $\rho_{ab}(T)$, of $CaRu_{1-x}Cr_xO_3$ for $1.7 < T < 350$ K at zero magnetic field is shown in **Fig. 4.19 (a)** (logarithmic scale). At 1.7 K, the resistivity for x=0.36 compound is increased by 3 orders of magnitude from that of the x=0 sample. Although the low temperature resistivity undergoes significant changes with x, the metallic behavior essentially remains for all x except for x=0.36. However, as seen in **Fig. 4.19 (a)**, $\rho_{ab}$ for $T < 100$ K rises and becomes less temperature-dependent with increasing x.

For x=0.36, $\rho_{ab}$ shows a slight nonmetallic behavior below 20 K and a sharp break in the slope at $T_C$ =100 K (see **Fig. 4.19 (b)**), which according to the Fisher-Langer theory is the consequence of scattering off short-range spin fluctuations in the neighborhood of $T_C$. We note that the Fisher-Langer behavior for other concentrations is not as strong as that for x=0.36[108]. Finally, the negative magnetoresistance ratio at 7 T and 2 K varies from 15% to 20% for x=0.15, 0.18, 0.22 and 0.36.

The absence of metal insulator transition, an uncharacteristic result of impurity doping in perovskite ruthenates, may be associated with the fact that only two of the three Cr $t_{2g}$ levels are occupied and electron hopping between the $Cr^{4+}$ and $Ru^{4+}$ $t_{2g}$ orbitals is energetically favorable, so the dynamic itinerant character of the d-electrons is retained. The impurity doping, however, introduces defects and disorder raising the electrical resistivity at low temperatures. This less metallic behavior for large x could be also associated with a site percolation of nearest neighbor Ru-Ru bonds[110]. The disruption of Ru connectivity affects the orientation of the $RuO_6$ octahedra (tilting angle), which to a great extent determines the properties of the ruthenates.

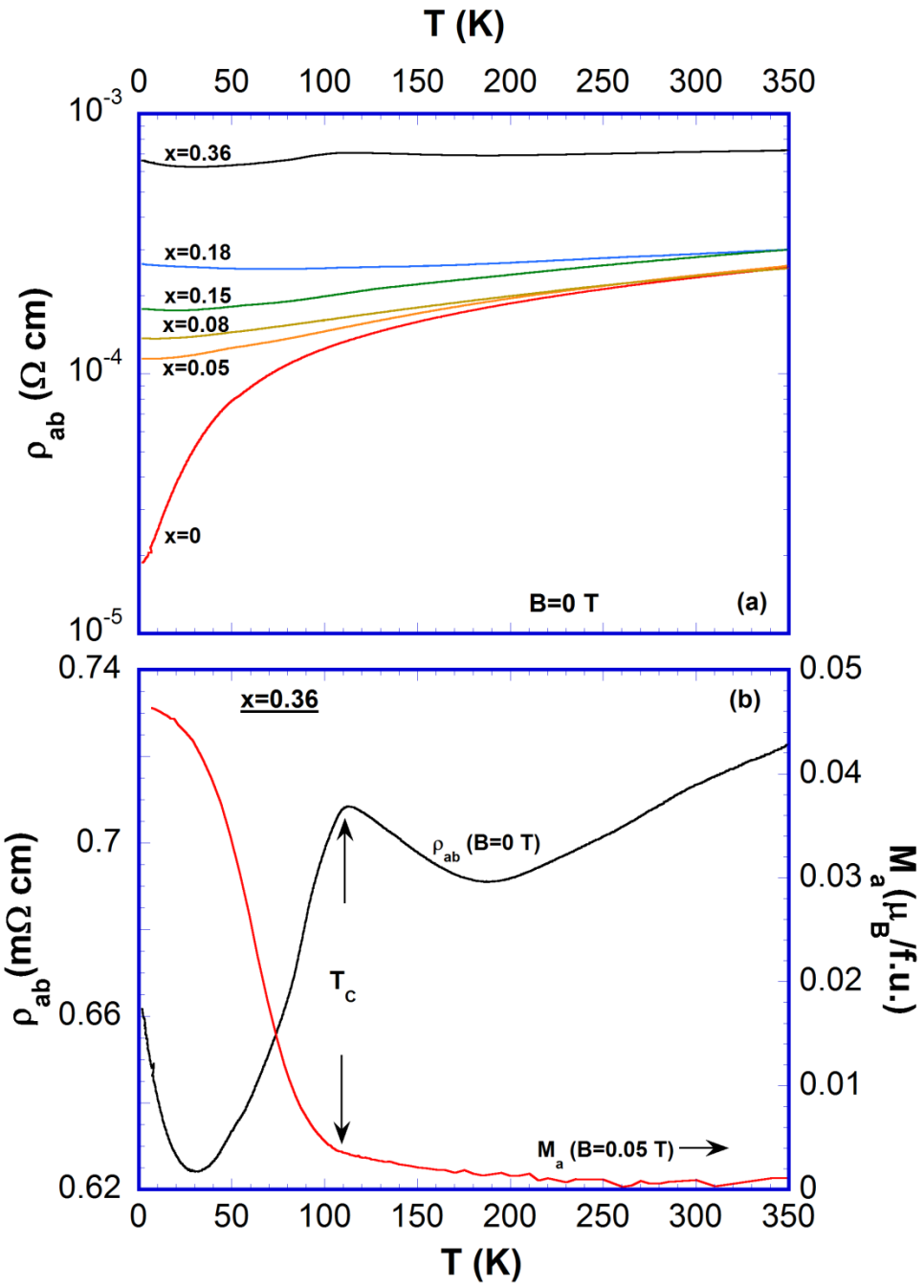


**Fig. 4.19 (a)** Basal plane resistivity, $\rho_{ab}$, on a logarithmic scale vs. temperature for x=0, 0.05, 0.08, 0.15, 0.18 and 0.36. **(b)** $\rho_{ab}$, (*left scale*) and magnetization, M, (*right scale*) as a function of temperature for x=0.36.

From the foregoing discussions on the physical properties of $CaRu_{1-x}Cr_xO_3$, a T-x phase diagram for $0 < x < 0.36$ could be sketched. As shown in the **Fig. 4.20**, the system evolves from a paramagnetic ground state to a ferromagnetic state abruptly at x=0.05.

The Curie temperature, $T_C$, (as well as the Curie-Weiss temperature, $\theta_{CW}$) increases with x until it reaches a plateau around x=0.18 before decreasing down to lower values for higher x. The increase in $T_C$ and $\theta_{CW}$ reflects stronger ferromagnetic interactions between spins as x increases. Similar trend in $\chi_0$ with x persuades an enhanced DOS induced by less extended Cr 3d orbital. The metallic behavior is retained throughout the range of Cr substitution with the Fisher-Langer behavior observed at $T_C$. Although no metal insulator phase transition is discerned up to x=0.36, a non-metallic character of electrons is evolved at low temperatures and becomes stronger with x, which might be a result of percolation effect as explained earlier.

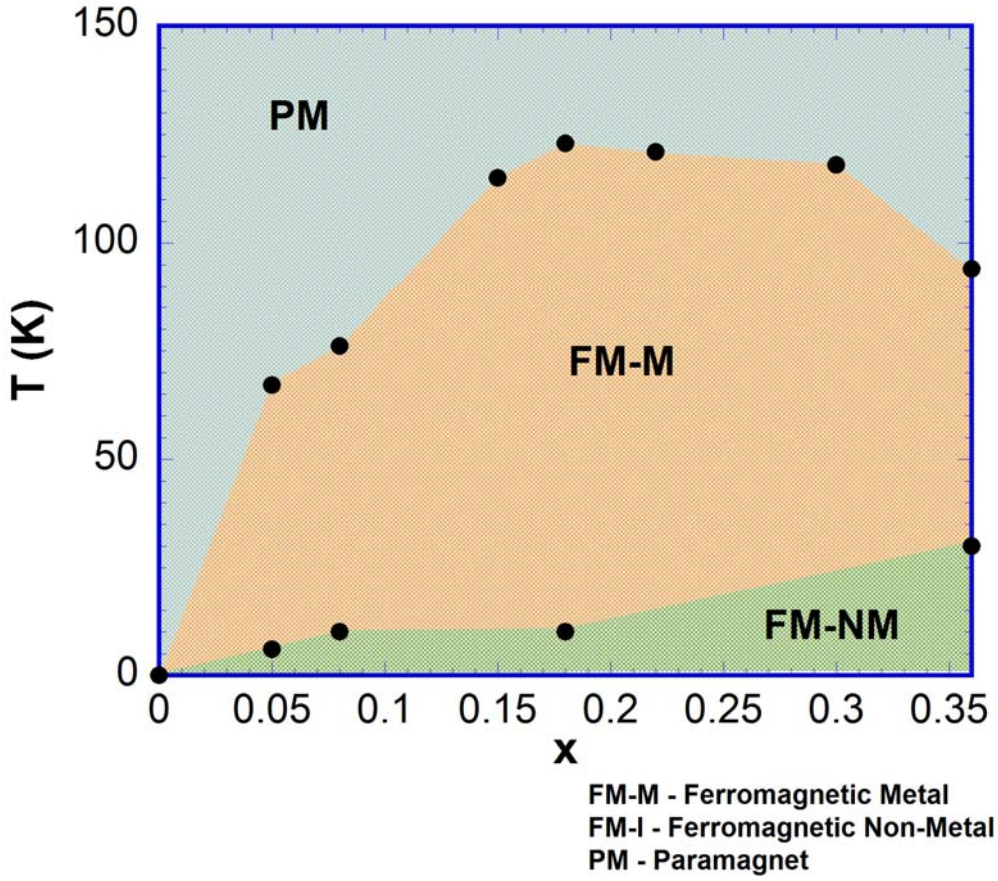


**Fig. 4.20** A simplified x-T phase diagram of $CaRu_{1-x}Cr_xO_3$ for $0 \leq x \leq 0.36$.

Unlike other 3d impurity doping in $SrRuO_3$, which reduce $T_C$ and show a metal to insulator transition, the Ru 4d electrons and the Cr 3d electrons are strikingly synergistic, leading to a highly enhanced exchange interaction and/or narrowed bandwidth favorable for ferromagnetism. This is particularly unusual for the perovskite ruthenates as

ferromagnetism exists only in a structure that allows no significant distortions of Ru-O-Ru bond angle[86].

### 4.4 Mott-like bi-layered calcium ruthenate (n=2):

$Ca_3Ru_2O_7$ is a double layered member (n=2) of the multilayered RP series and has two layers of Ru-O octahedral per unit cell. The bi-layered compounds in the series are of particular interest due to their borderline properties. $Sr_3Ru_2O_7$ bridges the metallic ferromagnet $SrRuO_3$ (n=∞) and the paramagnetic Fermi liquid $Sr_2RuO_4$ (n=1) and has a metamagnetic quantum critical point[76] associated with borderline metallic ferromagnetism. $Ca_3Ru_2O_7$ is an intermediate between the bad metal $CaRuO_3$ (n=∞) and the Mott insulator $Ca_2RuO_4$ (n=1). Because of the borderline nature of properties bi-layered calcium ruthenate will be a useful window to probe the physics of materials near a metal insulator transition.

$Ca_3Ru_2O_7$ is characterized by a non-metallic conductivity for $T < 48$ K, antiferromagnetic ordering up to $T_N$=56 K and "bad metal" conductivity, linear in temperature for $T > T_N$[83]. The compound features different in-plane anisotropies of the magnetization and magnetoresistance demonstrating a strong coupling between spin, charge and lattice. Band structure calculations[111] and experimental observations[112] show that the basic magnetic structure is ferromagnetic (FM) bi-layers with antiferromagentic (AFM) coupling. The FM density of states in Local Spin Density Approximation (LSDA)[111] band structure calculations suggests that the bi-layers are almost half metallic.

#### 4.4.1 A few intriguing problems in $Ca_3Ru_2O_7$:

The virtue of the bi-layered calcium ruthenate lies in the variety of novel physical phenomena that are inherited in the system. The list below highlights the set of properties of the compound that have drawn our attention in the past few years.

• *Huge anisotropy* – Magnetic field applied along the crystal's principal axes show case an anisotropic response to their magnetic and transport properties along different directions[112]

• *Antiferromagnetism* – The system shows an antiferromagnetic transition at $T_N$=56 K, for low applied magnetic fields[83]

• *Ferromagnetism* – A field induced ferromagnetic behavior appears at $B_C$=6 T, when field applied parallel to a axis, the magnetic easy axis[113].

• *Metamagnetism* – Along the magnetic easy axis, the magnetization of the compound shows an abrupt jump to reach a fully polarized state at $B_C$=6 T[114].

• *Mott-like transition* – There is a sudden increase in resistivity by about a factor of 20 that signifies a transition of the system from metal to insulator, at $T_{MI}$=48 K[83].

• *Antiferromagnetic metallic state* – For a narrow range of temperatures, 48 < T < 56 K, the system stays in antiferromagnetic state where the electrons tend to be itinerant too[83].

• *Tunneling Magnetoresistance* – The spin polarization along the magnetic easy axis leads to a drop in the interlayer resistivity by an order of magnitude[115].

• *Colossal Magnetoresistance* – Along the magnetic hard axis, an unconventional colossal magnetoresistance occurs at higher magnetic fields, where the ferromagnetic state becomes surprisingly unfavorable for electron conduction[116].

• *Quantum Oscillations* – Oscillations in magnetoresistance are observed that are periodic in 1/B and B along different magnetic field directions[117].

• *Non-linear conduction* – A non-Ohmic current-voltage characteristic has been observed and bounded to the Antiferromagnetic Mott state (0 < T < 48 K)[118].

Every one of the physical phenomena listed above has a wealth of scientific information in its own dimensions. Hence it is impulsive that the coexistence of those interesting physical properties in the compound would kindle the fire for a vigorous and systematic study on the compound. Even though it is vital to study the whole spectrum of the compound's behavior, my investigations on the subject revolve only around a few intriguing problems that had been challenging us for quite some time now.

**4.4.2 Crystal structure:**

Single crystals of $Ca_3Ru_2O_7$ were grown using both flux and floating zone techniques and characterized by single crystal X-ray diffraction, Laue X-ray diffraction, Scanning Electron Microscopy, electron diffraction and Transmission Electron Microscopy (TEM) techniques. $Ca_3Ru_2O_7$ crystallizes in orthorhombic structure with lattice parameters of $a$=5.3720(6) Å, $b$ =5.5305(6) Å, and $c$=19.572(2) Å with space group $A2_1ma$. A schematic of the crystal structure is presented in **Fig. 4.21 (a)**, where the $RuO_6$ layers are indicated as red octahedra. The TEM image that explains the double

layered nature of the compound is depicted in **Fig. 4.21 (b)**. The dark grey spots in the image represent the Ru-O layers and the lighter ones the Ca-O.

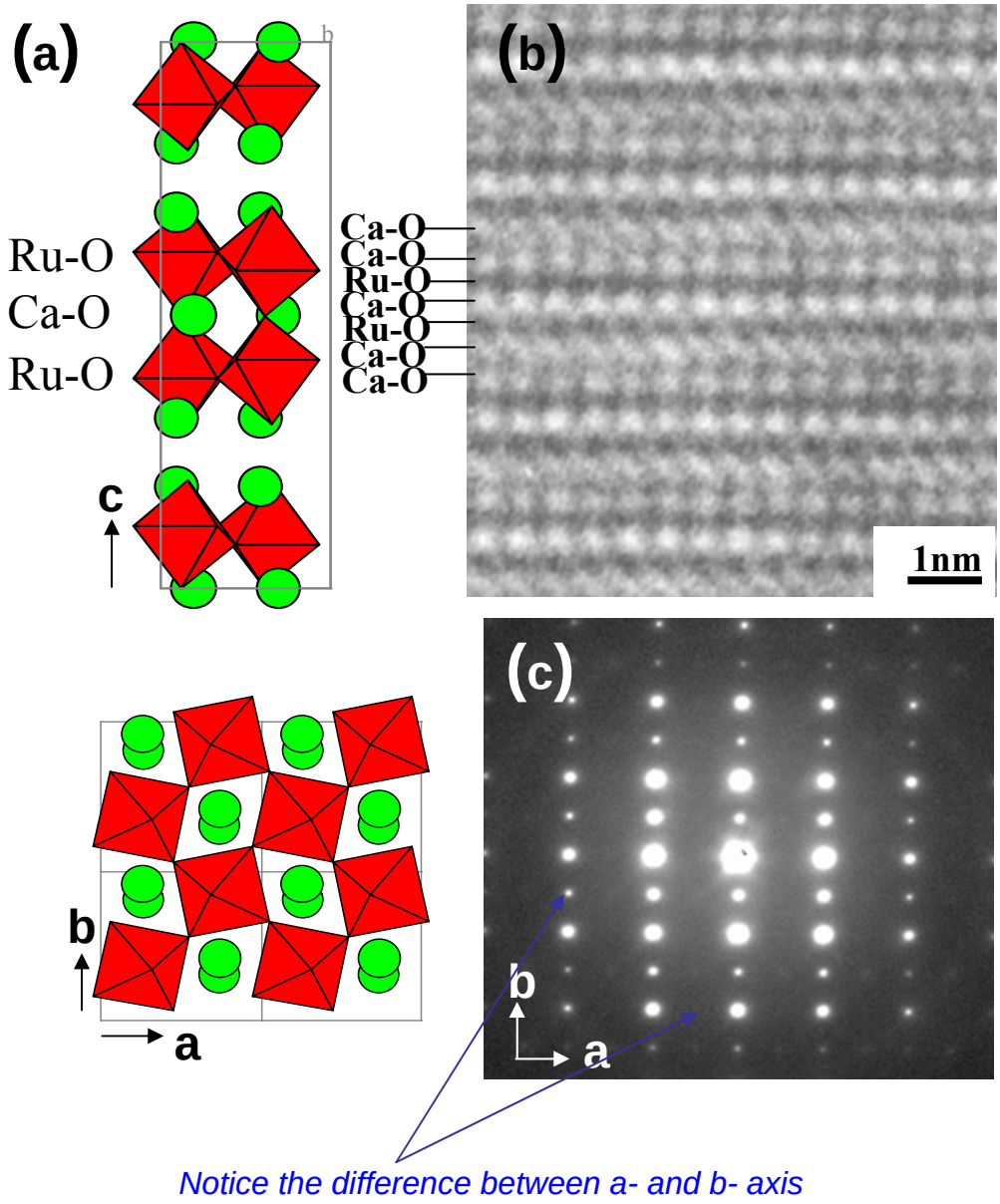


**Fig. 4.21 (a)** Crystal structure of $Ca_3Ru_2O_7$, projected along the c axis (*top figure*) and the ab plane (*bottom figure*). **(b)** The TEM image depicts the double layered nature of the compound and **(c)** the electron diffraction image reveals the anisotropic nature within the basal plane of $Ca_3Ru_2O_7$[113].

The crystal structure is severely distorted by a tilt of the $RuO_6$ octahedra as seen in **Fig. 4.21 (a)**. The tilt projects primarily onto the *ac* plane (153.22°), while it only slightly affects the *bc* plane (172.0°)[113]. These bonding angles are crucial in defining

anisotropic spin-orbital-lattice coupling within the basal plane. These crucial bond angles directly impact the band structure and are the origin of the anisotropic properties in the compound. The structural anisotropy in the basal plane is clear from the electron diffraction spectrum and the difference between a axis and b axis is quite obvious in **Fig. 4.21 (c)**.

### 4.4.3 Magnetic ground state and thermodynamics:

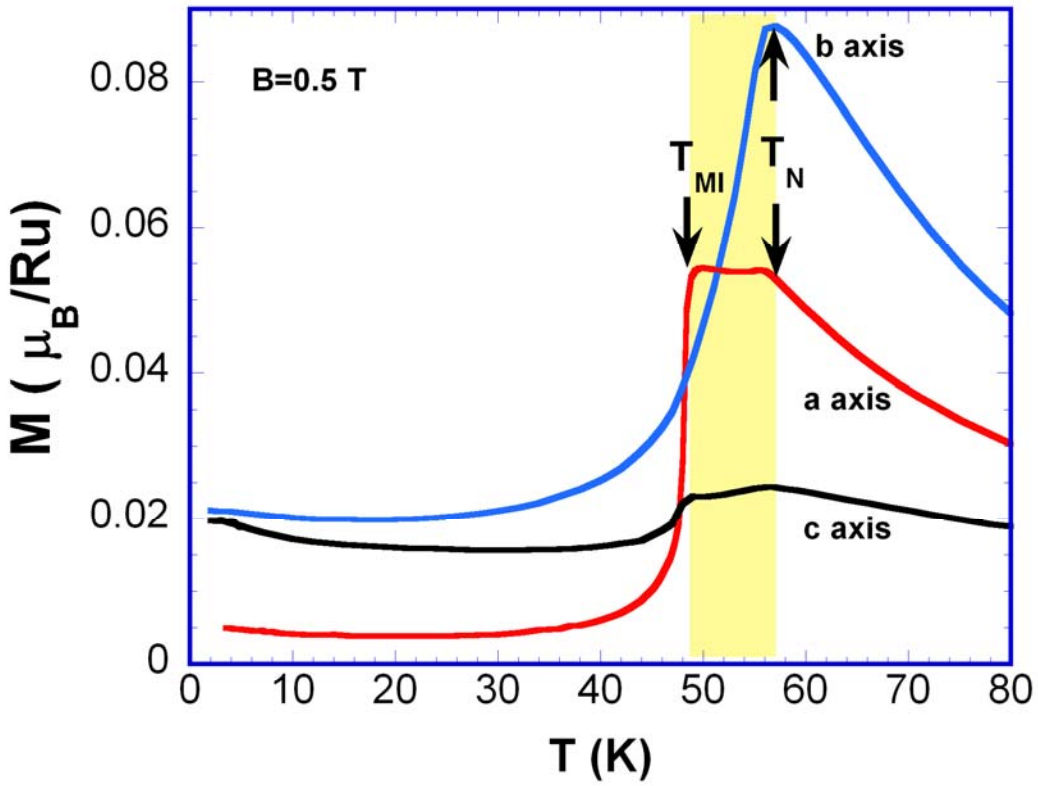


**Fig. 4.22** Temperature dependence of Magnetization, M (T), for magnetic fields applied parallel to the three principal crystal axes with B=0.5 T.

$Ca_3Ru_2O_7$ shows an AFM ordering at $T_N$=56 K and transition from a metal to a low temperature poorly conductive or insulating phase at $T_{MI}$=48 K[83] (The transport properties will be discussed in the following sections). **Fig 4.22** shows the low field M (T) for the different crystallographic axes. For field applied along a axis, the magnetic easy axis, M (T) features two phase transition temperatures, $T_N$=56 K and $T_{MI}$=48 K. In contrast, M (T) for the b axis exhibits no anomaly corresponding to $T_{MI}$ but a sharp peak at $T_N$ as shown in the **Fig. 4.22**. When B is applied along c axis, the magnetization is similar to that of a axis but the magnitude is very weak when compared to the other axes.

The highly anisotropic magnetic properties of $Ca_3Ru_2O_7$ are used to determine the magnetic easy a axis and to identify twinned crystals that often show a small kink at 48 K in the b-axis susceptibility.

The magnetic anisotropy is further emphasized when magnetic field is scanned at constant temperatures. **Fig 4.23** displays the isothermal magnetization at T=2 K with magnetic fields applied along all the three crystal axes. For B||a, the magnetization shows a linear response to the applied magnetic field up to 6 T, corresponding to the antiferromagnetic ground state. At B=6 T, a first-order metamagnetic transition occurs, which leads to a spin-polarized or ferromagnetic state with a saturation moment $Ms=1.73\mu_B$ /Ru[114], as shown in **Fig 4.23**. The observed saturation moment equals more than 85% of a hypothetical saturation magnetization $2\mu_B$ /Ru expected for an S=1 system. The transition is sensitive to temperature as it slightly decreases for increasing T and disappears completely for $T > T_{MI}$.

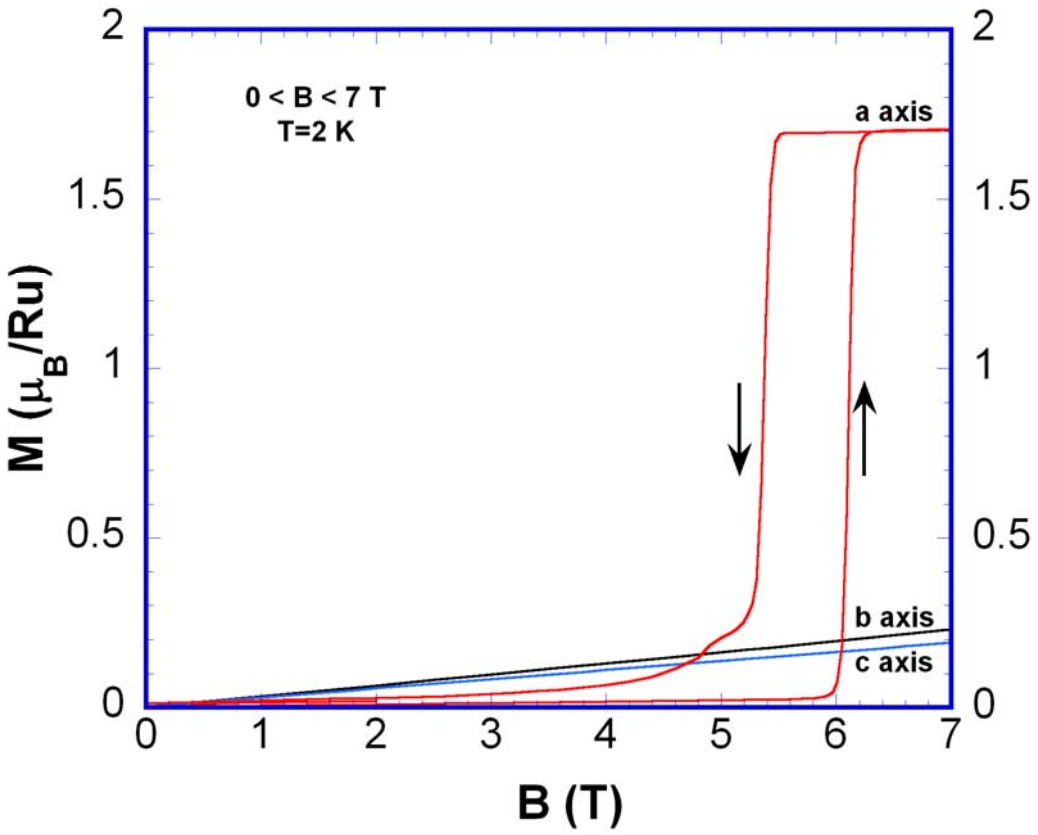


**Fig. 4.23** Magnetic isotherms, M (B), for magnetic field applied along different crystallographic axes at T=2 K.

For B applied along the other crystal directions, the system remains in the antiferromagnetic ground state up to an applied field of 7 T as is clear from the magnetization's linear response to the magnetic field. The evolution of the difference in magnetic states at relatively high magnetic fields along different axes in the crystal is displayed in **Fig. 3** of reference[113]. As B||a increases, $T_{MI}$ shifts slightly, whereas $T_N$ remains essentially unchanged initially and becomes rounded eventually. On the other hand, when B is parallel to the b axis, $T_N$ decreases with increasing B at approximately a rate of 2 K/T as explained in the reference[113]. Markedly, the magnetic ground state for B||b axis and B||c axis remain antiferromagnetic, entirely different from that for B||a axis.

The magnetization measurements imply that the $RuO_6$ layers themselves are ferromagnetically ordered, with an AF stacking[112]. The three possible AF stackings[111] along c axis are

(1) Ferromagnetic bi-layers stacked antiferromagnetically i.e. *_UU _ DD _ UU _*

(2) Bi-layers that are internally antiferromagnetically aligned, stacked in a FM fashion i.e. *_UD _ UD _ UD _* or

(3) Bi-layers that are internally antiferromagnetically aligned, stacked in an AF fashion, i.e. *_UD _ DU _ UD_*.

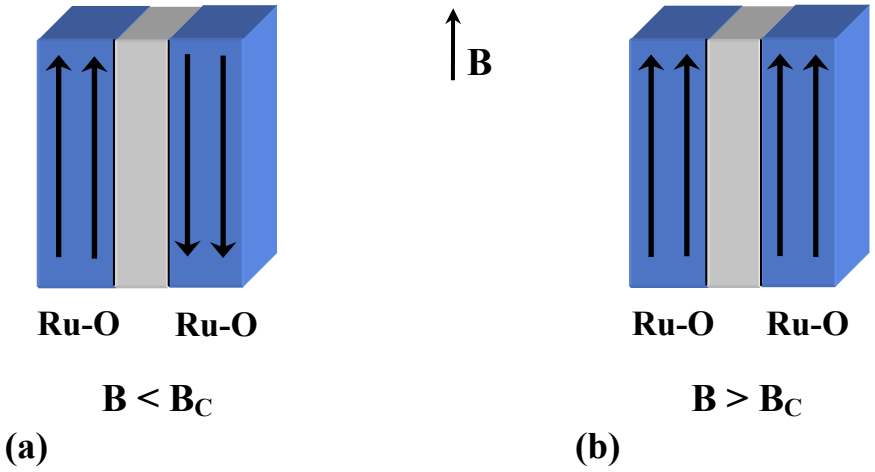


**Fig. 4.24** Spin configuration in $Ca_3Ru_2O_7$ for **(a)** $B < B_C$ and **(b)** $B > B_C$.

Neutron scattering experiments, done on these crystals, favor the ordering that involves the ferromagnetic bi-layers stacked antiferromagnetically along the c axis[119] as shown in **Fig. 4.24**. The FM interaction within a bi-layer is much stronger when

compared to the AFM coupling between the layers as suggested by the LSDA calculations[111].

The high temperature paramagnetic phase (150 < T < 350 K) follows the modified Curie-Weiss law, $\chi = \chi_0 + \frac{C}{(T - \theta_{CW})}$ (equation 4-1). The temperature independent susceptibility, $\chi_0$, a measure of density of states at the Fermi level, is unusually larger in this compound than in most metals. This might have resulted from the localized electrons at the Fermi energy or from the partial gapping of the Fermi surface. The effective moment, $\mu_{eff}$, calculated from the Curie constant, C, ($\mu_{eff}$=2.82 $\sqrt{C}$) is 2.86 $\mu_B$[112], which is comparable to the expected value (=2.83 $\mu_B$) for a spin 1 system. The Curie-Weiss temperatures along the three crystal directions are different and their values are +72, and +59 K respectively for a and b axes. The estimated Curie-Weiss temperatures are all positive, which are unusual for antiferromagnets as the antiferromagnetic interactions at higher temperatures are represented by negative $\theta_{CW}$. These positive values for $\theta_{CW}$ indeed indicate dominating ferromagnetic interactions between Ru ions within the bi-layers at high temperatures. However, the ferromagnetic layers are coupled antiferromagnetically hence confirming the spin arrangement given in **Fig. 4.24** for $Ca_3Ru_2O_7$[112]. Furthermore, this anisotropy in $\chi$ (T) in the paramagnetic metallic state suggests an anisotropic exchange and/or strong but anisotropic electron correlations in $Ca_3Ru_2O_7$.

In addition, low temperature specific heat measurements for 1.7 < T < 20 K of $Ca_3Ru_2O_7$ reveal an unusually large density of states near the Fermi surface: Even in the "insulating" phase the electronic specific heat coefficient ($\gamma$ = 37 mJ/mol-$K^2$)[83] is much larger than most "good" metals. Even though it is comparable to that of $SrRuO_3$, which is a well-known itinerant ferromagnet ($\gamma$ = 30 mJ/mol-$K^2$)[88, 120, 121] and to superconducting $Sr_2RuO_4$ ($\gamma$ = 45 mJ/mol-$K^2$)[122], it is far larger than that expected for a "classic" insulator. The speculation is that nearly localized (heavy) carriers near the Fermi surface may contribute to the electrical conductivity and angular resolved photoemission studies support this[123].

### 4.4.4 Antiferromagnetic metallic state:

Even though there are several interesting behaviors feature in the inter-plane ($\rho_c$) and intra-plane ($\rho_a$) resistivity curves for 1.7 < T < 350 K (fig 4.25), I would like to point out a few of them here.

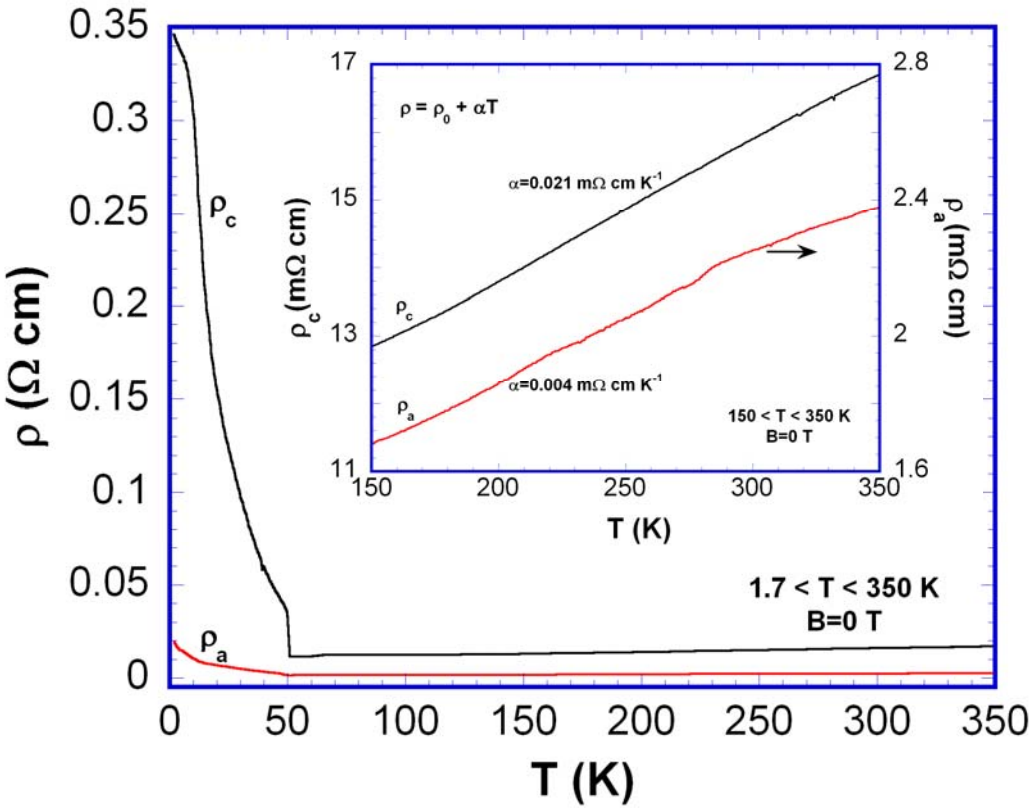


**Fig. 4.25** Temperature dependence of resistivity for $Ca_3Ru_2O_7$ at B=0 T for $1.7 \leq T \leq 350$ K.

The resistivity shows metallic behavior[83] ($d\rho/dT > 0$) for T > 56 K along the two current directions and follows a linear dependence in T for 150 < T < 350 K (see the inset). The resistivity values are relatively large with 15.9 mΩ cm and 2.25 mΩ cm along $\rho_c$ and $\rho_a$ respectively at room temperature, indicating a narrow 4d band. The differences in the temperature dependences of inter and intra plane resistivities at high temperatures support the magnetic susceptibility measurements and also suggest an anisotropic electron correlation. At T=48 K, there is a rapid increase in ρ (T) signaling a transition to a less conducting or an insulating state. This abrupt jump in resistivity varies from 6 to 18 times, depending on samples. For instance, the sample that was measured to show the characteristic as shown in **Fig. 4.25**, registered an increase of about 21 and 8 for $\rho_c$ and $\rho_a$

respectively at $T_{MI}$. The resistivity ρ (T) exhibits a small thermal hysteresis in the vicinity of $T_{MI}$. This hysteresis, together with the abrupt χ (T) and ρ (T) changes at $T_{MI}$ demonstrates that the transition is first order. Unlike the metal to insulator transition in other systems, e.g. $V_2O_3$, where the resistivity increases by several orders of magnitude just below $T_{MI}$[124, 125], ρ (T) of $Ca_3Ru_2O_7$, approaches a saturation value at low temperature (see **Fig. 4.26**). The observed larger inter-plane ρ (T) when compared to the intra-plane ρ (T) is expected for a staggered layered system. However, the exciting feature is the antiferromagnetic metallic (AFM-M) state that lies in between the Neel temperature, $T_N$, and the metal-insulator transition, $T_{MI}$, ($48 < T < 56$ K).

**Fig. 4.26 (a)** shows the temperature dependence of the electrical resistivity, ρ (T), of $Ca_3Ru_20_7$ for $1.7 < T < 80$ K for inter-layer ($\rho_c$) and intra-layer ($\rho_a$) directions (left scale) and the response of the c axis lattice parameter to the changes in temperature (right scale) for the same temperature range. For $48 < T < 56$ K there is a relatively weak but well-defined metallic characteristic in ρ (T) (see **Fig. 4.26 (b)**). The ρ in this regime shows a linear dependence in temperature corresponding to a Fisher-Langer like behavior. The metallic conductivity in the AFM phase behaves differently for magnetic fields applied along different directions. The response to the applied field reminds us of a half-metallic characteristic and will be discussed in the next section. There is a huge anisotropy in ρ (T) below $T_{MI}$ where $\rho_c$ (T)/$\rho_a$ (T) ~ 18 at T=1.7 K. Likewise, a slight (001)/(100) anisotropy is observed also for $T > T_{MI}$ in the metallic phases. Nevertheless the AFM-M region ($\Delta T$=8 K) is not broad enough to conclude any physical aspects.

X-ray diffraction studies in the temperature range $12 < T < 100$ K exhibit a rapid decrease in the c-axis lattice parameter at $T_{MI}$[83] as shown in **Fig. 4.26 (a)** (right scale). However, no systematic changes in the ab plane are observed in the temperature regime. A collapse of the c-axis lattice parameter would be expected to enhance the overlap of orbitals and hence the metallic state. But here the collapse conversely leads to a gapped, nonmetallic ground state, as evidenced by an abrupt metal-nonmetal transition at $T_{MI}$=48 K[83]. This unconventional behavior develops as a result of Jahn-Teller distortions of the $RuO_6$ octahedra induced by the c axis shortening. The octahedral distortion lowers the $d_{xy}$ orbitals relative to $d_{zx}$ and $d_{yz}$ orbitals with a possible orbital distribution of ($n_{xy}/n_{zx}$ $n_{yz}$, 2/2)[126]. Consequently, an AFM and OO phase can occur, explaining the poor metallic

behavior for $T < T_{MI}$ and $B < B_C$. This is consistent with Raman-scattering studies[126] of $Ca_3Ru_2O_7$, which reveals the opening of a charge gap, $\Delta_c \sim 0.1$ eV at $T_{MI}$ and the concomitant softening and broadening of an out-of-phase O phonon mode.

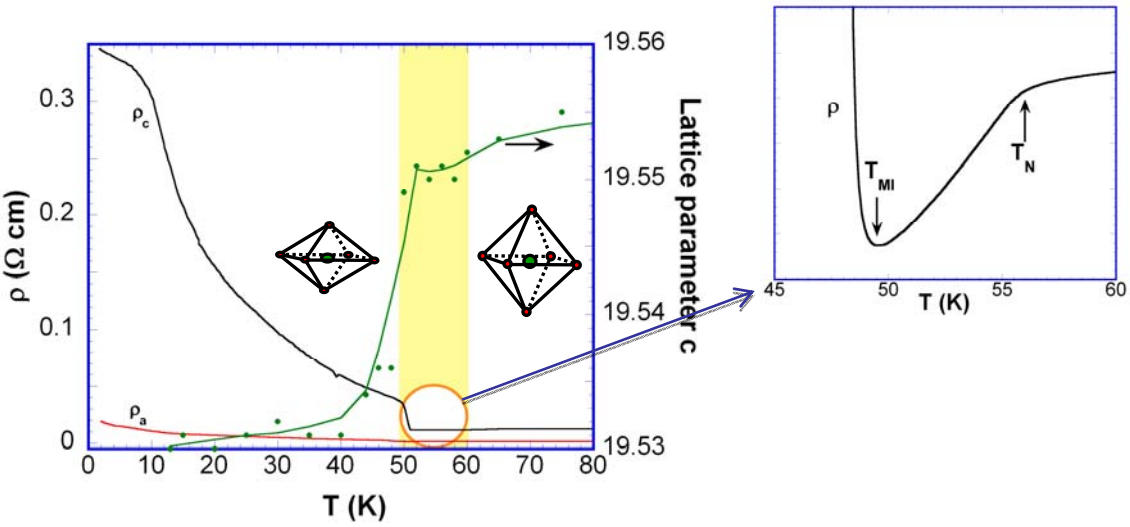


**Fig. 4.26** Temperature dependence of **(a)** inter-plane ($\rho_c(T)$) and intra-plane ($\rho_a(T)$) resistivities in the left scale and lattice parameter c in the right scale. **(b)** Zoomed portion of the $\rho_c(T)$ curve for 45 K ≤ T ≤ 60 K to show the region of antiferromagnetic metallic state (48 K ≤ T ≤ 56 K)[115].

Furthermore, Hall Effect measurements performed on the cubic crystals of bi-layered calcium ruthenate revealed that there is a change in the charge carriers right at the $T_{MI}$. The Hall resistance is estimated by measuring the voltage along the b axis with electric current and magnetic field applied along a and c axes respectively. **Fig. 4.27** shows the Hall resistance ($R_H$) of $Ca_3Ru_2O_7$ as a function of temperature for the temperature range $1.7 < T < 300$ K. The $R_H$ at lower temperatures ($T < 48$ K) is negative suggesting that the electrons are the charge carriers for conduction. The notable characteristic of the curve is that it shows a sharp jump close to the $T_{MI}$ where there is depreciation in the negative value of $R_H$. The Hall resistance value ultimately reaches a positive value at T=48 K and holds its sign for higher temperatures up to T=300 K. The change in sign for $R_H$ persuades that the charge carriers change from one type to the other for $Ca_3Ru_2O_7$ at temperatures close to the $T_{MI}$. This behavior is consistent with the work done by Y Yoshida et.al.[127].

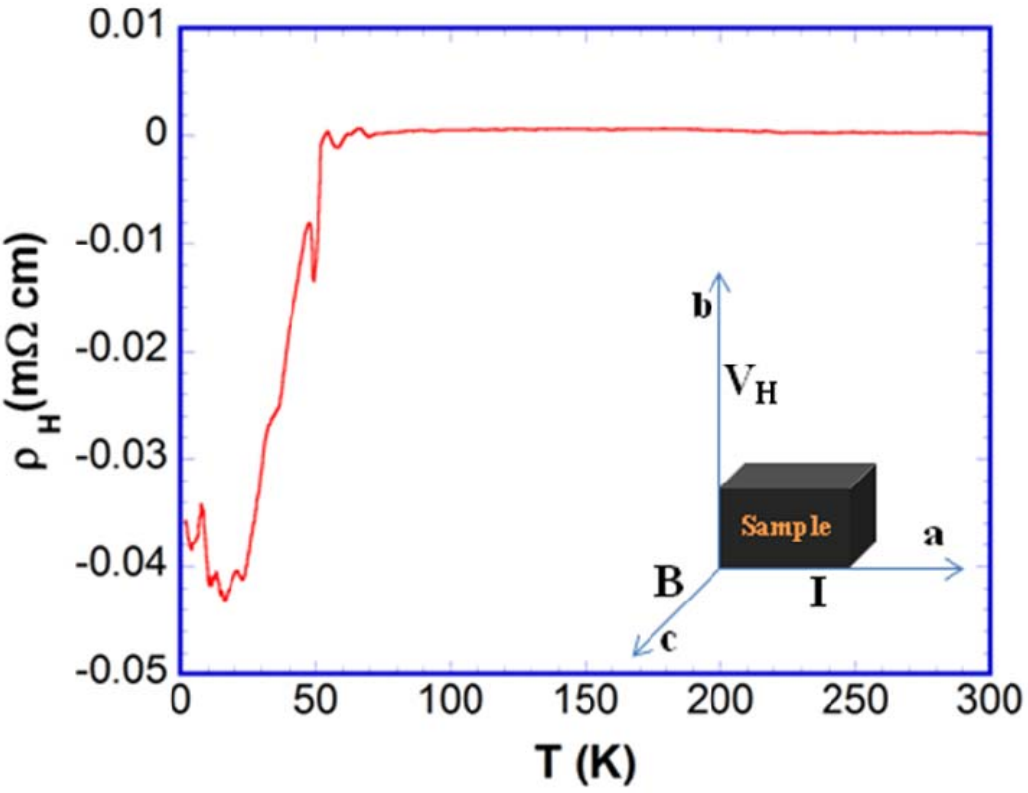


**Fig. 4.27** $R_H$ vs. T in $Ca_3Ru_2O_7$ for $1.7 \leq T \leq 300$ K when B||c axis=7 T.

**4.4.5 Nearly half-metallic characteristic:**

The LSDA band structure calculations done by DJ Singh et.al.[111] suggest a nearly half-metallic behavior for $Ca_3Ru_2O_7$. The resistivity response to the magnetic field applied along different crystal directions supports the band structure calculations as well. Shown in **Fig. 4.28** is the temperature dependence of the c-axis resistivity, $\rho_c$, at a few representative B, which is applied along a axis (**Fig. 4.28 (a)**) and the b axis (**Fig. 4.28 (b)**), respectively. As evident from the figure, the metal-insulator transition is pushed to lower temperatures when magnetic field is applied along the b axis. On the other hand, $T_{MI}$ increases with the transition getting rounded off and ultimately showing a semiconducting behavior for B||a axis[128]. This behavior is typical of a half-metal where one spin channel behaves metallic while the other insulating simultaneously.

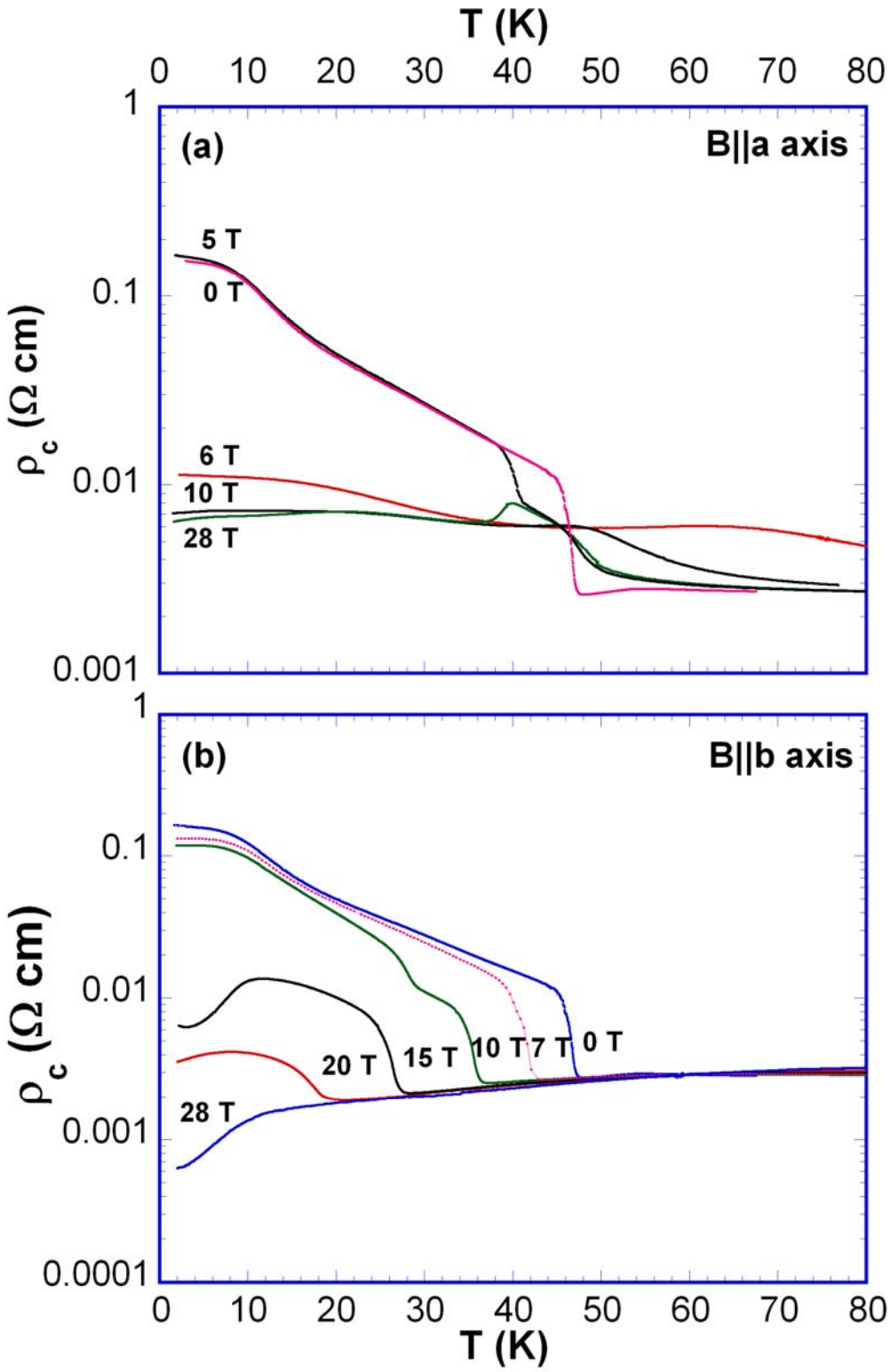


**Fig. 4.28** Temperature dependence of the *c*-axis resistivity, $\rho_c$, at a few representative B up to 28 T applied along **(a)** a axis and **(b)** b axis for $1.7 \leq T \leq 80$ K[128].

Furthermore, for B||a axis, $\rho_c$ at low temperatures decreases abruptly by about an order of magnitude when B > 6 T, the field at which the first order metamagnetic transition leads to the spin-polarized state. This reduction in $\rho_c$ is attributed to the tunneling effect[115] and will be explained later in this chapter (section 4.4.6). Further increase in B (up to 28 T) only results in slightly higher resistivity at low temperatures. However, what is unexpected is the behavior of $\rho_c$ when B is applied along b axis. For B||b axis, the magnetic hard axis, the Mott state collapses approximately at a rate of 2 K/T and disappears for B > 20 T[128] as shown in **Fig. 4.28 (b)**. The drop in resistivity at lower temperatures for B||b axis is around three orders of magnitude against the one order of magnitude drop at the spin polarization along the easy axis.

Even though $\rho_c$ drops by three orders of magnitude and shows a fully metallic state when B||b, the temperature dependence of $\rho_c$ at B||b=30 T does not at all obey the $T^2$ dependence expected for a Fermi liquid. Instead, $\rho_c$ exhibits an unusual $T^{1.2}$ dependence[115] in the supposedly fully spin-polarized state where the spin degree of freedom should be eliminated. The low power-law temperature dependence of $\rho$ normally implies strong scattering. While magnon scattering might partially account for this behavior, the anomalous temperature dependence of $\rho_c$ once again suggests an unusual scattering mechanism(s) that governs not only the ground state but also persists well into the high temperature regime. A detailed discussion will be presented in the following sections.

**4.4.6 Tunneling Magnetoresistance:**

The 85% spin polarization along the magnetic easy axis is reflected in the electrical conductivity of the compound. An inverse relation between the magnetization and the magnetoresistance exists where the resistivity drops by an order of magnitude at the metamagnetic transition critical field, $B_C$. The inter-plane resistivity, $\rho_c$, as a function of applied magnetic field parallel to a axis at T=5 K is shown in **Fig. 4.29** (left scale) and the isothermal magnetization, M, at T=5 K for a axis also is shown in **Fig. 4.29** (right scale). $\rho_c$ shows a first order transition in the vicinity of 6 T, apparently driven by the first order metamagnetic transition which leads to the spin-polarized state with a saturation moment, $M_S$=1.73 $\mu_B$/Ru.

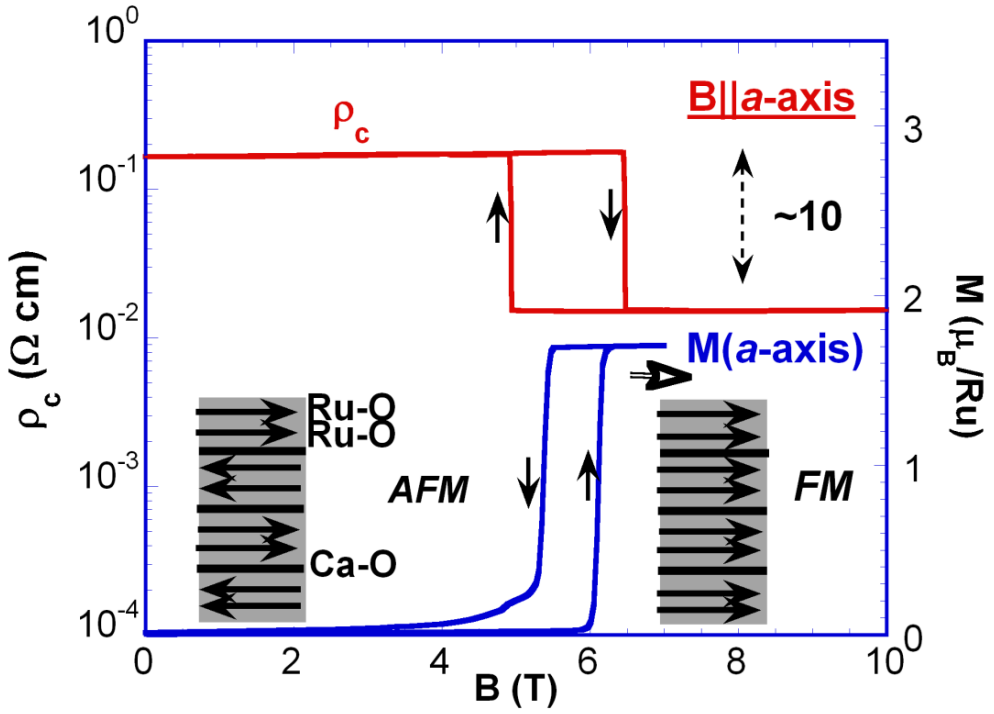


**Fig. 4.29** Field dependence of the inter- layer resistivity, $\rho_c(B)$, (*left scale*) and that of the magnetization, M (B), (*right scale*) at T=5 K showing the coupling of spin polarization with the electron transport[115].

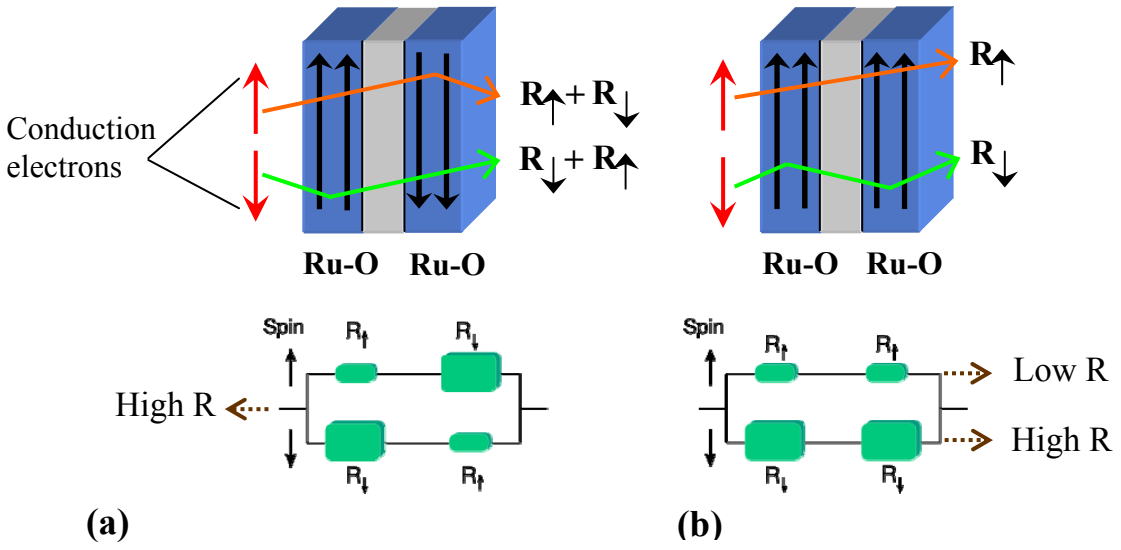


**Fig. 4.30** Electron conduction processes in Ru-O/Ca-O/Ru-O layer junction when the magnetic layers are **(a)** antiferromagnetic ($B \leq 6$ T) and **(b)** ferromagnetic ($B > 6$ T).

The reduction of $\rho_c$ at $B_C$ (=6 T) is attributed to a tunneling effect facilitated by a field-induced coherent motion of spin-polarized electrons. Because of the layered nature,

the spin-polarized Ru-O planes sandwiched between insulating (I) Ca-O planes form an array of FM/I/FM junctions (see **Fig. 3 (a)** of reference[115]) that enhances the probability of tunneling and thus electronic conductivity. However, what is entirely unexpected is the drop in $\rho_c$ for B parallel to the hard axis i.e. b axis, where we did not see any evidence for spin polarization. To make the scene more interesting, the resistivity drop when field is applied parallel to b axis is two orders of magnitude larger than that for B parallel to the easy axis (a axis), i.e., $\rho_c(30\ T)/\rho_c(0) = 10^{-1}$ for B||a but $10^{-3}$ for B||b at T=0.6 K[115]. This is completely contrary to the anisotropy in the magnetization explained in section 4.4.4.

The negative magnetoresistance is in general driven by the reduction of spin scattering[129] and as a result one would expect a metallic state in the spin polarized regime. But it is astonishing that despite having a spin-polarized state along the easy axis no fully metallic state is achieved in $Ca_3Ru_2O_7$. In fact, a further increase in B to 30 T only results in a linear increase of the resistivity with B, which is explained in detail in the next section (section 4.4.7).

**4.4.7 Colossal Magnetoresistance by avoiding a FM State:**

In addition to the tunneling magnetoresistance along the magnetic easy axis as a result of the spin-polarized sate, an entirely unexpected behavior is resulted when magnetic field is applied parallel to the magnetic hard axis. We observed evidence for an unusual Colossal Magnetoresistance realized only when B is perpendicular to the easy axis of magnetization. This CMR phenomenon is fundamentally different from those of all other magnetoresistive systems, which are primarily driven by spin polarization.

Shown in **Fig. 4.31** is the field dependence of the resistivity for $\rho_c$ (right scale) for T = 0.4 K and 0 < B < 45 T with B applied along a, b and c axes. As shown in the figure, $\rho_c$ is extraordinarily sensitive to the orientation of B. An abrupt drop of $\rho_c$ by an order of magnitude at B=6 T is observed along the easy axis that corresponds to the first order metamagnetic transition (shown in the **Fig. 4.31** (left scale)). The physics behind this tunneling magnetoresistance has been explained in section 4.4.6. However, the field dependence of $\rho_c$ at higher fields contradicts our conventional wisdom on metals and deserves a deeper insight. As B is increased further from 6 to 45 T, $\rho_c$ increases linearly with B by more than 30%. This linear behavior is interesting in its own right since a quadratic dependence in field is expected for regular metals[130]. As spin scattering is

already reduced to its minimum at B = 6 T, the linear increase can arise only from orbital degrees of freedom that hinders the electrons from hopping through spin-orbit coupling.

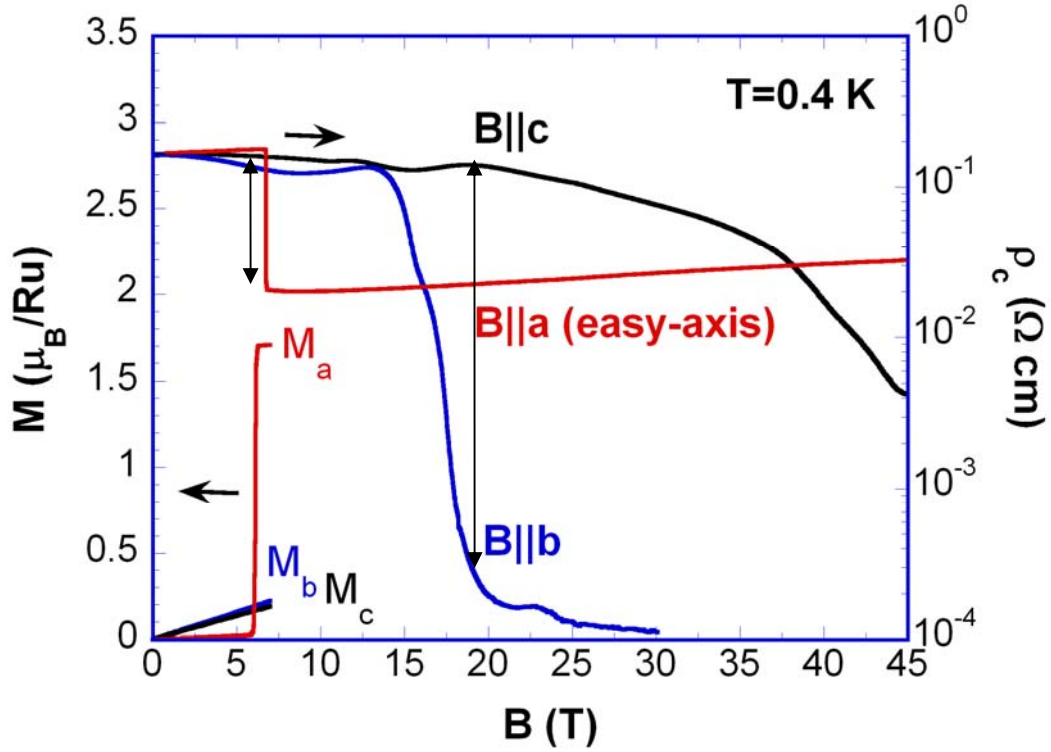


**Fig. 4.31** Magnetic field dependence of Magnetization, M (B), (*left scale*) and that of the inter-plane resistivity ($\rho_c$(B)) (*right scale*) at T=0.4 K for all the crystallographic axes. The drop in resistivity for B||b axis is much more than that for B||a axis, suggesting the dominance of orbitals on the electronic conductivity. Note that the resistivity measurements were performed in an applied field up to B=45 T.

For B||b axis (i.e. along magnetic hard axis), there is no spin-flop transition and the system remains AFM. In sharp contrast with $\rho_c$ for B||a axis, where the resistivity drops by one order of magnitude at B=6 T, $\rho_c$ for B||b axis rapidly decreases by as much as 3 orders of magnitude at $B_C$=15 T. When the 85% spin polarization could manage only one order of magnitude drop in resistivity, the magnetic field applied perpendicular to the easy axis triggered a resistivity drop that is 2 orders of magnitude more than that for B||a axis. Since the fully polarized state for B||a > 6 T can reduce $\rho_c$ by only 1 order of magnitude, even a fully polarized state along b axis at high fields, if it happens at all, still cannot account for the 3 orders of magnitude decrease in $\rho_c$ when B||b > 15 T. This fact

indicates that the spin degree of freedom alone is not at all enough to explain the unusual behavior observed in **Fig. 4.31**.

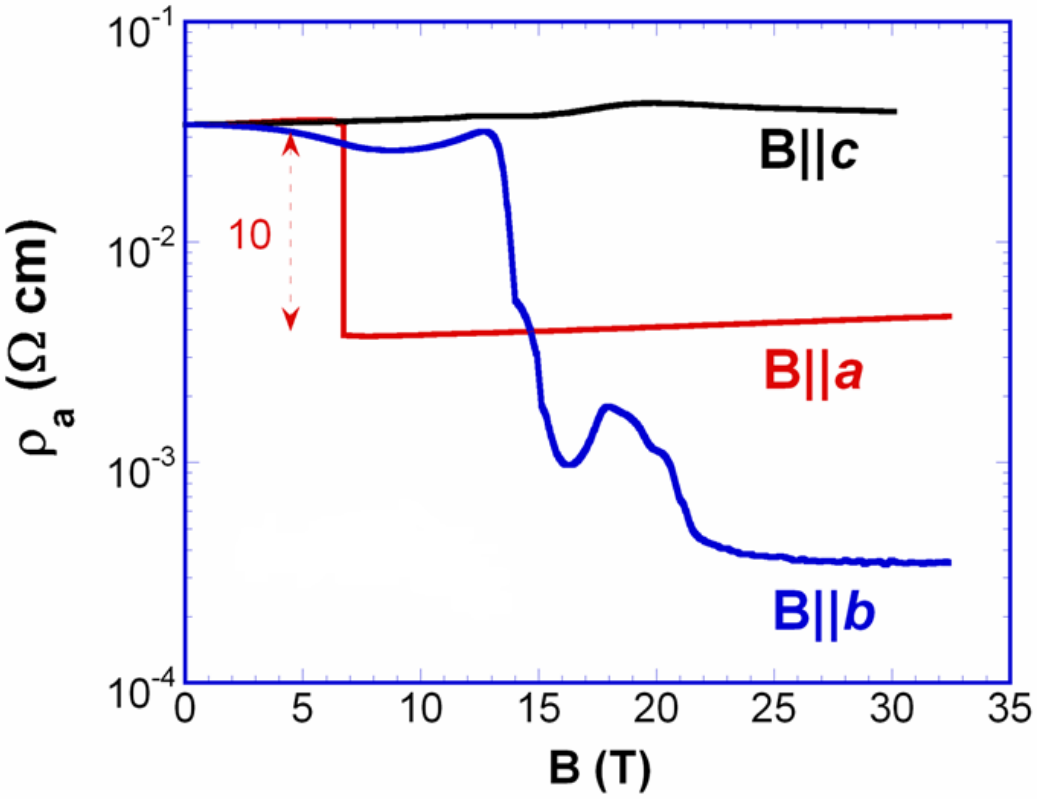


**Fig. 4.32** Magnetic field dependence of the intra-plane resistivity ($\rho_a$(B)) at T=0.4 K for 0 ≤ B ≤ 33 T along the three crystallographic axes.

Furthermore, for B||c-axis, $\rho_c$ displays slow Shubnikov-de Haas oscillations, signaling the existence of very small Fermi surface cross sections. They must be associated with the motion of the electrons in the ab-plane or $d_{xy}$ orbitals. The analyses of the oscillations for $\rho_c$ will be provided in the following section (section 4.4.8). But the feature I would like to discuss here is the higher field resistivity behavior for B||c against that along a axis. For B||a, $\rho_c$ increases linearly with B, as discussed earlier, whereas for B||c the inter-plane resistivity decreases as B is increased. Remarkably, for B||c > 39 T, $\rho_c$ is much smaller than that for B||a[116]. If we quantify the change in resistivity from 0 to 45 T, $\rho_c$ decreases by a factor of 7 for B||a and 40 for B||c. Hence, it is clear that at higher magnetic fields the fully polarized or the ferromagnetic state i.e. when B applied along a axis, is least preferred by electrons for conduction. It is striking that a fully spin-polarized

state, which is essential for magnetoresistance in all other magnetoresistive materials[130, 131], is the least favorable for conduction in $Ca_3Ru_2O_7$.

It is worth mentioning that the intra-plane resistivity ($\rho_a$) and inter-plane resistivity ($\rho_c$) behave very similarly when sweeping the magnetic field along the crystal axes. **Fig. 4.32** shows the field dependence of $\rho_a$ at T=0.4 K for $0 < B < 33$ T applied along a, b and c axes. For B||a, the decrease in $\rho_a$ is also 1 order of magnitude, the same as that of $\rho_c$, suggesting that the reduction in both $\rho_a$ and $\rho_c$ at $B_C$ is driven by the same in-plane spin polarization. For B||b, however, $\rho_a$ decreases by 2 orders of magnitude when $B > B_C$, confirming our reasoning that the spin-polarized state is indeed not favorable for electron conduction.

A direct comparison between the field dependence of inter-plane and intra-plane resistivities at T=0.4 K for field applied along b axis is displayed in **Fig. 4.33**. The critical field $B_C$ separates two distinct behaviors. For lower applied magnetic fields before a drop in resistivity occurs i.e. $B < B_C$, $\rho_a$ ($\sim 10^{-2}$ Ω cm) is smaller than $\rho_c$ ($\sim 10^{-1}$ Ω cm). However, the opposite is true for higher applied fields i.e. $B > B_C$, with $\rho_a \sim 10^{-3}$ Ω cm and $\rho_c \sim 10^{-4}$ Ω cm. This striking behavior may reflect a change in effective dimensionality driven by B and hence an incoherent-coherent crossover[132]. In general, the electron transport along c axis in an anisotropic layered system could be either incoherent or coherent. In an incoherent transport, the electrons are scattered many times before each tunneling event as the intra-layer scattering rate ($1/\tau$) is much higher than the effective inter-layer hopping integral ($t_c$) and hence the motion from one layer to the other is rather diffusive. The band states and a Fermi velocity perpendicular to the layers cannot be defined and hence the Fermi surface is not three dimensional. In the opposite limit i.e. in a coherent state, the system behaves more 3-D like and the inter-layer transport could also be very well described by Boltzmann transport theory. Hence if the layers are coherently coupled, the electrons will change layers without significant loss in its phase due to a less scattering rate. In our case, the B driven increase in effective dimensionality, which could be analogous to that driven by temperature as detected in reference[133] and discussed in reference[134], reduces the electron correlation effects and results in the incoherent-coherent crossover. This increase of coherency is expected to enhance

itinerancy of the conduction electrons and thus a smaller inter-plane resistivity, $\rho_c$, when $B > B_C$. The crossover, if any, has a lesser impact on the intra-plane resistivity $\rho_a$.

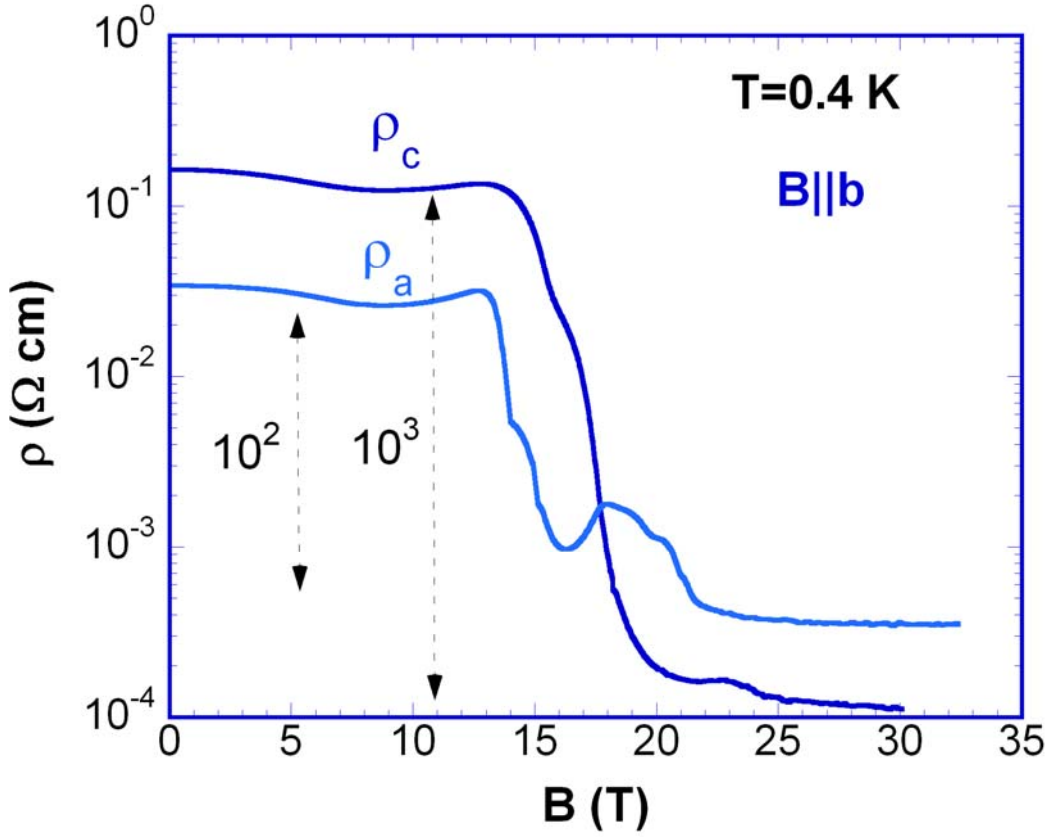


**Fig. 4.33** Magnetic field dependence of the inter-plane ($\rho_c$) and intra-plane ($\rho_a$) resistivities at T=0.4 K for $0 \leq B \leq 33$ T applied along b axis

While the abrupt, simultaneous transitions in both M and ρ shown in **Fig. 4.29** suggest a strong spin-charge coupling when B||a axis, it is also clear that the spin-polarized state can, at the most, lower the resistivity by one order of magnitude. Then, what could be the explanation for a reduction of resistivity by three orders of magnitude when B||b axis, where the spin-polarized state is destabilized? It is this issue that reflects the physics fundamentally different from that driving other magnetoresistive materials including the manganites where a spin-polarized state is essential for CMR. The results from the temperature dependence of resistivity for B||a and b axes in a wide range of magnetic field ($0 < B < 28$ T)[115] coupled with its field dependence for B||a, b and c axes[116] provide coherent and comprehensive evidence of the role of the orbital ordering. The electron kinetic energy hinges on the spin-orbital-lattice coupling in such a way that

applying magnetic field, B, along the magnetic easy axis (a axis) precipitates a spin-polarized state via a first-order metamagnetic transition. But this does not lead to a full suppression of the Mott state, whereas applying B along the magnetic hard axis (b axis) does, giving rise to a resistivity reduction of three orders of magnitude.

**4.4.8 The orbital physics:**

It becomes increasingly clear that the unconventional behavior observed in the bi-layered ruthenate is predominantly associated with the role of the orbital degree of freedom and its coupling to the spin and lattice degrees of freedom. As shown in **Fig. 4.26**, the abrupt decrease in the c-axis lattice parameter at $T_{MI}$ suggests a Jahn-Teller distortion that lifts the degeneracy of the occupied $t_{2g}$ orbitals by lowering the energy of the $d_{xy}$ orbital relative to that of the $d_{yz}$ and $d_{xz}$ orbitals and facilitates the orbital ordering.

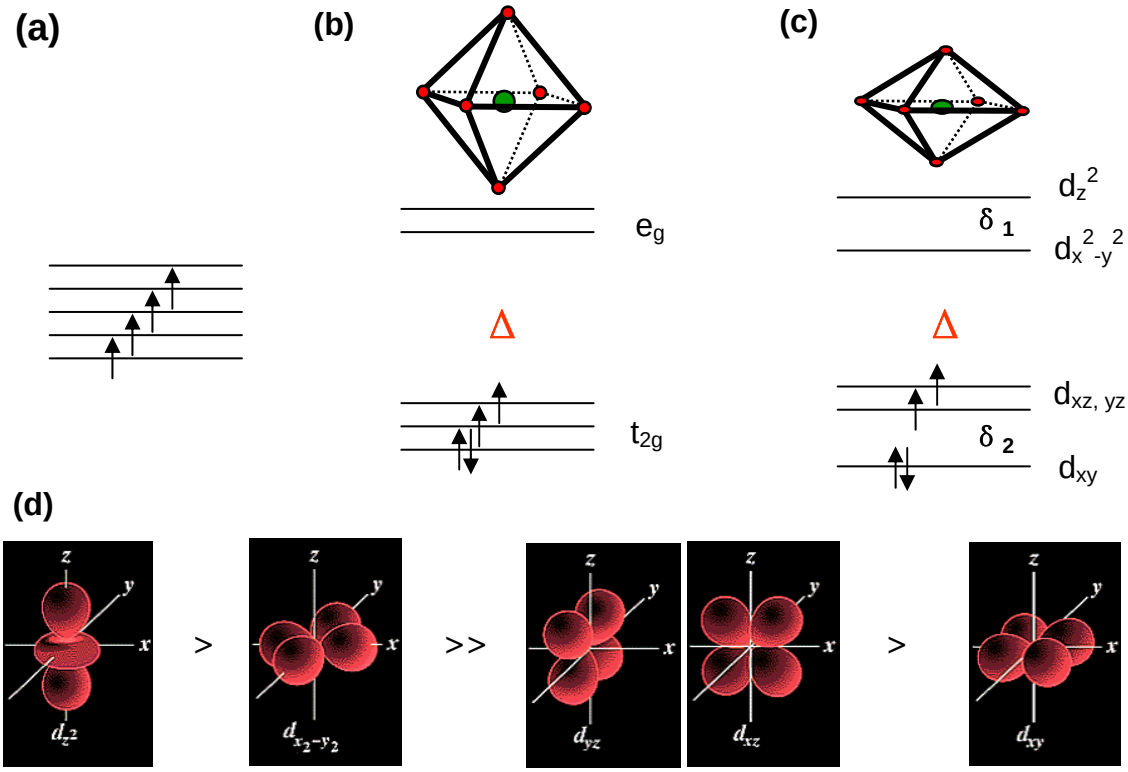


**Fig. 4.34** A schematic representation of spin configuration in $Ru^{4+}$ ion **(a)** in an isolated ion **(b)** in an octahedral field **(c)** in $Ca_3Ru_2O_7$ after Jahn-Teller distortions. **(d)** The range of energy distribution in the d orbitals after the degeneracy is being lifted by Jahn-Teller distortion.

To probe the role of orbital degrees of freedom in the observed unconventional CMR along the magnetic hard axis, a direct comparison of ρ and M would do a great favor, if done for corresponding temperatures. At low temperatures, say T=0.4 K, where we have the anomalous CMR along B||b axis, the magnetization measurements were not possible as the critical field ($B_C$= 15 T for T=0.4 K) does not fall within the limitations of a SQUID magnetometer. For achieving this comparison, we performed magnetic and electron transport measurements in the selected temperature range 40 < T < 56 K, for which $B_C$ along both a and b axes falls within the range of using a SQUID magnetometer. Shown in **Fig. 4.35** are M (top panel) and $\rho_c$ (bottom panel) as a function of B for B||a (left panel) and B||b (right panel) within the chosen temperature range, 40 < T < 52 K. **Fig. 4.35 (a)** displays M as a function of B for B||a axis. At 40 K, M(B) is still very similar to the one at low temperatures (see **Fig. 4.23**) but with slightly lower saturation moment, $M_S$ (= 1.6$\mu_B$/Ru) and critical field, $B_C$ (= 5.8 T). For 41 < T < 45 K, a second transition develops at $B^* > B_C$, suggesting an intermediate FM state for $B_C < B < B^*$, which is not fully polarized along a axis. One possible interpretation could be that the spins are rotating away from a axis due to a strong magnetoelastic coupling as a result of the change in c axis lattice parameter near $T_{MI}$ (see **Fig. 4.26**). Hence a stronger field is required to realign these spins along a axis[116]. Since the spin rotation tends to become stronger as T approaches $T_{MI}$, $B^*$ increases with T. At $B_C$, M is about 1 $\mu_B$/Ru and increases by 0.6 $\mu_B$/Ru at $B^*$. Only half of the ordered spins are thus aligned with a axis in the spin reorientation (SR) region for $B_C < B < B^*$. $B_C$ decreases with T and vanishes near $T_N$=56 K.

Unlike for B||a axis, M for B||b axis is unsaturated at $B > B_C$ and rounded at $B_C$ without hysteresis, suggesting a second-order transition (see **Fig. 4.35 (b)**). Noticeably, the b axis M at 7 T always converges to 1 $\mu_B$/Ru, which is corresponding to 50% spin polarization and is independent of T. Clearly, $M_S$ for B||b axis is always smaller than that for B||a axis in spite of the spin reorientation that partially enhances M for B||b axis.

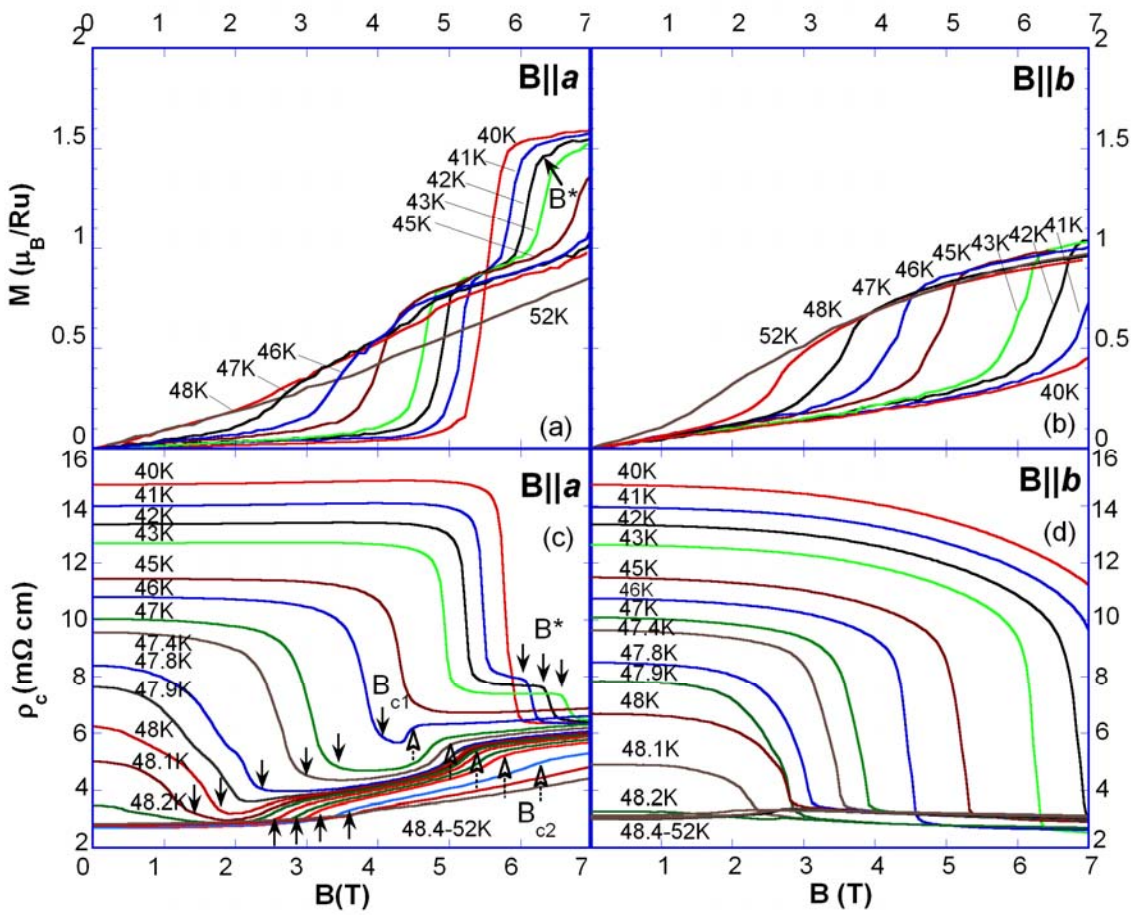


**Fig. 4.35** Isothermal magnetization, M (B), for field applied parallel to **(a)** a axis and **(b)** b axis for temperature range $40 \leq T \leq 52$ K. Magnetic field dependence of inter-plane resistivity ($\rho_c(B)$) when field applied along **(c)** a axis and **(d)** b axis in the same temperature range.

The corresponding $\rho_c$ as a function of B for B||a and b axes are displayed in **Figs. 4.35 (c)** and **(d)** respectively. For B||a axis, $\rho_c$ at 40 K shows an abrupt drop at $B_C$ similar to that at low temperatures with a magnetoresistance ratio $\Delta\rho/\rho(0) = 58\%$, where $\Delta\rho=\rho(7T) - \rho(0)$. In the range $41 < T < 45$ K, $\rho_c$ for B||a decreases initially at $B_C$, and then further at $B^*$ with a total $\Delta\rho/\rho(0)$ similar to that at 40 K. Clearly, for $T < 45$ K, $\rho_c$ perfectly mirrors the behavior of M for B||a axis, suggesting a strong spin-charge coupling in this region[116]. However, for $T > 46$ K, a valley develops in $\rho_c$; the beginning and the end of this valley define two fields, $B_{C1}$ ($B_{C1} = B_C$ for $T < 46$ K) and $B_{C2}$. The valley broadens with increasing T ($B_{C1}$ decreases with T, while $B_{C2}$ increases). The critical fields $B_{C1}$ and $B_{C2}$ for different temperatures are tabulated in **Table 4.2**.

**Table 4.2** *$B_{C1}$ and $B_{C2}$ in $Ca_3Ru_2O_7$ for various temperatures when B||a axis*.

| S. No. | T (K) | $B_{C1}$ (T) | $B_{C2}$ (T) |
|---|---|---|---|
| 1 | 45.0 | 4.42 | 4.42 |
| 2 | 46.0 | 3.96 | 4.53 |
| 3 | 47.0 | 3.28 | 4.80 |
| 4 | 47.4 | 2.93 | 5.02 |
| 5 | 47.8 | 2.31 | 5.20 |
| 6 | 47.9 | 2.04 | 5.31 |
| 7 | 48.0 | 1.82 | 5.36 |
| 8 | 48.1 | 1.53 | 5.42 |
| 9 | 48.2 | 0.80 | 5.47 |
| 10 | 48.4 | 0 | 5.68 |

The valley changes its shape for T > 48.2 K, where the slope at $B_{C1}$ is now positive and $B_{C1}$ increases with T. An important point is that the field dependence of $\rho_c$ for 46 < T < 52 K does not track the field dependence of M (compare **Figs. 4.35 (a)** and **(c)**). This lack of parallel behavior of M and $\rho_c$ is precisely a manifestation of the crucial role of the orbital degrees of freedom that dictates the electron hopping mechanism for B||a[116].

Furthermore, $M_S$ for B||b axis (**Fig. 4.35 (b)**) is always smaller than $M_S$ for B||a axis (**Fig. 4.35 (a)**) and yet the reduction in $\rho_c$ for B||b axis (**Fig. 4.35 (d)**) is always much larger than that for B||a axis (**Fig. 4.35 (c)**). For example, at 42 K and 7 T, $\Delta\rho/\rho(0)$ = 50% with $M_S$ = 1.52 $\mu_B$/Ru for B||a, and $\Delta\rho/\rho(0)$ = 80% with $M_S$ = 1.03 $\mu_B$/Ru for B||b. Note that the difference in both $M_S$ and $\Delta\rho/\rho(0)$ between B||a and b axes is 35%[116].

The temperature dependence of M (left scale) and $\Delta\rho/\rho(0)$ at 7 T (right scale) for B||a and b axes is summarized in **Fig. 4.36 (a)**. Such an inverse correlation between M and $\Delta\rho/\rho(0)$ suggests that the spin-polarized state is indeed detrimental to the CMR. For T > $T_{MI}$, the metallic state is recovered for B < $B_{C1}$. However, for B > $B_{C2}$, applying B along a axis leads to a rapid increase in $\rho_c$ with positive $\Delta\rho/\rho(0)$ reaching as high as 112%, whereas applying B along b axis results in essentially no changes in $\rho_c$.

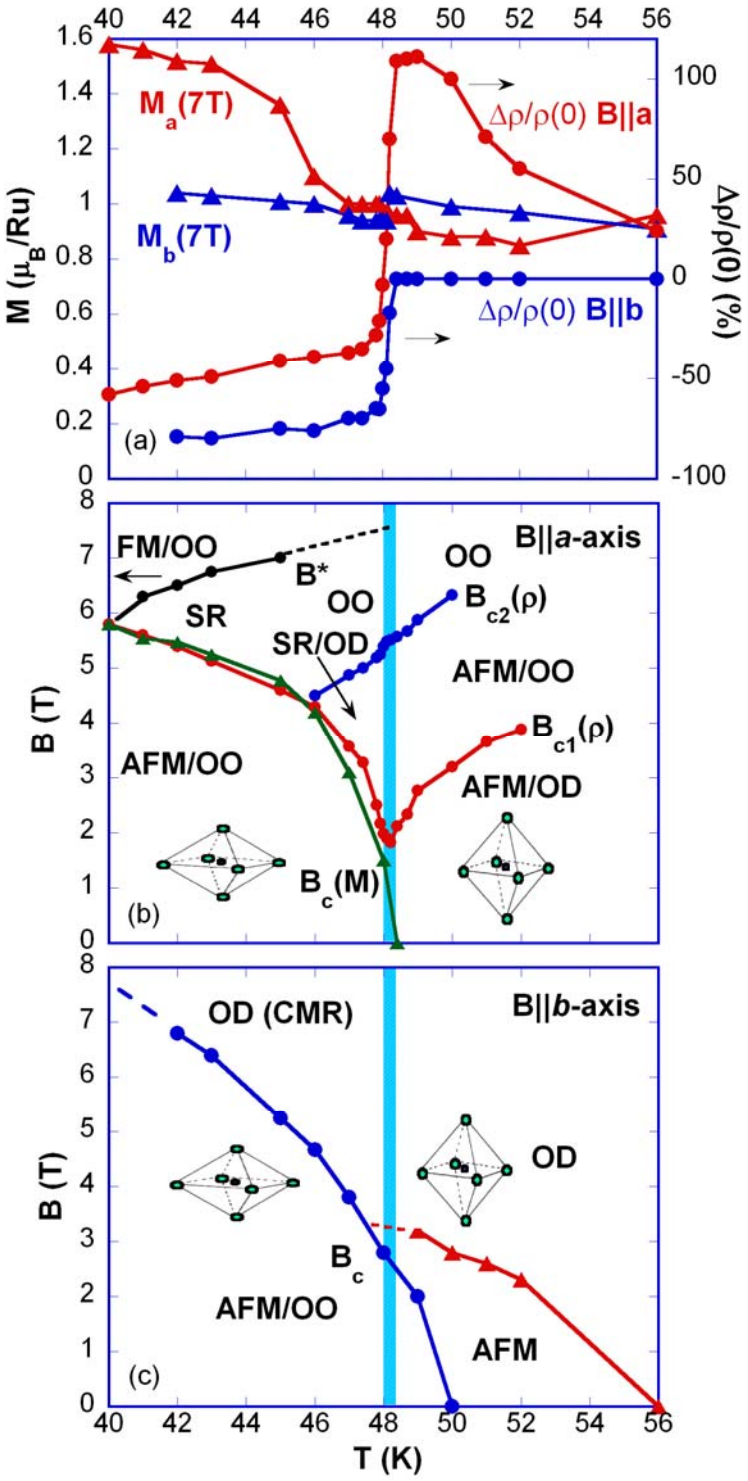


**Fig. 4.36 (a)** Temperature dependence of M (*triangles*) and Δρ/ρ(0) (*solid circles, right scale*) at 7 T for B||a and b axes. **(b), (c)** Phase diagrams plotted as B vs T summarizing various phases for B||a and b axes, respectively.

As is known, for B<6 T, the Mott-like state is due to the OO facilitated by the c-axis shortening at $T_{MI}$[126, 128]. When B||a >6 T, the magnetic state becomes FM with the OO remained and stabilized by the FM state. The orbital order is either a ferro-orbital (FO) or an antiferro-orbital (AFO) configuration. Hence the system is in either a FM-FO or a FM-AFO state. The former inhibits the hopping of the 4d electrons because of Pauli Exclusion Principle, while the latter permits inter-site transitions but at the expense of Coulomb energy. Therefore, despite showing one order of magnitude drop in $\rho_c$ due to the spin polarization when B > 6 T, a fully metallic state can never be reached for B||a axis. In fact, the linear increase in $\rho_c$ with increasing B for B||a > 6 T, as shown in **Fig. 4.31**, may manifest a strengthened OO via the enhanced FM state. Conversely, applying B along b axis steadily suppresses the AFM state[128], removing the orbital order through spin-orbit interaction when $B > B_C$. Such an orbitally disordered (OD) state drastically increases the electron mobility, therefore leading to CMR. On the other hand, applying B along the c axis has a noticeable impact on spin and orbital configurations for B > 35 T where $\rho_c$ drops rapidly and becomes much smaller than $\rho_c$ for B||a axis[116]. This suggests that the electronic state for B||a axis is the most resistive one.

The magnetic and transport behavior shown in **Fig. 4.35** is remarkably consistent with rapid changes of the Ru-O phonon frequency with B seen in Raman studies (**Fig. 2 (b)** in reference[126]), providing complementary evidence for the evolution of the field-induced magnetic and orbital phases. While applying B along b axis clearly favors CMR, applying B||a axis generates a rich phase diagram (see **Figs. 4.36 (b)** and **(c)**). As shown in **Fig. 4.36 (b)** (note that $B_{C1}(\rho)$ and $B_{C2}(\rho)$ indicate the curves generated based on ρ, and $B_C(M)$ based on M), below 40 K, B drives the system from an AFM-OO to a FM-OO state, and for 40 < T < 48 K the system enters a region of SR characterized by $B_C$ and B. For 46 < T < 48.2 K, the valley seen only in $\rho_c$ signals an onset of an OD state at $B_{C1}$ and then a reoccurring OO state at $B_C$ characterized by a sharp increase in $\rho_c$. For 48.2 < T < 56 K, the system changes from an AFM-OD to an AFM-OO phase when $B > B_{C1}$. The evolution of the magnetic orbital configuration is associated with the Jahn-Teller coupling, which appears in the vicinity of $T_{MI}$.

### 4.4.9 Shubnikov-de Haas oscillations:

Oscillatory magnetoresistance periodic in 1/B or Shubnikov-de Haas effect is a manifestation of oscillations of the density of states at the Fermi surface due to the Landau level quantization. Hence observations of the SdH effect are possible in metals where the carrier mean-free path is sufficiently long and resistivity is sufficiently low. For most of the oxides, the resistivity is much higher and the mean-free paths may be comparable to the lattice spacing, hence observations of the SdH effect are not common. Given such a nonmetallic state at lower temperatures in $Ca_3Ru_2O_7$ (see **Fig. 4.23**), the quantum oscillations in $\rho_c$ is unexpectedly observed when B is applied parallel to c and rotated within the ac plane. However, the anisotropic nature of the Fermi surface dictates a diverse nature in the oscillations along these directions.

Orbital ordering can be effectively manipulated, and therefore probed via altering the spin-orbit coupling. It is this understanding that has motivated our further investigations on this system by measuring magnetoresistance oscillations with B applied along different orientations. In the preceding sections, I discussed the results on the inter-plane resistivity for magnetic field applied parallel to a and b axes. In this section, I present inter-plane resistivity, $\rho_c$, with B rotating within the ac-plane for temperatures ranging from 0.4 K to 1.5 K and magnetic field B up to 45 T. The results reveal slow yet strong SdH oscillations in the ac-plane with frequencies ranging from 30 to 117 T. These oscillations are highly angular dependent and intimately correlated with a fully spin-polarized ferromagnetic state.

**Fig. 4.37** shows the magnetic field response of the $\rho_c$ at T=0.6 K when B is swept from a to c axis, $0 < \theta < 90^o$ in the field range, $0 < B < 32$ T, where $\theta$ is the angle between the magnetic field and a axis. For $\theta=90^o$ i.e. when B||c axis, oscillations in resistivity are observed as reported by G Cao et.al.[115] in the absence of metamagnetism, signaling the existence of very small Fermi surface cross sections. Local density approximation calculations[135] for $Sr_3Ru_2O_7$, which shares common aspects with $Ca_3Ru_2O_7$, find the Fermi surface very sensitive to small structural changes. In particular, the $d_{xy}$ orbitals give rise to small lens shaped Fermi surface pockets. The observed oscillations must then be associated with the motion of the electrons in the ab plane, i.e., with the $d_{xy}$ orbitals. The oscillations in $\rho_c$ correspond to extremely low frequencies $f_1$=28

T and $f_2$=10 T. Based on crystallographic data[136] and the Onsager relation $F_0=A(h/4\pi^2e)$ (e is the electron charge, h is Planck constant), these frequencies correspond to a cross-sectional area of only 0.2% of the first Brillouin zone. From the T dependence of the amplitude, the cyclotron effective mass is estimated to be $\mu_c$ = (0.85±0.05) $m_e$. This is markedly smaller than the enhanced thermodynamic effective mass (~3) estimated from the electronic contribution $\gamma$ to the specific heat[83, 112]. There are two possible sources for this discrepancy: (1) The cyclotron effective mass is measured in a large magnetic field that quenches correlations, while the specific heat is a zero-field measurement and (2) $\mu_c$ only refers to one closed orbit, while the thermodynamic effective mass measures an average over the entire Fermi surface. In addition, the Dingle temperature $T_D=h/4\pi^2k_B\tau$, a measure of scattering, is estimated to be 3 K[117], comparable to those of good organic metals.

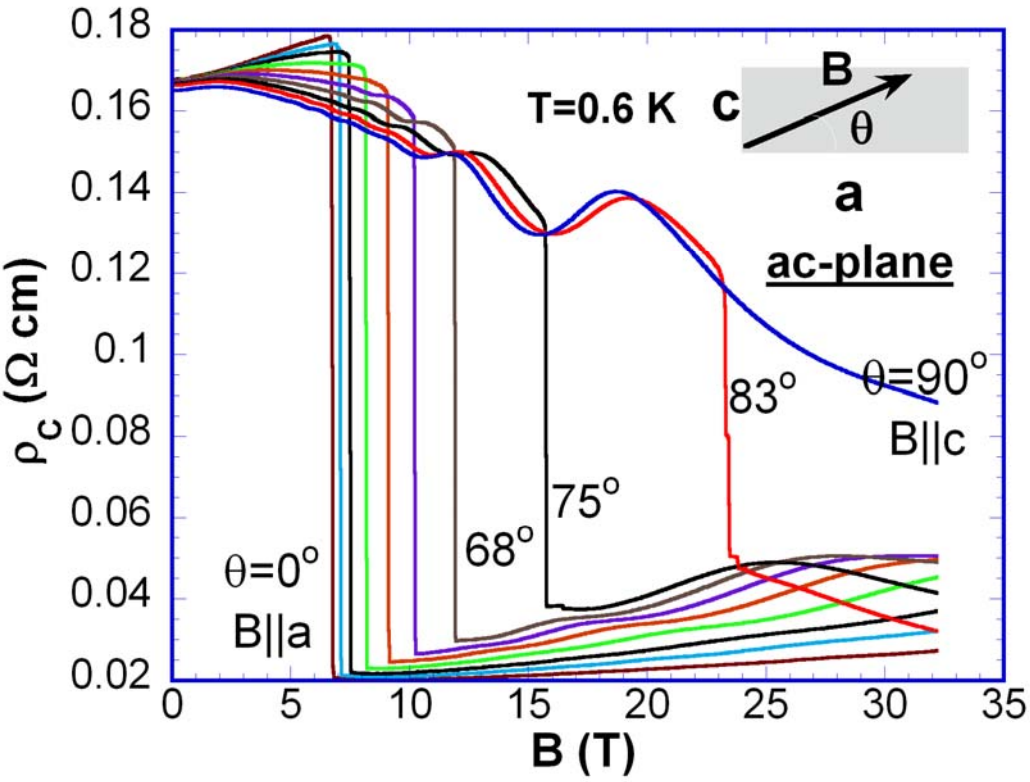


**Fig.4.37** $\rho_c$ as a function of B for field applied along different angles in the ac plane at T=0.6 K[115].

When the magnetic field is rotated away from c axis, there is a precipitous drop in $\rho_c$ which gets up to one order of magnitude at B=$B_C$ when B||a axis (refer to section 4.4.6

for explanations on the first order transition for B||a). However, my focus in this section will remain on the region away from both a and c axes for $B > B_C$, where SdH oscillations reappear for $11 < \theta < 49^o$ in the ac plane. These oscillations inherit a vastly different behavior than that observed along the c axis as explained in the following paragraphs.

The field dependence of $\rho_c$ (on a logarithmic scale) for B rotating in the ac plane (B||a axis $\theta$=0° and B||c axis $\theta$=90°) at T=0.4 K is shown in **Fig. 4.38 (a)** for B ranging from 11 to 45 T. $B_C$ occurs at 6 T for B||a axis, and increases with increasing $\theta$, i.e., as B rotates towards c axis. The striking finding is that strong SdH oscillations are qualitatively different for $11° < \theta < 56°$ and $56° < \theta < 90°$. It is then likely that the vicinity of $\theta$=56° marks the onset of the melting of the OO state as B rotates further away from the easy axis of magnetization (a axis)[117]. This destabilizes the FM state, and thus the OO state via direct coupling to the field or the spin-orbit interaction. However, this is only possible perturbatively, because the spin-orbit interaction is quenched by crystalline fields. Consequently, the electron mobility increases drastically, explaining the largely enhanced conductivity for $56° < \theta < 90°$.

For $\theta < 56°$ the strong oscillations occur only for $B > B_C$ and with frequencies significantly larger than the ones previously observed for B||c axis. For clarity, the data has been reproduced in **Fig. 4.38 (b)** that exhibits $\rho_c$ on a linear and enlarged scale for $B > B_C$. For $0° < \theta < 56°$ and $B > B_C$, $\rho_c$ increases with both B and $\theta$, and displays oscillatory behavior only for $11° < \theta < 56°$. While the extremal orbits responsible for the oscillations are facilitated by the FM state, it is remarkable that no oscillations are seen when $\theta=0^o$ (B||a axis), where the FM state is fully established at $B_C$=6 T. In contrast, no oscillations were discerned for B rotating within the bc plane at B up to 45 T[117]. The bc plane is perpendicular to the easy axis of magnetization and has no FM component[115, 137], suggesting a critical link of the SdH oscillations to the fully polarized FM state. The FM and the different projections of the tilt angles of the $RuO_6$ octahedra onto the ac and bc planes[136] are expected to affect the Fermi surface.

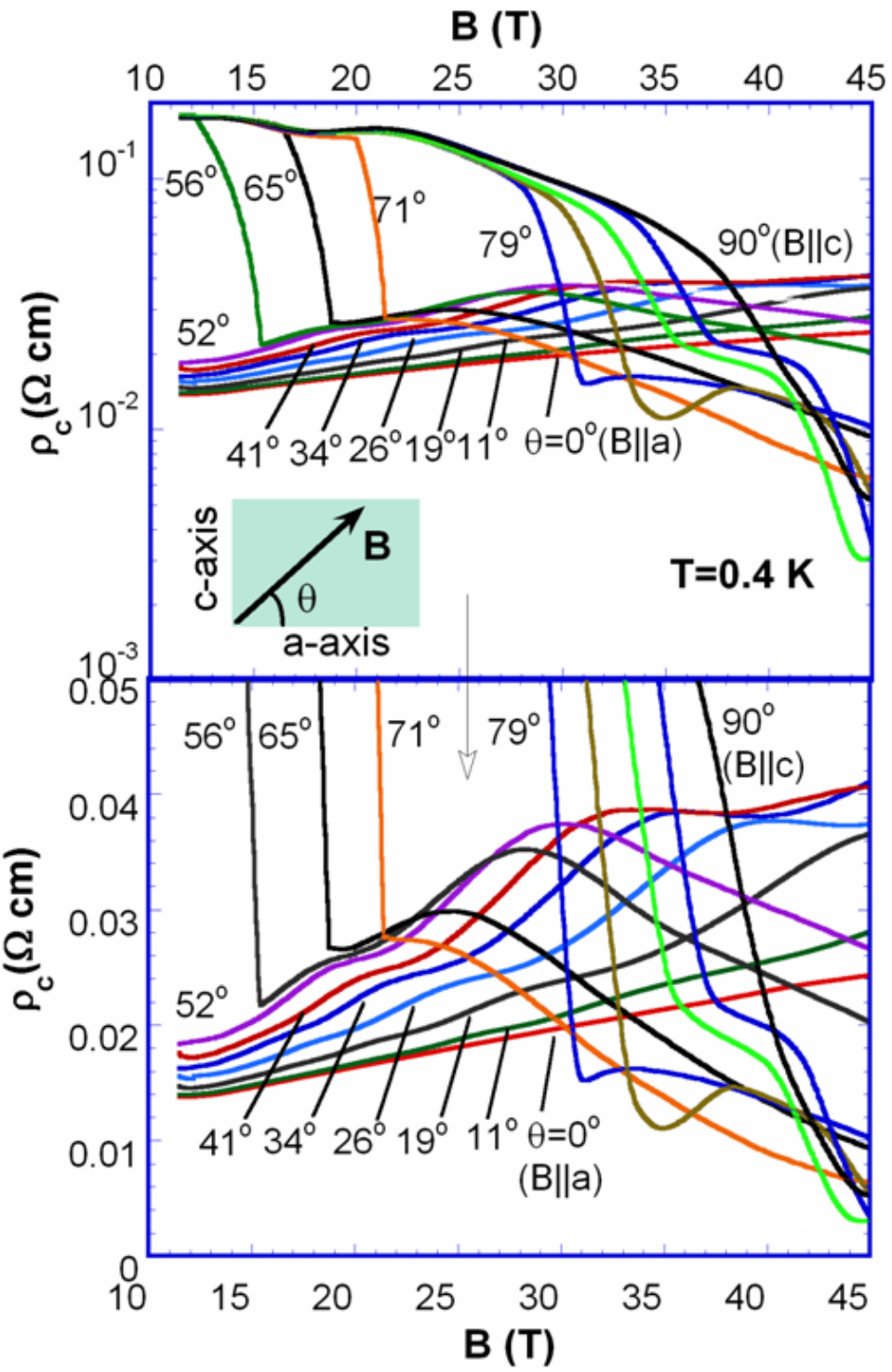


**Fig. 4.38 (a)** $\rho_c$ for B rotating in the ac-plane with θ=0 and 90° corresponding to B||a and B||c, respectively; **(b)** Enlarged $\rho_c$ for clarity. Note that $\rho_c$ is in logarithmic scale in **(a)** and B changes from 11 to 45 T in both **(a)** and **(b)**.

On the other hand, for $56° < \theta = 90°$, the oscillations disappear for $B > B_C$ but are present for $B < B_C$, accompanying the much more conducting phase at high fields, as shown in **Figs. 4.38 (a)** and **(b)**. The frequency of the oscillations seen for $B < B_C$ remains essentially unchanged with theta for $65° < \theta < 90°$. Since the $d_{xy}$ orbitals are believed to be responsible for the oscillations along B||c axis, the nearly constant frequency upon tilting of B suggests that the oscillations in the absence of the metamagnetism originate from a nearly spherical pocket of the same $d_{xy}$ orbitals. Conversely, the oscillations for $11° < \theta < 56°$ and $B > B_C$ could be associated with a configuration of the FM state and ordered $d_{zx}$ and/or $d_{yz}$ orbitals. These orbitals offer only limited electron hopping (as confirmed by a larger $\rho_c$), and thus lower density of charge carriers and longer mean free path which in turn facilitates electrons to execute circular orbits[117].

**Fig. 4.39** shows the amplitude of the SdH oscillations as a function of 1/B for several representative $\theta$ at T=0.4 K (**Fig. 4.39 (a)**) and 1.5 K (**Fig. 4.39 (b)**). The SdH signal is defined as $\Delta\rho/\rho_{bg}$, where $\Delta\rho=(\rho_c - \rho_{bg})$ and $\rho_{bg}$ is the background resistivity. $\rho_{bg}$ is obtained by fitting the actual $\rho_c$ to a polynomial. The Fast Fourier Transformation (FFT) yields the same frequencies as those determined from **Figs. 4.39 (a)** and **(b)**.

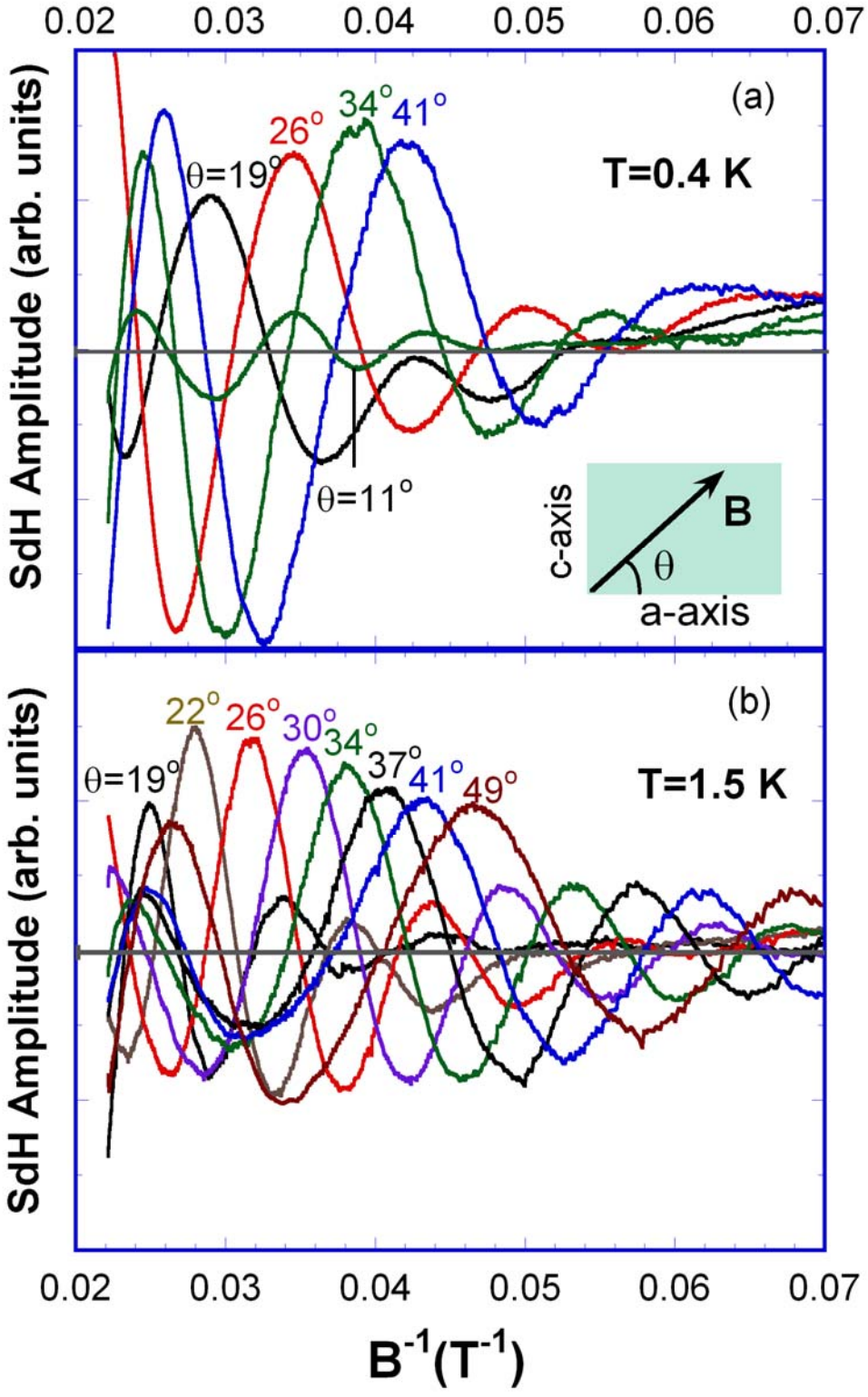


**Fig. 4.39** The amplitude of the quantum oscillations as a function of inverse field, $B^{-1}$ for various θ and for **(a)** T=0.4 and **(b)** 1.5 K.

The result from the FFT is shown as **Fig. 4.40** for a representative $\rho_c$ at T=1.5 K and θ=26°. Clearly, the oscillations are strong and slow, and their phase and frequency shift systematically with changing θ. The oscillations vanish for θ > 56°, suggesting that the extremal cross section responsible for the oscillations is highly susceptible to the orientation of B. SdH oscillations are usually rather weak in metals[130]; the remarkably strong oscillatory behavior for 11° < θ < 56° may arise from an extremal orbit with a flat dispersion perpendicular to the cross section, so that a large constructive interference can occur. It is also noted that the 1/cosθ-like behavior seen in **Figs. 4.39 (a)** and **(b)** may imply the cylindrical Fermi surface elongated along the c axis, which favors the two-dimensional conductivity. With further increasing θ (=56°), the impact of B on the Fermi surface becomes even more dramatic and the closed orbit is no longer observed. The closed orbit is possibly replaced by open ones that do not contribute to oscillations.

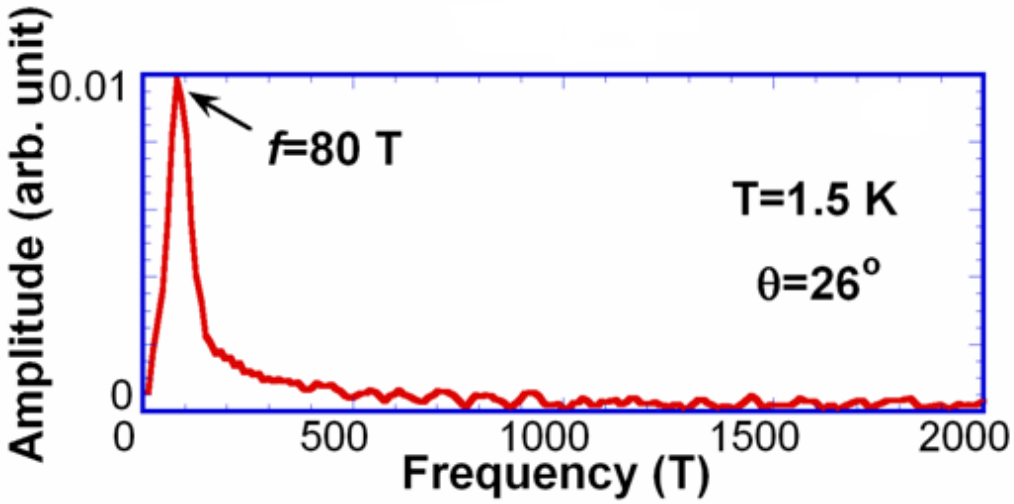


**Fig. 4.40** Estimation of frequency of oscillations using FFT for a particular temperature and angle (1.5 K and 26° away from a axis)

**Fig. 4.41** illustrates the angular dependence of the SdH frequency for T=0.4 and 1.5 K (left scale) and $B_C$ (right scale). The unusual feature is that the frequency is temperature dependent, increasing about 15% when T is raised from 0.4 to 1.5 K. The frequency for B > $B_C$ rapidly decreases with increasing θ and reaches about 45 T in the vicinity of θ=56°, whereas the frequency for B < $B_C$ stays essentially constant for θ > 56°. The oscillations become difficult to measure in the vicinity of $B_C$. This is expected if $B_C$ is associated with the melting of OO. The frequencies for B > $B_C$ are significantly larger

than those for $B < B_C$, suggesting the former oscillations either originate from different electron orbits or a restructured Fermi surface[117]. The angular dependence of $B_C$, on the other hand, is rather weak for $\theta < 56°$ but becomes much stronger for $\theta > 56°$. Note that $\rho_c$ displays a weak plateau at high magnetic fields and $\theta$ approaching 90°, which disappears for the B||c axis because the FM state is no longer energetically favorable. Such an inverse correlation between the frequency and $B_C$ reinforces the point that the FM state reconstructs the Fermi surface and facilitates the oscillatory effect. It is evident that the vicinity of $\theta$=56° or $52 < \theta < 65°$ marks a crossover region between the FM-OO state and the orbital degenerate (OD) state as shown in **Fig. 4.41**.

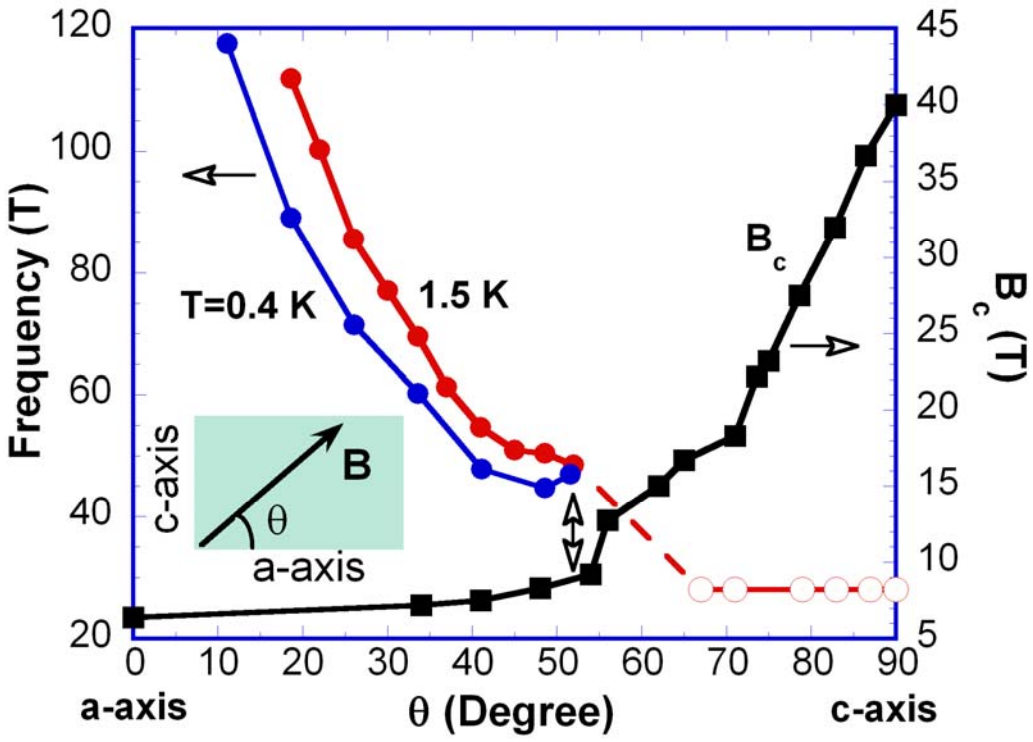


**Fig. 4.41** The angular dependence of the frequency (solid circles for $B > B_C$, and empty circle for $B < B_C$) for T=0.4 K and 1.5 K and the metamagnetic transition $B_C$ (solid squares) (*right scale*).

### 4.4.10 Oscillatory magnetoresistance periodic in B

For B||(110), $\rho_c$ also shows oscillations in the magnetoresistance as displayed in **Fig. 4.42**. The striking behavior is that these oscillations are periodic in B, instead of 1/B, with a period of $\Delta B$=11 T and persistent up to 15 K. This highly unusual observation is corroborated by plotting the data both as a function of 1/B (**Figs. 4.42 (a)** and **(b)**) and B

(**Figs. 4.42 (c)** and **(d)**). The oscillations die off rapidly, if B slightly departs from the (110) direction (within ±5°).

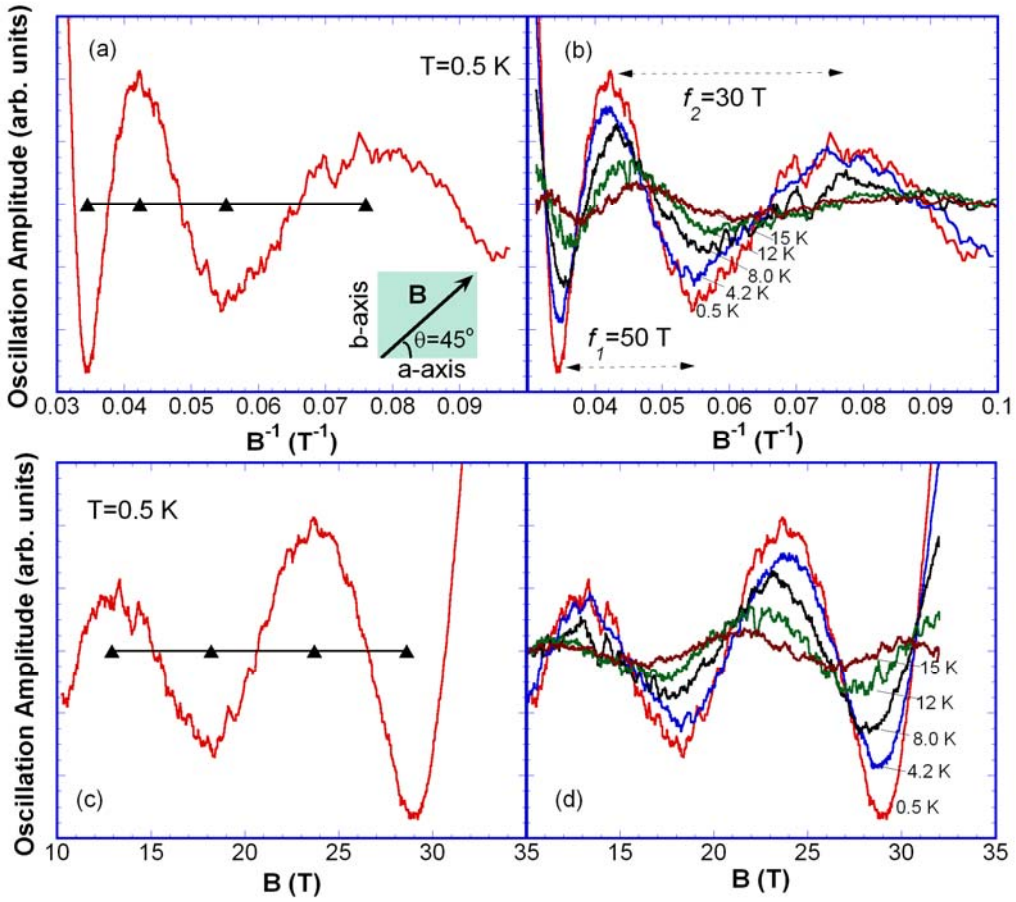


**Fig. 4.42 (a)** The amplitude of the quantum oscillations as a function of B for B||[110] and T=0.5 K and **(b)** for various temperatures up to 15 K. **(c)** The amplitude of the quantum oscillations as a function of inverse field $B^{-1}$ for B||[110] and T=0.5 K and **(d)** for various temperatures up to 15 K.

Oscillations in the magnetoresistivity periodic in 1/B (SdH effect) are a manifestation of the constructive interference of quantized extremal orbits of Fermi surface cross sections perpendicular to the field. Due to the Pauli principle the electrons are bound to follow the Fermi surface. The projection of the real space trajectory of a free electron onto a plane perpendicular to B reproduces the k-space trajectory rotated by π/2 and scaled by a factor cℏ/|e|B. Hence, trajectories with constructive interference in real space are expected to be periodic in B rather than 1/B. Oscillations in the magnetoresistivity periodic in B are realized in some mesoscopic systems and always

related to finite size effects. Examples are (i) the Aharanov-Bohm (AB) effect[130, 138, 139], (ii) the Sondheimer effect[130, 140] and (iii) the edge states in quantum dot[141]. Each of the cases shares a common feature in them: a geometrical confinement. The AB interference occurs when a magnetic flux threading a metallic loop changes the phase of the electrons generating oscillations in the magnetoresistance and is observed only in mesoscopic conductors, but not in bulk materials. The Sondheimer effect requires a thin metallic film with the wave function vanishing at the two surfaces. The thickness of the film has to be comparable with the mean free path. This gives rise to boundary scattering of the carriers that alters the free electron trajectories and the possibility of interference. Finally, the edge states require a quantum Hall environment with real space confinement[141].

Since the bulk material has no real space confinement for the orbits of the carriers, the most likely explanation for the periodicity as a function of B is a Fermi surface cross section that changes with field. The $t_{2g}$ orbitals have off-diagonal matrix elements with the orbital Zeeman Effect, and hence couple directly to the magnetic field. Consequently, the magnetic field could lead to a dramatic change of the Fermi surface if it points into a certain direction. Note that the pockets involved are very small and susceptible to external influences. If there is more than one conducting portion of the Fermi surface, occupied states can be transferred from one pocket to another with relatively small changes in the external parameters. This is also consistent with the 15% of change in the frequency when T is raised from 0.4 to 1.5 K[117] shown in **Fig. 4.41**. Indeed, the amplitude of the oscillations follows the Lifshitz- Kosevich behavior expected for SdH oscillations (see **Fig. 4.43**). It is noted that the AB effect at finite T would show the same amplitude dependence[142]. What is still perplexing is that the cross section of the observed pocket is only 0.2% of the Brillouin zone, so the position of the Fermi energy is fixed at the non-quantized level of other Fermi surface branches. In such a situation, the density of states oscillates only against 1/B. In addition, if the origin of the oscillations periodic in B is ascribed to the Landau quantization, it is then perplexing as to why there are no SdH oscillations in the (110) direction, together with the oscillations periodic in B.

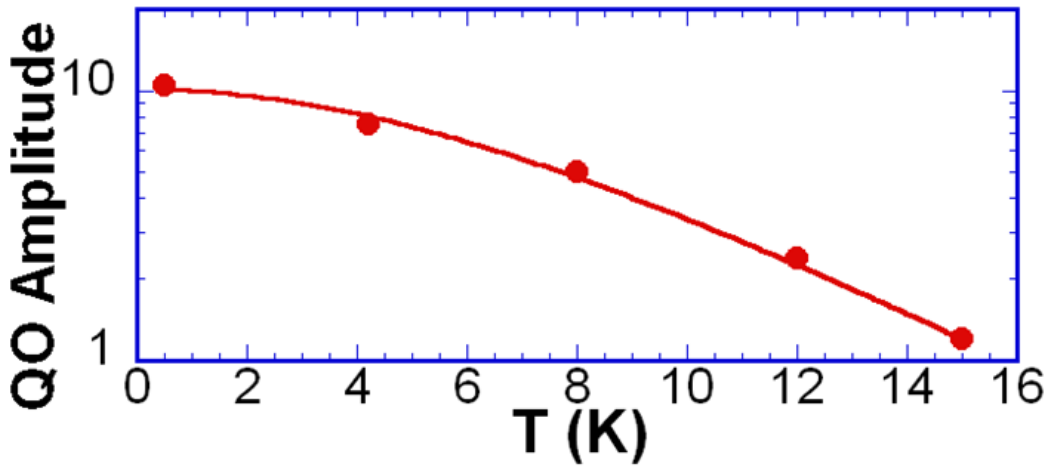


**Fig. 4.43** The amplitude of the quantum oscillations for various temperatures up to 15 K.

The observations of the magnetoresistance oscillations in $Ca_3Ru_2O_7$ periodic both in B and 1/B reflect the crucial dependence of the quantized orbits on the orientation of B. The novel phenomena highlight the critical role of the orbital degrees of freedom embodied via the coupling of the $t_{2g}$ orbitals to the magnetic field. Not long ago, a theoretical study using the Hubbard model with Coulombic and phononic interactions predicts the existence of a ferromagnetic orbital ordered state and colossal magnetoresistance in the ruthenates[143]. The phase diagram generated in this study shows that the ferromagnetic orbital ordered state is stabilized when both the inter-orbital Coulomb interaction and the phonon self-trapping energy are sufficiently strong. The study also suggests a possible colossal magnetoresistive behavior due to a strong competition between ferromagnetic and antiferromagnetic states. The general agreement between the theoretical and experimental results further validates the crucial role of the orbital ordering in driving the complex phenomena.

**4.4.11 Non-linear conduction:**

The orbital ordered state might also be manifested by a possible density wave below $T_{MI}$. A resistivity measurement performed by G Cao et.al.[128] revealed a non-ohmic behavior above the threshold field, $E_T$, which suggests sliding density wave transport[144]. The onset of the nonlinear conduction is also evidenced by the current-voltage (I-V) characteristic discussed in the reference[128]. An S-shaped nonlinear behavior is observed at B=0, but the rapidly increasing resistivity with decreasing temperature below $T_{MI}$ creates ambiguity due to possible self-heating. However, convincing discussions are

provided in the reference[128] that the non-linear conduction is intrinsic and not due to self heating. Nevertheless, the formation of the density wave below $T_{MI}$, although subject to a thorough investigation, would provide additional evidence for the existence of the orbital-ordered state brought about by the highly anisotropic spin-lattice-orbital coupling.

RP Guertin et.al.,[118] have also reported a non-Ohmic d.c. current-voltage characteristics in $Ca_3Ru_2O_7$, including negative differential resistivity (NDR) for all $T < T_{MI} = 48$ K. A more common form of NDR is seen in "N" shaped characteristics, e.g. the Gunn Effect[145] or the Esaki (Tunnel) diode[146]. A current induced promotion of the carriers from a high to low mobility band facilitates the NDR in such cases. The "S"-NDR in $Ca_3Ru_2O_7$ might be a result of polarons that gets localized for $T < T_{MI}$. Given the low dimensionality of the bi-layered structure, a polaronic charge density wave (CDW) may begin to propagate above a critical current bias[144] causing the S-NDR. The non-Ohmic behavior shown in **Fig. 2** of reference[118] is a property associated exclusively with the AFM-I phase of $Ca_3Ru_2O_7$, not the AFM-M phase. Not only is the effect quenched at zero field for $T > T_{MI} = 48$ K (**Fig. 2**), but it is also quenched when a magnetic field of sufficient magnitude and orientation is applied above that needed to switch the system from the AFM-I phase to the field induced ferromagnetic metallic phase.

**4.4.12 Sensitivity of $Ca_3Ru_2O_7$ to chemical doping:**

One of the critical characteristics of the bi-layered calcium ruthenate is its sensitivity to the oxygen content. Its ground state is very sensitive to the oxygen treatment as is evident from the temperature dependence of electrical resistivity for as grown and oxygenated samples in **Fig. 4.44**. The temperature dependence of the resistivity for the oxygen-rich $Ca_3Ru_2O_7$ i.e. $Ca_3Ru_2O_{7+\delta}$ shows a similar metallic nature as that of the as grown compound for temperatures higher than $T_N$. But what is distinguished is the response of the resistivity at lower temperatures. The electrons pretend to follow the same trend as that of the $Ca_3Ru_2O_7$ immediately after the AFM ordering ($T_N$) to falter soon by choosing to show the opposite behavior for further lower temperatures. At T=30 K, the resistivity curve displays a down turn and indicates a brief metallic behavior in the temperature range $1.7 < T < 30$ K. The metallic behavior can be readily induced by other impurity doping, such as La[136], also confirming that the observed metallic behavior is an impurity induced one. Hence it will not be fair to claim

the observed metallic state at lower temperatures to be an intrinsic property of the stoichiometric $Ca_3Ru_2O_7$ as reported in reference[147].

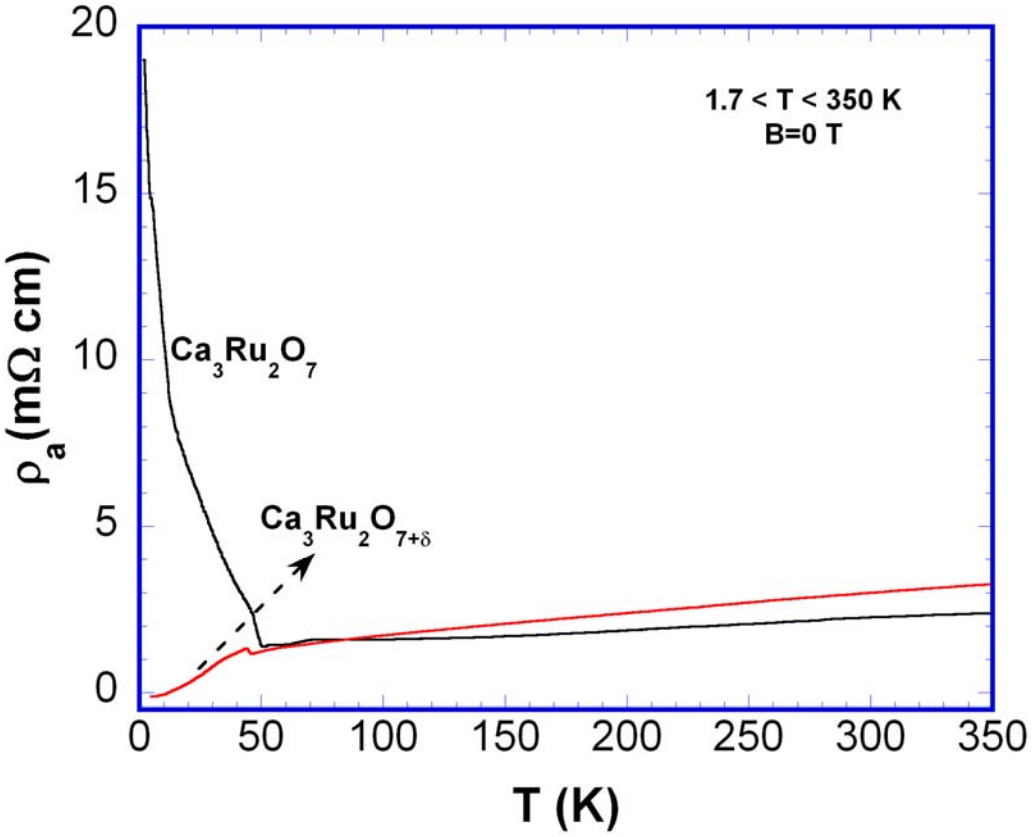


**Fig. 4.44** Temperature dependence of a axis resistivity, $\rho_a(T)$, for as grown ($Ca_3Ru_2O_7$) and oxygenated ($Ca_3Ru_2O_{7+\delta}$) samples.

Substituting iso-electronic Sr for Ca in $Ca_3Ru_2O_7$ broadens the $T_N$ whereas the magnitude decreases slowly with Sr concentration. As x is increased in $(Ca_{1-x}Sr_x)_3Ru_2O_7$, the magnetization becomes almost isotropic in the ab plane suggesting that the $RuO_6$ octahedra are untilted as in pure $Sr_3Ru_2O_7$. Moreover, the temperature dependence of resistivity shows a transition from metallic to non-metallic state in the temperature range $48 < T < 56$ K and washes out the AFM-M region, a unique feature of $Ca_3Ru_2O_7$. The heat capacity measurements done on the single crystals of Sr substituted $Ca_3Ru_2O_7$ shows the magnetic transition at $T_N$, which is roughly mean field in shape[148]. However, the difference in specific heat at the transition is too large for an itinerant electron spin-wave picture and too small for associating the transition with the ordering of localized spins.

Very dilute doping of trivalent La[136] (≤ 5%) for divalent Ca in $Ca_3Ru_2O_7$ prompts rapid and simultaneous changes in both the magnetic and transport properties. The AFM-M phase persists in $(Ca_{1-x}La_x)_3Ru_2O_7$ up to x=0.04, which is followed by a fully metallic ground state. A large sudden drop in the magnetoresistivity up to 20 T defines a transition that is highly hysteretic and becomes irreversible at low temperatures and with La doping. Unlike $Ca_2RuO_4$, where ferromagnetism is instantly induced in the antiferromagnetic host by La doping[149], $Ca_3Ru_2O_7$ shows no ferromagnetic ordering when La doped, but readily becomes a ferromagnet in modest magnetic fields. The impact of La doping on $Ca_3Ru_2O_7$ is much more drastic than that of Sr doping, implying the importance of the added electron from the $La^{3+}$ ion.

### 4.4.13 Impact of Cr substitution on $Ca_3Ru_2O_7$:

The doping studies on the Ca site of $Ca_3Ru_2O_7$ revealed interesting results with band filling through La substitution showing more drastic impact than that of band width control by Sr doping. In this section, I will focus on the transport and thermodynamic studies of $Ca_3Ru_2O_7$ with Cr substituted on the Ru site. The single-crystal x-ray diffraction data show that $Ca_3(Ru_{1-x}Cr_x)_2O_7$ ($0 \leq x \leq 0.20$) compositions are iso-structural with a modest variation of lattice parameters as given in **Table 4.3**.

**Table 4.3** *Lattice parameters and unit cell volume tabulated for different x in* $Ca_3(Ru_{1-x}Cr_x)_2O_7$.

| S. No. | Cr concentration x | Lattice parameter a (Å) | b (Å) | c (Å) | Volume V ($Å^3$) |
|---|---|---|---|---|---|
| 1 | 0 | 5.3721 | 5.5302 | 19.572 | 581.46 |
| 2 | 0.05 | 5.3617 | 5.5123 | 19.521 | 576.96 |
| 3 | 0.17 | 5.3756 | 5.5090 | 19.5414 | 578.70 |
| 4 | 0.20 | 5.3731 | 5.4834 | 19.510 | 574.81 |

The orthorhombic crystal symmetry is retained throughout the extent of the doping i.e. for Cr concentration upto x=0.20. The unit cell volume, V, decreases by around 1.2 % from x=0 to x=0.20, which is similar to the difference in V observed for (Ca, Sr)$Ru_{1-x}Cr_xO_3$ ($0 < x < 0.36$). The systematic decrease in the lattice parameters might suggest a presence of $Cr^{4+}$ ions in the compound.

The compounds' response to applied magnetic field is displayed in **Fig. 4.44**, which shows the magnetization, M, of $Ca_3(Ru_{1-x}Cr_x)_2O_7$ as a function of temperature T. The system's magnetic anisotropy, one of the highlighting characteristics of the pure compound, is retained up to x=0.20 as demonstrated in the magnetization along a axis ($M_a$) (**Fig. 4.45 (a)**) and in that along b axis ($M_b$) (**Fig. 4.45 (b)**) at B = 0.5 T for all x. The noticeable feature in the figure is the lowering of $T_{MI}$ and the rapidly raising $T_N$ with Cr substitution while keeping the temperature dependence M (T) similar to that for x = 0. This is particularly true for $M_a$ where $T_{MI}$ and $T_N$ are separated by the AFM-M state that extends over an interval of 70 K ($T_{MI}$ = 23 K and $T_N$ = 93 K for x = 0.20) (**Fig. 4.45 (a)**). It is very significant that the AFM-M region is broadened from 8 K for x=0 to 70 K for x=0.20[150]. The temperature dependence of $M_b$ deviates from the classical antiferromagnetic behavior of $Ca_3Ru_2O_7$ and shows an upturn at $T_{MI}$ for $x > 0$ (**Fig. 4.45 (b)**). But the trend of increasing $T_N$ with x observed in $M_a$ is exhibited in $M_b$ too. In the M (T), $M_a > M_b$ between $T_{MI}$ and $T_N$, and hence the magnetic easy axis is along **a-**axis for $T < T_{MI}$, same as the pure sample[83, 116], which realigns along the **b-**axis in the AFM-M state.

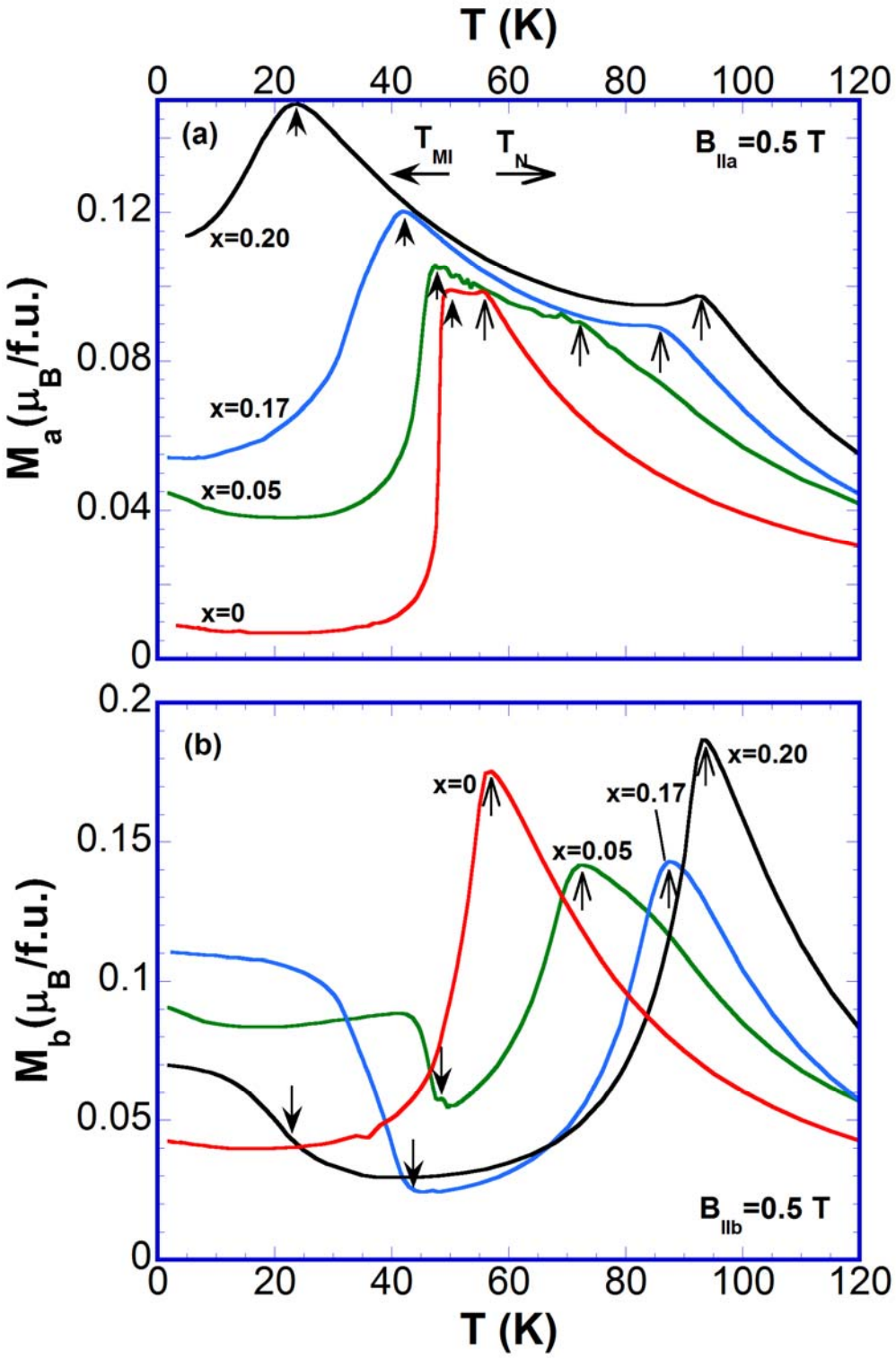


**Fig. 4.45** Magnetization, M, as a function of temperature, T, for **(a)** a axis, $M_a$, and **(b)** b axis, $M_b$, at B = 0.5 T for all x.

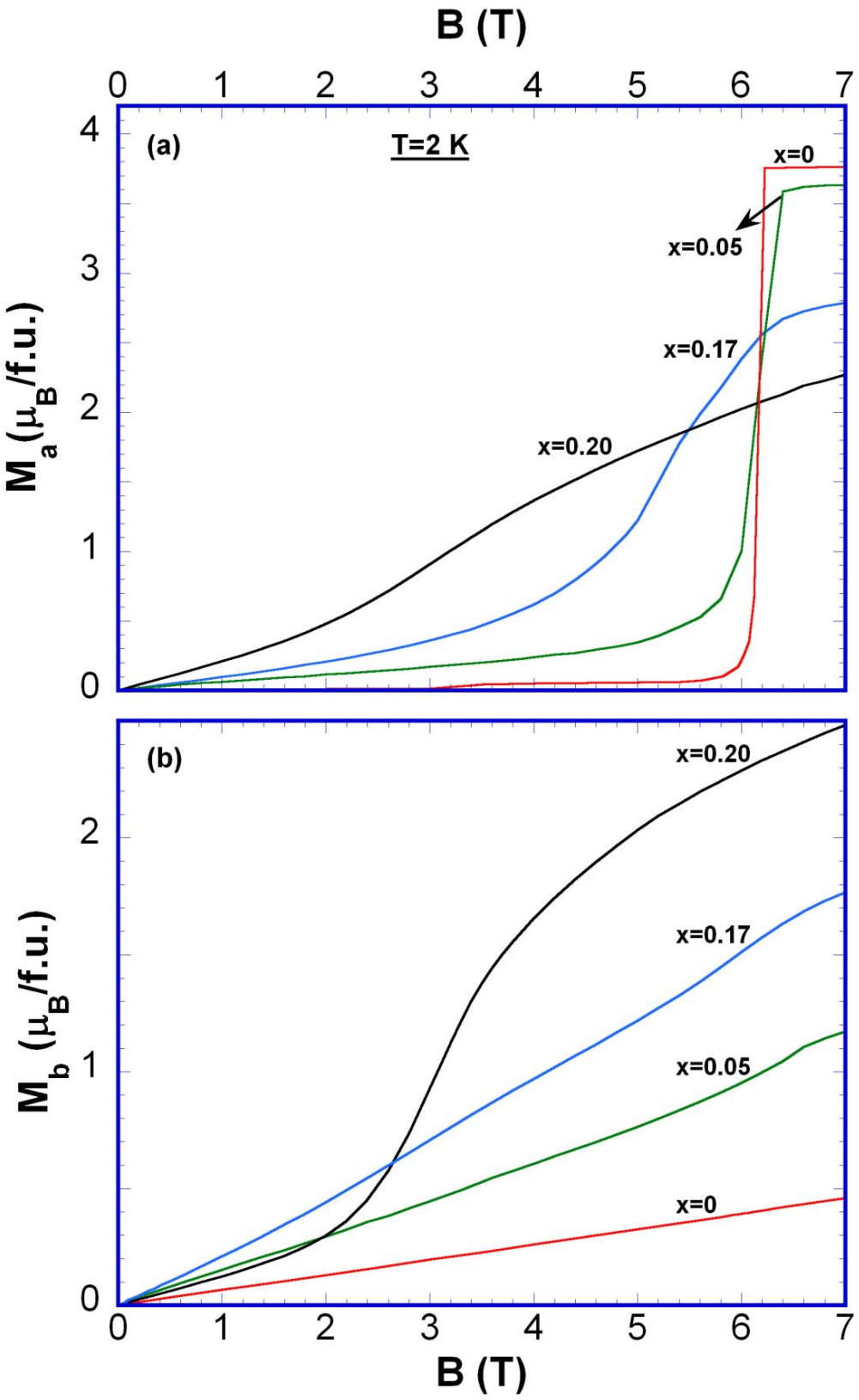


**Fig. 4.46** The magnetic isotherms for **(a)** a ($M_a$) and **(b)** b ($M_b$) axes at T=2 K for all x.

Shown in **Fig. 4.46** are the magnetic isotherms along different directions viz. $M_a$ (**Fig. 4.46 (a)**) and $M_b$ (**Fig. 4.46 (b)**) at T=2 K for different x in $Ca_3(Ru_{1-x}Cr_x)_2O_7$. $M_a(B)$ shows a metamagnetic transition for x=0 at $B_C$=6 T, as explained earlier, with a saturated moment 1.73 $\mu_B$/Ru reflecting an 85% spin polarization of the S=1 system. For x > 0, the jump in magnetization survives but with a reduction in the ordered moment. As x is increased from 0 to 0.20, the spin polarization at B=7 T is reduced from 85% to 30% correspondingly. The change in saturation moment, $M_S$, for an increase in x is listed in **Table 4.5** for different x. **Fig. 4.46 (b)** shows the b axis isothermal magnetization, $M_b(B)$ at T=2 K for different x. The magnetization for x=0 is linear in B confirming the antiferromagnetic ground state of the pure compound. But when x is increased, the system deviates from the linear field dependence and shows signs of spin polarization at substantial magnetic fields. The magnetic moment increases from less than 0.03 $\mu_B$/ion (~0.05 $\mu_B$/f.u.) to 0.55 $\mu_B$/ion (~1.1 $\mu_B$/f.u.) for $0 \leq x \leq 0.20$ at B=7 T which is around 30% spin polarization of a spin 1 system. Note that the moment at $B_{\|b}$=7 T for x=0.20 is close to that at $B_{\|a}$=7 T, which might suggest that the magnetic easy axis is rotated away from a axis with an increase in x.

**Table 4.4** *Ordering temperatures ($T_{MI}$ and $T_N$), Curie-Weiss fit parameters ($\theta_{CW}$, $\chi_0$ and $\mu_{eff}$) and saturation moment ($M_S$) along a axis for $Ca_3(Ru_{1-x}Cr_x)_2O_7$ (0 < x < 0.20).*

| S. No. | Cr concentration x | Ordering temperature (K) | | Curie-Weiss temperature $\theta_{CW}$ (K) | Temperature independent susceptibility $\chi_0$ (x$10^{-3}$ emu/mole) | Magnetic moment ($\mu_B$/ion) | |
|---|---|---|---|---|---|---|---|
| | | $T_{MI}$ | $T_N$ | | | $\mu_{eff}$ | $M_S$ |
| 1 | 0 | 48 | 56 | +72 | 1.313 | 2.86 | 1.73 |
| 2 | 0.05 | 46 | 72 | +79 | 1.941 | 2.74 | 1.59 |
| 3 | 0.17 | 42 | 86 | +101 | 1.682 | 2.45 | 0.98 |
| 4 | 0.20 | 23 | 93 | +99 | 2.057 | 2.68 | 0.58 |

Note that $T_{MI}$ decreases whereas $T_N$ increases with x hence broadening the AFM region that lies between them.

The anisotropy in magnetic properties is extended to the high temperature paramagnetic phase too as in the pure $Ca_3Ru_2O_7$. However, the paramagnetic state for all the orientations follow the Curie-Weiss law, $\chi = \chi_0 + \frac{C}{(T - \theta_{CW})}$ (equation 4-1), throughout the doping range. The magnetic data, when B||a axis, in the temperature range 200 < T < 350 K is fitted to the Curie-Weiss law and the different fit parameters are tabulated in **Table 4.4**. Temperature independent susceptibilities for all x, including x=0, fall in the range of m emu/mole and hence an enhanced density of states near the Fermi level is expected. As x increases, $\chi_0$ shows a small increase in the value and the increasing $\chi_0$ suggests a further enhancement in $N(E_F)$. The estimated Curie-Weiss temperatures are all positive as in the pure compound and increase further with x. The positive $\theta_{CW}$ and the antiferromagnetic ordering affirm an antiferromagnetic stacking of ferromagnetic layers along the c axis[112] in these compounds. The effective moment, $\mu_{eff}$, estimated for $Ca_3(Ru_{1-x}Cr_x)_2O_7$ decreases from 2.86 $\mu_B$/magnetic ion for x=0 to 2.45 $\mu_B$/magnetic ion for x=0.17[150]. Even though $\mu_{eff}$ show a decrease with x, the values are comparable to that of an S=1 spin expected for a system containing $Ru^{4+}$ and $Cr^{4+}$ ions. The fit parameters along other directions also follow similar trend and hence not shown here. The change in $T_N$ and $T_{MI}$ with Cr concentration when b is applied parallel to a axis (observed in **Fig. 4.45**) is also tabulated in **Table 4.4**. The $T_{MI}$ decreases with x whereas $T_N$ shows the opposite trend and hence the region between those transition temperatures (i.e. the AFM-M region) is significantly broadened as a result of Cr doping on $Ca_3Ru_2O_7$. For instance, the AFM-M regime for x=0.20 exhibits a window as broad as 70 K.

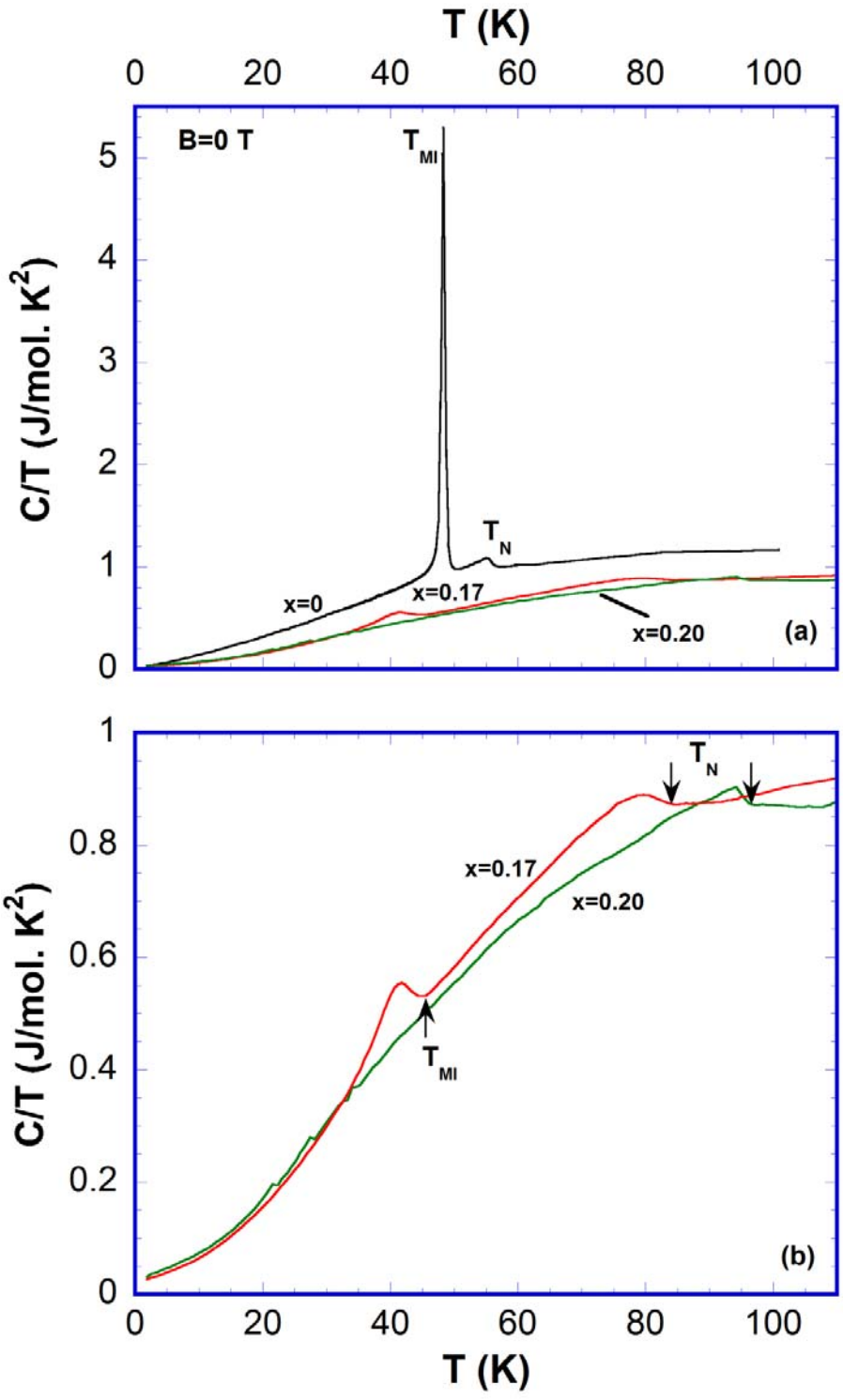


**Fig. 4.47 (a)** Temperature dependence of specific heat, C, expressed as C/T vs. T at B=0 T for x=0, 0.17 and 0.20. **(b)** Zoomed portion of C/T vs. T for x=0.17 and 0.20 to show the broadened AFM-M state.

**Fig. 4.47 (a)** shows the temperature dependence of specific heat (C/T vs. T) of $Ca_3(Ru_{1-x}Cr_x)_2O_7$ (x=0, 0.17 and 0.20) at B=0 T for 1.8 < T < 110 K. For x=0, the ordering temperatures are 48 K and 56 K corresponding to the metal insulator transition ($T_{MI}$) and the antiferromagnetic transition ($T_N$) respectively. As x increases, the AFM-M state lying between $T_{MI}$ and $T_N$ broadens as shown in **Fig. 4.47 (b)** and as explained in the last paragraph. Low temperature specific heat data was fitted to the relation,

$$C=\gamma T + \beta T^3 \qquad (4\text{-}5)$$

to estimate the electronic contribution, γ, and the phononic contribution, β, to the specific heat. The y intercept in C/T vs. $T^2$ graph (not shown here) reveals 37 mJ/mol. $K^2$ as the γ for x=0[83]. The estimated γ for x > 0 are 30.9 and 38.4 mJ/mol. $K^2$ for x=0.17 and 0.20 respectively, which are comparable to that of the pure compound suggesting a similar strength of electron correlation in the Cr substituted compounds. The slope of the C/T vs. $T^2$ graph (also not shown here) gives an estimated value for β. The estimated values suggest that the lattice contribution to the specific heat increases with the Cr concentration. The fit parameters are listed in **Table 4.5**.

**Table 4.5** *Electron and phonon contributions to the specific heat of $Ca_3(Ru_{1-x}Cr_x)_2O_7$ at B=0.*

| S. No. | Cr concentration x | Electronic contribution γ (mJ/mol. $K^2$) | Phonon contribution | |
|---|---|---|---|---|
| | | | β (x$10^{-4}$ mJ/mol. $K^3$) | $T_D$ (K) |
| 1 | 0 | 37.0 | 1.27 | 450 |
| 2 | 0.17 | 30.9 | 3.00 | 338 |
| 3 | 0.20 | 38.4 | 3.06 | 336 |

**Fig. 4.48** documents the change of $T_N$ and $T_{MI}$ with Cr concentration (tabulated in **Table 4.4**) and three magnetic/orbital phases separated by estimated transition lines. The decrease in $T_{MI}$ signals a delocalization effect due to Cr doping, implying that the Cr valence is more likely to be $Cr^{4+}$ ($3d^2$) rather than $Cr^{3+}$ ($3d^3$), in which the three half-filled $t_{2g}$ orbitals are relatively stable against delocalization. The increase in $T_N$ marks an

enhanced exchange coupling between the nearest neighboring spins. This is also manifested in $SrRu_{1-x}Cr_xO_3$ and $CaRu_{1-x}Cr_xO_3$ where the FM state is strongly enhanced[95, 96, 151] or generated[108] respectively.

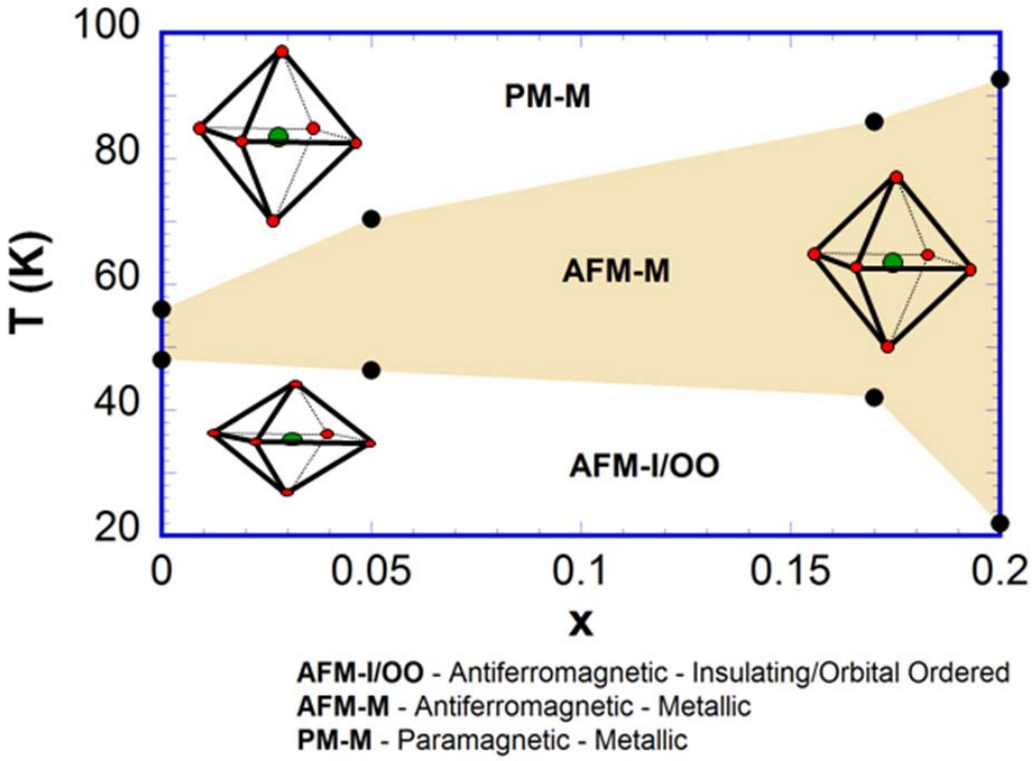


**Fig. 4.48** The x dependence of $T_N$ and $T_{MI}$ for $Ca_3(Ru_{1-x}Cr_x)_2O_7$ ($0 < x < 0.20$).

The "S"-NDR observed in pure $Ca_3Ru_2O_7$ is restricted solely to the insulating antiferromagnetic region and is absent in the metallic antiferromagnetic region, $48 < T < 56$ K, or the paramagnetic metallic phase, $T > 56$ K. This suggests that the unusual secondary conduction mechanism responsible for the non-Ohmic behavior is associated more closely with the electron transport than with the magnetic order in $Ca_3Ru_2O_7$. This is true as magnetic ordering is a necessary but not sufficient condition for the appearance of S-NDR in the heavy transition metal oxides[83]. This non-linear I-V characteristic is retained in $Ca_3(Ru_{1-x}Cr_x)_2O_7$ ($0 < x < 0.20$) for the AFM-I state. **Fig. 4.48** shows the I-V characteristics of $Ca_3(Ru_{1-x}Cr_x)_2O_7$ with x=0.05, 0.17 and 0.20. For x=0.05, the non-Ohmic behavior exists up to T=45 K that marks an onset of antiferromagnetic metallic state ($T_{MI}$=46 K). For $T > 45$ K, the non Ohmic behavior disappears to give an Ohmic response thereafter (see **Fig. 4.49 (a)**). **Fig. 4.49 (b)** shows the I-V characteristics of 17% Cr substituted $Ca_3Ru_2O_7$. As seen from the figure, the non-linear conduction for x=0.17

too is restricted to the AFM-I state as for the lower concentrations of Cr and the linearity in I-V shows up for T > 40 K i.e. in the proximity of the $T_{MI}$. However, the steepness of the S-NDR changes significantly with x as the curve exhibits a more rounded structure for higher x. For temperatures above $T_{MI}$ the compound shows the normal linear characteristics (not shown here) expected for a metal. The wiggling seen right after the NDR is repeatable and might be a sign of system's response to the critical current. For x=0.20, the curve shows less nonlinear behavior. The non linearity could have been spotted easily if the data were taken at much lower temperatures than 10 K, where the AFM-I state is prominent. But the thermal fluctuations that arise as a result of self heating are so high for these crystals that controlling T at temperatures lower than 10 K is extremely challenging. It is clear that the non-linear I-V characteristic is restricted to the AFM-I or the AFM-OO state in $Ca_3(Ru_{1-x}Cr_x)_2O_7$ too.

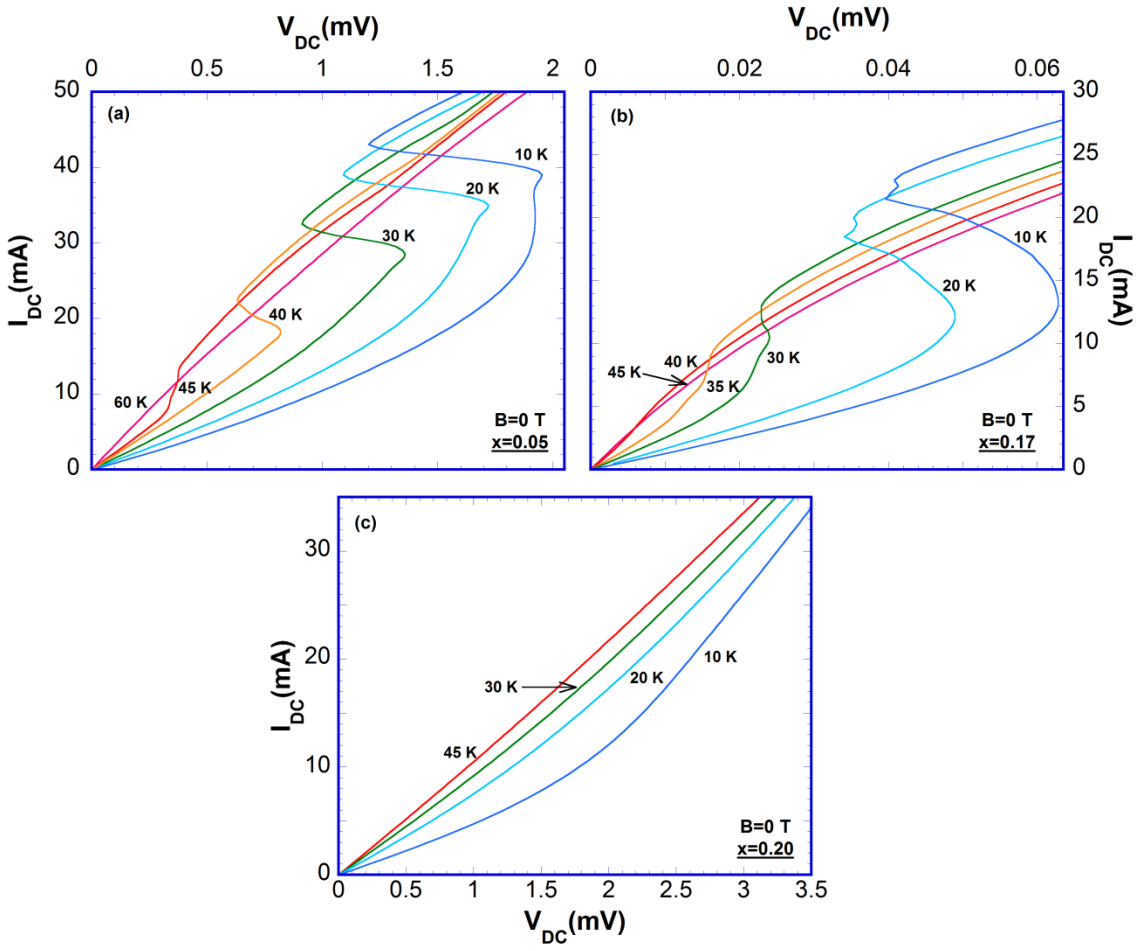


**Fig. 4.49** I-V characteristics at B=0 T for **(a)** x=0.05, **(b)** x=0.17 and **(c)** x=0.20 for different temperatures.

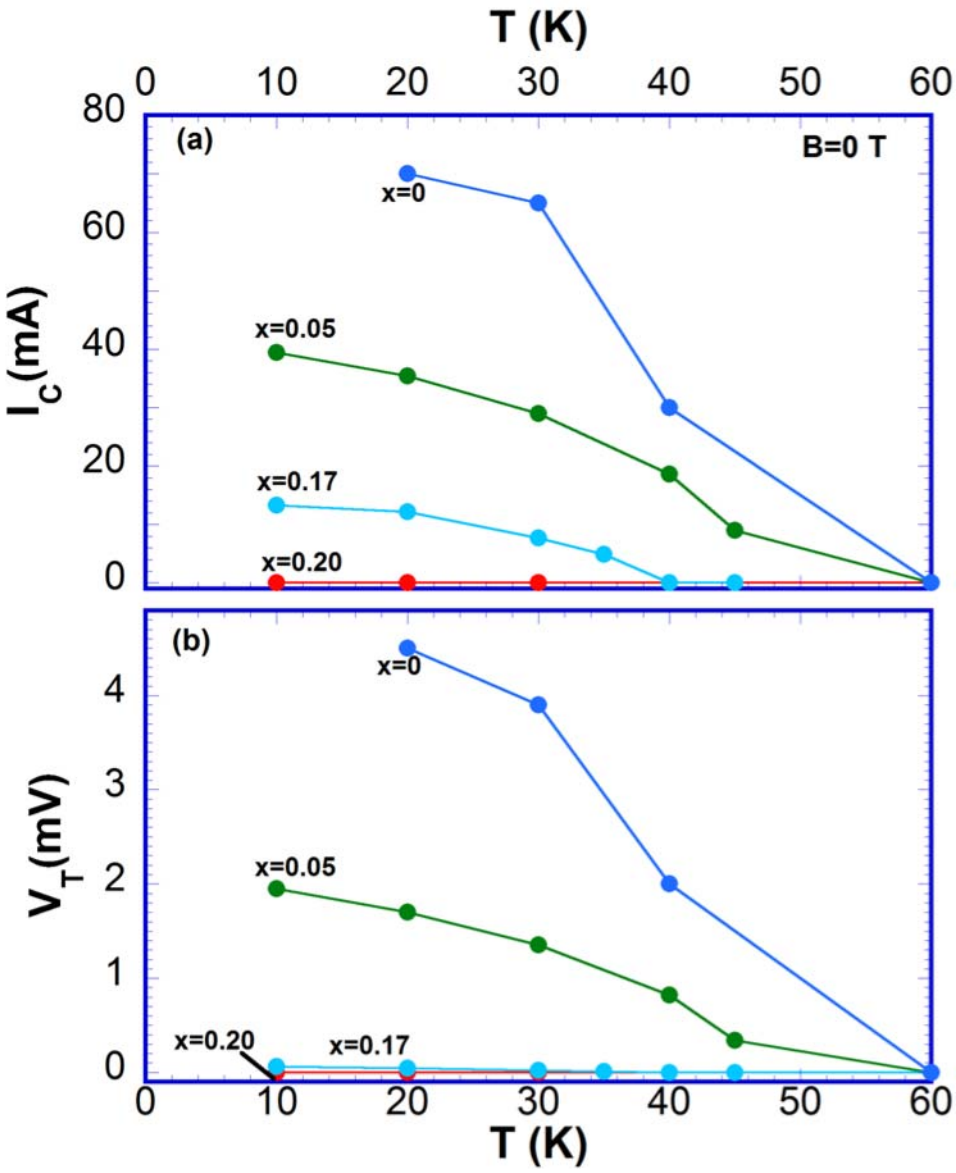


**Fig. 4.50** x dependence of **(a)** critical current ($I_C$) and **(b)** threshold voltage ($V_T$) for different temperatures viz. T= 20, 30, 40 and 60 K at B=0.

The **Figs. 4.50 (a)** and **(b)** shows the Cr concentration dependence of critical current, $I_C$ and threshold voltage, $V_T$ for different temperatures at B=0 respectively. As seen from **Fig. 4.49**, the critical current is the maximum for the lowest possible temperature and keeps dropping as the temperature is raised further. For sufficiently higher temperatures i.e. $T > T_{MI}$, it is pushed to zero and the S bend is not a characteristic of the I-V curve anymore. The critical current also decreases with x for a selected temperature and both the trends are depicted clearly in **Fig. 4.50**. The $I_C$ at T=20 K, for instance, is 70 mA for x=0 and decreases to 0 for x=0.20 through 35 mA and 15 mA for

x=0.05 and 0.17 respectively. This might suggest a drop in the critical carrier drift velocity ($v_d$) or carrier concentration (n) or a combination of both as temperature and/or Cr content is increased. Similarly the threshold voltage also decreases with the Cr concentration and temperature.

This nonlinear response hardly has any magnetic field dependence. Even for B=7 T, where the system shows a strong spin polarization along the easy axis, there is no alterations observed to the non-ohmic behavior (hence the data is not shown here). This confirms the statement that the conduction mechanism responsible for this nonlinear behavior is more electron transport driven than it is magnetic state dependent.

Let us focus our attention to the thermodynamics of a representative composition, x = 0.17, that shows significant changes in the physical behavior yet preserving the basic characteristics of the pure compound concurrently. Shown in **Fig. 4.51** is $M_a$ and $M_b$ at B = 0.5 T as a function of T for x = 0.17, for which $T_{MI}$ = 42 K and $T_N$ = 86 K. As seen in the pure compound, the transitions enclose the AFM-M region with the only change being a further extension induced as a result of Cr inclusion. The AFM-M window is now enhanced to 44 K in size for 17% Cr substituted compound[150]. Also illustrated in the figure (right scale) is the temperature dependence of specific heat C divided by T, C/T, at B = 0. Two anomalies in C/T that are mean-field like confirm the 2nd order phase transitions at $T_{MI}$ and $T_N$. The transition anomaly at $T_{MI}$ is sharper with an approximate jump $\Delta C \sim 0.31$ R (the gas constant R = 8.314 J/mole K); and the other near T = 83 K (slightly lower than $T_N$ = 86 K) is broader with a smaller $\Delta C \sim 0.28$ R[150].

A fit of the low-T data to $C = \gamma T + \beta T^3$ for $1.7 < T < 30$ K yields $\gamma \sim 31$ mJ/mol K and $\beta \sim 3.0\times10^{-4}$ mJ/mol $K^3$ that are the coefficients of the electronic and phonon contributions to C, respectively. The measured transition entropy ($\Delta S$) is approximately 0.037 R, clearly much smaller than 2Rln3 (or 2Rln4), which is expected for complete ordering of localized S = 1 (or S=3/2) spins. On the other hand, AFM ordering among itinerant spins, e.g., as in a spin-density wave (SDW), should produce $\Delta S \sim \Delta\gamma T_N$. Formation of a SDW is also consistent with the mean-field-like step in C, for which $\Delta C \sim (1.43)\ \Delta\gamma T_N$, which yields $\Delta\gamma / R \sim 0.0024$ $K^{-1}$. This value, much larger than expected, suggests that the anomaly at $T_N$ is inconsistent with both conventional itinerant and localized pictures of AFM ordering as also observed in $(Ca_{1-x}Sr_x)_3Ru_2O_7$[148] and thus

indicates a more complex spin ordering. Correspondingly, if the transition at $T_{MI}$ is due to formation of a charge density wave, then the expected entropy change $\Delta S \sim \Delta\gamma T_{MI}$ yields $\Delta\gamma/R \sim 8.8\times10^{-4}$ $K^{-1}$.

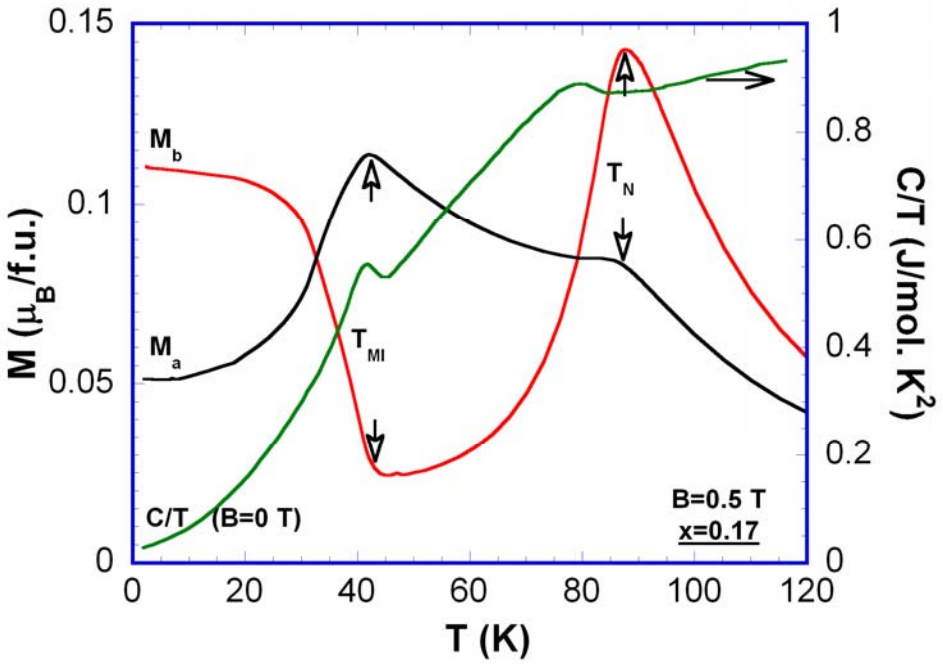


**Fig. 4.51** The temperature dependence of magnetization M for x = 0.17 for both a axis ($M_a$) and b axis ($M_b$) at B = 0.5 T (*left scale*). *Right scale*: C/T for x = 0.17 as a function of T.

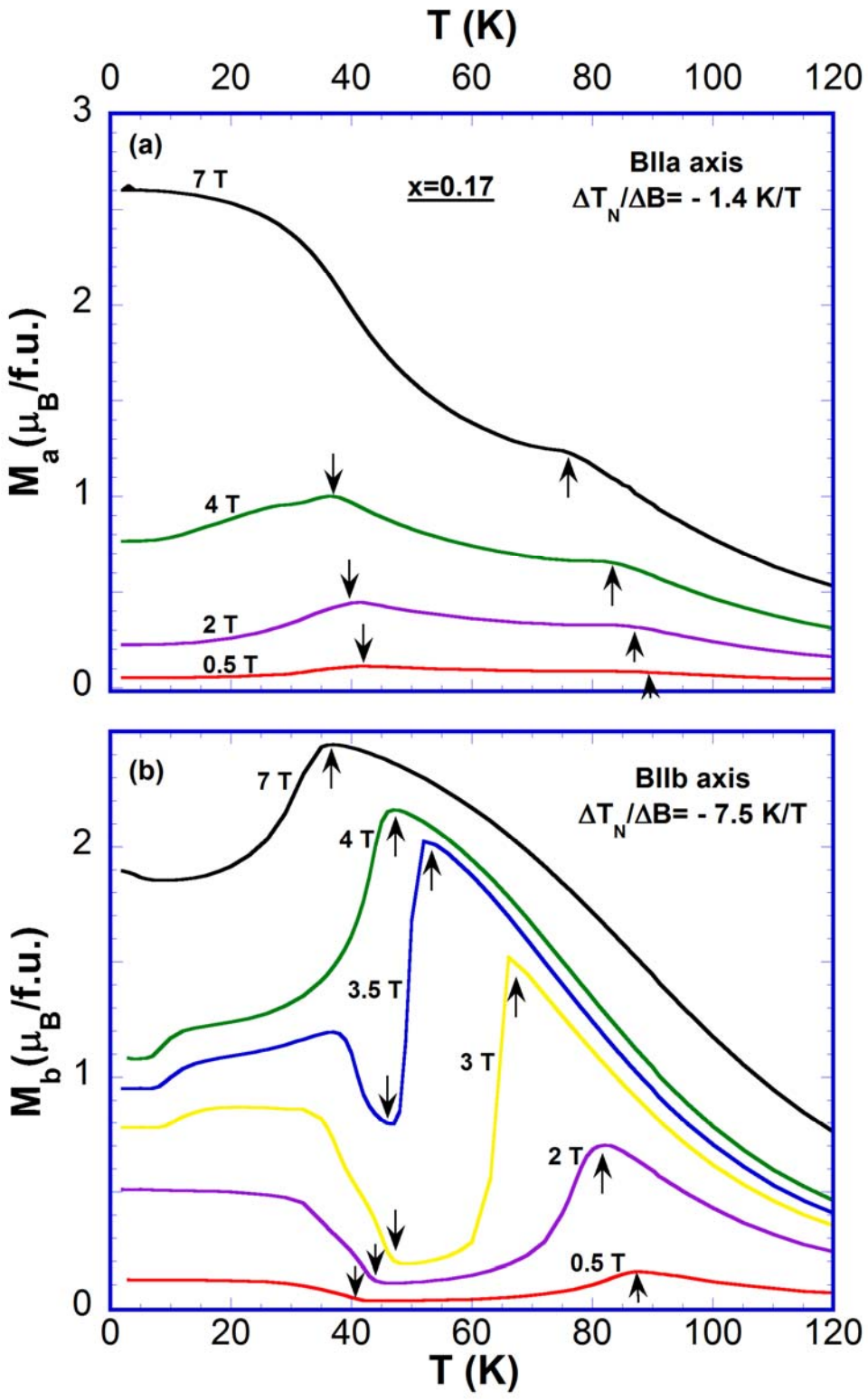


**Fig. 4.52** The temperature dependence of magnetization M for x = 0.17 **(a)** for a-axis ($M_a$) and **(b)** b-axis ($M_b$) for various magnetic inductions B up to 7 T.

The magnetization behaves extraordinarily with temperature, as shown in **Figs. 4.52 (a)** and **(b)**, where $M_a$ and $M_b$ vs. T are plotted at various fields for x = 0.17. For B||a-axis, the anomalies for both $T_{MI}$ and $T_N$ shift only slightly downward with increasing B and eventually become rounded off at higher fields. For instance, $T_N$ decreases at a rate of $\Delta T_N/\Delta B$ = -1.4 K/T, which is a nominal rate at which $T_N$ would decrease for a classical antiferromagnet. For B > 6 T, the magnetic state is driven into a FM state similar to the behavior of un-doped samples (x = 0). However, for B||b-axis, $T_N$ is readily suppressed at an astonishing rate of $\Delta T_N/\Delta B$ = -7.5 K/T[150]. Furthermore, there is an upturn in $M_b$ observed below $T_{MI}$ that appears to result from a slight spin canting in the AFM state. The fact that $T_{MI}$ initially increases with B and the transition becomes indistinct for B > 3.5 T suggests that some type of spin canting develops with increasing B.

The observed significant difference in the decrease of the compound's Neel temperature with field applied along different axes is recorded in **Table 4.6**. For instance, with an applied field of 0.5 T, the $T_N$ stays at 86 K for both the directions. To drop the $T_N$ to 76 K a field upto 7 T has to be applied along a axis, whereas this drop in $T_N$ is achieved with a much smaller field, say, 2 T along b axis. This suggests that the magnetic lattice is softened along b axis than along a axis. The soft nature of the Cr included Ru magnetic lattice along this direction might indicate a subtle difference in the coercivities of Cr and Ru sub-lattices in this direction. This unique spin set up in the compound opens up a door or two for the existence of a spin-valve behavior that is explained later.

**Table 4.6** *$\Delta T_N/\Delta B$ for x=0.17 when B||a axis and B||b axis*.

| S. No. | Applied field B (T) | Neel Temperature $T_N$ (K) | |
|---|---|---|---|
| | | When B||a axis | When B||b axis |
| 1 | 0.5 | 86 | 86 |
| 2 | 2.0 | 85 | 78 |
| 3 | 3.0 | - | 66 |
| 4 | 3.5 | - | 52 |
| 5 | 3.7 | - | 48 |
| 6 | 4.0 | 83 | 46 |
| 7 | 7.0 | 76 | 36 |

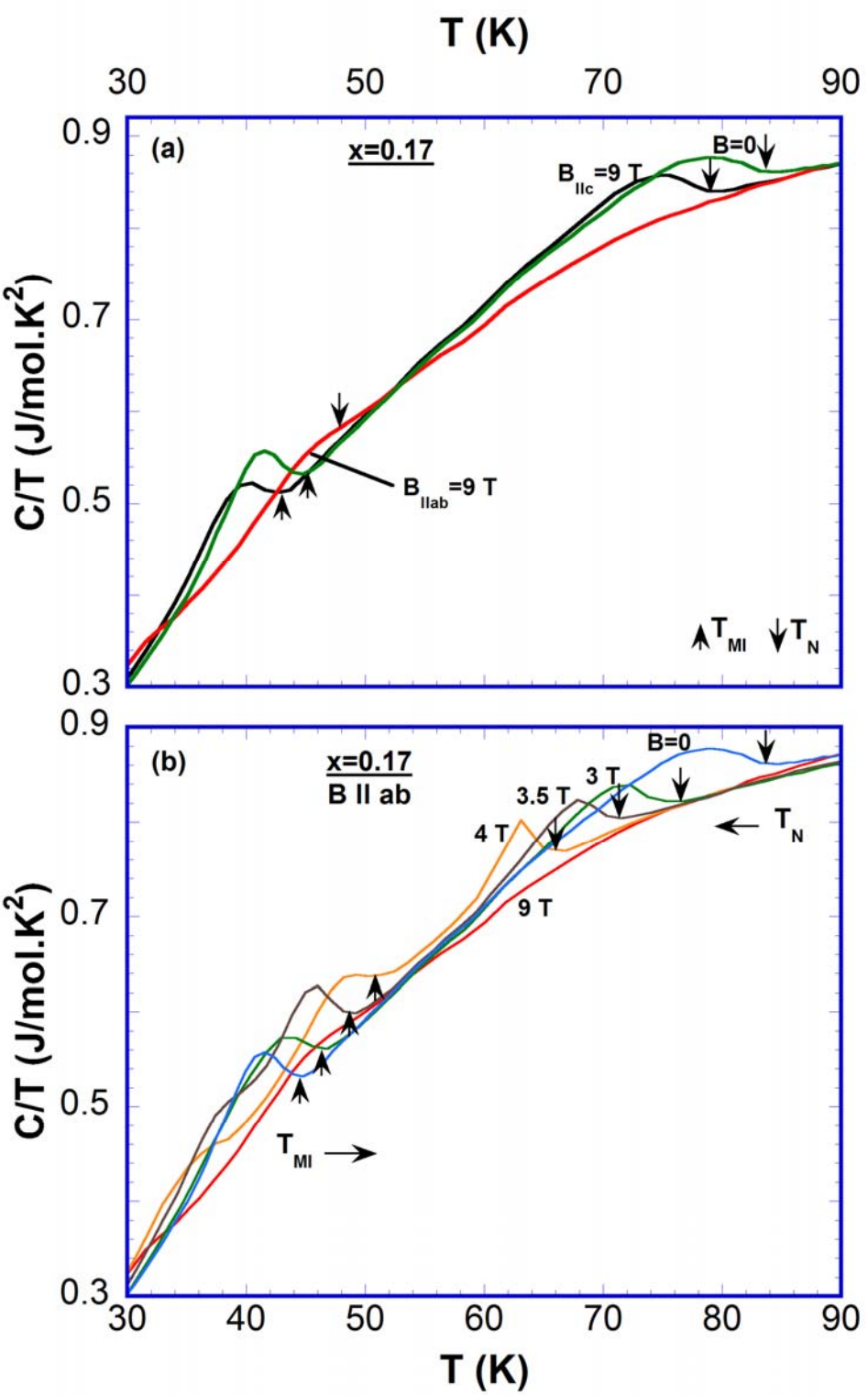


**Fig. 4.53** C/T vs. T for x=0.17 **(a)** when B=0 and 9 T along ab plane and c axis **(b)** when B=0, 3, 3.5, 4 and 9 T along ab plane.

The unusual magnetic properties observed in the compound are supplemented by the specific heat measurements done on it. The temperature dependence of C/T for B=0 and 9 T applied along c axis and ab plane is shown in **Fig. 4.53 (a)**. For B||c = 9 T, $T_N$ changes from 83 K to 78 K, which is less than but close to the drop in $T_N$ observed in the magnetization along a axis. A similar drop in $T_{MI}$ is observed too, which preserves the extent of the AFM-M state as seen in the magnetic and transport properties measured in lower fields. However, the drop in the antiferromagnetic ordering temperature for B||ab is of more significance. $T_N$ drops to as low as 47 K at B=9 T reflecting the soft nature of the magnetic lattice involving a selected concentration of Cr ions. But this drop is less than that would have been observed in the magnetization along b axis for this applied field: the reason being the oblique B that is not exactly parallel to b axis here. The field dependence of $T_{MI}$ is opposite to that of $T_N$ as seen from **Fig. 4.53 (b)** that shows the temperature dependence of the specific heat for various magnitude of B applied along ab plane. As B is incremented along this direction, $T_N$ continues to decrease whereas $T_{MI}$ chooses to increase upto B=4 T. This leads to a scenario where the AFM-M state shrinks as field increases upto B=4 T as observed in the magnetization measurements where a canting of spins characterizes the crystal's b direction. Also it is noted that the magnetic ordering becomes sharper as field increases whereas the $T_{MI}$ becomes rounded under similar field changes.

Another unusual behavior of the compound, although a characteristic of few species of the ruthenate and iridate families, is the anomalous low temperature behavior of C with applied field. **Fig. 4.54** shows the low temperature part i.e. $1.7 < T < 9$ K, of the temperature dependence shown in **Fig. 4.53 (a)**. What is unusual about the graph is that the specific heat increases with B at lower temperatures where a drop in entropy is expected (conventional wisdom). However, the gamma is comparable. This merits further investigation.

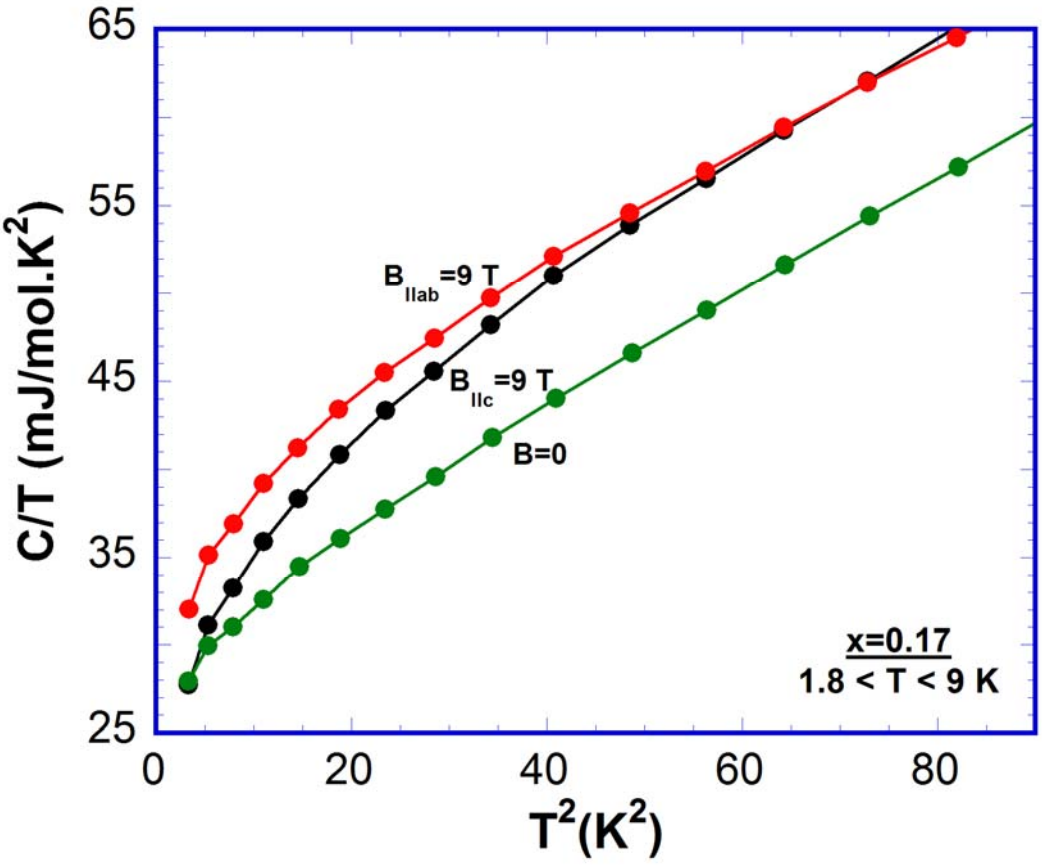


**Fig. 4.54** C/T vs. $T^2$ for x=0.17 when B=0 and 9 T along ab plane and c axis in the temperature range $1.8 \leq T \leq 9$ K.

The resistivity measurements on the compound in the presence of magnetic fields applied along different directions mimics the characteristics of a half metal. **Fig. 4.55** presents the temperature dependence of the resistivity ρ of x = 0.17 for B||a-axis and B||b-axis. The data covers the temperature range $1.7 \leq T \leq 120$ K for c axis resistivity ($\rho_c$) with B=0 and 7 T (**Fig. 4.55 (a)**) and for ab plane resistivity ($\rho_{ab}$) with B=0 and 12 T (**Fig. 4.55 (b)**). An intriguing feature here is that both $\rho_c$ and $\rho_{ab}$ at B = 0 sharply drop at and below $T_N = 86$ K despite the largely reduced Fermi surface at $T_N$ indicated by the reduction of γ.

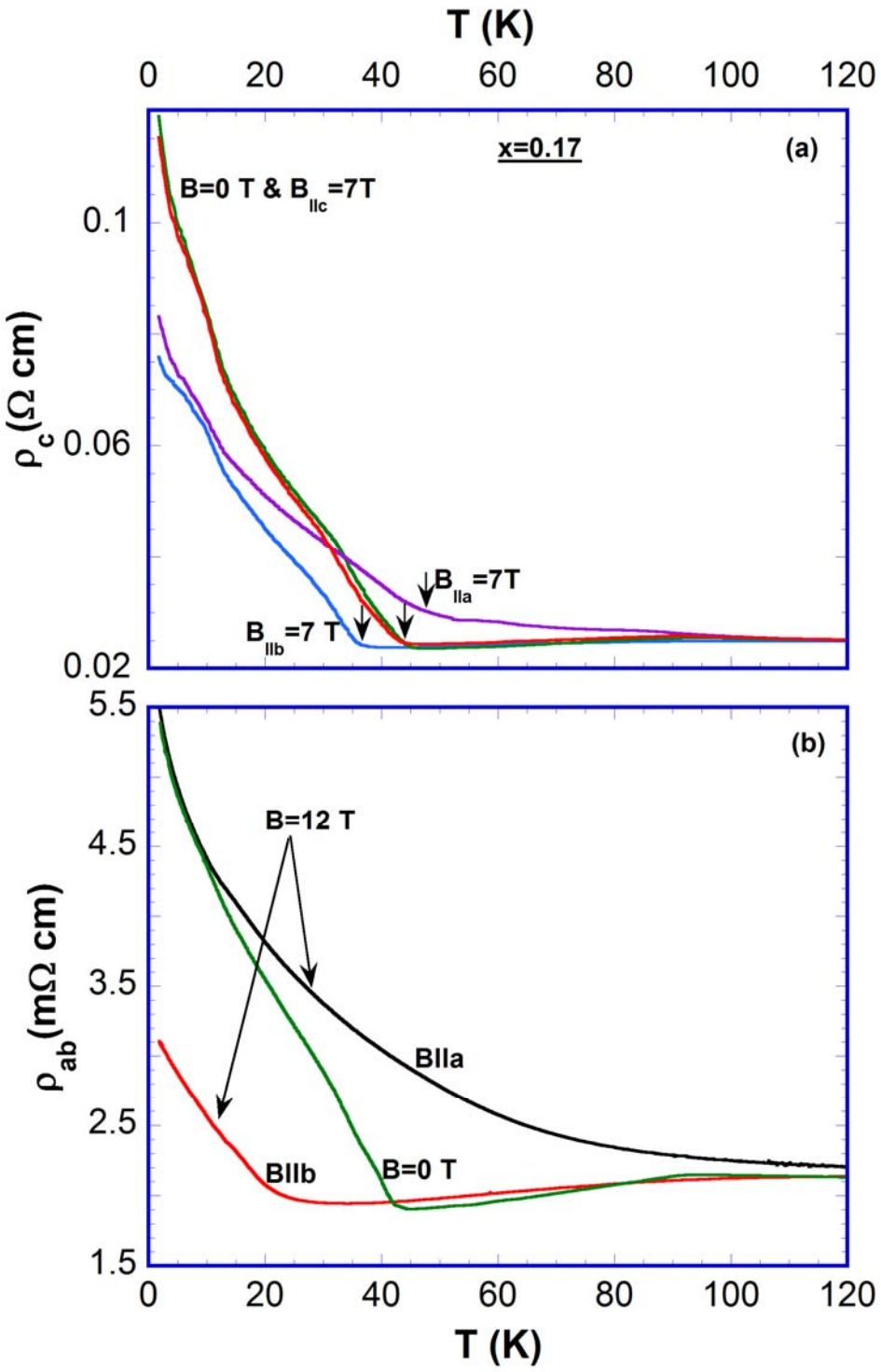


**Fig. 4.55** Temperature dependence of **(a)** $\rho_c$ for B||a-axis, ||b-axis and ||c-axis for B = 0 and 7 T. **(b)** $\rho_{ab}$ for B||a-axis and B||b-axis at B = 0 and 12 T, for x=0.17.

This behavior is surprisingly different from that of other AFM-M systems such as $Cr^{152}$, where the onset of $T_N$ accompanies a rise in resistivity, implying a critical role of

the spin degree of freedom in the AFM-M state. In fact, the conductivity of the AFM-M state is so strongly spin-dependent that it is extremely anisotropic: For B||a-axis, the AFM state becomes semiconducting with increasing B; and both $\rho_c$ and $\rho_{ab}$ increase significantly when B > 5 T, where a field-induced FM state emerges[150]. Itinerant electrons are evidently not favored in the field-induced FM state, similar to the behavior at x = 0[116]. Conversely, for B||b-axis, both $\rho_c$ and $\rho_{ab}$ decrease as B rises but do not exhibit a quadratic (Fermi liquid) temperature dependence in the AFM-M state. Clearly, the system in the range of $T_{MI} < T < T_N$ stays AFM metallic for B||b-axis, but at the same time becomes FM and semiconducting for B||a-axis. All these phenomena bear a striking resemblance to the behavior predicated for half-metallic systems[153].

The coupling between the electrons' conduction and spin is clearly depicted in **Fig. 4.56**. The figure shows the temperature dependence of $\rho_c$ with a range of magnetic field applied along a and b axis. For B||a axis (**Fig. 4.56 (a)**) the $T_{MI}$ increases linearly with B ultimately destroying the AFM-M state to become more semiconducting when the system shows a sizeable spin polarization. It is intriguing to know that for B||b axis, with the applied magnetic field the $T_{MI}$ increases upto a critical field of B=3.5 T and then decreases to lower temperatures to show a more metallic behavior at higher fields. As one would recall, the magnetic lattice tends to be softer along the crystal's b axis than that along a axis and there is a tendency for the spins to show canting along b axis. As we look closer, the valley like feature in the temperature dependence of magnetization that develops along this direction disappears at this critical field suggesting a close coupling between the conduction mechanism and the electron spin. More detailed investigation on this behavior with magnetic field scanned at different temperatures will be presented in the following sections.

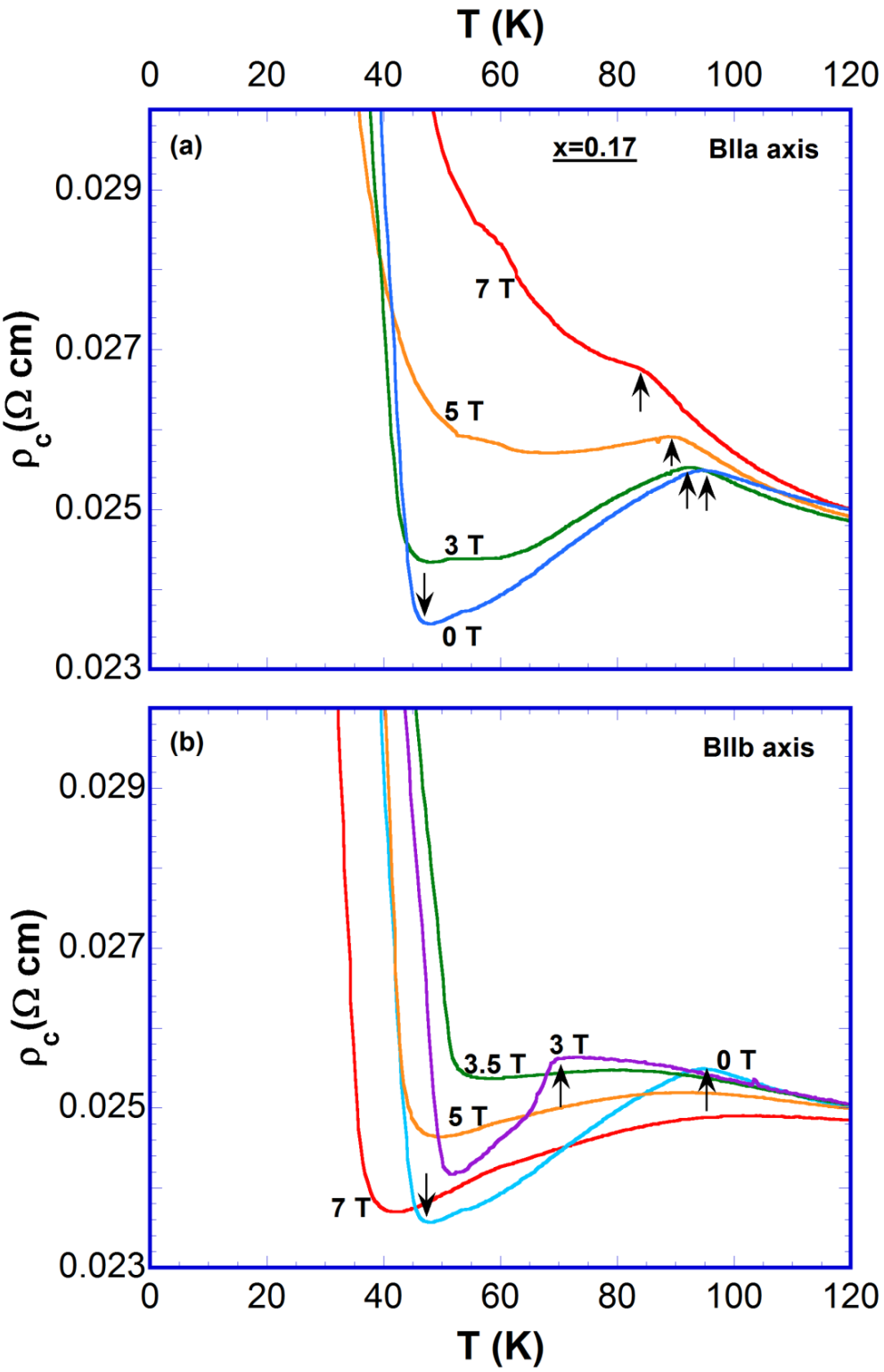


**Fig. 4.56** Temperature dependence of the c-axis resistivity, $\rho_c$, for x = 0.17 for **(a)** B||a-axis and **(b)** B||b-axis for various magnetic inductions up to 7 T.

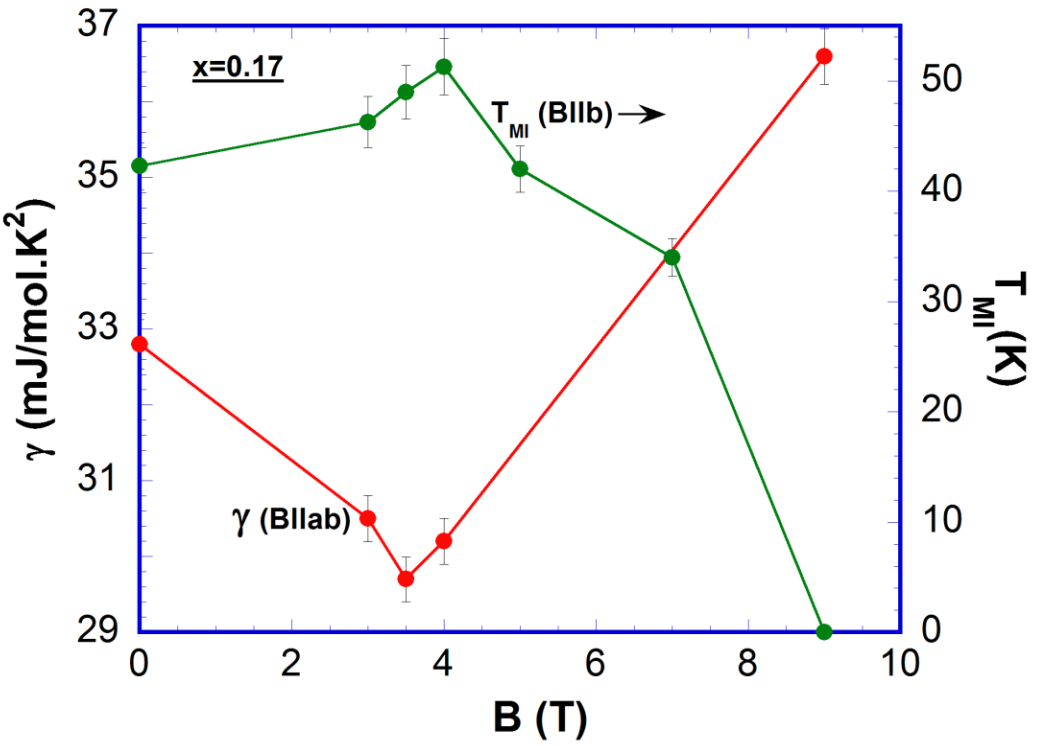


**Fig. 4.57** Electronic contribution to the specific heat, γ, vs. B when B||ab (*left scale*) and metal-insulator transition temperature, $T_{MI}$ vs. B when B||b (*right scale*) for x=0.17. *Note*: $T_{MI}$ for B=9 T is obtained from specific heat measurements done with B||ab.

The critical nature of the magnetic field is persuaded further in **Fig 4.57** which shows the field dependence of $T_{MI}$ when B||b (right scale) and gamma, the electronic contribution to the specific heat when B||ab (left scale). γ, the coefficient of $T^2$ in the relation $C=\gamma T^2 + \beta T^3$, decreases with the magnetic field along this direction as shown in the figure. For zero magnetic field, the value sits at 31 mJ/mol.$K^2$, which is comparable to the electronic contribution for the pure compound as reported in reference[95, 148] and as described earlier in this thesis suggesting a similar electronic distribution in the Cr doped crystals lattice too. As the magnetic field is increased, a small decrease in gamma with magnetic field happens until B reaches 3.5 T corresponding to an inhibited electron correlation or a less metallic behavior. For B > 3.5 T, there is an enhancement in the electron's contribution to specific heat where gamma increases from 29 to 37 mJ/mol.$K^2$ at B=9 T clearly mirroring the enhanced electron mobility with applied field in the system. A portrait of the electrons' dramatic behavior was demonstrated by the field dependence of $T_{MI}$ too. For increasing B upto 3.5 T, the less metallic nature of the

compound is shown by the increasing $T_{MI}$. Once B reaches the critical value of 3.5 T, the $T_{MI}$ decreases and the system reaches a more metallic state as complimented by the increased gamma for higher B upto 9 T in this direction.

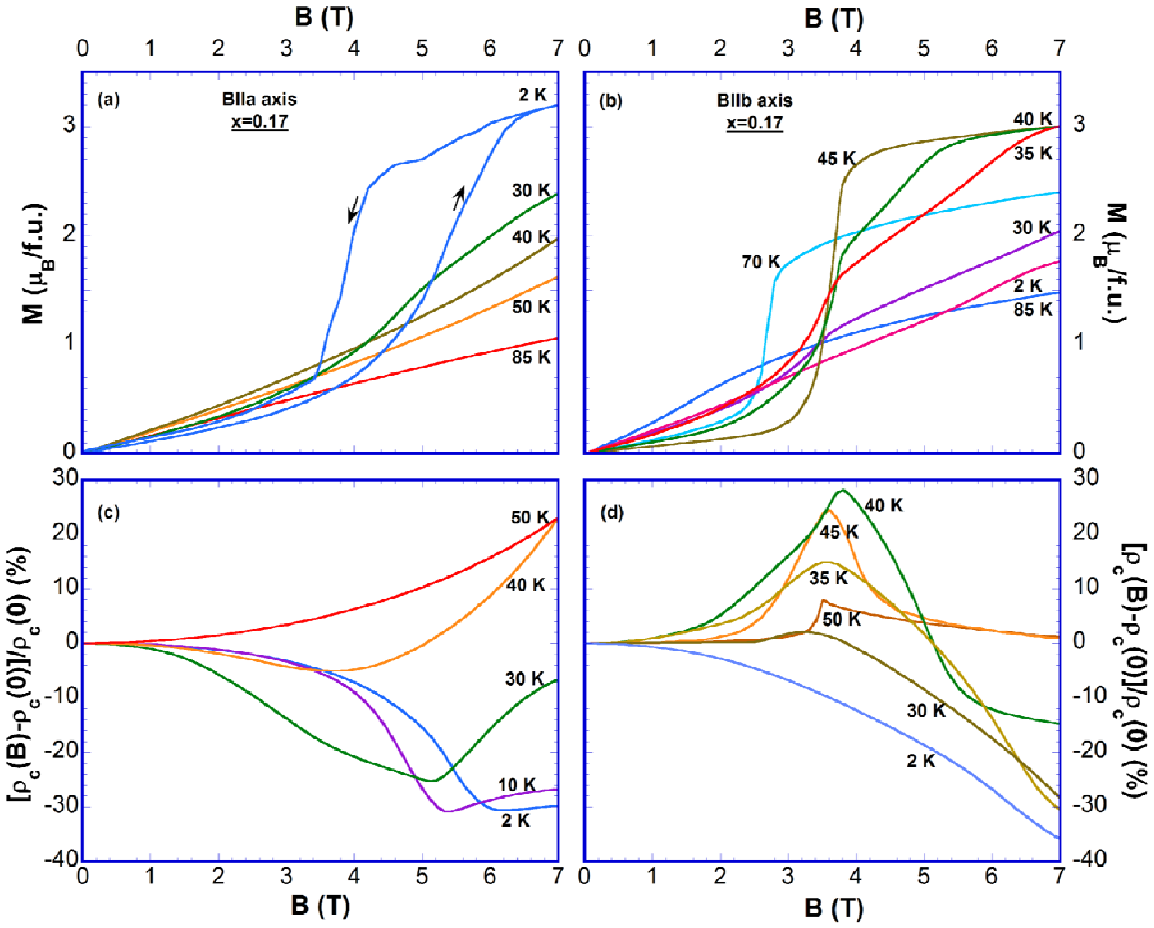


**Fig. 4.58** Field dependence of M for **(a)** $M_a$ and **(b)** $M_b$ and field dependence of the magnetoresistivity ratio defined as $[\rho_c(B)-\rho_c(0)]/\rho_c(0)$ for **(c)** B||a-axis and **(d)** B||b-axis for $2 \leq T \leq 85$ K.

From the above paragraphs it is clear that the material behaves anomalously in a selected range of B and T and a deeper investigation is required to disclose the complexity. To gain adequate knowledge on the prevailing issue, a series of isothermal measurements was performed on the magnetic and transport properties of $Ca_3(Ru_{0.83}Cr_{0.17})_2O_7$. **Fig. 4.58** shows the field dependence of M and the magnetoresistivity ratio defined as $[\rho_c(B)-\rho_c(0)]/\rho_c(0)$ for B||a-axis and B||b-axis and $2 \leq T \leq 85$ K. For B||a-axis and $T \leq 30$ K, a metamagneitc transition is observed with hysteresis similar to that for x = 0 but with a smaller ordered moment $M_s$ and at a lower

critical field $B_C$ (= 5 T) (**Fig. 4.58 (a)**). The metamagnetic transition weakens as T rises and disappears for T > 30 K[150]. For B||b-axis, M has linear field dependence with no metamagnetic transition until T > 30 K, and maximizes in the range of 35 < T < 45 K via two transitions, converging to $M_s$ ~3 $\mu_B$/f.u at 7 T, which is slightly smaller than that for B||a-axis (**Figs. 4.58 (a)** and **(b)**). This process is reversed for B||b-axis, implying the magnetic easy axis rotates from the a-axis to the b-axis. Although at T ≤ 30 the extrapolated $M_s$ for B||b-axis is notably smaller than that for B||a-axis, $[\rho_c(7T)-\rho_c(0)]/\rho_c(0)$ for B||b-axis is greater in magnitude than that for B||a-axis. Such an inverse relation between magnetization and transport anisotropy confirms the existence of a new magnetoresistance mechanism governed by orbital ordering[116], compared to all other magnetoresistive materials that are driven primarily by spin polarization.

For T > 30 K, $\rho_c(B)$ for B||a-axis generally rises as B increases, with $[\rho_c(7T)-\rho_c(0)]/\rho_c(0)$ reaching more than 20%. Moreover, $\rho_c(B)$ for B||b-axis peaks at a critical field $B_{C2}$ before declining. This phenomenon is particularly fascinating as $B_{C2}$ represents an onset of spin polarization, thus a reduction of spin scattering should be anticipated, as observed (and discussed earlier) for composition x = 0 (when B||b-axis) and other related materials. This behavior occurs in the range of 35 < T < 65 K but becomes most pronounced in the range of 35 < T < 50 K[150]. **Fig. 4.59** elaborates the field dependence of both $[\rho_c(B)-\rho_c(0)]/\rho_c(0)$ and M(B) for a few representative temperatures in this range viz. 40 K, 43 K and 47 K. At T=40 K, the magnetization shows a little bent at $B_{C2}$ before partially saturating above $B_{C1}$. The window enclosing $B_{C2}$ and $B_{C1}$ is approximately 1.5 T in width and it decreases to less than 1 T for T=43 K before becoming negligible at higher temperatures viz. 47 K. The magnetoresistivity for these temperatures modify accordingly showing a broader to steeper transition as T is increased upto 47 K as shown in the figure.

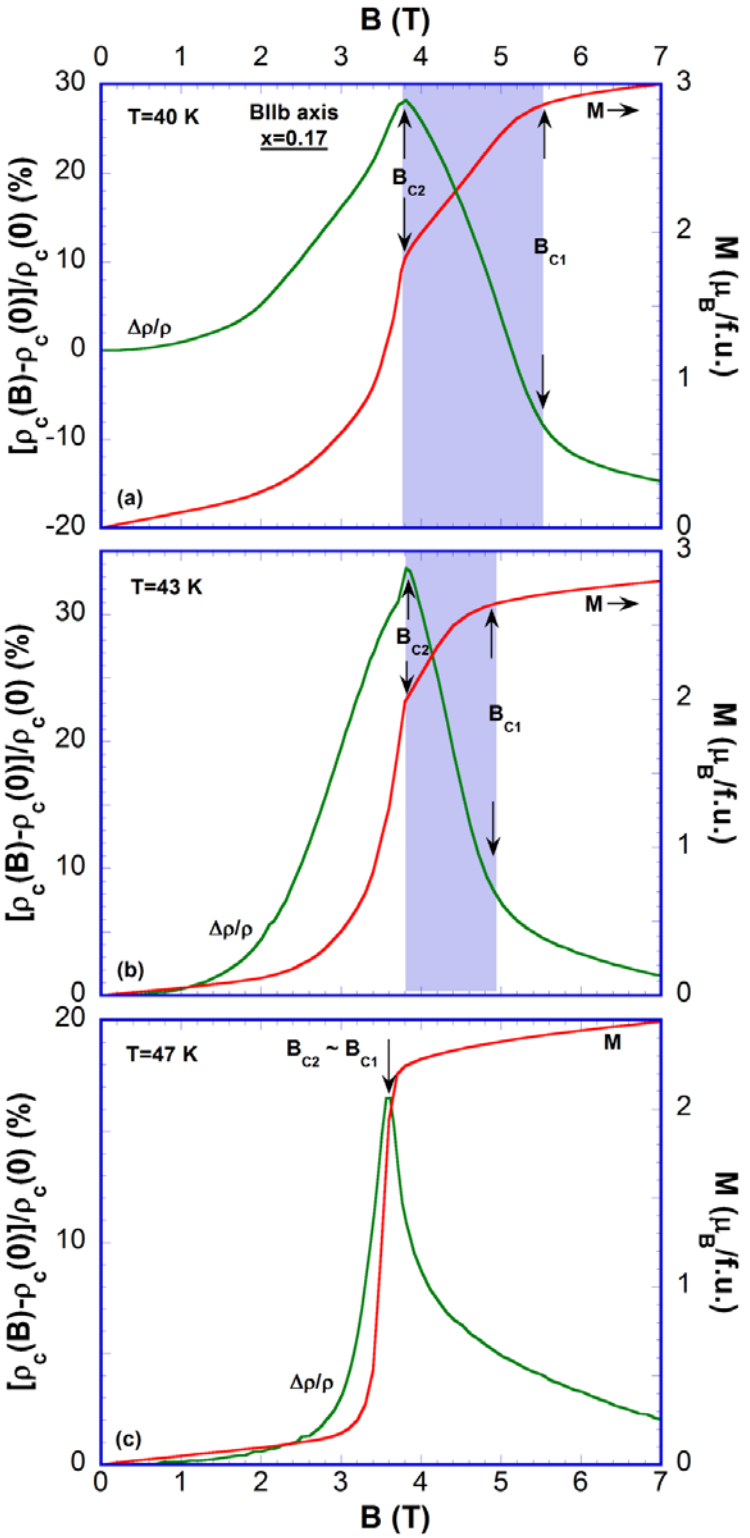


**Fig. 4.59** The field dependence of $[\rho_c(B)-\rho_c(0)]/\rho_c(0)$ and M (*right scale*) for B||b-axis at **(a)** T = 40 K, **(b)** 43 K and **(c)** 47 K.

Another intriguing feature of these graphs is that for $B > B_{C1}$, at T=47 K for instance, the resistivity is higher than that for $B < B_{C1}$[150]. Our conventional wisdom would direct us to believe a less resistive character of electrons in the state where the spins are polarized than the ground state when the spin scattering is evidently more pronounced.

These anomalous magnetic and transport properties are unique to the optimal Cr doped bi-layered calcium ruthenate compound. The behavior of the Cr-doped layered structure can be associated with a spin-valve scenario, as sketched in **Fig. 4.60**. To understand the spin configuration of the compound it is useful to recall the spin structure in the pure compound here. The magnetic state for x=0 consists of ferromagnetic bi-layers stacked antiferromagnetically with the inter-bilayer coupling far weaker than the magnetic interaction within a bi-layer. Cr substitution results in a Ru-O layer being replaced by a Cr-O layer in some bi-layers; for x=0.17, the replacement is likely to occur on average in every 2 or 3 bi-layers. Although it is difficult to observe the extremely weak super-lattice peaks expected in single crystal x-ray diffraction, the strong anomalies seen in C suggest that the Cr substation is not entirely random. The presence of the Cr-O layer causes a spin canting at low fields and temperatures, which gives rise to the upturn in $M_b$ at $T_{MI}$ (**Fig. 4.52 (b)**). The magnetization of each Ru-O layer in a un-substituted bi-layer, or hard magnetic bi-layer, is pinned due to the strong exchange coupling within the bi-layer, whereas the magnetization of a Cr-O layer in a substituted bi-layer, or soft magnetic bi-layer, is freer to rotate with B because of the interrupted or weakened exchange coupling and/or different coercivities of the Cr-O and Ru-O layers[150]. Anti-parallel alignment in the soft magnetic bi-layer is achieved when the spin in the Cr-O layer switches at $B=B_{C2}$.

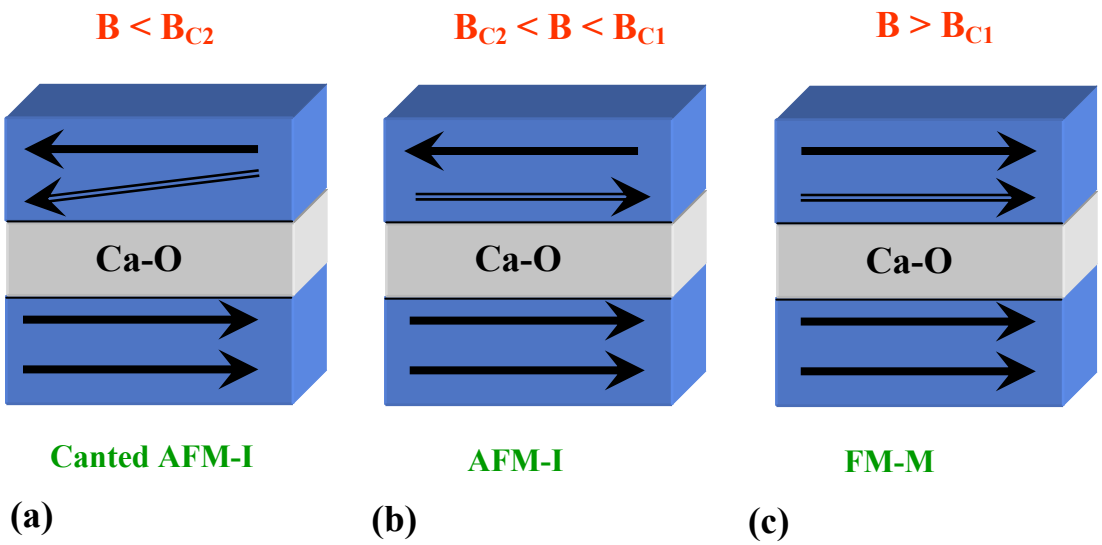


**Fig. 4.60** Spin configuration in $Ca_3(Ru_{1-x}Cr_x)_2O_7$, x=0.17 for **(a)** $B < B_{C2}$, **(b)** $B_{C2} < B < B_{C1}$ and **(c)** $B > B_{C1}$. Note that the double-line arrow indicates spin in the Cr-O layer.

This spin switching enhances the overall magnetization observed at $B_{C2}$ but, at the same time, changes the density of states for the up-spin and down-spin electrons at Fermi surface, significantly increasing probability of scattering of both the up-spin and down spin electrons within each Cr-O and Ru-O layer in the soft magnetic bi-layer having the anti-parallel alignment; thus a sharply increased resistivity manifested by the pronounced peak in $[\rho_c(B)-\rho_c(0)]/\rho_c(0)$ (**Figs. 4.58** and **4.59**)[150]. As B further rises, the remaining anti-parallel spins of Ru-O layers in both the soft and hard bi-layers also switch, finally completing the spin alignment at $B=B_{C1}$. Since conduction occurs in parallel for the two spin channels and scattering is now zero for the up-spin electrons and finite for down-spin electrons. Consequently, total spin scattering is drastically reduced, leading to a rapid drop in $\rho_c$ by as much as 40%, which is much larger than that seen in thin film multi-layers[131]. While $B_{C1}$ decreases with T, $B_{C2}$ increases slightly with T and disappears at T > 45 K (**Fig. 4.59 (c)**). This may be due to a reduction in the difference in soft and hard layer coercivities that become insignificant compared to the applied field at higher temperatures; as a result, switching may occur almost simultaneously for both the Cr-O and Ru-O layer, resulting in one sharp transition at $B_{C1}$, which persists up to 70 K.

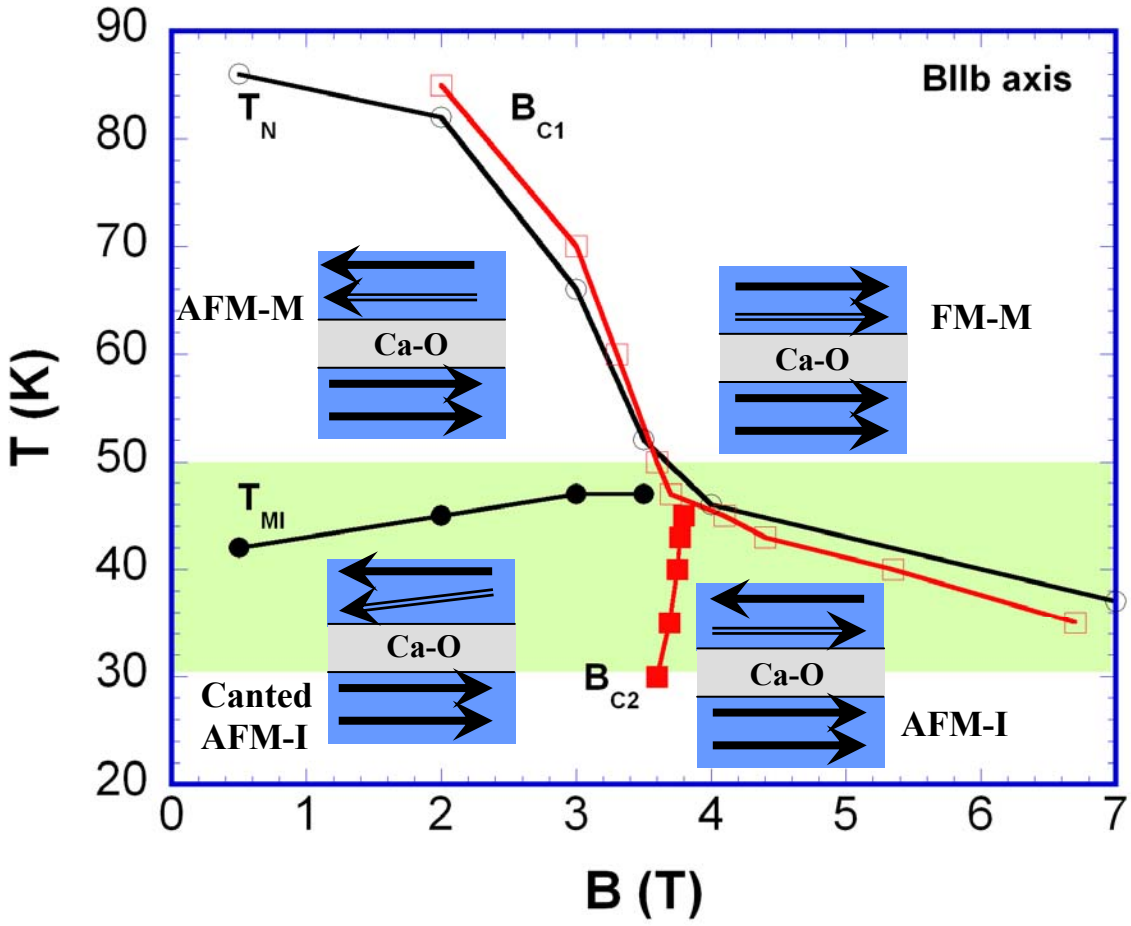


**Fig. 4.61** T-B diagram that represents different spin configurations in $Ca_3(Ru_{0.83}Cr_{0.17})_2O_7$.

**Fig. 4.61** shows a conclusive B-T phase diagram based on the discussions presented in the above paragraphs for B||b-axis. It is revealing that all transitions, $T_N$, $T_{MI}$, $B_{C1}$ and $B_{C2}$, meet at a tetra-critical point at B=3.8 T and T=45 K. It is in the vicinity of this point that the prominent spin-valve behavior exists.

# Chapter Five

# Conclusions and Recommendations

## 5.1 Conclusions:

In the RP series of ruthenium oxides, both the magnetic and the transport properties strongly depend on the relative orientation of the corner-shared $RuO_6$ octahedral, which is the building block of every compound. This structure dependence of physical properties persuades a strong coupling of lattice, charge, orbital and spin degrees of freedom in these compounds in general. In the present study, I have concentrated on the thermodynamics and transport properties of the calcium members of the RP ruthenates i.e. $Ca_{3n}Ru_nO_{3n+1}$, where n is the number of $RuO_6$ layers in a unit cell. Earlier investigations[11, 82, 83, 84] on the series reveal an evolution of physical properties as the number of $RuO_6$ layers or the dimension of the compounds is altered. However, my attention in the present work was focused more on the perovskite ($n=\infty$) and the bi-layered (n=2) calcium ruthenates, which provide a wealth of information on both conventional and unconventional physics. Being part of the Ca compounds of the RP series, these compounds are prone to more crystal distortions, courtesy, relatively smaller $Ca^{2+}$ ionic size. Both the ruthenates showed a variety of physical phenomena including intriguing borderline properties in one way or the other, with the crystal structure distortions playing a significant role. It is clear that the systems' ground state is unstable and is very sensitive to external perturbations viz. applied magnetic field, chemical doping etc. Hence a perturbative approach, chemical doping in particular, in these strongly correlated electron compounds prospered high yields and formed the keynote of this thesis.

### 5.1.1 Perovskite ruthenates:

Despite being the most extensively studied members of the RP series, the perovskite ruthenates still have a large territory to be conquered. $SrRuO_3$, possessing a crystal symmetry close to an ideal perovskite, lives up to the expectations of the band structure calculations by being an itinerant ferromagnet with $T_C$=165 K[84]. The reduced saturation moment ($M_S$=1.1 $\mu_B$/Ru) witnesses the itinerancy nature of the ordered spins. The itinerant electrons follow Fermi liquid theory at low temperatures as explained in section 4.3.1. However, the anomalous temperature dependence of resistivity at higher

temperatures pushes this system more towards the 'bad' metal category. The experimental results along with the theoretical predictions, point to a strong self doping by O 2p electrons to be behind the occurrence of an itinerant ferromagnetism in the compound. External perturbations like magnetic field and chemical doping are very effective in a more detailed understanding of the ground state, as the physical properties depend on the relative orientation of the corner shared $RuO_6$ octahedra. The chemical substitution studies in the compound so far had suppressed the ferromagnetic component and followed it up with a metal insulator transition. For instance, a thermodynamic and transport study on $SrRu_{1-x}Mn_xO_3$[94] crystals revealed that a ferromagnetic to antiferromagnetic state evolves, which is accompanied with a Mott transition leading up to a possible QCP at a critical Mn concentration. Whereas the Cr substitution study on $SrRuO_3$[108], which is the main theme of the current study portraits a completely different picture. The ferromagnetism in the parent compound is unusually enhanced in $SrRu_{1-x}Cr_xO_3$ by raising the $T_C$ from 165 K to 290 K for $0 < x < 0.30$. Unlike other 3d impurity doping, which reduce the $T_C$, the Ru 4d electrons and the Cr 3d electrons are strikingly synergistic, leading to a highly enhanced exchange interaction and/or narrowed bandwidth favorable for ferromagnetism. NMR studies[96] indicate that Cr is in $Cr^{3+}$ state and Ru is in a mixed valence state ($Ru^{4+}$ and $Ru^{5+}$). A broadened Ru $t_{2g}$ band and a possible $Ru^{4+}(d^4)$–$O^{2-}$–$Ru^{5+}(d^3)$ as well as $Ru^{4+}(d^4)$–$O^{2-}$–$Cr^{3+}(d^3)$ double-exchange interaction are hence viable. This exchange interaction involves the $Cr^{3+}$ in the ferromagnetic ordering and enhances the ordering temperature.

On the other hand, $CaRuO_3$ has a more distorted structure compared to that of $SrRuO_3$. The $RuO_6$ octahedra are rotated and tilted by an angle, making the interaction between electrons in the two Ru ions to be different than it were in its Sr counterpart. As a result, the band is narrow and induces a paramagnetic ground state with no long range ordering observed down to 30 mK[98]. In the meanwhile, the band is not narrow enough to localize the electrons and therefore the compound behaves as an itinerant electron system, but still not itinerant up to the level of Fermi liquid. This break down of Fermi liquid theory may suggest a magnetic instability that might occur at T=0 K. The intermediate bandwidth range in $CaRuO_3$ hence makes it more vulnerable to external perturbations viz. chemical substitution. It appears to be a common occurrence that with

only a slight impurity doping, the paramagnetic $CaRuO_3$ inevitably evolves into a magnetically ordered state. For instance, nonmagnetic ion substitutions in $CaRuO_3$ bring out the spin frustration in the compound and show enhanced moment below respective critical temperatures. However He and Cava[99] have shown that for M=Mn, Fe and Ni in $CaRu_{1-x}M_xO_3$, the system forms 'inhomogeneous' ferromagnetic materials. While almost every substitution (viz. Na[105], Sr[84], Sn[89] etc.) brought out a spin glass type ordering (with Rh[106] being an exception), Cr substitution abruptly induced ferromagnetism in $CaRuO_3$[108] with a saturation moment in the vicinity of 0.4 $\mu_B$/f.u. at Cr concentration, x=0.18. More contracted Cr 3d electrons replacing Ru 4d electrons favor a fairly narrower bandwidth and in turn a enhanced $N(E_F)$ results in ferromagnetism that was observed even for a small level of Cr doping. In contrast to He's[99] observation of critical temperature's inertness to substitution ion concentrations, $T_C$ in $CaRu_{1-x}Cr_xO_3$ shows a strong x dependence. Also largely unexpected is the presence of itinerant metamagnetism with Cr doping that evolves into a two step transition when x reaches 0.15. Indeed, the metamagnetism may occur in a nearly ferromagnetic metal that is characterized by a maximum in magnetic susceptibility[154]. However, the robust ferromagnetic behavior and the two-step metamagnetic transition in $CaRu_{1-x}Cr_xO_3$ suggest a complex, unique band structure resulted from the 3d-4d electron coupling. Another unexpected feature is the anisotropy in the magnetic properties as a result of Cr doping, which is not present otherwise. Cr ion develops a strong spin-orbit coupling in the system, in spite of the cubic nature of the crystals. It is worth mentioning that Cr doping could neither induce metamagnetic transitions nor influence any anisotropy in the physical properties of $SrRu_{1-x}Cr_xO_3$.

The drastic changes in the magnetic behavior of $CaRu_{1-x}Cr_xO_3$ and $SrRu_{1-x}Cr_xO_3$ with Cr doping conspicuously accompany no metal-insulator transition which is often observed for other impurity doping[89, 94, 97, 106]. This may be associated with the fact that in $Cr^{4+}$ ion, only two of the three Cr $t_{2g}$ levels are occupied and electron hopping between the $Cr^{4+}$ and $Ru^{4+}$ $t_{2g}$ orbitals is energetically favorable. Hence the dynamic itinerant character of the d-electrons is retained. The impurity doping, of course, introduces defects and disorder raising the electrical resistivity at low temperatures and this less metallic behavior for large x could be also associated with a site percolation of the

nearest neighbor Ru-Ru bonds[110]. The disruption of Ru connectivity affects the orientation of the $RuO_6$ octahedra (tilting angle), which to a great extent determines the properties of the ruthenates. Unlike all other impurity doping for the Ru site, slight Cr-doping facilitates the presence of the ferromagnetism that is extremely delicate in the perovskite ruthenates. Apparently, the Ru 4d-electrons and Cr 3d-electrons are unusually synergistic to promote ferromagnetism in these materials.

**5.1.2 Bi-layered calcium ruthenate:**

The n=2 members of the RP series (viz. $Ca_3Ru_2O_7$ and $Sr_3Ru_2O_7$) are very special as their position in the series demand them to display borderline properties. Their extreme sensitivity to external perturbations makes them one of the best hunting grounds to look for intriguing physical phenomena. For instance, the bi-layered calcium ruthenate inherits a huge variety of novel physical phenomena in it. The compound's novelty is revealed by its response to the applied magnetic field along different orientations and to the chemical substitution that followed. Even though the magnetization along b axis shows a sole transition at 56 K as a result of AFM spin ordering, the magnetization along a axis exhibits an additional transition at 48 K corresponding to a metal insulator transition[83]. At $B_C$=6 T, the system becomes a ferromagnet along a axis via a first order metamagnetic transition that polarizes 85% of the spins, but stays an antiferromagnet along the other directions. The extensive magnetic measurements persuade the magnetic ground state of the compound to be an A type antiferromagnet with AFM stacking of FM layers along c axis[112].

As mentioned at the start of this chapter, structure distortions play a vital role in determining the compound's physical behavior. The crystal structure of $Ca_3Ru_2O_7$ is severely distorted by a tilt of the $RuO_6$ octahedra, which projects primarily onto the ac plane, while it only slightly affects the bc plane[113]. These crucial bond angles have direct impact on the band structure and are the origin of the anisotropic properties of the compound. The transport and magnetic studies of $Ca_3Ru_2O_7$ for temperatures ranging from 0.4 to 350 K and magnetic fields B up to 45 T lead to strikingly different behavior when the field is applied along the different crystal axes. A ferromagnetic state with full spin polarization is achieved for B||a axis ($B_C$=6 T), magnetic easy axis, that drives the resistivity to drop by an order of magnitude. This drop in resistivity is a reflection of the

coherent motion of the charge carriers resulted by the FM/I/FM arrangement of RuO-CaO-RuO layers (similar to spin filters) once the spins are polarized[115].

But a colossal magnetoresistance[116], up to three orders of magnitude drop, was realized only for B||b axis ($B_C$=15 T), magnetic hard axis. Since 85% spin polarization along a axis attributes to only one order of magnitude drop, even a 100% spin polarization along b axis at higher fields, if that happens at all, could not account for the three order of drop in resistivity. This tells that the driving force for this CMR is not spin polarization as we would expect for a conventional CMR. For B||c axis, SdH oscillations are observed with frequencies 28 T and 10 T that is followed by a less resistive state than that for B||a, where the compound reaches a fully polarized state. Hence, in contrast with standard colossal magnetoresistive materials, which are primarily driven by spin polarization, the FM phase is the least favorable for electron hopping. Moreover, the field dependence of the $\rho_c$ measured with B along a axis in the temperature range $40 < T < 56$ K (see **Fig. 4.34**) shows a valley that could not be correlated with the magnetic field dependence of M. This behavior represents the crucial role of orbital degree of freedom in the conduction mechanism. To be specific, the experimental results persuade that the compound's Mott state at low temperatures and low fields is due to the orbital ordering that happens as a consequence of the c axis collapse (Jahn-Teller effect) at $T_{MI}$ (see **Figs. 4.26** and **4.33**). For B||a > 6 T, the field induced FM state stabilizes the OO state and hence a fully metallic state is never achieved. Whereas for B||b > $B_C$, the OO is removed by spin-orbit coupling and hence the electron mobility is increased leading to the CMR. All these results discussed in chapter 4 are complimented by the Raman spectroscopy studies[126] to provide a coherent picture illustrating that orbital order and its unusually strong coupling to lattice and spin degrees of freedom drive the exotic electronic and magnetic properties of $Ca_3Ru_2O_7$.

Furthermore, SdH oscillations that are vastly different from those along c axis reappear when magnetic field is swept through the ac plane. For B rotating within the ac-plane, slow and strong SdH oscillations periodic in 1/B are observed for low temperatures ($T \leq 1.5$ K)[117]. These oscillations are angular dependent and intimately correlated with the FM state. Moreover, the $1/\cos\theta$-like behavior of the oscillations when B is swept in the ac plane (see **Fig. 4.38**) may imply a cylindrical Fermi surface elongated along the c

axis, which favors the two-dimensional conductivity. However, for magnetic field applied along the ab-plane, oscillations are also observed but periodic in B[117]. The magnetoresistance oscillations periodic in B are common only in some mesoscopic systems and persist up to T=15 K in $Ca_3Ru_2O_7$. While the SdH effect suggests the presence of small FS pockets in the Mott-like state, the B-periodic oscillations, an exotic quantum phenomenon, may be a result of anomalous coupling of B to the $t_{2g}$ orbitals that makes the FS field dependent.

Recent density functional calculations have suggested that $Ca_3Ru_2O_7$ is a nearly half-metallic system[111]. When magnetic field is applied along a and b axes, the AFM-M region between the two transitions (viz. $T_{MI}$ and $T_N$) responded in exact opposite sense i.e. semiconducting behavior for B||a and enhanced metallicity for B||b, a characteristic of a half metal. However, the AFM-M state exists only over an 8 K interval between the two transitions[83], which is too narrow for the essential physics to be fully revealed and investigated. Therefore, we pursued transport and thermodynamic studies of $Ca_3(Ru_{1-x}Cr_x)_2O_7$ with $0 \leq x \leq 0.20$ as Cr substitution greatly widens the stability range of the AFM-M regime to 70 K[150] by depressing $T_{MI}$ and drastically raising $T_N$. The studies revealed a few striking phenomena as a result of the 4d – 3d electron coupling in this Ru-Cr system. One set of data persuaded a half-metallic behavior where the AFM-M state evolved to exhibit a semiconducting characteristic along one direction (for B||a axis) and an enhanced metallic property along the other (for B||b axis). This anisotropic transport behavior also affirms the dominance of electron's spin in its transport in the compound.

The second important observation pertains to the spin valve behavior observed for the first time in a bulk material; a single crystal in our case. A string of systematic magnetic and electrical resistivity measurements performed on the 17% Cr substituted bi-layered calcium ruthenate[150] i.e. $Ca_3(Ru_{0.83}Cr_{0.17})_2O_7$, suggested that the magnetic lattice involving Ru-Cr ions are instrumental in inducing a spin-valve behavior. Along a preferred crystal direction (b axis) the compound shows a canting of AFM spins that develops as B is increased. The magnetic lattice tends to be soft in this direction which was obvious from the unusually large $\Delta T_N/\Delta B$ (~7.5 K/T). But the layers involving the un-substituted Ru still stay hard magnetically. Cr substitution hence creates a layered structure with alternating soft and hard magnetic bi-layers. This special Cr induced spin

configuration facilitates subtle intermediate anitparallel spin alignments within a layer, in a certain field range ($B_{C2} < B < B_{C1}$), as seen in **Fig. 4.60** to induce a spin-valve behavior for B||b-axis.

Previous to our work, the spin-valve phenomenon was realized solely in heterostuctural multilayer films and never observed in a bulk material[131]. This work presents strong evidence that for the first time spin-valve behavior occurs in a bulk material whose properties also resemble a half metallic system.

**5.2 Recommendations:**

The electron correlation effects and phase transitions can be better understood when specific heat measurements are conducted on a material. $CaRuO_3$, although an itinerant system, is not a Fermi liquid yet. The breakdown of Fermi liquid theory is realized through the $T^{3/2}$ dependence of low temperature ($T < 20$ K) resistivity of the compound. This might be a prelude to a quantum critical behavior as it is quite often than is not. Specific heat measurements on $CaRuO_3$ would provide more insight into the system particularly on the potential QCP in the compound. The measurements done on the pure sample could then be extended to the chemically substituted compounds too to explore the underlying interesting physics. Specific heat measurements, without any second thought, are one of the powerful tools available for doing the job. For instance, specific heat studies done at zero and non-zero magnetic fields on a similar compound $SrIrO_3$[104] revealed the system's possible proximity to QCP.

A more detailed isothermal magnetization studies on the 18% Cr substituted $CaRuO_3$ indicated a behavior very close to a switching effect. Although the magnetic field dependence of M has little to no effect on the orientation of the single crystal, the resistivity of the compound strongly depends on the relative orientation of the magnetization and the electric current. The magnetoresistance experiments done on the compound reflects the spin polarization but in a rather complicated way as shown in **Fig. 5.1**. There are few features that are worth mentioning here. First, when B and I are directed parallel to each other there is a sharp resistivity drop of 20% corresponding to the observed spin polarization. But the MR does not show any symmetric effect when the magnetic field is reversed as one would have expected, since electron conduction should be the same when the spins are aligned parallel irrespective of the up or down nature of

them. Rather it chose to behave antisymmetrically as shown in **Fig. 5.1 (a)**. Second, when B and I are aligned perpendicular, the effect is reversed where for the positive field it shows a positive MR, increasing the resistivity by a few percent. Similar to the effect of B||I scenario, the MR shows an opposite effect for the field reversal as shown in **Fig. 5.1 (b)**. The possible explanation for this peculiar effect would involve a detailed interpretation of the domain wall dynamics of the material. However, in simpler terms, the charge carriers are deflected in the opposite directions in the two domains of M, which induces a circulating current in the vicinity of the domain wall. Now when this induced current ($I_{ind}$) is parallel to the applied current ($I_{app}$), it yields a negative MR as in the positive B side of the **Fig. 5.1 (a)**. On M reversal, the induced circulating current changes direction giving a situation where the applied and the induced currents are antiparallel that induces a positive MR. Hence it will pave way for an antisymmetric MR such as the one observed in this system. Similar explanation holds true when $I_{app}$ and $I_{ind}$ (i.e. I and B) are perpendicular to each other, where too the relative direction of the circulating current determines the nature of the MR whether positive or negative. The third observation from the experiment is that the drop/jump in MR is not uniform if we compare it on both sides of the zero line of the field. This could be explained by the fact that the circulating current is non-uniform due to Hall Effect that drives the non-uniformity in the MR as M is reversed. These preliminary results help us have a bird's-eye view of the underlying physics and it could only trigger a more vigorous investigation to understand the dynamics of the spins in the microscopic level of the compound and not much more than that. This complicated behavior deserves a more careful study that leads to a deeper insight into this intriguing problem.

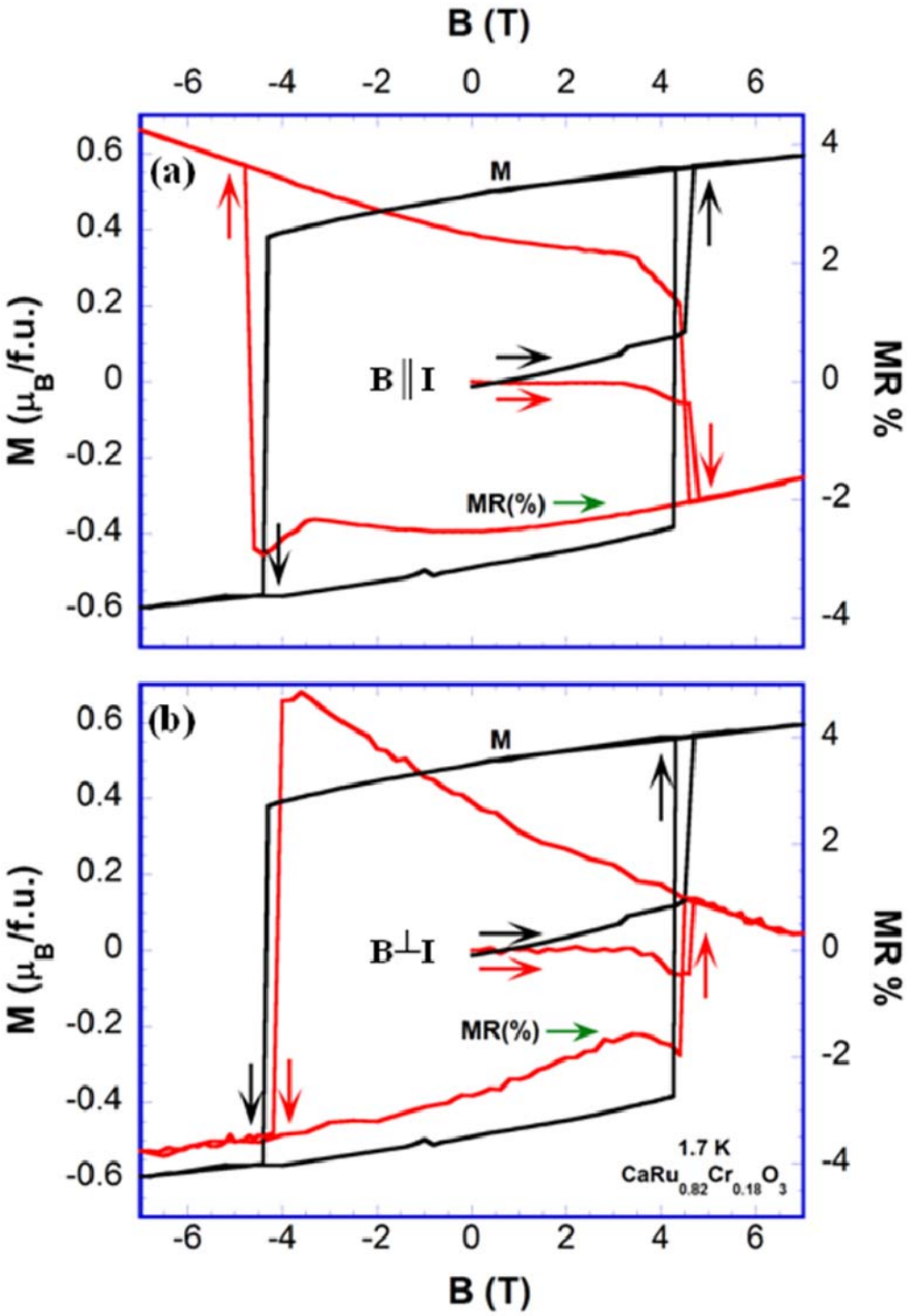


**Fig 5.1** Isothermal magnetic field dependence of magnetization, M, (left scale) and magnetoresistance, MR, (right scale) when **(a)** B||I and **(b)** B⊥I, at T=1.7 K for $CaRu_{0.82}Cr_{0.18}O_3$ in the applied field range $-7 \leq B \leq 7$ T.

Even though, the Cr substituted $CaRuO_3$ that we studied so far unveiled a wealth of information, we believe that characterizing a whole spectrum of compounds involving

Ru and Cr ions will have much in store. However, the synthesis difficulty of higher Cr concentrations in $SrRu_{1-x}Cr_xO_3$ and $CaRu_{1-x}Cr_xO_3$ hinder us from doing it. For instance, the compounds with large x in $CaRu_{1-x}Cr_xO_3$ would reveal a FM semiconductor (refer to **Fig. 4.20**), which might find potential applications. Whereas, a higher Cr concentration in $SrRu_{1-x}Cr_xO_3$ would represent a compound that displays itinerant spin polarization at temperatures above room temperature. On the other hand, a lower Cr concentration might very well help us tune the DOS and to understand the basic physics behind the abrupt FM observed in Cr doped $CaRuO_3$, as the transition is very abrupt for x as small as 0.05.

The rich orbital and magnetic phase diagram in $Ca_3Ru_2O_7$ is precipitated by the interplay between the applied magnetic field, magnetic exchange and spin orbit coupling. Although the origin is likely to be orbital ordering, the intense physics behind these interesting phenomena in $Ca_3Ru_2O_7$ still needs an extensive investigation. As I have been emphasizing throughout this thesis, chemical substitution is one of the few potential ways to understand this highly correlated compound. So far only the Ca site has been targeted for chemical substitution and both Sr and La doping yielded fruitful results. The transition metal ion was substituted for the first time with Cr and it responded with a rare spin-valve behavior in a bulk system. Similar surprises could be expected of the system when Ru is substituted with other 3d, 4d or 5d transition metal ions. Other substitutions like Mn, Ti, Ir, Rh etc. for Ru might alter the DOS and/or the spin configuration of the system in a different/similar way as Cr does. Thus they will help explore new phenomena and at the same time would help to dig deep into the AFM-M and the half metallicity frontiers.

Another possible path that could be taken from here is the Cr substitution studies on other compounds of the RP series too, as every member of the series reacts to doping and significantly so to Cr. The Cr-Ru electron coupling favors electron interactions in these compounds and it would only be better if Ru is substituted in a compound like $Sr_4Ru_3O_{10}$, for instance. It is a triple layered member of the RP series that lies between a robust ferromagnet ($SrRuO_3$, $n=\infty$) in one side and a metamagnet ($Sr_3Ru_2O_7$, n=2) on the other. Aptly so, it shows a borderline magnetism[11] with ferromagnetic behavior ($T_C$=102 K) along c axis (perpendicular to the layers) and a metamagnetism along the basal plane ($B_C$=3 T). Moreover, the specific heat capacity measurements, done on this compound

show its proximity to a quantum critical point[155]. The substitution for Sr ion in the form of La and Ca on this system have already provided promising results[79], which are examples to show that the band filling is more effective than the structure distortion in this system. These substantial works illustrate that the rare borderline magnetism in $Sr_4Ru_3O_{10}$ is highly sensitive to $g(E_F)$ that is critically linked to band filling and structural distortions, which should motivate one to dope on the Ru site too.

To facilitate a better understanding of the physics behind these exotic compounds, along with the above mentioned works done in-house, we also get an extended help from elastic and non-elastic neutron scattering techniques to reveal their magnetic structure and the magnetic interactions in them. Only this quest to explore new phenomena could drive us further in the direction of developing novel materials.

**References:**


1. PA Cox, Transition Metal Oxides, Clarendon, Oxford (1995)
2. KA Müller and JG Bednorz, Science **237** 1133 (1987)
3. Y Moritomo, A Asamitsu, H Kuwahara and Y Tokura, Nature **380** 141 (1996)
4. Y Tokura and N Nagaosa, Science **288** 462 (2000)
5. SA Wolf, DD Awschalom, RA Buhrman, JM Daughton, S von Molnár, ML Roukes, AY Chtchelkanova and DM Treger, Science **294** 1488 (2001)
6. J Daugton and J Granley, The Industrial Physicist **5** 22 (1999)
7. G Kotliar and D Vollhart, Physics Today **57** 53 (2004)
8. R Dreizler, E Gross, Density Functional Theory, Plenum Press, New York (1995)
9. AM Boring and JL Smith, Los Alamos Science **26** 90 (2000)
10. P Fazekas, Lecture Notes on Electron Correlation and Magnetism – Series of Modern Condensed Matter Physics – Vol. **5**, World Scientific, Singapore (1999)
11. G Cao, WH Song, YP Sun and XN Lin, Solid Stat. Comm. **131** 331 (2004)
12. SN Ruddlesden and P Popper, Acta. cryst. **11** 54 (1958)
13. http://chemed.chem.purdue.edu/genchem/topicreview/bp/ch12/crystal.php
14. Stephen Blundell, Magnetism in condensed matter, (Oxford University Press, New York) (2001)
15. Oleg Krupin, Dichroism and Rashba effect at magnetic crystal surfaces of rare earth metals, Chapter **8** (Inaugural-dissertation, Fachbereich Physik, Freie Universität Berlin) (2004)
16. A Lehmann-Szweykowska et. al., J. Phys.: Cond. Matt. **13** 3607 (2001)
17. T Egami and D Louca, J. Superconductivity **12** 23 (1999)
18. Laurent-Patrick Levy, Magnetism and Superconductivity, Springer (2000) (chapter 2 from here)
19. L Landau, Zeits. f. Physik, **64** 629 (1930)
20. WA Harrison, Solid state theory, McGraw-Hill Book Co. (1970)
21. JM Ziman, Principles of the theory of solids, Cambridge University Press (1972)
22. P Langevin, J. de Physique, **4** 678 (1905)
23. CA Wert and RM Thomson, Physics of solids, McGraw-Hill Book Co. (1970)
24. P Weiss, J. de Physique **6** 667 (1907)

25. W Pauli, Zeits. f. Physik **41** 81 (1927)
26. JH Van Vleck, Quantum Mechanics - The key to understanding Magnetism, Nobel Lecture, 8 December (1977)
27. EC Stoner, Proc. Roy. Soc., A **169** 339 (1939)
28. A Abragam, Principles of Nuclear Magnetism, Oxford University Press, (1961)
29. HL Schläfer, G Gliemann, Basic Principles of Ligand Field Theory, Wiley Interscience (New York) (1969)
30. GK Woodgate, Elementary Atomic Structure, McGraw-Hill (1970)
31. LH Thomas, Nature (London), **117** 514 (1926)
32. HN Russell and FA Saunders, Astrophysical Journal, **61** 38 (1925)
33. L Pauling, J. Am. Chem. Soc. **53** 1367 (1931)
34. RC Evans, An Introduction to Crystal Chemistry, Cambridge university press, (1964)
35. C Noce, A Vecchione, M Cuoco and A Romano, Ruthenate and Rutheno-Cuprate Materials, Springer (2003)
36. H Yamada, AJ Bhattacharyya and J Maier, Adv. Functional Materials, **16** 525 (2005)
37. HA Jahn and E Teller, Proc. R. Soc. London, A **161** 220 (1937)
38. JB Goodenough, Magnetism and the Chemical Bond, Interscience Publ., (New York-London) (1963)
39. G Khaliullin, Progress of Theoretical Physics, **160** 155 (2005)
40. G Khaliullin and S Maekawa, Phys. Rev. Lett., **85** 3950 (2000)
41. NF Mott, Proc. R. Soc. London, A **382** 1 (1982)
42. NF Mott, Metal-Insulator Transitions, Taylor & Francis (London) (1990)
43. DB McWhan, TM Rice and JP Rameika, Phys. Rev. Lett., **23** 1384 (1969)
44. A Georges, G Kotliar, W Krauth and MJ Rozenberg, Rev. Mod. Phys. **68** 13 (1996)
45. RG Moore, J Zhang, VB Nascimento, R Jin, J Guo, GT Wang, Z Fang, D Mandrus and EW Plummer, Science **318** 615 (2007)
46. AV Shubnikov and NN Sheftal, Growth of crystals, Vol.3, Consultants Bureau (1962)

47. F Rosenberger, Fundamentals of crystal growth I, Springer-Verlag (1981)
48. T Feder, issues & events, Physics Today **60** 26 Aug (2007)
49. Instruction manual – SC II–MDH–11020 Single crystal growing apparatus, NEC Machinery Corporation, September (2002)
50. Technical report, Crystal Systems Inc., No. FZ-E-002, March (1997)
51. K Kitamura, S Kimura, J. of Cryst. Growth **48** 469 (1980)
52. X Lin, Ph.D. dissertation, University of Kentucky (2006)
53. G Cao, Ph.D. Dissertation, Temple University (1992)
54. G Cao, SC McCall, JE Crow and RP Guertin, Phys. Rev. B 56 5387 (1997)
55. BD Cullity and SR Stock, Elements of X-ray diffraction, Addison Wesley publishing Co. (1978)
56. MT Postek, KS Howard, AH Johnson and KL McMichael, Scanning Electron Microscopy, A Student's Handbook, Ladd Research Industries (1980)
57. NW Ashcroft, ND Mermin, Solid State Physics, Saunders (1976)
58. User's Manual, Powder X-ray Diffractometer, Scintag
59. www.chem.uky.edu/parkin
60. http://www.engr.uky.edu/emc/facilities/sem.html
61. http://www.mos.org/sln/SEM/tour20.html
62. DC Bell, Energy Dispersive X-ray analysis in the electron microscope, BIOS Scientific publishers Ltd., (2003)
63. Courtesy: http://hyperphysics.phy-astr.gsu.edu/hbase/solids/squid.html#c1
64. http://www.nanomagnetics.org/instrumentation_and_characterization/squid_magnetometers.php
65. User's manual, MPMS® XL, Quantum Design
66. User's manual - Model 2400 series SourceMeter®, Keithley
67. User's manual - Model 2182 Nanovoltmeter, Keithley
68. JC Lashley, MF Hundley, A Migliori, JL Sarrao, PG Pagliuso, TW Darling, M Jaime, JC Cooley, WL Hults, L Morales, DJ Thoma, JL Smith, J Boerio- Goates, BF Woodfield, GR Steward, RA Fisher and NE Phillips, Cryogenics **43** 369 (2003)
69. Brochure, Advanced Heat capacity and He-3 option, Quantum Design

70. User's manual - PPMS® Heat Capacity option – Quantum Design
71. S Sachdev, Science **288** 475 (2000)
72. Y Maeno, H Hashimoto, K Yoshida, S Nishizaki, T Fujita, JG Bednorz and F Lichtenberg, Nature **372** 532 (1994)
73. K Ishida, H Mukuda, Y Kitaoka, K Asayama, ZQ Mao, Y Mori and Y Maeno, Nature **396** 658 (1998)
74. GM Luke, Y Fudamoto, KM Kojima, MI Larkin, B Nachumi, YJ Uemura, Y Maeno, ZQ Mao, Y Mori and H Nakamura, Nature **394** 558 (1998)
75. R Jin, Yu Zadorozhny, Y Liu, DG Schlom, Y Mori and Y Maeno, Phys. Rev. B **59** 4433 (1999)
76. SA Grigera, RS Perry, AJ Schofield, M Chiao, SR Julian, GG Lonzarich, SI Ikeda, Y Maeno, AJ Millis and AP Mackenzie, Science **294** 329 (2001)
77. RP Perry, LM Galvin, SA Grigera, AJ Schofield, AP Mackenzie, M Chiao, SR Julian, SI Ikeda, S Nakatsuji and Y Maeno, Phys. Rev. Lett. **86** 2661 (2001)
78. M Crawford, RL Harlow, W Marshall, Z Li, G Cao, RL Lindstrom, Q Huang and JW Lynn, Phys. Rev. B **65** 214412 (2002)
79. S Chikara, V Durairaj, WH Song, YP Sun, XN Lin, A Douglass, G Cao and P Schlotmann, Phys. Rev. B **73** 224420 (2006)
80. JJ Randall and R Ward, J. Am. Chem. Soc. **81** 2629 (1959)
81. A Kanbayasi, J. Phys. Soc. Jpn. **41** 1876 (1976)
82. S Nakatsuji and Y Maeno, Phys. Rev. Lett. **84** 2666 (2000)
83. G Cao, S McCall, JE Crow and RP Guertin, Phys. Rev. Lett. **78** 1751 (1997)
84. G Cao, S McCall, M Shepard, JE Crow and RP Guertin, Phys. Rev. B **56** 321 (1997)
85. RJ Cava, The Royal Soc. Chem. (2004)
86. I Mazin and DJ Singh, Phys. Rev. B **56** 2556 (1997)
87. L Klein, JS Dodge, CH Ahn, JW Reiner, L Mieville, TH Geballe, MR Beasley and A Kapitulnik, J. Phys.: Cond. Matter. **8** 10111 (1996)
88. PB Allen, H Berger, O Chauvet, L Forro, T Jarlborg, A Junod, B Revaz and G Santi, Phys. Rev. B **53** 4393 (1996)

89. G Cao, S McCall, J Bolivar, M Shepard, F Freibert, P Henning, JE Crow and T Yuen, Phys. Rev. B **54** 15144 (1996)
90. L Klein *et al.*, Phys. Rev. Lett. **77** 2774 (1996)
91. MS Laad and E Muller-Hartmann, Phys. Rev. Lett. **87** 246402 (2001)
92. PA Cox et al., J. Phys. Cond. Matt. **16** 6221 (1983)
93. G Cao, Y Xin, CS Alexander and JE Crow, Phys. Rev. B **63** 184432 (2001)
94. G Cao, S Chikara, XN Lin, E Elhami, V Durairaj and P.Schlottmann, Phys. Rev. B **71** 035104 (2005)
95. L Pi, A Maignan, R Retoux and B Raveau, J. Phys.: Cond. Matt. **14** 7391 (2002)
96. ZH Han, JI Budnick, WA Hines, B Dabrowski, S Kolesnik and T Maxwell, J. of Phys-Cond. Matt. **17** 1193 (2005)
97. T He and RJ Cava, J. Phys: Cond. Matt. **13** 8347 (2001)
98. TC Gibb, RG Greatrex, NN Greenwood and P Kaspi, J. Chem. Soc. (Dalton Trans.) 1253 (1973)
99. T He and R J Cava, Phys. Rev. B **63** 172403 (2001)
100. K Yoshimura, T Imai, T Kiyama, KR Thurber, AW Hunt and K Kosuge, Phys. Rev. Lett. **83** 4397 (1999)
101. T Kiyama, K Yoshimura, K Kosuge, H Michor and G Hilscher, J. Phys. Soc. Jpn. **67** 307 (1998)
102. T Kiyama, K Yoshimura and K Kosuge, J. Phys. Soc. Jpn. **68** 3372 (1999)
103. H Mukuda, K Ishida, Y Kitaoka, K Asayama, R Kanno and M. Takano, Phys. Rev. B **60** 12279 (1999)
104. G Cao, V Durairaj, S Chikara, LE DeLong, S Parkin and P Schlottmann, Phys. Rev. B **76** 100402(R) (2007)
105. M Shepard, G Cao, S McCall, F Freibet and JE Crow, J. Appl. Phys. **79** 4821 (1996)
106. G Cao, F Freibert and JE Crow, J. Appl. Phys. **81** 3884 (1997)
107. V Hardy, B Raveau, R Retoux, N Barrier and A Maignan, Phys. Rev. B **73** 094418 (2006)
108. V Durairaj, S Chikara, XN Lin, A Douglass, G Cao, P Schlottmann, ES Choi and RP Guertin, Phys. Rev. B **73** 214414 (2006)

109. JB Goodenough, JM Longo and JA Kafalas, Mat. Res. Bull. **3** 471 (1968)
110. JW Essam, in Phase Transitions and Critical Phenomena, edited by C Domb and MS Green, (Academic Press, London, 1972), vol. 2, p. 197
111. DJ Singh, S Auluck Phys. Rev. Lett. **96** 097203 (2006)
112. S McCall, G Cao and JE Crow, Phys. Rev. B **67** 094427 (2003)
113. G Cao, L Balicas, Y Xin, JE Crow and CS Nelson, Physica C **387** 247 (2003)
114. S McCall, G Cao, JE Crow, et al. Physica B **246** 144 (1998)
115. G Cao, L Balicas, Y Xin, E Dagotto, JE Crow, CS Nelson, and DF Agterberg, Phys. Rev. B **67** 060406(R) (2003)
116. XN Lin, ZX Zhou, V Durairaj, P Schlottmann and G Cao, Phys. Rev. Lett. **95** 017203 (2005)
117. V Durairaj, XN Lin, ZX Zhou, S Chikara, E Elhami, P Schlottmann and G Cao, Phys. Rev. B **73** 054434 (2006)
118. RP Guertin, J Bolivar, G Cao, S McCall, JE Crow, Solid Stat. Comm. **107** 263 (1998)
119. Y Yoshida, SI Ikeda, H Matsuhata, N Shirakawa, CH Lee and S Katano, Phys. Rev. B **72** 054412 (2005)
120. G Cao, S McCall, JE Crow and RP Guertin, Phys. Rev. B **56** 5387 (1997)
121. G Cao, S McCall, JE Crow and RP Guertin, Phys. Rev. B **56** 2910(R) (1997)
122. S Nishizaki, Y Maeno, S Farner, S Ikeda and T Fujita, J. Phys. Sot. Japan **67** 560 (1998)
123. AV Puchkov, MC Schabel, DN Basov, T Startseva, G Cao, T Timusk and ZX Shen, Phys. Rev. Lett. **81** 2747 (1998)
124. DB McWhan, JP Remeika, TM Rice, WF Brinkman, JP Maita and A Menth, Phys. Rev. Lett. **27** 941 (1971)
125. SA Carter, TF Rosenbaum and P Metcalf, Phys. Rev. B **48** 16841 (1993)
126. JF Karpus, R Gupta, H Barath, et al. Phys. Rev. Lett. **93** 167205 (2004)
127. Y Yoshida, SI Ikeda, N Shirakawa, J. of the Physical Society of Japan **76** 085002 (2007)
128. G Cao, L Balicas, XN Lin, S Chikara, E Elhami, V Durairaj, JW Brill, RC Rai and JE Crow, Phys. Rev. B **69** 014404 (2004)

129. Y Tokura, Colossal Magnetoresistive Oxides (Gordon and Beach Science, Australia, 2000)
130. AB Pippard, Magnetoresistance in Metals (Cambridge University Press, Cambridge, 1989).
131. EY Tsymbal and DG Pettifor, Solid State Physics, edited by Henry Ehrenreich and Frans Spaepen Vol. **56** p. 113(Academic Press, New York, 2001)
132. The incoherent-coherent crossover behavior in the correlated systems was suggested by DMFT - J Merino et al., Phys. Rev. B **61** 7996 (2000)
133. T Valla et al., Nature (London) **417** 627 (2002)
134. AJ Millis, Nature (London) **417** 599 (2002)
135. DJ Singh and II Mazin, Phys. Rev. B **63** 165101 (2001)
136. G Cao, K Abbound, S McCall, JE Crow and RP Guertin, Phys. Rev. B **62** 998 (2000)
137. G Cao, L Balicas, Y Xin, JE Crow and CS Nelson, Phys. Rev. B **67** 184405 (2003)
138. CWJ Beenakker and H van Houten, Solid State Physics edited by H. Ehrenreich and D Turnbull, Vol. **44** p.65 (Academic Press, New York, 1991)
139. RA Webb, S Washburn, CP Umbach and RB Laibowitz, Phys. Rev. Lett. **54** 2696 (1985)
140. EH Sondheimer, Phys. Rev. **80** 401 (1950)
141. A Yacobi, R Schuster and M Heilblum, Phys. Rev. B **53** 9583 (1996)
142. P Schlottmann and AA Zvyagin, J. Appl. Phys. **79** 5419 (1996)
143. T Hotta and E Dagotto, Phys. Rev. Lett. **88** 017201 (2002)
144. G Gruner, Density Waves in Solids (Addison- Wesley, New York, 1994)
145. JB Gunn, Solid State Comm. **1** 88 (1963)
146. FK Manasse, Semiconductor Electronics Design **(**Prentice Hall, Englewood Cliffs, 1977)
147. E Ohmichi, Y Yoshida, SI Ikeda, N Shirakawa and T Osada, Phys. Rev. B **70** 104414 (2004)
148. V Varadarajan, S Chikara, V Durairaj, XN Lin, G Cao and JW Brill, Solid Stat. Comm.**141** 402 (2007)

149. G Cao, S McCall, V Dobrosavljevic, CS Alexander, JE Crow and RP Guertin, Phys. Rev. B **61** 5053(R) (2000)
150. G Cao, V Durairaj, S Chikara, LE DeLong and P Schlottmann, Phys. Rev. Lett. **100** 016604 (2008)
151. B Dabrowski, O Chmaissem, PW Klamut, S Kolesnik, M Maxwell, J Mais, Y Ito, BD Armstrong, JD Jorgensen and S Short, Phys. Rev. B **70** 014423 (2004)
152. Eric Fawcett, Rev. Mod. Phys. **60** 209 (1988)
153. RA de Groot, FM Mueller, PG van Engen and KHJ Buschow, Phys. Rev. Lett. **50** 2024 (1983)
154. EP Wohlfarth, P Rhodes, Philos. Mag. **7** 1817 (1962)
155. G Cao, S Chikara, JW Brill and P Schlottmann, Phys. Rev. B **75** 024429 (2007)

# Mr. Vinobalan Durairaj

## Personal Details

**Date of Birth**: 18th May 1979 **Place of Birth**: Tirunelveli (Tamilnadu, India)

## Education

**Ph.D.** (Physics), University of Kentucky, Lexington, KY, USA, Dec 2008 (Expected)
***Thesis:*** A systematic study of thermodynamic and transport properties of layered $Ca_{n+1}(Ru_{1-x}Cr_x)_nO_{3n+1}$ (funded in part by the Dissertation Year Fellowship)
***Advisor:*** Dr. Gang Cao, Professor in Physics, University of Kentucky, KY, USA
**M.S.** (Physics), University of Kentucky, Lexington, KY, USA, Dec 2005
**M.Sc.** (Physics), Pondicherry University, Pondicherry, PY, India, May 2001
**B.Sc.** (Physics), Manonmaniam Sundaranar University, Tirunelveli, TN, India, May 1999

## Professional Experience

**Medical Physicist,** 2007–present
West Physics Consulting, LLC, Atlanta, USA
**Graduate Research Assistant, *Novel Materials Lab,*** 2002–2007
*Advisor*: Dr. Gang Cao, Professor in Physics, University of Kentucky, Lexington, USA
**Graduate Teaching Assistant,** 2002–2007
Department of Physics and Astronomy, University of Kentucky, Lexington, USA
**Junior Research Fellow, *Space Physics Lab*** (A unit of Indian Space Research Organization)**,** 2001–2002
*Supervisor*: Dr. M N Sasi, Scientist SG, Vikram Sarabhai Space Center, Thiruvananthapuram, India
**Visiting Research Student, *Inter-University Center for Astronomy and Astrophysics***, 2000
*Supervisor*: Dr. Jayant Vishnu Narlikar, Founder & Director, IUCAA, Pune, India

## Scholastic and Professional Honors

- Commonwealth Research Award 2006–2007, University of Kentucky, Lexington, USA, 2007
- Dissertation Year Fellowship – topped the list of 45 nominations that represented different disciplines from as many as 20 colleges of University of Kentucky, Lexington, USA, 2006–2007
- Graduate Research and Teaching Assistantships, Department of Physics and Astronomy – include Kentucky Graduate Scholarship by University of Kentucky, Lexington, USA, 2002–2006
- Commonwealth Research Award 2005–2006, University of Kentucky, Lexington, USA, 2006
- International Travel Student Support Award, University of Kentucky, Lexington, USA, 2005
- SNS–HFIR Users Meeting Scholarship, Oak Ridge National Lab, Oak Ridge, USA, 2005
- Domestic Travel Student Support Award, University of Kentucky, Lexington, USA, 2005
- Junior Research Fellowship, ISRO, Department of Space, Government of India, 2001–2002

## Communications (Please refer to the attached publication list)

– Coauthored 17 papers in leading journals (including 3 Physical Review Letters & 9 Physical Review Bs)
– Delivered lectures (including 10 invited talks) and presented posters in professional conferences/seminars

## Professional Affiliations

- American Association of Physicists in Medicine (AAPM)
- American Physical Society (APS)
- Neutron Scattering Society of America (NSSA)
- SNS/HFIR Users Group (SHUG)

## Publications in Peer-reviewed Journals:

*(Including 3 Physical Review Letters and 9 Physical Review B's)*

1. BJ Kim, Hosub Jin, SJ Moon, JY Kim, BG Park, CS Leem, Jaejun Yu, TW Noh, C Kim, SJ Oh, ***V Durairaj***, G Cao, E Rotenberg, JH Park – 'Novel $J_{eff} = 1/2$ Mott state induced by relativistic spin-orbit coupling in $Sr_2IrO_4$' – *Phys. Rev. Lett.* **101** 076402 (2008)
2. G Cao, ***V Durairaj***, S Chikara, LE De Long, P Schlottmann – 'Observation of strong spin valve effect in bulk $Ca_3(Ru_{1-x}Cr_x)_2O_7$' – *Phys. Rev. Lett.* **100** 016604 (2008)
3. A Bautista, ***V Durairaj***, S Chikara, G Cao, KW Ng, AK Gupta – 'A study of the Mott transition in $Ca_3Ru_2O_7$ by tunneling spectroscopy' – *Solid State Comm.* **148** 240 (2008)
4. G Cao, ***V Durairaj,*** S Chikara, LE Delong, S Parkin, P Schlottmann – 'Non-Fermi-liquid behavior in nearly ferromagnetic $SrIrO_3$ single crystals' – *Phy. Rev. B* **76** 100402(R) (2007)
5. L Shlyk, S Kryukov, ***V Durairaj***, S Parkin, G Cao, LE De Long – **'**Crystal structure, magnetic and electronic properties of a $Ba_3InRu_2O_9$ single crystal' – *J. of Magnetism and Magnetic Materials* **319** 64 (2007)
6. G Cao, ***V Durairaj***, S Chikara, S Parkin, P Schlottmann – 'Partial antiferromagnetism in spin-chain $Sr_5Rh_4O_{12}$, $Ca_5Ir_3O_{12}$ and $Ca_4IrO_6$ single crystals' – *Phys. Rev. B* **75** 134402 (2007)
7. V Varadarajan, S Chikara, ***V Durairaj***, XN Lin, G Cao, JW Brill – 'Specific heat of $(Ca_{1-x}Sr_x)_3Ru_2O_7$ single crystals' – *Solid State Comm.* **141** 402 (2007)
8. S Chikara, ***V Durairaj***, WH Song, YP Sun, XN Lin, A Douglass, G Cao – 'Borderline magnetism in $Sr_4Ru_3O_{10}$: Impact of dilute La and Ca doping on itinerant ferromagnetism and metamagnetism' – *Phys. Rev. B* **73** 224420 (2006)
9. ***V Durairaj,*** S Chikara, XN Lin, A Douglass, G Cao, P Schlottmann, ES Choi, RP Guertin **–** 'Highly anisotropic magnetism in Cr doped perovskite ruthenates' – *Phys. Rev. B* **73** 214414 (2006)
10. ***V Durairaj,*** XN Lin, S Chikara, E Elhami, A Douglass, G Cao, ZX Zhou, P Schlottmann **– '**Observation of oscillatory magnetoresistance periodic in 1/B and B in $Ca_3Ru_2O_7$' – *Phys. Rev. B* **73** 054434 (2006)
11. M Freamat, XN Lin, ***V Durairaj,*** S Chikara, G Cao, JW Brill **– '**Thermodynamic properties of the spin-chain compound $Pr_3RuO_7$' – *J. de Phys. IV* **131** 339 (2005)
12. M Freamat, XN Lin, ***V Durairaj,*** S Chikara, G Cao, JW Brill **– '**Thermal and magnetic properties of the spin-chain Material $Pr_3RuO_7$' – *Phys. Rev. B* **72** 014458 (2005)
13. XN Lin, ZX Zhou, ***V Durairaj,*** P Schlottmann, G Cao **– '**Colossal magnetoresistance by avoiding a ferromagnetic state in the Mott system $Ca_3Ru_2O_7$' – *Phys. Rev. Lett.* **95** 017203 (2005)
14. G Cao, S Chikara, XN Lin, E Elhami, ***V Durairaj,*** P Schlottmann **– '**Itinerant ferromagnetism to insulating antiferromagnetism: A magnetic and transport study of single crystal $SrRu_{1-x}Mn_xO_3$ $(0 \leq x < 0.60)$' – *Phys. Rev. B* **71** 035104 (2005)
15. G Cao, L Balicas, XN Lin, S Chikara, E Elhami, ***V Durairaj,*** JW Brill, RC Rai, JE Crow **– '**Destruction of an orbitally ordered and spin polarized state: Colossal magnetoresistance in $Ca_3Ru_2O_7$' – *J. of Electronic Materials* **33** 11 (2004)
16. G Cao, XN Lin, S Chikara, ***V Durairaj,*** E Elhami **– '**High temperature weak ferromagnetism on the verge of a metallic state: Impact of dilute Sr doping on $BaIrO_3$' – *Phys. Rev. B* **69** 174418 (2004)
17. G Cao, L Balicas, XN Lin, S Chikara, E Elhami, ***V Durairaj,*** JW Brill, RC Rai, JE Crow **– '**Field tuned collapse of an orbitally ordered and spin–polarized state: Colossal magnetoresistance in the bilayered ruthenate $Ca_3Ru_2O_7$' – *Phys. Rev. B* **69** 014404 (2004)

## Presentations in Conferences/Seminars:

*(Including 10 Invited and 19 contributed talks)*

1. ***V Durairaj*** – 'A systematic study of thermodynamics and transport properties of $Ca_{n+1}(Ru_{1-x}Cr_x)_nO_{3n+1}$' – *Condensed Matter Seminar, Department of Physics & Astronomy, University of Kentucky,* Lexington, USA, 2 Sept 2008 – *Invited*
2. ***V Durairaj,*** S Chikara, A Sim, T Qi, G Cao – 'Antiferromagnetic metallic state and spin-valve behavior in Cr doped $Ca_3Ru_2O_7$' – *The 4$^{th}$ Annual Departmental Research Poster Session, University of Kentucky*, Lexington, USA, 18 Aug 2007 – *Poster*
3. ***V Durairaj,*** S Chikara, A Sim, T Qi, G Cao – 'Development and synthesis of novel electronic materials – Thy art of growing single crystals' – *The 4$^{th}$ Annual Departmental Research Poster Session, University of Kentucky*, Lexington, USA, 18 Aug 2007 – *Poster*

4. ***V Durairaj,*** S Chikara, S Parkin, G Cao – 'Partial antiferromagnetism in spin-chain $Sr_5Rh_4O_{12}$, $Ca_5Ir_3O_{12}$ and $Ca_4IrO_6$ single crystals' – *The 4th Annual Departmental Research Poster Session, University of Kentucky*, Lexington, USA, 18 Aug 2007 – *Poster*
5. J Kim, Hosub Jin, SJ Moon, JY Kim, BG Park, CS Leem, Jaejun Yu, TW Noh, C Kim, SJ Oh, ***V Durairaj***, G Cao, JH Park – 'A novel J=1/2 Mott insulator realized in $Sr_2IrO_4$' – *The 10th Asia Pacific Physics Conference,* Pohang, Korea, 23 August 2007 – *Invited*
6. ***V Durairaj*** – 'Antiferromagnetic metallic state in bilayered calcium ruthenate: A synergistic impact of Cr substitution' – *Material Science Division Seminar, Indra Gandhi Center for Atomic Research,* Kalpakkam, India, 18 May 2007 – *Invited*
7. ***V Durairaj*** – 'Synergistic 4d–3d electron coupling in Cr substituted ruthenates' – *Physics Seminar, The Institute of Mathematical Sciences,* Chennai, India, 16 May 2007 – *Invited*
8. ***V Durairaj*** – 'Synergistic 4d–3d electrons – Impact of Cr substitution in ruthenates' – *Seminar, Department of Physics, Indian Institute of Technology Madras,* Chennai, India, 15 May 2007 – *Invited*
9. G Cao, ***V Durairaj***, S Chikara, P Schlottmann – 'Colossal magnetoresistance by avoiding a ferromagnetic state in Mott system $Ca_3Ru_2O_7$ – *The International Conference on Strongly Correlated Electron Systems*, Houston, USA, 13–18 May 2007 – *Poster*
10. ***V Durairaj*** – 'Antiferromagnetic metallic state in bilayered calcium ruthenate: A synergistic impact of Cr substitution' – *School of Physical Sciences, Jawaharlal Nehru University,* New Delhi, India, 9 May 2007 – *Invited*
11. ***V Durairaj,*** S Chikara, G Cao, P Schlottmann – 'Antiferromagnetic metallic state: A thermodynamic and transport study of $Ca_3(Ru_{1-x}Cr_x)_2O_7$' – *APS March Meeting,* Denver, USA, 5–9 March 2007
12. A Bautista, ***V Durairaj,*** S Chikara, G Cao, KW Ng – 'Measurement of the Mott insulating gap in $Ca_3Ru_2O_7$ by tunneling spectroscopy' – *APS March Meeting,* Denver, USA, 5–9 March 2007
13. A Douglass, ***V Durairaj***, S Chikara, G Cao, S Parkin, P Schlottmann – 'Antiferromagnetism and geometrical frustration in one dimensional $Ca_5Ir_3O_{12}$ and $Ca_4IrO_6$ single crystals' – *APS March Meeting*, Denver, USA, 5–9 March 2007
14. S Chikara, ***V Durairaj***, G Cao, JW Brill, P Schlottmann – 'Possible quantum criticality and coexistence of spontaneous ferromagnetism and field-induced metamagnetism in triple layered $Sr_4Ru_3O_{10}$' – *APS March Meeting*, Denver, USA, 5–9 March 2007
15. G Cao, S Chikara, ***V Durairaj***, S Parkin, P Schlottmann – 'Magnetic anisotropy and geometrical frustration in the Ising spin-chain system $Sr_5Rh_4O_{12}$' – *APS March Meeting*, Denver, USA, 5–9 March 2007
16. V Varadarajan, S Chikara, ***V Durairaj***, XN Lin, G Cao, JW Brill - 'Specific heat of $(Ca_{1-x}Sr_x)_3Ru_2O_7$ single crystals' – *APS March Meeting*, Denver, USA, 5–9 March 2007
17. ***V Durairaj*** – 'Synergistic 3d & 4d electrons – Impact of Cr substitution on ruthenates' – *Condensed Matter Seminar, Department of Physics & Astronomy, University of Kentucky,* Lexington, USA, 17 Oct 2006 – *Invited*
18. ***V Durairaj,*** XN Lin, S Chikara, A Douglass, A Sim, G Cao – 'Impact of Cr substitution on double layered Calcium ruthenate: A magnetic and transport study of $Ca_3(Ru_{1-x}Cr_x)_2O_7$' – *The 3rd Annual Departmental Research Poster Session, University of Kentucky*, Lexington, USA, 18 Aug 2006 – *Poster*
19. ***V Durairaj,*** A Douglass, XN Lin, S Chikara, A Sim, G Cao – 'Synthesis and thermodynamics of novel electronic materials – Exploring the world of complexity' – *The 3rd Annual Departmental Research Poster Session, University of Kentucky,* Lexington, USA, 18 Aug 2006 – *Poster (Award winner)*
20. ***V Durairaj***, E Elhami, S Chikara, XN Lin, A Douglass, G Cao, P Schlottmann, ES Choi, RP Guertin – 'Itinerant ferromagnetism in Cr doped perovskite ruthenates' – *APS March Meeting,* Baltimore, USA, 13–17 Mar 2006
21. XN Lin, ***V Durairaj,*** ZX Zhou, S Chikara, A Douglass, V Varadarajan, VA Bondarenko, JW Brill, P Schlottmann, G Cao – 'Observation of oscillatory magnetoresistance periodic in *1/B* and *B* in $Ca_3Ru_2O_7$' – *APS March Meeting,* Baltimore, USA, 13–17 Mar 2006
22. S Chikara, ***V Durairaj***, WH Song, YP Sun, XN Lin, A Douglass, G Cao – 'Borderline magnetism in $Sr_4Ru_3O_{10}$: Impact of dilute La and Ca doping on itinerant metamagnetism and ferromagnetism' – *APS March Meeting*, Baltimore, USA, 13–17 Mar 2006
23. ***V Durairaj*** – 'Unusual colossal magnetoresistance and quantum oscillations in Mott-like system $Ca_3Ru_2O_7$' – *The Institute of Mathematical Sciences,* Chennai, India, 9 Nov 2005 – *Invited*

24. ***V Durairaj,*** E Elhami, XN Lin, S Chikara, A Douglass, G Cao, P Schlottmann, ES Choi, RP Guertin – 'Itinerant ferromagnetism and metamagnetism in Cr doped perovskite ruthenates' – *Indo-US Conference on Novel and Complex Materials*, Kolkata, India, 26–29 Oct 2005 – *Poster*
25. XN Lin, ***V Durairaj,*** G Cao, P Schlottmann, SE Nagler, M Lumsden, ZX Zhou – 'Orbital physics: Unusual colossal magnetoresistance and quantum oscillations in the Mott System $Ca_3Ru_2O_7$' – *SNS-HFIR Users Meeting*, Oak Ridge, USA, 11–13 Oct 2005 – *Poster*
26. M Freamat, XN Lin, ***V Durairaj,*** S Chikara, G Cao, JW Brill – 'Thermodynamic properties of the spin-chain compound, $Pr_3RuO_7$'–*ECRYS-2005,* Cargese, France, 21–27 Aug 2005–*Poster*
27. ***V Durairaj,*** XN Lin, S Chikara, E Elhami, VA Bondarenko, JW Brill, G Cao, S Parkin, L Balicas, Y Xin– 'Quantum oscillations and competing ground states in triple-layered $Sr_4Ru_3O_{10}$'–*Workshop on Novel Electronic Materials,* Lexington, USA, 25–27 Apr 2005–*Poster*
28. XN Lin, ***V Durairaj,*** S Chikara, E Elhami, G Cao, ZX Zhou, P Schlottmann – 'Colossal magnetoresistance by avoiding a ferromagnetic state in the Mott system $Ca_3Ru_2O_7$' – *Workshop on Novel Electronic Materials*, Lexington, USA, 25–27 Apr 2005
29. XN Lin, ***V Durairaj,*** S Chikara, E Elhami, G Cao, ZX Zhou, P Schlottmann – 'Orbitally driven behavior: Mott transition, quantum oscillations and colossal magnetoresistance in bilayered $Ca_3Ru_2O_7$' – *Workshop on Novel Electronic Materials,* Lexington, USA, 25–27 Apr 2005 – *Poster*
30. M Freamat, XN Lin, ***V Durairaj,*** S Chikara, G Cao, JW Brill – 'Thermodynamic properties of $Pr_3RuO_7$' – *Workshop on Novel Electronic Materials,* Lexington, USA, 25–27 Apr 2005 – *Poster*
31. E Elhami, XN Lin, S Chikara, ***V Durairaj,*** G Cao – 'High temperature weak ferromagnetism on the verge of a metallic state: Impact of dilute Sr doping on $BaIrO_3$' – *Workshop on Novel Electronic Materials,* Lexington, USA, 25–27 Apr 2005 – *Poster*
32. S Chikara, XN Lin, E Elhami, ***V Durairaj,*** G Cao, P Schlottmann – 'From itinerant ferromagnetism to insulating anti-ferromagnetism: A magnetic and transport study of single crystal $SrRu_{1-x}Mn_xO_3$ ($0 \le x < 0.60$)' – *Workshop on Novel Electronic Materials,* Lexington, USA, 25–27 Apr 2005 – *Poster*
33. ***V Durairaj,*** XN Lin, S Chikara, E Elhami, VA Bondarenko, JW Brill, G Cao, S Parkin, L Balicas, Y Xin – 'Quantum oscillations and competing ground states in triple-layered $Sr_4Ru_3O_{10}$' – *APS March Meeting*, Los Angeles, USA, 21–25 Mar 2005
34. G Cao, ***V Durairaj,*** E Elhami, XN Lin, S Chikara – 'Magnetic and transport study of single crystal $SrRu_{1-x}Cr_xO_3$ ($0 \le x < 0.15$) with increased Curie temperature' – *APS March Meeting*, Los Angeles, USA, 21–25 Mar 2005
35. XN Lin, ***V Durairaj,*** S Chikara, E Elhami, G Cao, L Balicas, P Schlottmann, JE Crow – 'Orbitally driven behavior: Mott transition, quantum oscillations and colossal magnetoresistance in bilayered $Ca_3Ru_2O_7$' – *APS March Meeting*, Los Angeles, USA, 21–25 Mar 2005
36. M Freamat, XN Lin, ***V Durairaj,*** S Chikara, G Cao, JW Brill – 'Thermodynamic properties of $Pr_3RuO_7$' – *APS March Meeting*, Los Angeles, USA, 21–25 Mar 2005
37. S Chikara, XN Lin, E Elhami, ***V Durairaj,*** G Cao, P Schlottmann – 'From itinerant ferromagnetism to insulating anti-ferromagnetism: A magnetic and transport study of single crystal $SrRu_{1-x}Mn_xO_3$ ($0 \le x < 0.60$)' – *APS March Meeting*, Los Angeles, USA, 21–25 Mar 2005
38. E Elhami, G Cao, XN Lin, S Chikara, ***V Durairaj*** – 'High temperature weak ferromagnetism on the verge of a metallic state: Impact of dilute Sr doping on $BaIrO_3$' – *APS March Meeting*, Los Angeles, USA, 21–25 Mar 2005
39. ***V Durairaj*** – 'Anti-ferromagnetic spin systems without Neel order' – *Graduate Student Post-Doc Seminar, Department of Physics and Astronomy, University of Kentucky,* Lexington, USA, 2 Feb 2005 – *Invited*
40. ***V Durairaj,*** G Cao, Y Xin, S Alexander, JE Crow, P Schlottmann – 'High temperature weak ferromagnetism and "diamagnetism" in bilayered $Sr_3Ir_2O_7$' – *APS March Meeting*, Montreal, Canada, 22–26 Mar 2004
41. G Cao, L Balicas, XN Lin, S Chikara, E Elhami, ***V Durairaj,*** RC Rai, JW Brill, JE Crow – 'Field tuned collapse of an orbitally ordered and spin-polarized state: Colossal magnetoresistance in bilayered ruthenate' – *APS March Meeting*, Montreal, Canada, 22–26 Mar 2004
42. ***V Durairaj* – '**Observational Cosmology' – *Colloquium, Raman School of Physics, Pondicherry University,* Pondicherry, India, 12 Aug 2000 – *Invited*
43. ***V Durairaj* – '**Observational Cosmology' – *Seminar, Vacation Students Programme, Inter-University Centre for Astronomy and Astrophysics,* Pune, India, 5 Jul 2000

## Unpublished Theses:

- ***Vinobalan Durairaj***, 'A systematic study of thermodynamic and transport properties of layered $Ca_{n+1}(Ru_{1-x}Cr_x)_nO_{3n+1}$' – *Advisor:* Dr. Gang Cao, Professor in Physics, University of Kentucky, Lexington, USA – Ph.D. dissertation, Dec 2008 (Proposed)
- ***Vinobalan D***, 'Curie temperature measurement of magnetic materials' – *Advisor:* Dr. K Srinivasa Manja, Reader in Physics, Pondicherry University, Pondicherry, India – M.Sc. dissertation, May 2001
- ***Vinobalan D***, 'Observational Cosmology' – *Advisor:* Dr. Jayant V Narlikar, Founder & Director, Inter-University Center for Astronomy and Astrophysics, Pune, India – 'Vacation Students Programme' research project, Jul 2000